Photodynamic antimicrobial chemotherapy against *Staphylococcus aureus* and *Escherichia coli* sensitized using indium (III) cationic porphyrins linked to core-shell magnetic nanoparticles

By

Lekgowa Collen Makola

A thesis submitted in fulfilment of the requirements for the degree of

MASTER OF SCIENCE

AT

RHODES UNIVERSITY

RHODES UNIVERSITY
Where leaders learn

December 2020

Declaration by candidate

I **Lekgowa Collen Makola** declare that the thesis **"Photodynamic antimicrobial chemotherapy against *Staphylococcus aureus* and *Escherichia coli* sensitized using indium (III) cationic porphyrins linked to core-shell magnetic nanoparticles"** hereby submitted to Rhodes University has not being previously submitted by me or anyone before for any degree requirements in any university; that is my work in design and execution, and all the materials contained herein have been duly acknowledged.

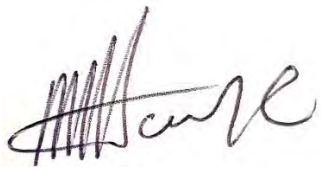

……..

L. Collen Makola

Student Number: G19M7505

Dedication

This work is dedicated to my beloved family Makgaolane Selina Monama, Nkwana Albert Monama, Motenabatho Elvis Makola, Tirelo Iren Nhlapo, Kgobise Stanley Makola, Tshehlana Add Makola, Comfort Makola, and my closest friend Aphiwe Sipokazi Ntsokwana.

Acknowledgements

I would like to take this wonderful opportunity to express my best regards to my research overseer and supervisor **Distinguished Professor Tebello Nyokong**. Thank you for turning a village boy into knowledge weaponized and industrious researcher. I highly appreciate the opportunity given to me to work with the Institute for nanotechnology innovation (INI) and S22 chemistry laboratory, Rhodes University.

It gives me a great pleasure to give thanks to many people who assisted me in carrying on my master's projects; my co-supervisor Professor John Mack, my mentors Dr. Muthumuni Managa and Dr. Balaji Babu, my colleague and friend "Dr." Donovan M. Mafukidze. Sincere gratitude to my host at the United States International University of Africa (USIU-A) Dr. Edith Amuhaya and her supportive and caring students (Abu, Ruben, Meggie, and Oscar) "*nalifurahiya chakula cha Nairobi; ugali na nyama choma, githeri, chapatti, pilau*". Thank you to Ms Gail Cobus, Dr. Jonathan Britton, Mr Francis Chindeka, S22 colleagues and friends, National Research Foundation (NRF) and Desmond Goddard (2019) for funding. Exceptional appreciation to my closely knit family for their everyday unreserved support and guidance.

Greatest thank you to the Heavenly Father God for protecting, guiding, and coordinating every step of my life "*give thanks in all circumstances; for it is God's will for you in Christ Jesus, 1 Thessalonians 5:18*".

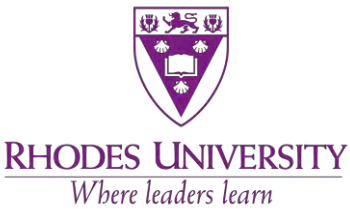

Abstract

Photodynamic antimicrobial chemotherapy (PACT) is a well-known antimicrobial therapy technique used against multi-drug resistant pathogens. In this study, the syntheses, characterization, photophysicochemical properties, and the applications of symmetrically and asymmetrically substituted cationic indium (III) porphyrins linked to silver/copper ferrite core-shell ($Ag/CuFe_2O_4$) magnetic nanoparticles (MNPs) as potential photosensitizers for PACT are reported. The synthesized complexes include axially modified porphyrins quaternized through an axial ligand. All the asymmetrically substituted porphyrins were linked to the NPs via an ester bond and the symmetrically substituted porphyrins were linked (peripherally and /or axially) via self-assembly (Ag-S and/or Ag-N). The impact of axial modification, peripheral substituents, conjugation to the NPs, the number of positive charges, and the chain length of the alkyl halides quaternizing agents on PACT efficacy and photophysicochemical properties of porphyrins were studied. High singlet oxygen quantum yields and antimicrobial log reductions were observed.

Lipophilicity and hydrophilicity of the porphyrins were also studies, where the complexes quaternized with methyl iodide showed relatively high hydrophilicity character. Upon in vitro PACT studies, the quaternized complexes were observed to have 0% viable colony, signifying their effectiveness. Moreover, the highest log reductions of 9.27 were observed against *S. aureus* and 9.58 were observed against *E. coli*.

The findings from this work delineate that singlet oxygen generation alone is not a distinct factor on the PACT efficacy of the porphyrin complexes, since some of the complexes have

practically the same singlet oxygen quantum but different PACT activity. However, other contributing factors including water solubility play a significant role.

Key words: photodynamic antimicrobial chemotherapy, photosensitizers, porphyrins, quaternize, magnetic nanoparticles, *Es*cherichia *coli*, *Staphylococcus aureus*.

Table of Contents

List of abbreviations

^{1}H-NMR	Proton Nuclear Magnetic Resonance
ADMA	Anthracene-9,10-diyl-bis-methylmalonate
AFM	Atomic force microscopy
CFU	Colony forming units
DCC	N,N-dycyclohexylcarbodiiamide
DCM	Dichloromethane
DDQ	2,3-dichloro-5,6-dicyanobenzoquinone
DLS	Dynamic light scattering
DMA	9,10-dimethylanthracene
DMF	Dimethylformamide
DMSO	Dimethylsulfoxide
DMSO-d_6	Deuterated dimethylsulfoxide
DNA	Deoxyribonucleic acid
DPE	Diphenyl ether
EDS	Energy dispersive X-ray spectroscopy
EDTA	Ethylendiaminetetraacetic acid
ESCA	Electron spectroscopy for chemical analysis
FDA	Food and Drug Administration
FT-IR	Fourier-transform infrared spectroscopy
HexI	Hexyl iodide

HLB	Hydrophilic-lipophilic balance
HOMO	Highest occupied molecular orbitals
HT	Hyperthermia therapy
IC	Internal conversion
ISC	Intersystem crossing
LED	Light-emitting diode
LUMO	Lowest unoccupied molecular orbitals
MCH	6-mercapto-1-hexanol
MeI	Methyl iodide
MNPs	Magnetic nanoparticles
MRI	Magnetic resonance imaging
MW	Microwave
NPs	Nanoparticles
OLA	Oleic acid
OLM	Oleyamine
PACT	Photodynamic antimicrobial chemotherapy
PDI	Polydispersity index
PET	Photo-induced electron transfer
PMT	Peltier cooled photomultiplier tube
PS	Photosensitizer
PSs	Photosensitizers
RB	Rose Bengal

ROS	Reactive oxygen species
RT	Room temperature
SA	Self-assembly
SPION	Superparamagnetic iron oxide nanoparticle
TCSPC	Time Correlated Single Proton
TEM	Transmission electron microscope
TFA	Trifluroacetic acid
TGA	Thermal gravimetric analysis
THF	Tetrahydrofuran
TLC	Thin layer chromatograph
TOF	Time of flight
UV-Vis	Ultraviolet-visible spectroscopy
XPS	X-ray photoelectron spectroscopy
XRD	X-ray powder diffraction
ZnTPP	Zinc tetraphenylporphyrin

List of symbols

*S	singlet excited state
$^1O_2$	singlet excited oxygen
$^3O_2$	molecular oxygen
Abs	absorbance/absorption
e-	electron
H-	proton
ϕ_Δ	singlet oxygen quantum yield
ϕ_F	fluorescence quantum yield
S_0	singlet ground state
t	time
T_3	triplet excited state
α	non-peripheral position
β	peripheral position
ε	molar extinction coefficient
ζ	zeta potential
λ	wavelength
τ_F	fluorescence lifetime

Problem statement

The globally emanating and rapidly growing resistance among various classes of virulent gram-positive and gram-negative bacteria towards well known and effective antibiotics has enticed researchers to search for alternative techniques for bacterial mitigation with less to no chance of developing resistance in a long run. Case in point, hospitals in the United States in 2013 reported a pronounced increase of Methicillin-resistant pathogens; amongst them is *Staphylococcus aureus* spa Type t002 isolates.

Photodynamic antimicrobial chemotherapy is a well-studied therapeutic technique and a possible alternative to antibiotic treatment for localized infection. This technology involves a combination of non-toxic compounds, known as photosensitizers (e.g. porphyrins), visible light of the appropriate wavelength to produce reactive oxygen species that initiate bacterial obliteration through oxidative cell damage. Most of the photosensitizers used in this therapeutic technique do not meet the criteria of becoming ideal photosensitizers, such as; chemical and photostability, water solubility, hydrophilic-lipophilic balance, high singlet oxygen generation, and recoverability after use. The synthesis of the photosensitizer should be easy with starting materials readily available. Sparing no effort towards developing ideal photosensitizers; cationic porphyrins linked to cytotoxic magnetic nanoparticles for highly enhanced photodynamic antimicrobial chemotherapy activity has been thoroughly studied in this thesis. Synergistic cytotoxicity is anticipated by the combination of the two entities; photosensitizers and magnetic nanoparticles. Moreover, the nanoparticles facilitate recovery and reuse of the materials.

Chapter 1

Introduction

This chapter provides an overview of the literature on porphyrins, magnetic nanoparticles, and conjugates of the two and their applications for photosensitization in photodynamic antimicrobial chemotherapy.

1.1 Photodynamic antimicrobial chemotherapy (PACT)

1.1.1 Background and mechanism

Photodynamic antimicrobial chemotherapy (PACT) also known as antimicrobial photodynamic therapy (aPDT) is a potential antimicrobial therapy that employs a combination of non-toxic photosensitizer (PS) (such as porphyrins) and light of an appropriate wavelength (ideally at the maximum absorption of the photosensitizer) [1]. The bacterial obliteration or mitigation in PACT is initiated by the lethal oxidative stress brought by reactive oxygen species (ROS) when light is irradiated on the target cells in the presence of molecular oxygen (O_2) [2]. ROS, mainly singlet oxygen ($^1O_2$) are responsible for cell death by reacting with various cellular components.

The mechanism behind porphyrin photosensitization during PACT is shown in **Fig. 1.1**. The photosensitizer is introduced to the bacterial solution or the targeted site, followed by irradiation (process **X** in **Fig. 1.1**) of the PS-bacterial mixture with the light of an appropriate wavelength (at λ_{max} of the PS), which consequently leads to photoexcitation of the PS from ground state (S_0) to its singlet excited state ($^*S_1$) [3]. The PS in the $^*S_1$ then undergo competing processes that might negatively or positively impact ROS generation. The PS in the $^*S_1$ may undergoes intersystem crossing (process **Y** in **Fig. 1.1**) to an excited triplet state ($^*T_3$) which results in the ROS generation [3,4]. The PS in the $^*T_3$ might undergo two co-existing processes for ROS generation, namely, **Type I** and **Type II** reactions [4].

Type I reaction involves a direct transfer of an electron (e^-) or a proton (H^+) from the PS in the $^*T_3$ to the substrates in the cell (e.g. water in the bacterial cell membrane), to generate radical ions, which consequently react with oxygen inducing cytotoxic ROS, typically

hydroxyl radicals (OH^-) and superoxide (O_2^-). These species are highly reactive and they penetrate through the bacteria cell effortlessly fast, causing extreme oxidative damage [5].

Type II process involves the transfer of energy from the PS in the $^*T_3$ to the triplet ground state molecular oxygen ($^3O_2$) resulting in the generation of $^1O_2$. Singlet oxygen is the molecular oxygen in its electronically excited state and is less stable; moreover, it is the predominant cytotoxic substrate amongst all the ROS in PACT. $^1O_2$ interact with various components within the cell such as proteins and the deoxyribonucleic acid (DNA) bases [6]. There are various mechanisms through which bacterial obliteration occurs as a result of these ROS; These include cross-linkage between the proteins, oxidative damage of the nucleic acids, proteins, and membrane lipids [6,7].

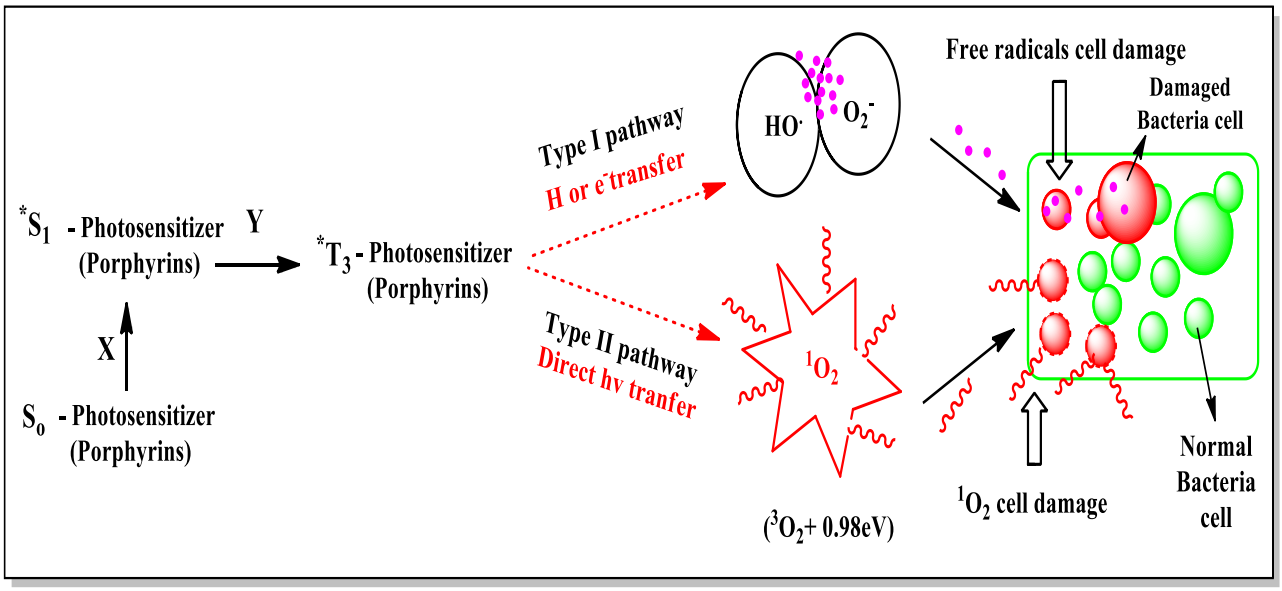

Fig. 1.1 Schematic illustration of photodynamic reaction on bacterial cell. S_0 = Ground state; $^*S_1$ = First singlet excited state; $^*T_3$ = Triplet excited state; X = Energy absorption; Y = Intersystem crossing; hv = Photon energy; $^3O_2$ = Ground state molecular oxygen; $^1O_2$ = Singlet oxygen.

1.1.2 Targeted bacteria cell walls and their susceptibility to PACT

Bacteria are predominantly classified into either Gram-positive (+) such as *Bacillus subtilis*, *Enterococcus faecalis*, *and Staphylococcus aureus* or Gram-negative (-) such as *Klebsiella pneumoni*, *Escherichia coli*, *Pseudomonas aeruginosa* [8]. In this study, both Gram (+) *Staphylococcus aureus* and Gram (-) *Escherichia coli* strains were used for PACT studies. The distinctive traits between Gram (+) and Gram (-) bacteria are the cell wall ultra-structure composition as shown in **Fig. 1.2**, which plays a vital role in the susceptibility of the strain towards treatment using PACT. Gram (-) bacteria are known to be more resistant towards PACT inactivation using various neutral and anionic photosensitizers (PSs) [9]. The absence of the protective layer (lipopolysaccharides) in the Gram (+) bacteria cell membrane makes it more susceptible to PSs, as a result of the presence of a relatively porous layer of lipoteichoic acid and peptidoglycan with no outer membrane as shown in **Fig. 1.2**.

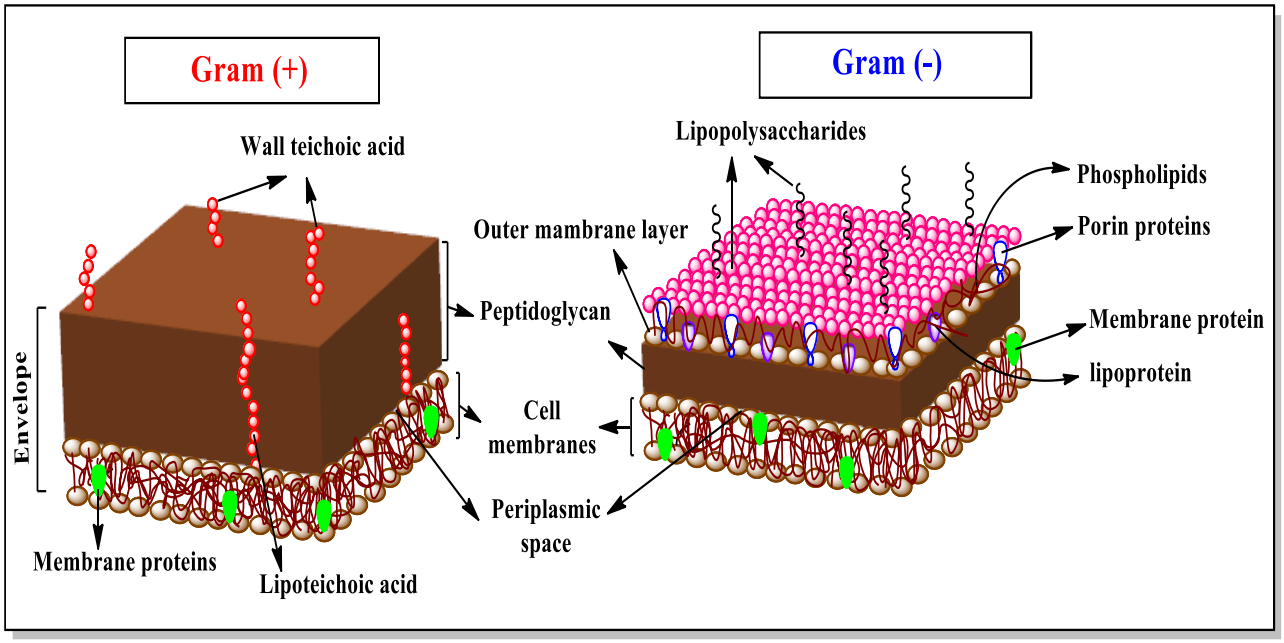

Fig. 1.2 Schematic representation of Gram (+) (**left**) and Gram (-) (**right**) bacteria cell wall and cytoplasmic membrane structure.

The cell wall of Gram (-) bacteria is less permeable by neutral and anionic PSs, however cationic PSs are known to interact effectively with the cell wall [10]. Various approaches have been used to inactivate Gram (-) bacteria, which involves the use of cell membrane disorganizing agents such as ethylendiaminetetraacetic acid (EDTA) to enhance their sensitivity [11]. There are various modes of bacteria obliterations by PSs in PACT as described in previous researches [12]. The first mode of oxidative destruction is based on the ability of the PS to bind and become localized in the cell membrane through either columbic or hydrophobic interactions. The cytotoxicity is then initiated through irradiation with light over the target site containing the PS. The second mode involves the interaction of the PS and the cell in a solution. PS generates ROS in solution, which can diffuse into the bacteria cell membranes and cause cell damage. The third mode involves the PS molecules penetrating the bacteria cell wall and directly interacting with the intracellular components (e.g. DNA, proteins). All the above-mentioned bacteria inactivation methods through PACT processes are complex and non-specific, the obliterations are known to be through various mechanisms; including functional damage, cell membrane damage, and/or morphological variation [8,13,14].

1.2 Porphyrins

1.2.1 Background (Structure and applications)

Porphyrins are a class of aromatic macrocycle organic compounds that are composed of four pyrrole entities joined at their alpha (α) carbon atom through methane bridges (=CH-) as shown in **Fig. 1.3**. The structure of porphyrin was first proposed in 1912 by Küster [15], however, it remained a dispute for some time due to the stability of this large aromatic molecule until Fischer and Zeile, later on, proposed the same structure when they

succeeded in synthesizing protoheme from pyrrolic starting materials in 1929 [16]**.** After many setbacks, a phenomenal breakthrough was achieved in 1954, which led the way to solve protein structures related to porphyrins, and consequently haemoglobin [17]. Porphyrins have a total of 26 π-electrons, of which an extended conjugated 18 π-electrons form a planar continuous system which is responsible for their aromatic behaviour [18]. Porphyrins are considered highly aromatic, based on Huckel's (4n+2) rule. One of the outcomes of the porphyrin conjugated system behaviour is the absorption within the visible region of the electromagnetic spectra. Porphyrins are famously known to be colours of life due to their fundamental significance in sustaining life in different ways; such as haemoglobin which stores and transports oxygen to various organs, chlorophyll for photosynthesis, and form various enzyme and vitamins required by our body for optimal functioning [19]. Synthetic porphyrin complexes show potential flexibility depending on the metal ions, peripheral substitution, and axial ligation. The choice of each porphyrin components or substituents are totally dependent on the applications.

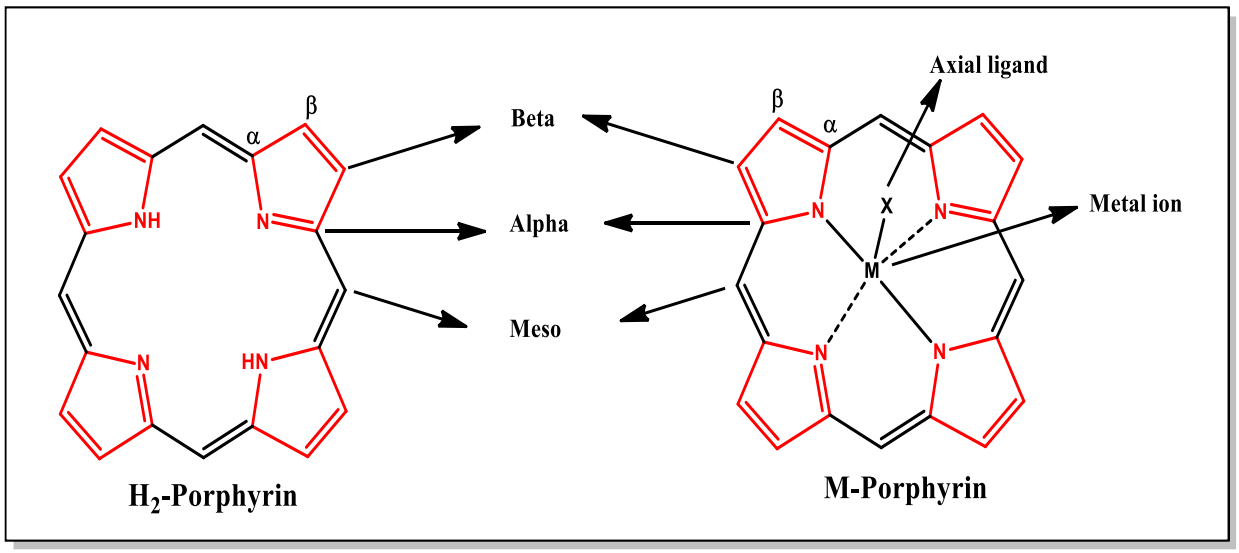

Fig. 1.3 Schematic representation of an unsubstituted free-base (**left**) and matalated (**right**) porphyrins showing beta (β), alpha (α), and meso structural positions.

There are three main points of substitution on the metalloporphyrin molecules (shown in **Fig. 1.3**) which allows structural modifications and may result in major alteration of the fundamental properties of the whole molecule. Moreover, synthetic porphyrins possess interesting photophysical, chemical, and biological properties that makes them ideal candidates for medicinal and industrial applications (**Fig. 1.4**). Clinical Applications of porphyrins in PACT includes the treatments of dermatological conditions [13]. Porphyrins have also been used in the treatment of topical human infections and consequently replacing skin-applied antibiotics [20,21]. Synthetic and bioinspired metalloporphyrins are also employed in the industries as reusable catalysts in oxidative bleaching of industrial dyes [22]. Most of these applications depend on the photophysical and photochemical properties possessed by these porphyrins. In this study, porphyrins are studied and employed for PACT.

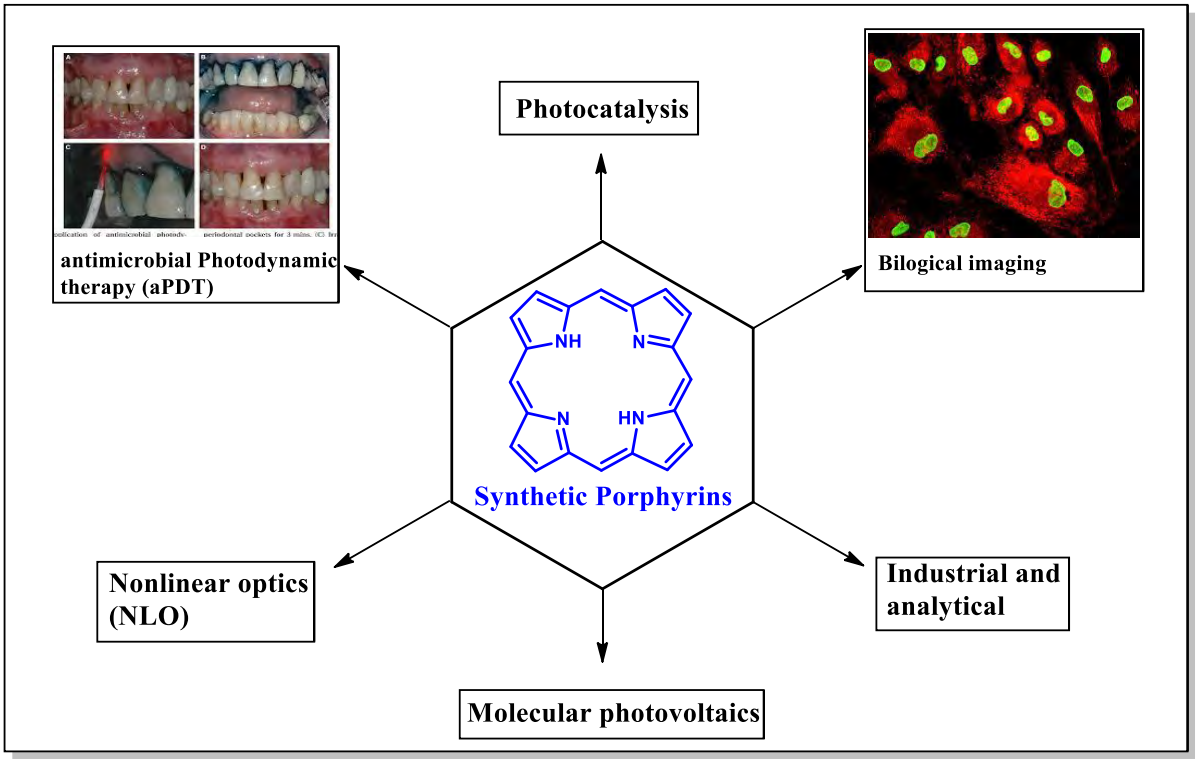

Fig. 1.4 Schematic illustration of some common applications of synthetic porphyrins and metalloporphyrins [13,19].

1.2.2 Synthesis

1.2.2.1 Symmetrically substituted porphyrins (tetra-substituted porphyrins; A_4, or B_4 type)

Because of the preparation simplicity of A_4 or B_4 type porphyrins they are popular. Moreover, they allow a possibility of further chemical modifications. The synthetic procedure generally involves one-step one-flask or two-steps one-flask reactions, through condensation of pyrrole in the presence of the desired aldehyde (**Scheme 1.1**) [23,24].

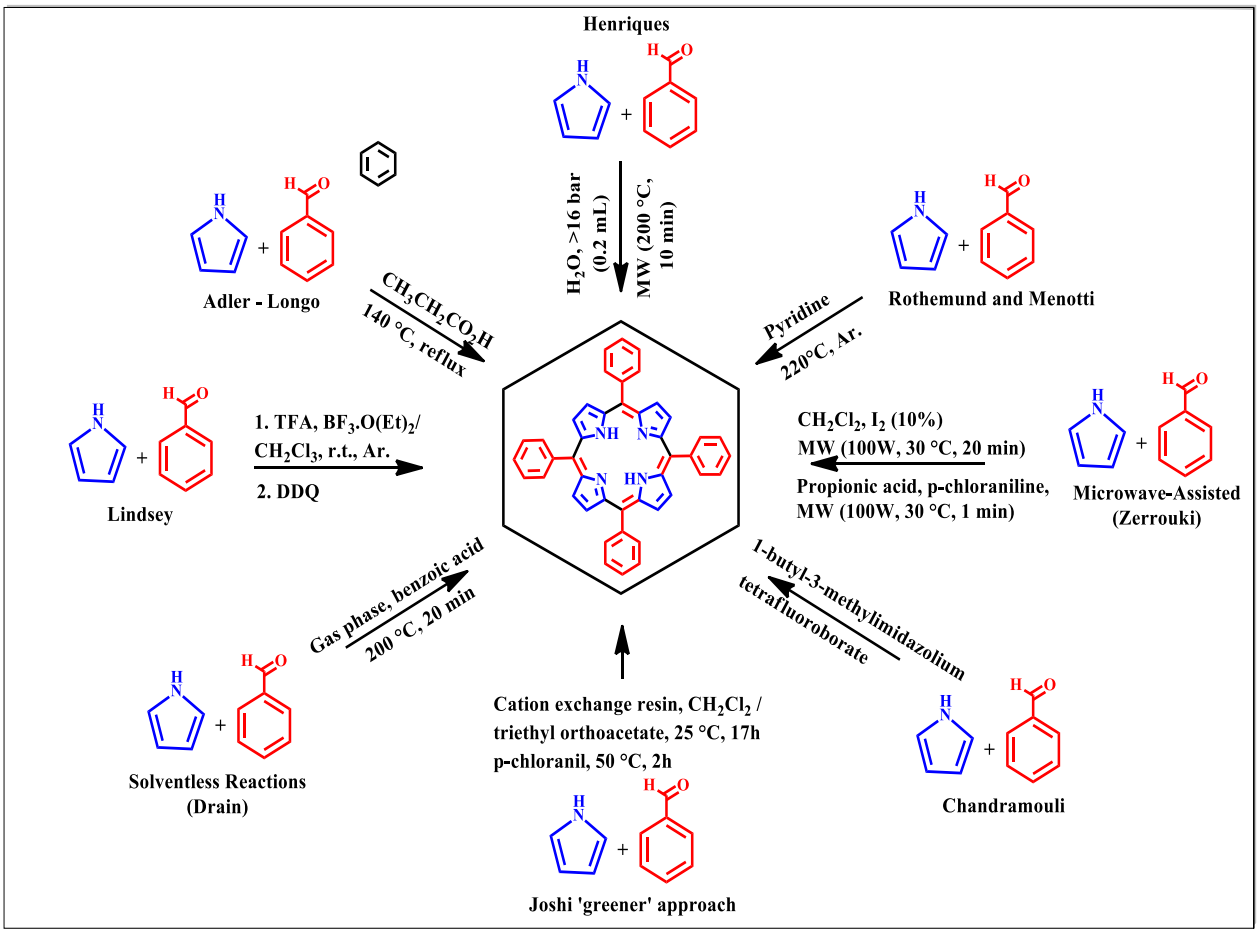

Scheme 1.1 Schematic illustration of various general synthetic procedures of a free-base porphyrin (tetraphenylporphyrin) and their conditions; MW = microwave, r.t. = Room temperature, Ar = Argon, TFA = Trifluroacetic acid, DDQ = 2,3-dichloro-5,6-dicyanobenzoquinone.

1.2.2.1.1 Rothemund and Menotti

The first people to synthesize meso-substituted tetraphenylporphyrin were Rothemund and Menotti [25], which opened a pathway for the synthesis of meso-substituted porphyrins (**Scheme 1.1**). The compound was attained by condensation of pyrrole and benzaldehyde using pyridine as a solvent in an isolated system at 220 °C for 24 h. As a result of these harsh conditions employed, the yield was relatively low (~10%).

1.2.2.1.2 Adler and Longo

In response to the challenge faced by Rothemund and Menotti later Adler and co-workers modified the reaction to milder conditions as shown in **Scheme 1.1** [26]. The procedure involved the reflux of pyrrole in propionic acid followed by the addition of benzaldehyde which afforded up to 20% of the porphyrin. The challenge in Adler and Longo method became the purification process as it involves the formation of tar in high quantity. Moreover, due to the acidic reaction condition involved, acid-sensitive functional groups such as hydroxyl, thiol, and amino groups do not result in the formation of the desired product [27]. This synthetic procedure was employed in this thesis.

1.2.2.1.3 Lindsey and co-workers

Lindsey and co-workers [28] came up with reaction conditions that can be utilized to synthesize porphyrins using acid-sensitive functional groups. Typically, Lindsey method involves two-step one-flak reaction where an equal ratio of pyrrole and benzaldehyde reacted in the presence of trifluoroacetic acid (TFA) or boron trifluoride etherate ($BF_3.OEt_2$) as catalysts and using dichloromethane (DCM) as a solvent under an inert atmosphere for 1

h. Furthermore, the prophyrinogen intermediate is converted into a porphyrin using 2,3-dichloro-5,6-dicyanobenzoquinone (DDQ) (**Scheme 1.1**).

1.2.2.1.4 Microwave-assisted and other methods

Other meso-substituted porphyrins synthetic procedures (**Scheme 1.1**) involve alternative energy sources or reaction media including microwave irradiation. Microwave-assisted synthesis of meso-substituted porphyrin by Zerrouki and co-workers [29] employs two-step synthetic microwave-activated approach to prepare A_4 or B_4 type meso-tetraphenylporphyrins. The conditions involve a mixture of pyrrole, benzaldehyde, and dichloromethane (DCM) in 10% molar equivalence of iodide exposed to microwave (MW) radiation, followed by an introduction of p-chloranaline. This procedure affords reasonable yields (~47%) and the reaction takes <30 min. Various microwave-assisted and solvent-free synthetic procedures have been reported and possess relative high yields within a short period of time without condensation or distillation processes [29–33].

1.2.2.2 Asymmetrical porphyrins (tetra-substituted porphyrins; A_3B, or B_3A type)

The synthesis of asymmetrical porphyrins follows the same synthetic procedures involved in the synthesis of symmetrical porphyrins however the major difference is the presence of two different aldehydes (A and B) and pyrrole [34,35]. The molar ratio of aldehydes of 1:3 (A: B) is commonly used for the synthesis of B_3A-type porphyrin. This molar ratio reduces the probability of the formation of A_4 or B_4 derivatives. The high molar ratio of aldehydes is used for a better statistical condensation to form B_3A-type porphyrin. The aldehyde molar ratio of 1:3 were used in this thesis.

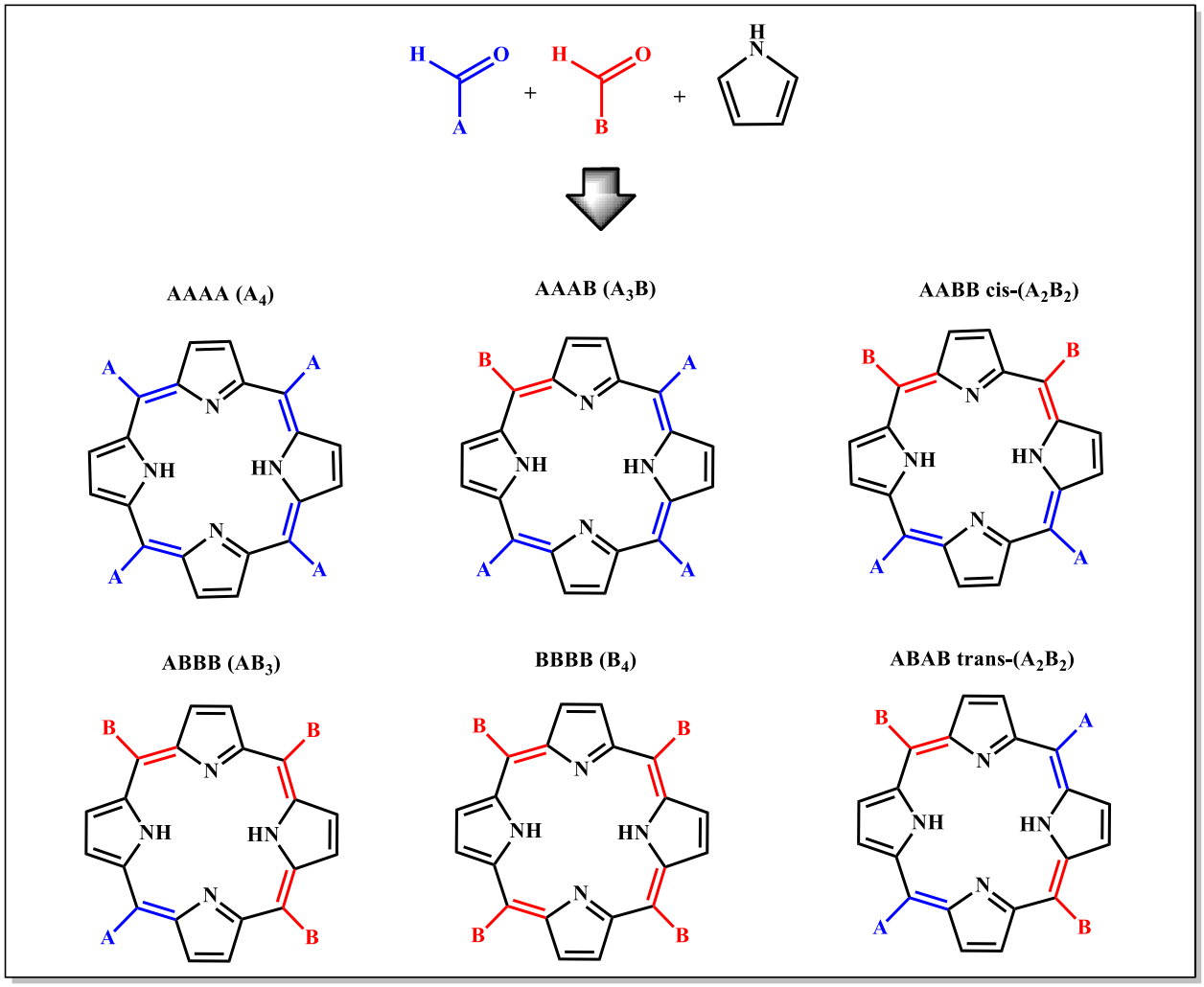

Scheme 1.2 Schematic illustration of possible porphyrin analogues resulting from crude product of general synthetic procedure of an asymmetrical porphyrin.

The molar ratio 1:3 thus results in a maximum of six possible (**Scheme 1.2**) porphyrin derivatives from a crude product, of which various separation techniques such as column chromatography can be employed to extract the porphyrin of interest from the mixture.

1.2.3 Electronic absorption spectra of porphyrins

The intense colour of porphyrins is due to their highly conjugated π-electron systems. They have astonishing UV-Visible absorption spectra characteristics in the visible region and ultraviolet, known as Q-bands (weak) and Soret band (intense), respectively, which are

delineated by **Fig. 1.5**. The spectra of the porphyrins has long been understood and explained in terms of the Gouterman's four-orbital model [36]. According to Gouterman's four-orbital model, the distinct absorption bands of porphyrins are as a result of transitions from the two highest occupied molecular orbitals (HOMOs); that is a_{1u} and a_{2u}, to the two lowest unoccupied molecular orbitals (LUMOs); that is a set of e_g, delineated by **Fig. 1.5** [37]. As a result of these transitions and further orbital mixing and splitting of the two energy states, Soret (B) band originating from the high energy state have greater oscillation strength and consequently Q-bands arising from lower energy state with less oscillation strength.

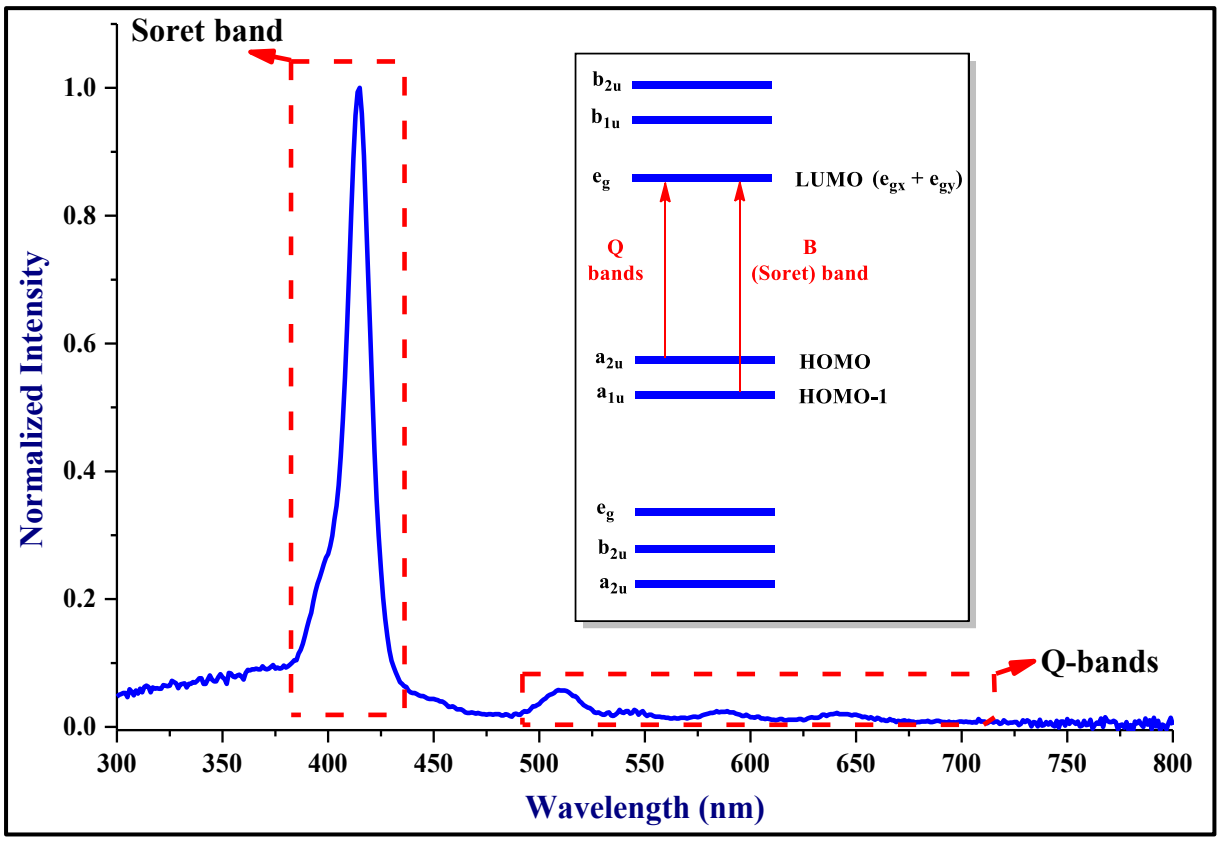

Fig. 1.5 UV-Visible absorption spectra of a free-base 5,10,15,20-tetra(4-pyridyl) porphyrin. Insert; Gouterman four orbital HOMOs and LUMOs electronic transitions showing the origin of Soret (B) band and Q-bands in a porphyrin molecule.

Four Q-bands are observed for a free-base as results of the N-H protons that splits the symmetry (**Fig. 1.5**) and only two bands for a mataloporphyrins. Soret band ranges between 380-500 nm and Q-bands between 500-750 nm depending on the porphyrins β and meso-substituents [37–39].

1.2.4 Photophysical and photochemical parameters of porphyrins

Photophysical parameters can be defined as the properties exhibited by a specific molecule through energy states transitions upon photoexcitation. Fluorescence quantum yields (ϕ_F) and lifetimes (τ_F), and singlet oxygen quantum yields (ϕ_Δ) of the porphyrins were studied. A porphyrin molecule subjected to the light of an appropriate wavelength can be photoexcited to singlet excited state ($S_0 \rightarrow {}^*S_1 \ldots {}^*S_n$) (**Fig. 1.1** and **Fig. 1.6**), where various competing processes take place upon relaxation of the molecule [40–42]. All these parameters can highly be impacted by the porphyrin substituents (meso and beta), the nature of the central metal, photo-induced electron transfer (PET), nature of the solvent, and temperature [43–46].

1.2.4.1 Fluorescence quantum yields (ϕ_F) and lifetimes (τ_F)

The fluorescence quantum yield (ϕ_F) of a fluorophore can be defined as the ratio between the numbers of photons emitted to the number of photons absorbed (**Eq. 1.1**) [47].

$$\phi_F = \frac{\text{number of photons emmited}}{\text{number of photons absorbed}} \qquad (\mathbf{1.1})$$

ϕ_F signifies the efficiency of photoemission or probability of an excited state being diactivated through fluorescence, that is the energy lost by the photoexcited molecule through the emission of light (process F, **Fig. 1.6**).

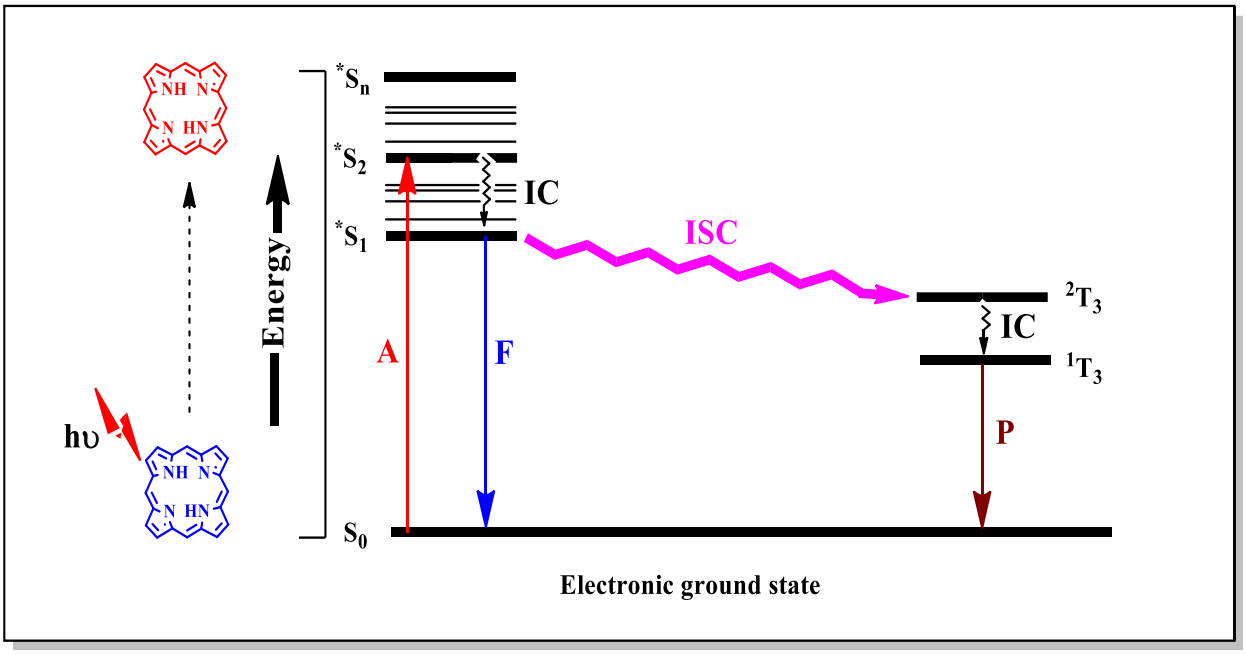

Fig. 1.6 A simplified Jablonski diagram for further illustration of photophysical processes of porphyrins: A = photon absorption; F = fluorescence; IC = internal conversion; ISC = intersystem crossing; P = phosphorescence; S_0 = Ground state; $^*S_1$ = First singlet excited state; $^*S_1$ = Second singlet excited state; $^*S_n$ = n singlet excited state; $^1T_3$ = First triplet excited state, $^2T_3$ = Second triplet excited state.

ϕ_F values in this study were determined using zinc tetraphenylporphyrin (ZnTPP) (ϕ_f^{Std} = 0.030 [48,49]) as a standard following the comparative methods reported in literature [50], using **Eq. (1.2)**.

$$\phi_F = \phi_F^{Std} \times \frac{F\, A^{std} n^2}{F^{Std} A \left(n^{Std}\right)^2} \qquad (1.2)$$

Where ϕ_F^{Std} is the fluorescence quantum yield of the standard, F and F^{Std} are the areas under the fluorescence curve for sample and standard, respectively. A and A^{Std} are the absorbance of the sample and standard, respectively. n and n^{Std} are the refractive indices of the solvent used for sample and standard, respectively. Fluorescence lifetimes (τ_F) can be

defined as the average time a molecule spends in its singlet excited state before any other competing processes (i.e. fluorescence or intersystem crossing) can take place through photon emission to the ground state [47]. Time-Correlated Single Proton Counting (TCSPC) was employed for τ_F studies.

1.2.4.2 Singlet oxygen quantum yield (ϕ_Δ)

Singlet oxygen quantum yield (ϕ_Δ) is the quantitatively measured parameter that depends on the efficiency of the molecule to convert its absorbed energy to ground state molecular oxygen (O_2) to generate singlet oxygen ($^1O_2$) [42]. The magnitude of ϕ_Δ is highly dependent on the molecule's ability to undergo intersystem crossing (ISC) to triplet excited state (**Fig. 1.6**). ISC positively impacts ϕ_Δ, and generally, ISC is facilitated by the heavy atom effect which is highly dependent on the substituents and metal ion of the porphyrins. ϕ_Δ is inversely proportional to ϕ_F since a highly fluorescent molecule will result in minimal ISC to populate the triplet excited state, consequently, a molecule with the lowest fluorescence quantum yield has a higher chance of generating high ϕ_Δ since it has a high probability of undergoing ISC to populate triplet excited state [51]. **Eq. (1.3)** was used to determine the singlet quantum yield for the compounds, where ZnTPP (ϕ_Δ = 0.53) [52] was used as a standard with 9,10-dimethylanthracene (DMA) used as a singlet oxygen quencher in dimethylformamide (DMF) [53].

$$\phi_\Delta = \phi_F^{Std} \times \frac{B.\ I^{Std}}{B^{Std}.\ I} \qquad (1.3)$$

where B and B^{Std} are photobleaching rates of the singlet oxygen quencher in the presence of porphyrin derivatives under investigation and the standard, respectively. I and I^{Std} are the rates of light absorption by the sample and standard, respectively.

1.2.5 Porphyrins in photodynamic antimicrobial chemotherapy (PACT)

Photodynamic antimicrobial chemotherapy of various porphyrins and metalloporphyrins is actively being studied on various gram (+) and gram (-) bacteria strains [13,54–56]. However, in this study, the focus is based on the linkage of the highly effective metalloporphyrins with functionalized magnetic nanoparticles for enhanced PACT activity. Porphyrin derivatives linked to magnetic nanoparticles are actively being studied as ideal PSs for numerous applications. **Table 1.1** [57-69] outlines a summary of reported porphyrins linked to magnetic nanoparticles for various applications including PACT.

Table 1.1. Porphyrins and metalloporphyrins linked to magnetic nanoparticles for various applications.

Porphyrin structure	**Porphyrin/nanomaterial interactions**	**Applications**	**Ref.**
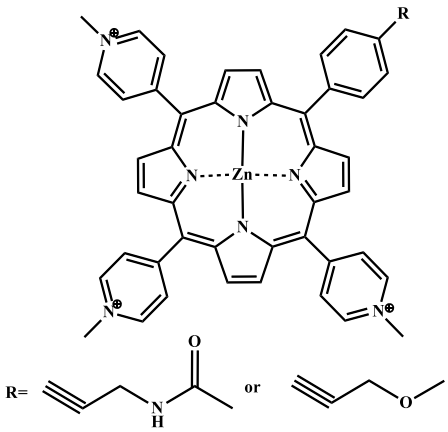	Covalently linked to native dextran T10-coated iron oxide (dextran/Fe_3O_4) nanoparticles through click chemistry	Photodynamic therapy	[57]
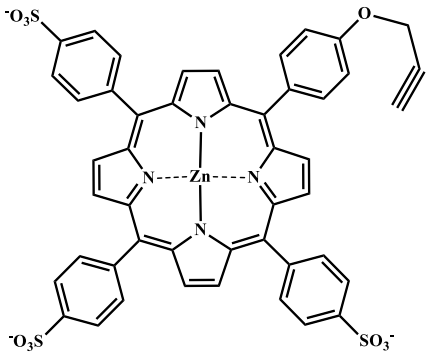	Covalently linked to native dextran T10-coated iron oxide (dextran/Fe_3O_4) nanoparticles through click chemistry	Photodynamic therapy	[57]

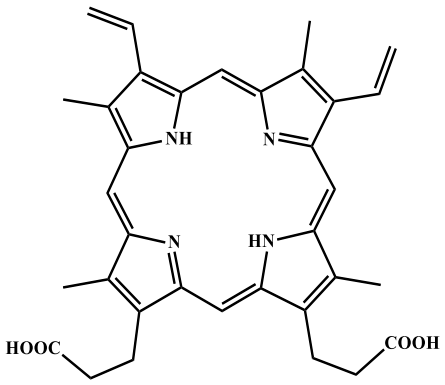	Covalently linked to silica coated magnetite nanoparticles (Si-Fe_3O_4)	biological imaging	[58]
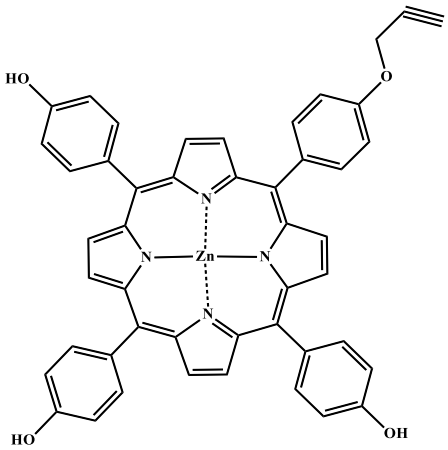	click reaction with azido-functionalized silica-coated superparamagnetic iron oxide (azido-Fe_3O_4@SiO_2) nanoparticles	Photodynamic therapy	[59]
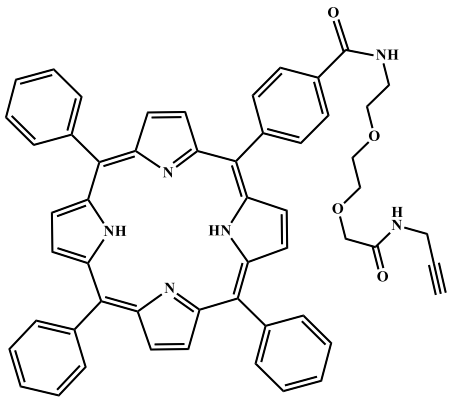	Clicked to superparamagnetic iron oxide nanoparticle (SPION)	Photodynamic therapy	[60]

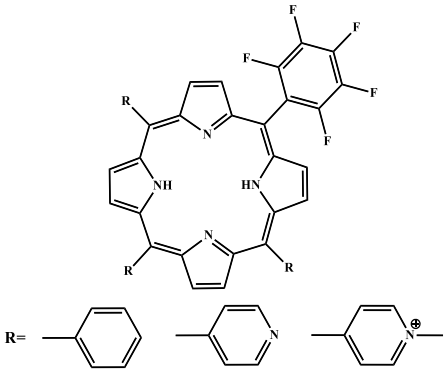	Covalently linked to cationic iron oxide silica nanomagnet (Si-Fe_3O_4)	Photodynamic antimicrobial chemotherapy or photodynamic inactivation	[61–63]
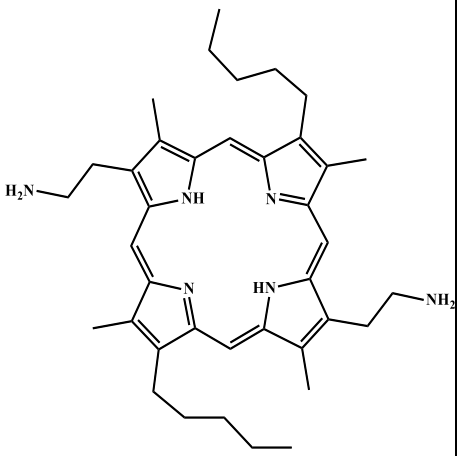	Covalently linked to functionalize superparamagnetic (Fe_3O_4) nanoparticles	Photodynamic therapy and hyperthermia therapy (HT)	[64]
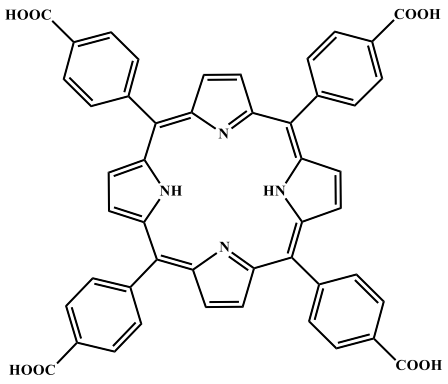	Covalently linked to magnetic cadmium ferrite ($CdFe_2O_4$) nanoparticles	Photodegradation of methylene blue	[65]

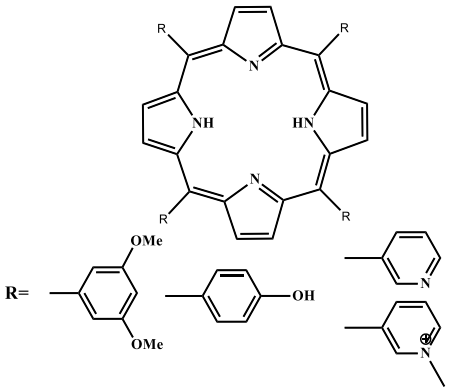	Direct mixing and self-assembly to gold-coated superparamagnetic iron oxide nanoparticles (SPIONs@Au)	Photodynamic antimicrobial therapy or Photodynamic inactivation	[66, 67]
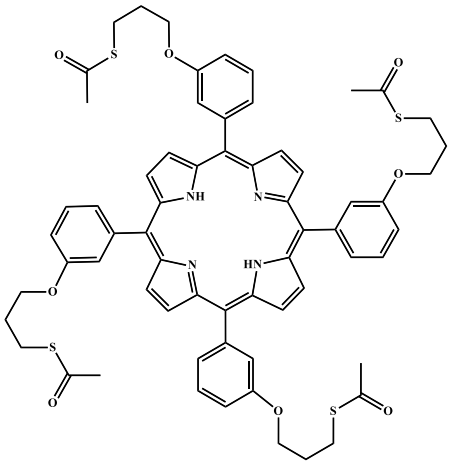	self-assembly to iron oxide-gold, core-shell nanoparticles (Fe_3O_4@Au)	Photodynamic therapy	[68]
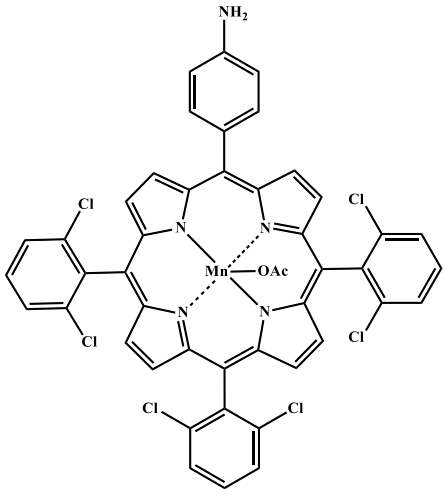	Covalently linked to silica magnetic nanoparticles (MNP@SiO_2)	Catalytic epoxidation	[69]

As outlined by **Table 1.1**, both symmetrically and asymmetrically substituted porphyrins linked to magnetic nanoparticles have been studied, this includes both neutral and cationic porphyrins. However, this outlined summary shows only one porphyrin conjugate which has been metalated and quaternized, with none for any PACT related application [**57**]. Moreover, the studies (**Table 1.1**) show no metalloporphyrins which are quaternized through an axial ligand and further linked to magnetic nanoparticles for any application. Thus, leaving a gap in search of both axially modified porphyrins and cationic porphyrins conjugated to magnetic nanoparticles for any applications. There are very few studies reported on hybridized bimetallic nanoparticles [**70**]. For the first time, cationic metalloporphyrins with positive charges on the meso-substituents or axial ligands conjugated to highly stable metal hybrid $Ag/CuFe_2O_4$ core-shell magnetic nanoparticles are being studied towards PACT in this thesis. Moreover, the conjugations through an axial ligand have been employed.

1.2.6 Porphyrins and their corresponding conjugates used in this work

Porphyrins synthesized in this work are both symmetrically and asymmetrically substituted with indium metal ions inserted in their cavity to enhance their photophysical and photochemical properties and further conjugated to $Ag/CuFe_2O_4$ magnetic nanoparticles. This study focuses on the photophysicochemical properties and PACT activity of cationic porphyrins since they are known to interact effectively with a broad spectrum of bacteria [**13**]. **Table 1.2** outlines the porphyrins used in this work (to be referred using assigned numbering throughout in this work) and their conjugates with magnetic NPs for PACT studies against *Staphylococcus aureus* and *Escherichia coli*. All the complexes used in this work are new except the free-base precursors 5-p-carboxyphenyl-10-15-20-(tri-4-pyridyl) (**a**)

[71], 5,10,15,20-tetra(4-pyridyl)-21H,23H-porphine (**b**) [24], 5,10,15,20-tetrakis(N-methylthiophenyl) porphyrin (**c**), and complex **4** [72]. Please note that complex **b** is also commercially available and it was used only as a precursor and it was not discussed or characterized in this work. However, the free-base porphyrin complexes **a** and **c** were not fully characterized and photophysicochemical properties were not explored in literature, and they are characterized and studied in this work.

Table 1.2. Porphyrins, metalloporphyrins and corresponding conjugates with Ag/$CuFe_2O_4$ magnetic nanoparticles (MNPs) synthesized in this work.

Molecular Structure	**Complex name**	**Porphyrin-NPs interaction [Conjugates]**	**Application/ Studies**
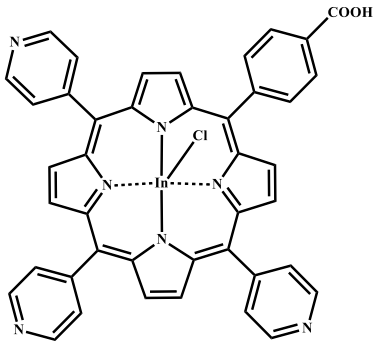	Indium-chloride 5-p-carboxyphenyl-10-15-20-(tri-4-pyridyl) porphyrin (**1**), (**New**)	Covalently linked to MCH-Ag/$CuFe_2O_4$ MNPs [**1**-MCH-Ag/$CuFe_2O_4$] and SA (Ag-N bond)	PACT (*S. aureus*) and Photophysics
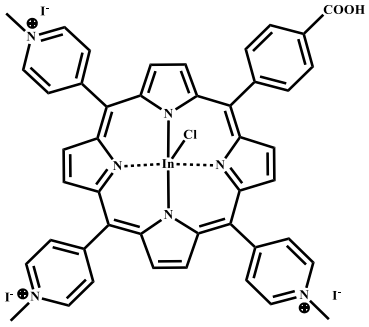	Indium-chloride 5-p-carboxyphenyl-10-15-20-(tris-4-methylpyridinium)-porphyrin triiodide (**1Q-MeI**), (**New**)	Covalently linked to MCH-Ag/$CuFe_2O_4$ MNPs [**1Q-MeI**-MCH-Ag/$CuFe_2O_4$]	PACT (*S. aureus* and *E. coli*) and Photophysics

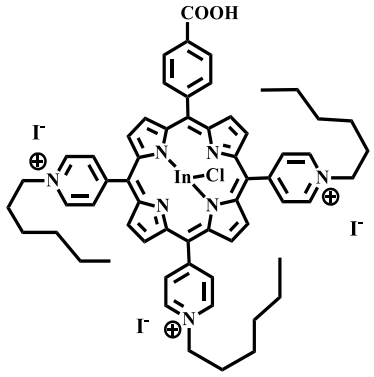	Indium-chloride 5-p-carboxyphenyl-10-15-20-(tris-4-hexylpyridinium)-porphyrin triiodide (**1Q-Hex**), (**New**)	Covalently linked to MCH-Ag/$CuFe_2O_4$ MNPs [**1Q-Hexl**-MCH-Ag/$CuFe_2O_4$]	PACT (*E. coli*) and Photophysics
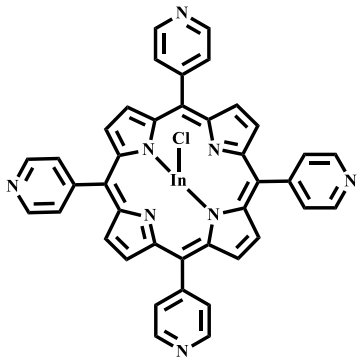	Indium-chloride 5,10,15,20-tetrakis(4-pyridyl) porphyrin (**2**), (**New**)	-	PACT (*E. coli*) and Photophysics
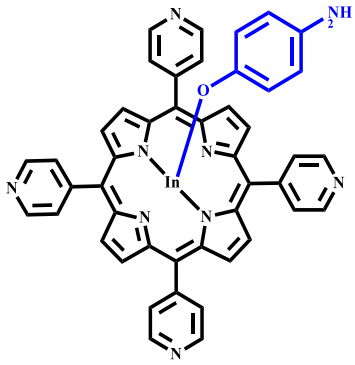	Indium-(4-aminophenyl) 5,10,15,20-tetrakis(4-pyridyl) porphyrin (**3**), (**New**)	-	PACT (*E. coli*) and Photophysics

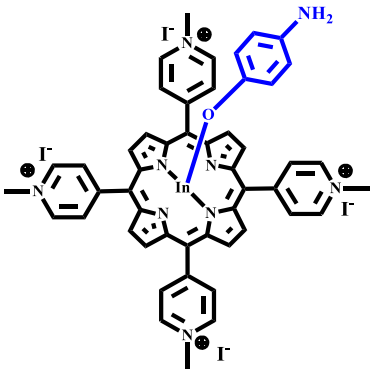	Indium (para-aminophenyl) 5,10,15,20-tetrakis(4-methylpyridinium)-tetraiodide porphyrin (**3Q-MeI**), (**New**)	SA on MCH-Ag/$CuFe_2O_4$ MNPs, axial ligand bond, [**3Q-MeI**-MCH-Ag/$CuFe_2O_4$], Ag-N bond.	PACT (*E. coli*) and Photophysics
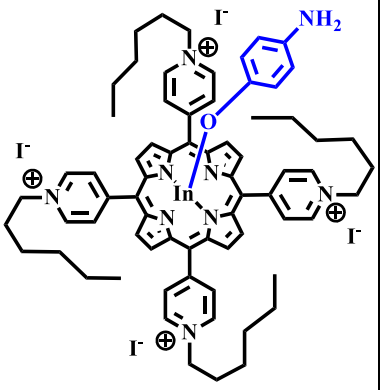	Indium (para-aminophenyl) 5,10,15,20-tetrakis(4-methylpyridinium)-tetraiodide porphyrin (**3Q-HexI**), (**New**)	SA on MCH-Ag/$CuFe_2O_4$ MNPs, axial bond [**3Q-HexI**-MCH-Ag/$CuFe_2O_4$], Ag-N bond.	PACT (*E. coli*) and Photophysics
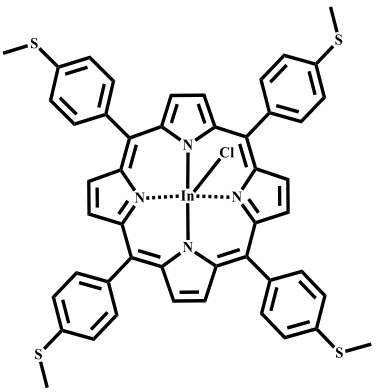	Indium-chloride 5-10-15-20-(tetrakis-4-methylthiophenyl)-porphyrin (**4**) [**72**]	-	PACT (*S. aureus*) and Photophysics

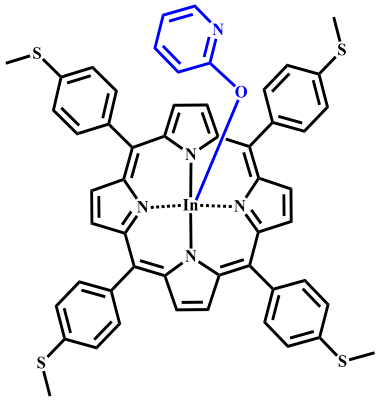	Indium-(2-pyridyl) 5-10-15-20-(tetrakis-4-methylthiophenyl)-porphyrin (**5**) (**New**)	SA on OLM-Ag/$CuFe_2O_4$) and MCH-Ag/$CuFe_2O_4$ NPs (Ag-S and Ag-N) [**5**-OLM-Ag/$CuFe_2O_4$] and [**5**-MCH-Ag/$CuFe_2O_4$], Ag-N bond.	PACT (*S. aureus*) and Photophysics
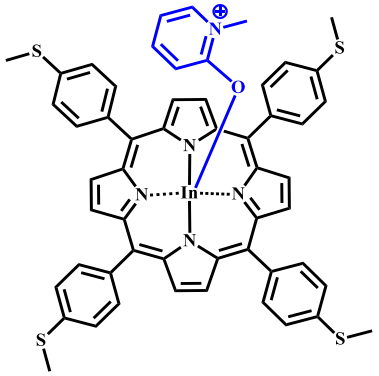	Indium-(2-methylpyridyl) 5-10-15-20-(tetrakis-4-methylthiophenyl)-porphyrin iodide (**5Q-MeI**) (**New**)	SA on OLM-Ag/$CuFe_2O_4$ and MCH-Ag/$CuFe_2O_4$ NPs through (Ag-S) [**5Q-MeI**-OLM-Ag/$CuFe_2O_4$] and [**5Q-MeI**-MCH-Ag/$CuFe_2O_4$], Ag-N bond.	PACT (*S. aureus*) and Photophysics

SA = self-assembly; **MeI** = Methyl iodide; **HexI** = Hexyl iodide; **MCH** = 6-Mercapto-1-hexanol; **OLM** = Oleyamine

In this study cationic indium porphyrins in which quaternizations were done either on the meso-substituents (**1Q-MeI**, **1Q-HexI**, **3Q-MeI**, **3Q-HexI**) or axial ligand (**5Q-MeI**) were synthesized in order to enhance solubility and reduce aggregation, thus consequently improving photophysical properties and PACT efficacy. Please note complex **5** quaternized using hexyl iodide was not attempted; hence only complex **5Q-MeI** is shown in **Table 1.2**.

1.2.7 Rationale

The effect of different factors or components that might influences photophysicochemical properties and PACT activities of the complexes were studied as follows;

- Complex **2** was compared to **4** for the effect of the pyridyl vs methylthiophenyl meso-substituents.
- Complex **1** was compared to **1Q-MeI** and **1Q-HexI**, and complex **3** was compared to **3Q-MeI** and **3Q-HexI**, and complex **5** was compared to **5Q-MeI** to study the effect brought by quaternization.
- Complexes **1Q-MeI** and **1Q-HexI** were compared to **3Q-MeI** and **3Q-HexI**, respectively, to study the effect brought by the number of positive charges.
- Complexes **2** and **4** were compared to **3** and **5**, respectively, to study the impact brought by axial ligation.
- Complexes **1Q-MeI** and **3Q-MeI** were compared to **1Q-HexI** and **3Q-HexI**, respectively, to study the effect brought by the alkyl chain lengths of the quaternizing agents on hydrophilicity character, photophysical properties, and PACT efficacy.
- Porphyrins were compared to their conjugates to study the effect brought by the MNPs.

- The effect of capping agent and size on PACT activity was studied by comparing oleyamine factionalized (OLM-Ag/$CuFe_2O_4$) MNPs and 6-mercapto-1-hexanol functionalized (MCH-Ag/$CuFe_2O_4$) MNPs.
- Susceptibility of *S. aureus* in comparison to *E. coli* towards PACT activity of cationic porphyrins was studied using complex **1Q-MeI** as an example.

1.3 Magnetic nanoparticles (MNPs)

1.3.1 Background (overview)

Magnetic nanoparticles (MNPs) are a set of colloidal particles typically with a size ranging between nanometer (nm) to micrometer (µm) and can be manipulated through the use of external magnetic fields, and they are commonly composed of cobalt, iron, nickel, chromium, manganese, or gadolinium and their chemical compositions [**73**]. Some of the highly magnetic nanoparticles such as cobalt and nickel are toxic and more prone to oxidation, rendering them of less interest. MNPs have been studied since the 1970s, and the research on their fundamental properties and potential practical applications are rapidly expanding. Ideal MNPs must have these combined properties; elevated thermal and photostability and reduced chance of aggregation in solution, relatively small, good biocompatibility, high magnetic saturation, and active surface for modifications [**74–76**]. MNPs with active sides for modification are of great interest as various stabilizing agents can be adsorbed on the surface to enhance their properties, which consequently broadens their applications. MNPs have been further modified with various metals through either capping to form core-shell nanoparticles or through the formation of dimers to enhance their properties [**70,77**]. MNPs in this study were employed due to their desired intrinsic properties, which include their ability to respond to external magnetic fields chemically

active surfaces, which allow possibilities of coating. Metallic (e.g Cu and Ag) nanoparticles are well known to be cytotoxic due to their ability to release metal ions which penetrated bacterial cell membranes [78]. The colloidal stabilities and biocompatibility of the MNPs made them ideal candidates in the biomedical field as drug carriers [79]. Other materials such as carbon nanotubes and peptides amino acids are being used as drug carriers, however, most of this materials lack solubility in aqueous media and some are sensitive to pH changes [80,81]. The most vital properties of MNPs are based on their response to the magnetic field, which can be studied and explained through hysteresis loops (**Fig. 1.7**). Hysteresis loop **Fig. 1.7**, starting from point 'a' (zero point); this is a point where the entire Weiss domains magnetism is balanced and any motion from an external magnet may result in an imbalance either to the positive magnetic saturation (point b) or opposite magnetic saturation (point e).

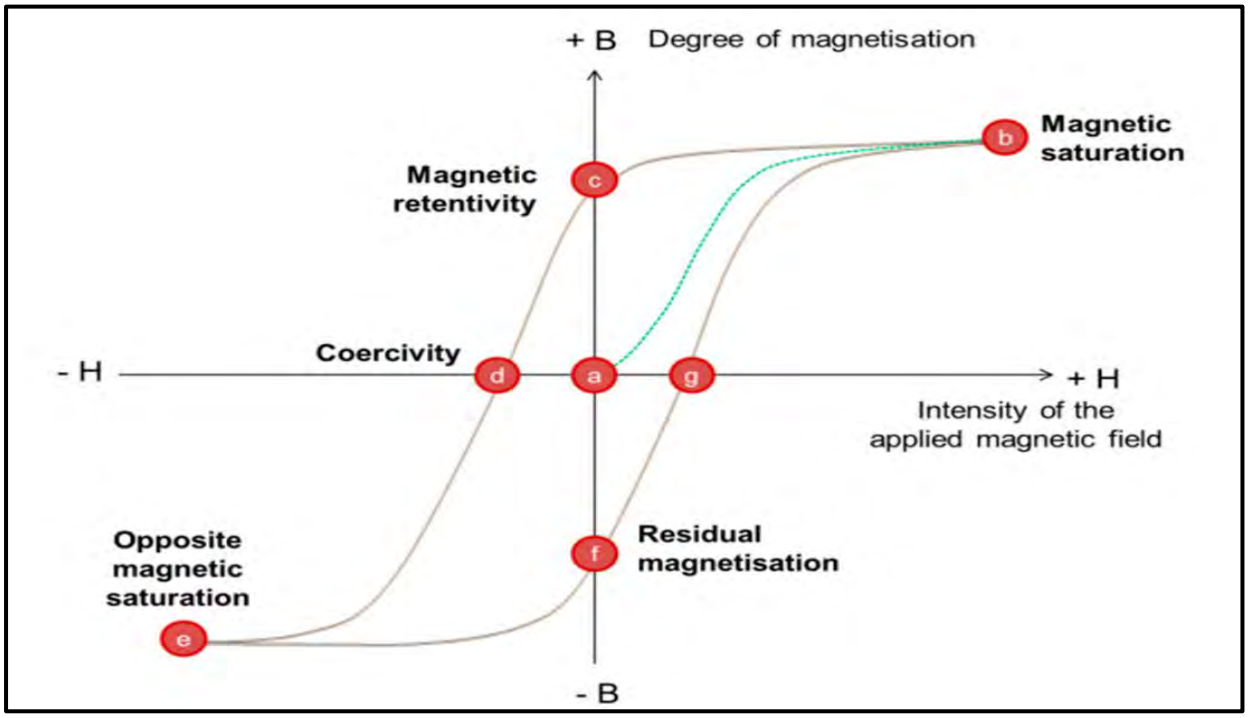

Fig. 1.7 A typical illustration of hysteresis loop of a magnetic material [76].

By applying the highest magnetic force (H) the MNPs may reach their highest point of magnetization known as magnetic saturation, depending on the direction of H, either point 'b' or 'e' can be reached, and the magnetic saturation will remain constant in the direction of applied H, this is due to the memory of magnetic flux retained by Weiss domains magnetism. Point 'c' and 'f' are as a result of the H being reduced to zero, and the degree of magnetization (B) does not go back to zero point but retain magnetism due to imbalance of Weiss domains of the nanoparticle. Point 'd' and 'g' (coercivity points) are the two points where magnetism is zero which corresponds to H required to remove the retained magnetic remanence and if the H is applied further the particles will once again reach their saturation points.

1.3.2 General syntheses and applications of MNPs

1.3.2.1 Synthesis of magnetic nanoparticles

The broad applications of magnetic nanometer-sized colloidal particles have driven researches towards finding various effective techniques in controlled synthesis of MNPs. There are various procedures in the synthesis of MNPs, which include hydrothermal, mechanochemical, thermal decomposition, co-precipitation, and aerosol [**76,79,82**]. Co-precipitation (**Scheme 1.3**) is by far a widely used technique in the synthesis of MNPs, which involves the preparation of Fe_2O_3 or any other MNPs in solution [**83,84**]. This procedure involves the use of Fe(II) ions and Fe(III) aqueous salts in solution under various conditions depending on the size or shape preferred.

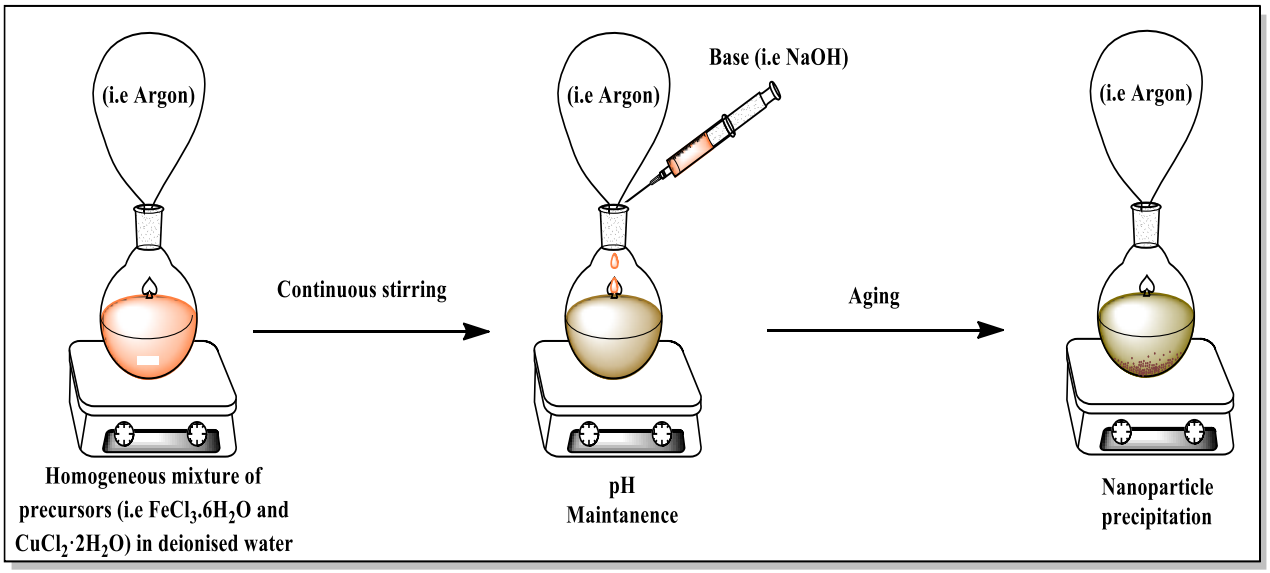

Scheme 1.3 Schematic illustration of co-precipitation synthetic procedure for MNPs

Commonly, the synthesis is done under an inert atmosphere to prevent oxidation of the ions and at room or elevated temperatures followed by the introduction of a base to facilitate precipitation [85]. Desired capping metal can be introduced together with the Fe(II) and Fe(III) ions to synthesize capped MNPs [86]. In this work $CuFe_2O_4$ MNPs were prepared through co-precipitation of Fe(III) and Cu(II) ions, followed by capping of the MNPs with silver acetate for further chances of surface modifications.

1.3.2.2 Surface modifications of magnetic nanoparticles

MNPs with functionalizable surfaces possess a high potential in numerous applications. Nearly all applications use functionalised nanoparticles either for enhancement of MNPs properties or towards long term storage in solution. For example pristine Fe_3O_4 MNPs are prone to aggregation in solution overtime. Through surface modification, NPs can be protected from themselves (electrostatic interactions) and surrounding environment [86]. There are different classes of surface modifiers or stabilizers; namely non-polymeric organic stabilizers, polymeric organic stabilizers, and inorganic materials [68].

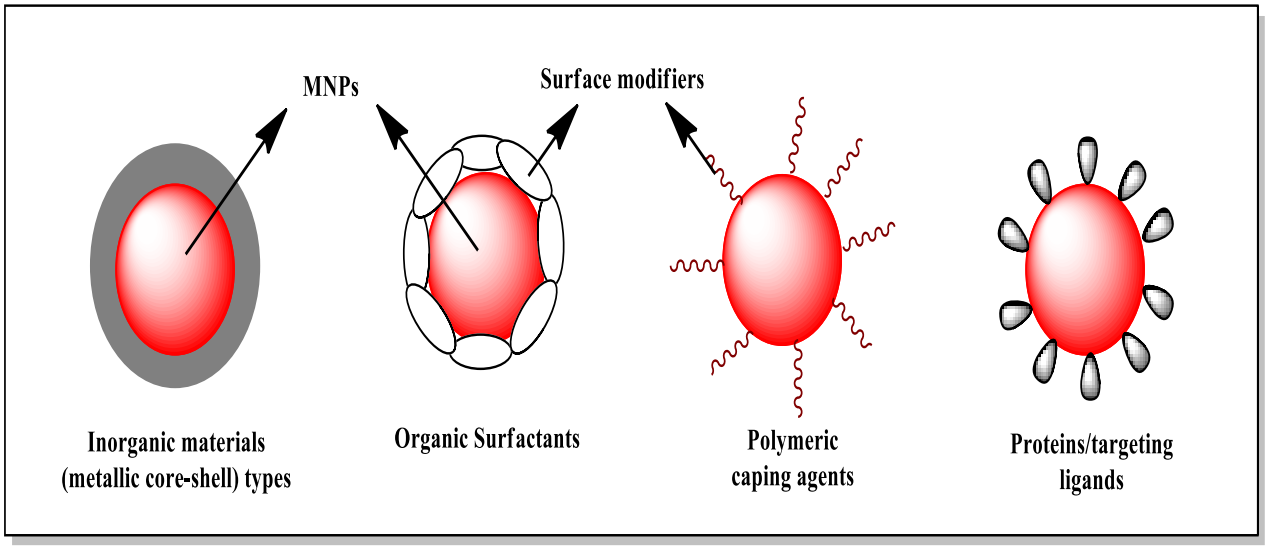

Fig. 1.8 A simple illustration of surface modification strategies on MNPs

Fig. 1.8 demonstrates various strategies for surface modification of MNPs [68,76,87–90]. Inorganic material or capping metals (i.e silver or gold) can be used to protect the core of NPs from oxidizing [77]. In this study both polymeric capping agents and metallic capping stabilizing strategies were used, through the use of copper and silver metals and stabilizing with oleyamine (OLM) and oleic acid (OLA) capping agents and further functionalizing with 6-mercapto-1-hexanol (MCH).

1.3.3 Applications of magnetic nanoparticles

MNPs have been explored for various applications due to their attractive fundamental properties. Moreover, significant developments have been made regarding MNPs over the past few decades. **Fig. 1.9** shows common application of MNPs in various fields [91–97]. Smaller-sized MNPs less than 30 nm are vastly explored for biomedical applications; such as drug nano-vehicles in PDT or as contrast agents for magnetic resonance imaging (MRI) [91,98].

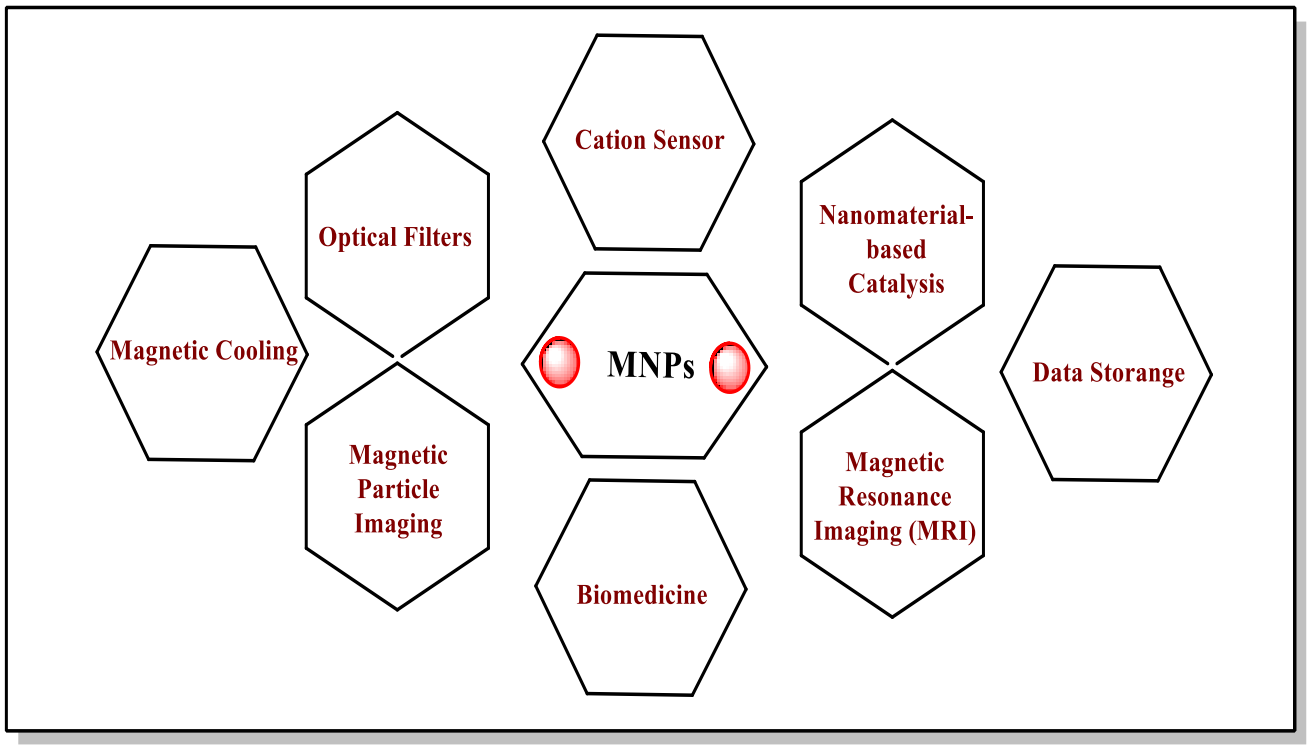

Fig. 1.9 Illustration of various emerging potential applications of magnetic nanoparticles.

Applications of MNPs in biomedicine include biomedical diagnosis and treatments. Functionalized MNPs are commonly used as potential candidates for cancer treatments. On the other hand MNPs are used in industries as catalyst supports, usually high surface area MNPs are preferred to chemically affix the catalyst [99]. In this study, the focus is based on the use MNPs ($Ag/CuFe_2O_4$) to enhance PACT activity of the porphyrins. MNPs used in this study possesses excellent properties including chemically active sites for further adsorption of secondary materials and also the advantage of their recoverability after being used [100].

1.4 Summarized aims and objectives of this study

Aims:

In this work, the focus is based on the study and application of cationic indium porphyrins linked to functionalized $Ag/CuFe_2O_4$ core-shell MNPs as potential photosensitizers. Photophysicochemical parameters and photodynamic antimicrobial chemotherapy activity

of the porphyrins and their corresponding conjugates against *S. aureus* and *E. coli* will be explored, compared, and discussed.

Objectives:

- **Porphyrins:** Synthesize symmetrically and asymmetrically substituted neutral and cationic indium (III) porphyrins, followed by characterization using appropriate analytical techniques to validate the successful synthesis of the complexes.
- **Silver-capped copper ferrite MNPs ($Ag/CuFe_2O_4$):** Synthesize OLM-$Ag/CuFe_2O_4$ MNPs, and further functionalized with 6-mercapo-1-hexanol (MCH) to form MCH-$Ag/CuFe_2O_4$ MNPs. Characterize the synthesized MNPs using appropriate characterization techniques.
- **Porphyrin-MNPs conjugates:** Covalent linkage of asymmetrically substituted indium (III) porphyrins to MCH-$Ag/CuFe_2O_4$ MNPs, and linkage of symmetrical porphyrins to both OLM-$Ag/CuFe_2O_4$ and MCH-$Ag/CuFe_2O_4$ MNPs through self-assembly ether through meso-substituents or axial ligand. Furthermore, characterizations were carried out to validate the conjugation using appropriate analytical techniques.
- **Studies and applications:** Study photophysical properties of all synthesized indium (III) porphyrins and conjugates. Perform PACT application of pristine porphyrins, nanoparticles alone, and their corresponding conjugates.

Methodology and Experimental

This section holds two chapters

Chapter 2: Reagents, instrumentations, and successful syntheses

Chapter 3: Failed attempted syntheses

Chapter 2

Reagents, instrumentations, and successful syntheses

This chapter outlines the successful methodologies or synthetic procedures, materials, and analytical instrumentations employed in this study, together with reagents and experimental setups for photodynamic antimicrobial chemotherapy.

2.1 Materials and Reagents

All the materials were procured from commercial suppliers; Sigma Aldrich, Unilab chemicals, Merk chemicals, Fisher chemicals, Loba Chemie, Fluka chemicals, and Davies Diagnostics. Reagents and solvents were used without any further purification unless stated otherwise.

2.1.1 General reagents and solvents

Dichloromethane (DCM), N,N dimethylformamide (DMF), methanol (MeOH), ethanol (EtOH), hydrogen peroxide, and acetone were purchased from Fisher chemical. Diethyl ether, chloroform, dimethylsulfoxide (DMSO), sulphuric acid, and tetrahydrofuran (THF) were purchased from Loba Chemie. Deuterated dimethylsulfoxide (DMSO-d_6), deuterated chloroform, deuterated water, cyclohexane, sodium hydroxide pallets, hydrochloric acid, molecular sieves 3Å, 1-octanol, and toluene were purchased from Sigma Aldrich. Ultra-pure water obtained from the installed purifying system from ELGA, Veolia water PURELAB, Flex system (Marlow, UK).

2.1.2 Reagents for porphyrins syntheses

Glacial acetic acid, pyrrole, propionic acid, methyl iodide (MeI), hexyl iodide (HexI), 2-hydroxypyridine, 4-hydroxypyridine, 4-nitrobenzaldehyde, 4-aminophenol, 4-methylthiobenzaldehyde, 4-bromobenzaldehyde, indium (III) chloride, 4-pyridinecarboxaldehyde, sodium hydride, anhydrous potassium carbonate, 4-formylbenzoic acid, silica gel 60 (0.04-0.063 mm), active neutral alumina oxide, and sodium acetate (NaOAc) purchased from Sigma Aldrich.

2.1.3 Reagents for MNPs synthesis and conjugations to porphyrins

Diphenyl ether (DPE), oleyamine (OLM), ethyl acetate, oleic acid (OLA), 6-mercapto-1-hexanol (MCH), N,N-dycyclohexylcarbodiiamide (DCC) were purchased from Sigma Aldrich. Iron (III) chloride hexahydrate, silver acetate (Ag(ac)), copper (II) chloride dehydrate were purchased from Unilab chemicals.

2.1.4 Materials for photophysical studies

9,10-Dimethylanthracene (DMA), anthracene-9,10-diyl-bis-methylmalonate (ADMA), rose bengal (RB), Zn-5,10,15,20-(tetraphenyl)-21H,23H-porphine (ZnTPP), LUDOX HS-40 colloidal silica were purchased from Sigma Aldrich.

2.1.5 Materials for photodynamic antimicrobial chemotherapy

Staphylococcus aureus KwikStick derived from (ATCC® 25923) and *Escherichia coli* (ATCC® 25922) were purchased from Davies Diagnostics, South Africa. Phosphate buffer saline (10 mM PBS) pH 7.4 was prepared using appropriate amounts of Na_2HPO_4 and NaOH to a pH of 7.4. Nutrient agar and bacteriological BBL Muller Hinton broth were purchased from Merk (Pty) Ltd South Africa.

2.2 Instrumentations

1. Ultraviolet-visible spectroscopy was used to record optical absorption spectra at room temperature using a **Shimadzu UV 2550 spectrophotometer**, using wavelength range 300-800 nm in a 1 cm path length cuvette.

2. Fluorescence emissions and excitation spectra were recorded on a **Varian Eclipse spectrofluorometer**. Excitation at soret band (crossover λ of standard and complex) and emission spectra recorded at 500-800 nm.
3. Fluorescence lifetimes were measured using a **time correlated single photon counting setup (TCSPC) (FluoTime 300, Picoquant GmbH)** with a diode laser (excitation source: LDH-P-420 with 10 MHz repetition rate, 88 ps pulse width, Picoquant GmbH). Fluorescence was detected under the magic angle with a Peltier cooled photomultiplier tube (PMT) (PMA-C 192N-M, Picoquant) and integrated electronics (PicoHarp 300E, Picoquant GmbH). A monochromator with a spectral width of 8 nm was used to select the required emission wavelength band. The response function of the system, which was measured with a scattering Ludox solution (DuPont), had a full width at half maximum (FWHM) of about 300 ps. The ratio of stop to start pulses was kept low (below 0.05) to ensure good statistics. All luminescence decay curves were measured at the maximum of the emission peak. The data were analysed using the FluoFit program (Picoquant, GmbH).
4. Singlet oxygen quantum yields were done using **Spectra-Physics^{R} primoScan OPO series**, driven by **Spectra-physics Quanta Ray INDI lab** with maximum pump energy of 750 mJ and output energy of 27 mJ coupled to **Shimadzu UV-2550 spectrophotometer** to record the DMA and ADMA degradation from t=0 to t=25 min in a 5 min interval.
5. Mass spectral data were collected with a **Bruker AutoFLEX III Smartbeam TOF/TOF Mass spectrometer**. The instrument was operated in positive ion mode using an m/z range of 400-1500 amu. The voltages of the ion sources were set at 19 and 16.7 kV for ion sources 1 and 2, respectively, while the lens was set at 8.50 kV and the reflector 1 and 2 voltages were set at 21 and 9.7 kV, respectively. α-Cyano- 4-hydroxycinnamic acid

was used as the MALDI matrix with a 337 nm nitrogen laser selected as the ionising source.

6. Elemental compositions of the NPs and the conjugates were qualitatively determined using energy dispersive X-ray spectroscopy (EDS), **INCA PENTA FET** coupled with the **VAGA TESCAM** operated at 20 kV accelerating voltage.
7. Proton Nuclear Magnetic Resonance (^{1}H NMR) spectra were recorded using **Bruker EMX 600 MHz and 400MHz** NMR spectrometer. The spectra were obtained under ambient temperature using deuterated solvents (D_2O, $CDCl_3$, and DMSO-d_6).
8. Fourier-transform infrared spectroscopy (FT-IR) spectra were obtained using a **Bruker Alpha model** FT-IR spectrometer with a **Platinum-ATR** with a range 500-4000 cm^{-1}.
9. X-ray powder diffraction (XRD) patterns were recorded on a **Bruker D8, discover instrument** equipped with a **Lynx Eye Detector**, using Cu Kα radiation (λ = 1.5405 A, Ni filter). Data were collected over the 2θ = 5-100° range, scanning at 1° min-1 with a filter time-constant of 2.5 s per step and a slit width of 6.0 mm. Samples were placed on a zero-background silicon wafer slide. The X-ray diffraction data were retreated using Eva (evaluation curve fitting) software. A baseline correction was performed on each diffraction pattern by subtracting a spine fitted to the curved background and the full width at half maximum values reported in this study were obtained from the fitted curves.
10. Dynamic light scattering (DLS) was used for hydrodynamic diameter (D_h) and Zeta potential (ζ) of the nanoparticles and nanoconjugates; measurements were done using a **Malvern Zetasizer Nanoseries, Nano-ZS90** (containing 633 nm helium neon laser), using disposable cuvettes and Zeta cell.

11. X-ray photoelectron spectroscopy (XPS) analysis was measured using an **AXIS UltraDLD (supplied by Kratos Analytical)** with an Al (monochromatic) anode equipped with a charge neutralizer. The following parameters were used: the emission was 10 mA, the anode (HT) was set at 15 kV, and the operating pressure was kept below 5×10^{-9} torr. A hybrid lens was used, and the resolution to acquire scans was set at 160 eV pass energy in slot mode. The centre used for the scans was set at 520 eV (width of 1205 eV) with steps of 1 eV and a dwell time of 100 ms. High-resolution scans were acquired using 80 eV pass energy in slot mode. The chemically distinct species were resolved using a nonlinear least squares curve fitting procedure.
12. Thermal gravimetric analysis (TGA), **Perkin Elmer TGA 8000 thermogravimetric analyser** was used to study the loading ratios of the porphyrins to the nanoparticles by analysing the decomposition profiles of the porphyrin, nanoparticles, and the corresponding nano conjugates with a temperature ranging between 50-800°C and nitrogen as purge gas. N_2 gas purge was used with a flow rate 20mL.min^{-1}, sample ranging from 1 to 4 mg was heated with temperature increase of 2°C.min^{-1}. Initially, temperature from 25°C was raised to 100°C and held for 10 min to eliminate moisture.
13. Transmission electron microscope (TEM) photographs were obtained from (TEM), **ZEISS LIBRA model 120** operated at 90 kV and 100kV, iTEM software was used for TEM micrographs processing; the samples were deposited on carbon TEM grids, using appropriate solvent.
14. The elemental analysis was conducted using a **Vario-Elementar Microcube ELIII**.
15. **Autoclave RAU-530D** was used for the sterilization and autoclaving of nutrient broth, nutrient agar and phosphate buffer and other various apparatus for PACT studies.

16. The optical density of the bacteria culture was monitored using the **LEDETECT 96 from LABXIM PRODUCTS**, using a 96 well microplate.
17. **High speed HERMLE Z233M-2 centrifuge** was used for the harvesting of the bacteria cells by centrifugation process. This was done to quench the growth of bacteria by washing of the broth using PBS solution repeatedly.
18. **PROVSM-3 Lab plus Vortex** mixer was used to homogenous bacteria-photosensitizer solution during PACT studies.
19. The incubation processes for the photodynamic antimicrobial chemotherapy was done using the **thermostatic oven**
20. Scanner from **Interscience for Microbiology scan® 500** was used for colony count and further determine the colony forming units (CFU)/mL of the bacteria.
21. Atomic force microscopy (AFM) measurement in tapping mode was carried out with **MFP-3D Origin supplied by Asylum** research (Oxford instruments company, USA). AFM analysis was done by drop casting followed by drying of the sample solutions on a freshly cleaved mica surface in an oven.

2.3 Porphyrin Syntheses

2.3.1 Synthesis of free-base porphyrin complexes 5-p-carboxyphenyl-10-15-20-(tri-4-pyridyl) (a) and 5,10,15,20-tetrakis(N- methylthiophenyl) (c), Scheme 4.1

The free-base porphyrins (**a** and **c**) were synthesized using Adler-Longo porphyrin synthesis procedure previously reported in numerous studies **[49,101,102]**. Step by step synthesis and purification of a free-base porphyrin is delineated in **Scheme 2.1**.

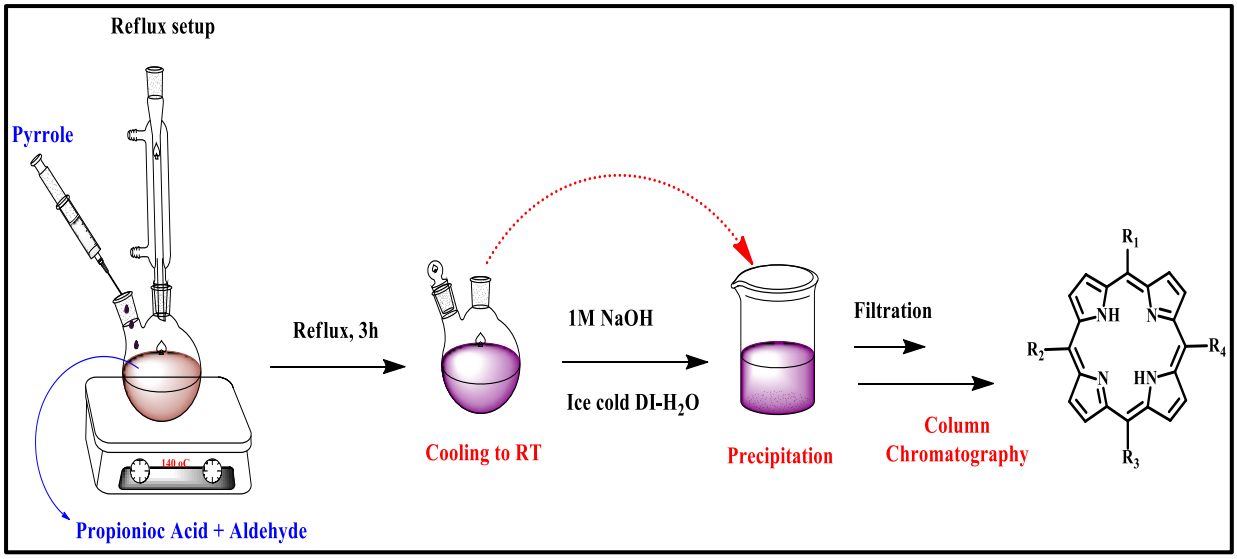

Scheme 2.1 Step by step schematic diagram illustrating a free-base porphyrin synthesis through Adler-Longo synthetic procedure.

Table 2.1 shows the reagents used for the synthesis of the free-base porphyrins, and complex **a** was discussed an example as follows; 4-formylbenzoic acid (300 mg, 2.00 mmol) and 4-pyridinecarboxaldehyde (0.73 mL, 5.99 mmol) were dissolved in 150 mL of propionic acid and brought to reflux temperature in a two necked flask, followed by dropwise addition of pyrrole (0.55 mL, 7.98 mmol). The mixture was heated under reflux for 3 h. The crude product was precipitated from the reaction using excess 1M NaOH solution in ice cold water to neutralize the propionic acid, then filtered and washed with water. Silica gel column chromatography was used to purify the compound using chloroform as an eluent to give a purple solid. The resulted compound was air dried in a fume hood.

a; Yield = 231 mg (38%), eluent chloroform; FTIR (cm^{-1}): 3302 (N-H pyrrole), 2839-2911 (C-H aromatic), 1707 (C=O carboxylic acid), 1597 (C=N pyridine). ^{1}H NMR (600 MHz,DMSO-d_6): δ, ppm -3.02 (s, 2H, NH pyrrole), 8.27-8.29 (m, 6H, pyridine), 8.34-8.37 (d, 2H, H_{ortho} Ar-COOH), 8.38-8341 (d, 2H, H_{meta} Ar-COOH), 8.87-8.83 (m, 8H, β pyrrole), 9.04-9.07 (m, 6H, pyridine), 13.24-13.40 (s, 1H, COOH). MALDI TOF-MS, calc 661.7, found 662.3 $[M]^{+}$. UV/visible (DMF),

λ_{max} nm (log ε): 417 (5.4), 514 (4.2), 548 (3.8), 587 (3.6), 644 (3.3). Anal. Calcd for $C_{42}H_{27}N_7O_2.H_2O$: C (74.11), H (4.26), N (14.41). Found: C (74.30), H (3.69), N (13.30).

c; Yield = 427 mg (62 %), eluent DCM; FTIR (cm^{-1}): 3311 (N-H pyrrole), 2840-2919 (C-H aromatic, CH_3). ^1H NMR (600 MHz, $CDCl_3$): δ, ppm -2.82 (s, 2H, NH pyrrole), 1.23 (s, 12H, methyl-H), 7.61-7.62 (d, 4H, β pyrrole), 7.81-7.82 (d, 4H, β pyrrole), 8.10-8.11 (d, 4H, Ar-H), 8.46-8.48 (m, 8H, Ar-H), 8.85 (s, 4H, Ar-H). MALDI TOF-MS, calc 798.2, found 799.5 $[M]^+$. UV/visible (DMF), λ_{max} nm (log ε): 424 (5.2), 517 (4.0), 557 (3.4), 595 (3.2), 651 (3.3). Anal. Calcd for $C_{48}H_{38}N_4S_4.H_2O$: C (72.15), H (4.79), N (7.01), S (16.05). Found: C (71.74), H (5.01), N (7.11), S (16.18).

Table 2.1 Synthesis of free-base porphyrin complexes **a** and **c**.

Complexes	Aldehydes	Pyrrole	Propionic acid (mL)	Reaction conditions	Precipitation/ Purification
a	4-formylbenzoic acid (300 mg, 2.00 mmol) and 4-pyridinecarboxaldehyde (0.73 mL, 5.99 mmol)	0.55 mL, 7.98 mmol	150	3 h, reflux	1M NaOH in ice cold water, Silica gel colum chromatograph using $CHCl_3$
c	4-methylthiobenzaldehyde (1.0 mL, 7.52 mmol)	0.52 mL, 0.752 mmol	105		1M NaOH in ice cold water, Silica gel colum chromatograph using DCM

$CHCl_3$ = Chloroform

2.3.2 Indium-chloride complexes; indium-chloride 5-p-carboxyphenyl-10-15-20-(tri-4-pyridyl) porphyrin (1), indium-chloride 5,10,15,20-tetrakis(4-pyridyl) porphyrin (2), and indium-chloride 5-10-15-20-(tetrakis-4-methylthiophenyl) porphyrin (4), Scheme 4.1

A similar synthetic procedure was used to synthesize all the neutral chloro indium complexes **1**, **2**, and **4** [72,103,104]. **Table 2.2** shows the amounts of the chemical reagents and solvents used upon synthesis of each complex. Complex **1** was used as an example to describe the synthetic procedure. Typically, complex **1** was synthesized as follows: as-prepared free-base complex **a** (500 mg, 0.76 mmol) was dissolved in 70 mL of glacial acetic acid followed by addition of Na(OAc) (0.62 g, 7.6 mmol) and $InCl_3$ (1 g, 4.5 mmol). The mixture was allowed to reflux for 5 h with continuous stirring. The progress of the reaction was monitored using UV-Vis absorption spectra. The collapse of the four Q-bands of free-base porphyrin to two Q-bands of the metalated porphyrin signified the completion of the reaction. The reaction was allowed to cool to room temperature, followed by extraction of the product using chloroform and water. The moisture in complex **1** was removed through filtering with $MgSO_4$, and chloroform was evaporated under reduced pressure, affording 193 mg of purple solid.

1; Yield = 193 mg (96.5 %); IR (cm^{-1}): 2839-2915 (C-H aromatic), 1707 (C=O carboxylic acid), 1598 (C=N pyridine). ^1H NMR (400 MHz, DMSO-d_6): δ, ppm 7.63-7.71 (d, 1H, β pyrrole), 7.79-7.89 (s, 1H, β pyrrole), 7.95-8.05 (d, 2H, pyridine), 8.08-8.16 (s, 2H, β pyrrole), 8.32-8.45(s, 2H, β pyrrole), 8.60-8.70 (S,2H, β pyrrole), 8.84-8.90 (d, 2H, H_{ortho} Ar-COOH), 8.98-9.14 (m, 12H, pyridine and H_{meta} Ar-COOH); MALDI TOF-MS: calc 809.85, found 774.5 $[M-Cl]^+$; UV/visible (DMF), λ_{max} nm (log ε): 426 (5.5), 561 (4.1), 600 (3.6). Anal. Calcd for $C_{42}H_{25}ClInN_7O_2.H_2O$: C (60.87), H (3.26), N (11.84), Found: C (60.55), H (4.71), N (11.26).

2; Yield: 562 mg (93 %); FT-IR (cm^{-1}): 2840-3130 (C-H aromatic, CH_3), 1590 (C=N pyridine). ^1H NMR (600 MHz, $CDCl_3$): δ, ppm = 8.16-8.17 (m, 8H, β pyrrole), 8.87 (s, 8H, meta Pyridine-H), 9.06-9.07 (m, 8H, ortho pyridine-H). MALDI TOF-MS, calc 766.9, found 731.9 $[M]^+$. UV/visible (DMF): λ_{max} nm (log ε): 424 (5.7), 563 (4.1), 601 (3.4). Anal. Calcd for $C_{40}H_{24}InN_8$. H_2O: C (65.68), H (3.31), N (15.32). Found: C (64.95), H (3.41), N (15.67).

4; Yield = 311.5 mg (86 %); FT-IR (cm^{-1}): 2840-2910 (C-H aromatic, CH_3). ^1H NMR (600 MHz, $CdCl_3$): δ, ppm 2.75 (s, 12H, methyl-H), 7.60-7.62 (d, 4H, β pyrrole), 7.65-7.67 (d, 4H, β pyrrole), 8.00-8.02 (d, 4H, Ar-H), 8.26-8.27 (d, 4H, Ar-H), 9.08 (s, 8H, Ar-H). MALDI TOF-MS, calc 947.1, found 946.3 $[M]^+$. UV/visible (DMF), λ_{max} nm (log ε): 433 (5.2), 566 (4.3), 609 (3.8). Anal. Calcd for $C_{48}H_{36}ClInN_4S_4.H_2O$: C (60.85), H (3.83), N (5.91), S (13.54). Found: C (60.99), H (3.75), N (5.67), S (13.12).

Table 2.2 Synthesis of neutral chloro indium porphyrin complexes (**1**, **2**, and **4**) from free base porphyrins.

Complexes	Free-base (mg, mmol)	Glacial acetic acid (mL)	$InCl_3$ (mg, mmol)	NaOAc (mg, mmol)	Reaction time (h)	Purification procedure
1	**a**; 500, 0.76	70	1000, 4.5	620, 7.6	5	Extract with water and $CHCl_3$, and $CHCl_3$ filtered through $MgSO_4$
2	**b**; 600, 0.97	20	400, 1.8	600, 7.31	5	Extract with water and $CHCl_3$
4	**c**; 350, 0.43	25	670, 3.01	750, 9.14	5	Extract with water and $CHCl_3$

$CHCl_3$ = Chloroform

2.3.3 Axial modified complexes; indium-(4-aminophenyl) 5,10,15,20-tetrakis(4-pyridyl) porphyrin (3) and indium-(2-pyridyl) 5,10,15,20-tetrakis-(4-phenylmethylthio) porphyrin (5), Scheme 4.2

Synthesis of axially modified complexes **3** and **5** were carried out using reported literature procedure with a few modification [**104–107**]. **Table 2.3** summarizes the reaction conditions and reagents used upon axial ligation. Complexes **3** used an example was synthesized as follows; as-prepared complex (**2**) (450 mg, 0.61 mmol) was placed into a 100 mL round bottom flask, followed by addition of dry toluene (15 mL), sodium hydride (0.1 g, 4.16 mg),

and 4-aminophenol (0.6 g, 0.61 mmol). The mixture was degassed under vacuum pump and subjected to argon gas (inert atmosphere) followed by heating to 80 ^{o}C for 24 h. The reaction was monitored by a thin layer chromatograph (TLC). After 24 h, the reaction was allowed to cool to room temperature and toluene was removed using rotary evaporator under reduced pressure. The crude product was purified through column chromatography using active neutral alumina as stationary phase and chloroform/THF as eluent, affording a dark purple solid 362 mg (**3**).

3; Yield: 362 mg (81 %); FT-IR (cm^{-1}): 3233-3348 (-NH_2, aniline amine), 2021-2965 (C-H aromatic, CH_3), 1590 (C=N pyridine), 1500 (C-N, primary aromatic amine). ^{1}H NMR (600 MHz, $CDCl_3$): δ ppm, 5.79-5.83 (m, 2H, meta-axial Aromatic), 4.89-4.95 (d, 2H, ortho-axial Aromatic), 6.55 (s, 2H, axial NH_2), 8.00-8.06 (m, 4H, β pyrrole), 8.29 (s, 4H, β pyrrole), 9.05-9.10 (m, 16H, Pyridine-H). MALDI TOF-MS, calc 839.16, found 838.0 $[M]^+$. UV/visible (DMF): λ_{max} nm (log ε): 424 (5.3), 564 (4.5), 600 (3.2). Anal. Calcd for $C_{46}H_{30}InN_9O$. H_2O: C (65.80), H (3.60), N (15.01). Found: C (67.16), H (3.87), N (15.58).

5; Yield = 139.7 mg (59.5 %), eluent DCM; FT-IR (cm^{-1}): 2841-2910 (C-H aromatic, CH_3), 1646 (C=N pyridine). ^{1}H NMR (600 MHz, $CdCl_3$): δ, ppm 1.25 (s, 12H, methyl-H), 6.23-6.25 (t, 1H, pyridine-H), 7.42-7.45 (t, 1H, pyridine-H), 7.63-7.64 (d, 4H, β pyrrole), 7.68-7.69 (d, 4H, β pyrrole), 7.83-7.84 (d, 2H, Pyridine-H), 8.02-8.04 (d, 4H, Ar-H), 8.28-8.29 (d, 4H, Ar-H), 8.48-8.50 (m, 4H, Ar-H), 9.10 (s, 4H, Ar-H). MALDI TOF-MS, calc 1006.0, found 1005.9 $[M]^+$. UV/visible (DMF), λ_{max} nm (log ε): 433 (5.4), 556 (4.0), 609 (3.8). Anal. Calcd for $C_{53}H_{40}InN_5OS_4$. H_2O: C (63.28), H (4.01), N (6.96), S (12.75). Found: C (62.87), H (3.92), N (6.67), S (12.17).

Table 2.3 Axial modification of the neutral chloro indium complexes **2** and **4**.

Complexes	Porphyrin to be modified	Axial ligand and NaH	Reaction solvent	Reaction conditions	Purification
3	**2** (450 mg, 0.59 mmol)	4-aminophenol (0.6 g, 5.5 mmol), NaH (0.1 g, 4.2 mmol)	Dry toluene 15 mL	80 ^{o}C, inert atmosphere (argon), 24 h	Column chromatograph; active neutral alumina using chloroform/THF (1:1) v/v
5	**4** (100 mg, 0.11 mmol)	2-hydroxypyridine (200 mg, 2.10 mmol), NaH (0.1 g, 4.16 mg)		Reflux, inert atmosphere (argon), 48 h	Column chromatograph; active neutral alumina using DCM as eluent

2.3.4 Quaternization to form complexes 1Q-MeI, 1Q-HexI, 3Q-MeI, 3Q-HexI, and 5Q-MeI, Scheme 4.3

Similar procedure was used for quaternization of complex **1** to form complexes **1Q-MeI** and **1Q-HexI**, complex **3** to form complexes **3Q-MeI** and **3Q-HexI**, and **5** to form complex **5Q-MeI** following reported procedures [**108–110**]. **Table 2.4** shows a summary of reagents and reaction condition employed upon quaternization, and the synthesis of complex **1Q-MeI** was discussed as an example as follows; as-prepared complex **1** (70 mg, 0.086 mmol) was dissolved in chloroform (15 mL) followed by addition of methyl iodide (3 mL). The reaction was allowed to reflux for 30 min, and the compound was precipitated out by washing with excess chloroform to remove unquaternized species using a centrifuge. Dark purple solid was dried in a fume hood, affording 63.2 mg

1Q-MeI; Yield = 63.2 mg (90.3 %); IR (cm^{-1}): 3320-3429 (O-H), 3028-3093 (C-H aromatic, -CH_3), 1715 (C=O carboxylic acid), 1698 (C=N pyridine); ^{1}H NMR (400 MHz, DMSO-d_6): δ, ppm 4.66-4.80 (m, 9H, methyl iodide -CH_3), 8.17-8.33 (d, 2H, β pyrrole), 8.40-8.47 (d, 1h, β pyrrole), 8.48-8.53 (d, 1H, β pyrrole), 8.92-9.07 (s, 6H, pyridine), 9.08-9.14 (d, 2H, Ar_{ortho}-COOH), 9.16-9.28 (d, 2H, Ar_{meta}-COOH), 9.29-9.59 (m, 10H, β pyrrole and pyridine); UV/visible (DMF), λ_{max} nm (log ε): 429 (5.0), 565 (4.0), 608 (3.6). Elemental Analysis: Anal. Calcd for $C_{45}H_{34}ClInN_7O_2.H_2O$: C (61.90), H (4.12), N (11.23), Found: C (61.56), H (3.65), N (10.77).

1Q-HexI; Yield = 84 mg (66.9 %); FT-IR (cm^{-1}): 1630 (C=N pyridine), 1711 (C=O carboxylic acid), 3015 (C-H aromatic, hexane -CH_3), 3100-3524 (O-H carboxylic acid). ^{1}H NMR (600 MHz, D_2O): δ, ppm 2.21 (s, 9H, hexyl terminal -CH_3), 2.71 (s, 12H, alkyl CH_2), 3.59 (s, 18H, alkyl CH_2), 9.05-9.06 (d, 8H, β pyrrole), 9.35-9.36 (d, 8H, meta pyridyl H), 9.32 (s, 8H, ortho

pyridyl H). UV/visible (DMF), λ_{max} nm (log ε): 433 (5.2), 564 (3.9), 605 (3.3). Anal. Calcd for $C_{60}H_{64}ClI_3InN_7O_2.H_2O$: C (49.83), H (4.46), N (6.78). Found: C (48.92), H (4.69), N (6.21).

3Q-MeI; Yield = 76 mg (65.0 %); FT-IR (cm^{-1}): 1518 (C-N axial ligand), 1642 (C=N pyridine), 3017 (C-H aromatic and methyl CH_3), 3314-3541 (-NH_2 axial ligand). ^{1}H NMR (600 MHz, DMSO-d_6): δ, ppm 4.85 (s, 12H, methyl H), 7.06-7.07 (d, 4H, axial aromatic H), 7.70-7.72 (d, 2H, axial -NH_2), 9.08-9.09 (d, 8H, β pyrrole), 9.36-9.39 (d, 8H, meta pyridyl H), 9.41 (s, 8H, meta pyridyl H). UV/visible (DMF), λ_{max} nm (log ε): 434 (5.9), 564 (3.4), 604 (3.2). Anal. Calcd for $C_{50}H_{42}I_4InN_9O.H_2O$: C (44.67), H (3.01), N (8.96). Found: C (45.57), H (3.09), N (9.41).

3Q-HexI; Yield: 82 mg (65.5 %), FT-IR (cm^{-1}): 1514 (C-N axial ligand), 1636 (C=N pyridine), 2814-2951 (C-H aromatic and hexane CH_3), 3314-3541 (-NH_2 axial ligand). ^{1}H NMR (600 MHz, D_2O): δ, ppm 1.47-1.52 (d, 12H, hexyl terminal -CH_3), 1.64 (s, 6H, alkyl CH_2), 2.10 (s, 12H, alkyl CH_2),), 2.33 (s, 4H, alkyl CH_2),), 2.51 (s, 18H, alkyl CH_2), 5.01 (m, 4H, axial aromatic H), 8.37 (s, 2H, axial -NH_2), 9.09-9.10 (s, 6H, ortho pyridyl H), 9.17-9.22 (m, 6H, β pyrrole), 9.28-9.30 (d, 2H, β pyrrole), 9.41-9.45 (t, 2H, ortho pyridyl H), 9.50-9.54 (t, 2H, meta pyridyl H), 9.63-9.64 (s, 6H, meta pyridyl H). UV/visible (DMF), λ_{max} nm (log ε): 431 (5.6), 564 (3.7), 605 (3.4). Anal. Calcd for $C_{70}H_{82}I_4InN_9O.H_2O$: C (49.81), H (4.90), N (7.47). Found: C (48.76), H (4.58), N (7.01).

5Q-MeI; Yield = 58.2 mg (72 %); FT-IR (cm^{-1}): 2851-2910 (C-H aromatic, CH_3), 1646 (C=N pyridine). ^{1}H NMR (600 MHz, DMSO-d_6): δ, ppm 2.75 (s, 12H, S-methyl-H), 2.88 (s, 3H, quaternized methyl-H), 5.73 (s, 1H, pyridine-H), 6.15-6.17 (t, 1H, pyridine-H), 6.30-6.33 (d, 1H, pyridine-H), 6.98-7.0 (d, 1H, pyridine-H), 7.12-7.13 (m, 1H, β pyrrole), 7.34-7.44 (m, 3H, β pyrrole), 7.73-7.75 (d, 6H, Ar-H), 7.94 (s, 2H, β pyrrole), 8.17 (s, 6H, Ar-H), 9.0 (s, 4H, Ar-H), 9.01 (s, 2H, β pyrrole). UV/visible (DMF), λ_{max} nm (log ε): 429 (4.9), 563 (3.8), 605 (3.5). Anal.

Calcd for $C_{54}H_{42}InN_5OS_4^+.H_2O$: C (63.58), H (4.15), N (6.87), S (12.57). Found: C (62.92), H (4.59), N (5.85), S (13.61).

Table 2.4 reagents and reaction conditions upon quaternization to form complexes **1Q-MeI**, **1Q-HexI**, **3Q-MeI**, **3Q-HexI**, and **5Q-MeI**.

Complexes	Complex to be quaternized	MeI/ HexI	Reaction solvent	Reaction conditions	Precipitation solvent
1Q-MeI	**1** (70 mg, 0.086 mmol)	MeI (3 mL)	Chloroform (15 mL)	30 min, Reflux	Excess chloroform
1Q-HexI	**1** (100 mg, 0.12 mmol)	HexI (1.5 mL)	DMF (10 mL)	Overnight, 70 °C	Excess diethyl ether
3Q-MeI	**3** (100 mg, 0.071 mmol)	MeI (1.5 mL)	DMF (10 mL)	30 min, 70 °C	Excess diethyl ether
3Q-HexI	**3** (100 mg, 0.059 mmol)	HexI (1.5 mL)	DMF (10 mL)	30 min, 70 °C	Excess diethyl ether
5Q-MeI	**5** (100 mg, 0.099 mmol)	MeI (1 mL)	DMF (15 mL)	24 h, Reflux	Excess THF

2.4 Syntheses of nanoparticles

2.4.1 $CuFe_2O_4$ magnetic nanoparticles, Scheme 2.2

Copper ferrite magnetic nanoparticles were synthesized using the conversional co-precipitation method [111] with modification as follows: A solution containing $FeCl_3 \cdot 6H_2O$ (2.22 g, 8.2 mmol) and $CuCl_2 \cdot 2H_2O$ (699 mg, 4.1 mmol) was dissolved in 75 mL of deionized water and stirred at an ambient temperature under a continuous flow of argon, in a closed system. After 10 min of stirring, NaOH (15 mL of 0.005M in deionized water) was added drop-wise with continuous stirring with magnetic stirrer.

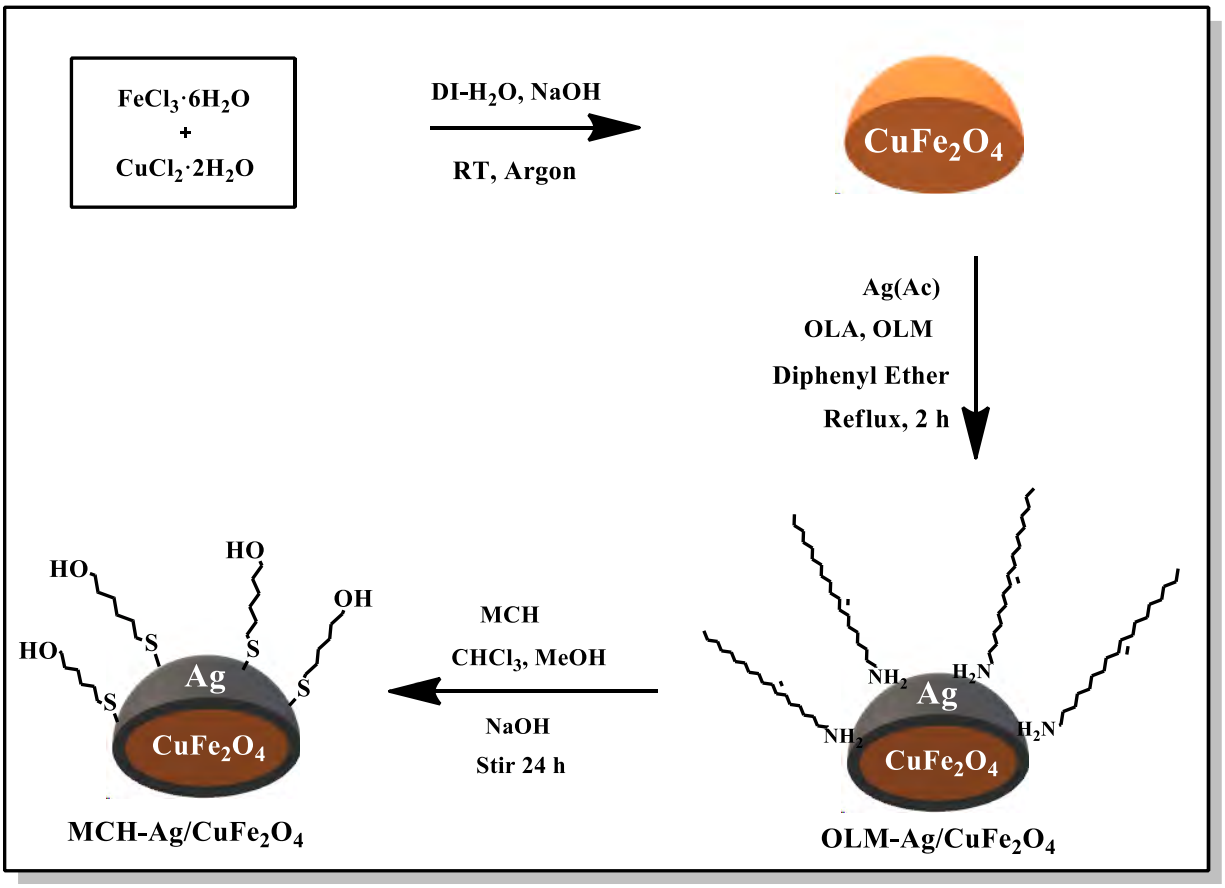

Scheme 2.2 Synthesis of oleyamine (OLM) and 6-mercapto-1-hexanol (MCH) functionalized $Ag/CuFe_2O_4$ core-shell MNPs. DI = deionized, OLA = oleic acid, RT= Room temperature.

During addition of NaOH, black-brown precipitate formed rapidly as a result of the formation of the copper ferrite nanoparticles. After addition of the base, the temperature of the mixture was elevated to 90°C and the stirring continued for 5 h at a constant temperature. The formed $CuFe_2O_4$ nanoparticles were collected and washed through centrifuging with water (4 × 40 mL) and ethanol (4 × 40 mL) then dried overnight in an air oven at 80°C.

2.4.2 OLM-Ag/$CuFe_2O_4$ magnetic nanoparticles, Scheme 2.2

Silver capped copper ferrite core-shell NPs were prepared using similar synthetic procedure for Ag/Fe_3O_4 and Au/Fe_3O_4 NPs [**112**] as follows: $CuFe_2O_4$ NPs (0.184 g) were dissolved in diphenyl ether (7.5 mL) in a three necked flask. Oleic acid (OLA, 0.75 mL), oleylamine (OLM, 3 mL) and Ag(ac) (0.28 g, 1.65 mmol) were introduced to the reaction vessel under an inert atmosphere of argon. The temperature was raised to ~200°C and kept constant for 2 h. The reaction was allowed to cool to room temperature with a continuous stirring overnight. The product was precipitated out of solution using ethanol and washed several times with ethanol through centrifuging and separated by external magnet then dried in a fume hood. The MNPs functionalized with OLM/OLA were represented as OLM-Ag/$CuFe_2O_4$ for simplicity.

2.4.3 MCH-Ag/$CuFe_2O_4$ magnetic nanoparticles, Scheme 2.2

OLA/OLM capped NPs were functionalized with MCH following reported procedure [**113**]. Typically, OLM-Ag/$CuFe_2O_4$ NPs (0.8 g) were dissolved in chloroform (5 mL) followed by addition of NaOH (1.5 g) into 15 mL of methanol and 0.2 mL of MCH. The mixture was continuously stirred overnight at 30 °C. The NPs were then precipitated using ethanol and

washed 3× with methanol and chloroform, then dried in a fume hood resulting in MCH-Ag/$CuFe_2O_4$ MNPs.

2.5 Formation of conjugates

2.5.1 Covalent conjugation of complex 1, 1Q-MeI, and 1Q-HexI to MCH-Ag/$CuFe_2O_4$ NPs, Scheme 2.3

Complexes **1** (25 mg, 0.027 mmol), **1Q-MeI** (25 mg, 0.018 mmol), or **1Q-HexI** (25 mg, 0.017 mmol) were dissolved in DMF 2.5 mL followed by addition of DCC (50 mg, 0.24 mmol) as a coupling agent, this procedure was reported elsewhere **[102]**. The mixtures were stirred for 24 h, to activate the carboxyl group of the porphyrins for ester coupling to the NPs. Then MCH-Ag/$CuFe_2O_4$ (20 mg) was introduced in to the mixtures. The reaction mixtures were stirred for 48 h at room temperature. After 48 h of the continuous stirring, ethyl acetate was introduced to the solution and the reaction vessel was placed in ice to precipitate out the conjugates (**1**-MCH-Ag/$CuFe_2O_4$, **1Q-MeI**-MCH-Ag/$CuFe_2O_4$ or **1Q-HexI**-MCH-Ag/$CuFe_2O_4$), and also to dissolve the unconjugated species. The conjugates were retrieved by centrifuge and further washed with MeOH and EtOH to remove the unreacted species and allowed to dry in a fume hood.

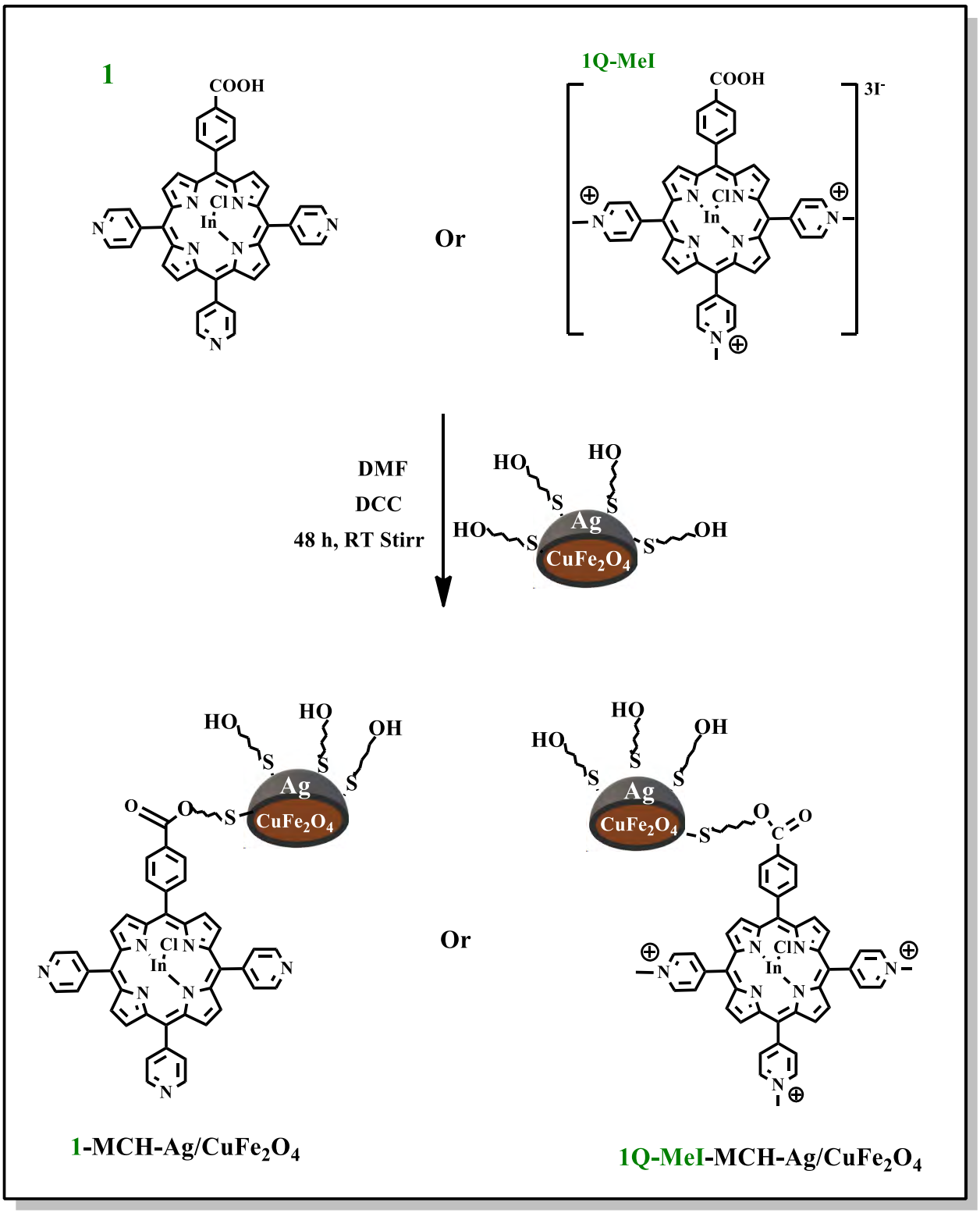

Scheme 2.3 schematic representations of complex **1** and **1Q-MeI** conjugated to MCH-Ag/$CuFe_2O_4$ through an ester bond, forming **1**-MCH-Ag/$CuFe_2O_4$ and **1Q**-MCH-Ag/$CuFe_2O_4$ complexes.

2.5.2 Self-assembly linkage of complex 3Q-MeI (Ag-N), 3Q-HexI (Ag-N), 5 (Ag-N and Ag-S), and 5Q-MeI (Ag-S) to OLM-Ag/$CuFe_2O_4$ and MCH Ag/$CuFe_2O_4$ NPs, Scheme 4.4

The linkage of the complexes **3Q-MeI** and **3Q-HexI** to MCH-Ag/$CuFe_2O_4$ NPs and complexes **5**, and **5Q-MeI** to both OLM-Ag/$CuFe_2O_4$ and MCH-Ag/$CuFe_2O_4$ NPs through self-assembly (Ag-S and/or Ag-N) was done following the reported procedures, with a few modifications being done [**113–115**]. Please note; **3Q-MeI** and **3Q-HexI** were only linked to MCH-Ag/$CuFe_2O_4$ NPs and not OLM-Ag/$CuFe_2O_4$ NPs. Complex **5** (35 mg, 0.036 mmol) or **5Q-MeI** (35 mg, 0.034 mmol) were dissolved in DMF (15 mL), followed by addition of either OLM-Ag/$CuFe_2O_4$ or MCH-Ag/$CuFe_2O_4$ NPs (17.5 mg). On the other hand either **3Q-MeI** (25 mg, 0.020 mmol) and **3Q-HexI** (25 mg, 0.017 mmol) were dissolved in DMF (10 mL), followed by addition of MCH-Ag/$CuFe_2O_4$ NPs (20.0 mg). The mixtures were stirred at 70°C and kept constant for 24 h. The product was precipitated out using ethanol, and washed with (1:1) ethanol and methanol 4× through centrifuging to remove species not linked to the NPs. Resulting conjugates were named **5**-OLM-Ag/$CuFe_2O_4$, **5Q-MeI**-OLM-Ag/$CuFe_2O_4$, **5**-MCH-Ag/$CuFe_2O_4$ and **5Q-MeI**-MCH-Ag/$CuFe_2O_4$. On the other hand, complexes **3Q-MeI** and **3Q-HexI** conjugates were named **3Q-MeI**-MCH-Ag/$CuFe_2O_4$ and **3Q-HexI**-MCH-Ag/$CuFe_2O_4$.

2.6 Antimicrobial methods

2.6.1 Photosensitizers

Most of the complexes and conjugates were not water soluble, hence for a fair comparison PACT studies were studied using 2% DMSO dissolved in PBS. Concentrations of 2.5, 5.0, 7.5, 10, and 12.5 µM (based on the porphyrin), were used during the optimization of the photosensitizers for complexes **1**, **1Q-MeI**, **1Q-HexI**, **3Q-MeI**, and **3Q-HexI**. Concentrations

1.5, 3.0, 4.5, 6.0, and 7.5 µM were used for **5** and **5Q-MeI**. This was done to observe the minimum concentration of the PS that obliterates 100% of the bacteria in 30 min of irradiation. 2.5 µM was observed to be the optimal concentration for **1**, **1Q-MeI**, **1Q-HexI**, **3Q-MeI**, and **3Q-HexI** on the other hand 1.5 µM was found to be optimal concentration for **5** and **5Q-MeI**. The optimal PS concentration contains viable colony suitable to conduct PACT time studies.

2.6.2 Bacterial strains and culture conditions

For PACT studies, gram (+) bacteria strain *Staphylococcus aureus* (ATCC® 25923) and gram (-) bacteria strain *Escherichia coli* (ATCC® 25922) were used to study the antibacterial activity of the synthesized complexes. The reported procedure involving the turbidimetric analysis was employed to perform PACT studies [**116**]. Bacteria crystals (either *S. aureus* or *E. coli*) were dissolved in a nutrient broth (6 mL) and allowed to grow aerobically incubated in a rotary shaker (~200 rpm) at 37°C for 48 h for *S. aureus* and 6 days for *E. coli*. The optical density of 0.6-0.7 was observed and the broth washed through centrifuging (4000 RPM for 10min, ×3) using PBS. The cultured bacterial strains were kept in 100 mL PBS (bacterial stork solution 10^{-2} dilution factor) and refrigerated. The bacteria-porphyrin solution was incubated for 30 min to internalize the PS, followed by placing of the solutions into two separate 24 microplates (for light and dark studies) each containing 3 mL from 6 mL working stork bacteria-porphyrin solution prepared above. One microplate was irradiated using 415 LED (with a 14 nm irradiation width) and the other plate was placed in the dark. The studies were done for 25 min, in 5 min intervals, inoculation (100 µL) over agar plates were done both for dark and light microplates, followed by incubation of the inoculated plates for 24 h

at 37°C. A control (bacteria solution without a PS) was also plated over agar plates at t = 0 min and t = 30 min and subjected to similar conditions for 24 h.

2.6.3 Light source and exposure

An irradiation chamber mounted with a light-emitting diode M415L4 (LED) fitted with a 24 well microplate where the LED is projected (see **Fig. 2.1**). The mounted LED can be replaced depending on the preferred irradiation wavelength as per photosensitizer used. In this work, 415 nm LED was employed, delivering maximum irradiance of 15.6 μW/mm^2. The LED is fixed on the top of the chamber facing the well microplate at the bottom. The bacteria-porphyrins solution in a 24 well microplate was exposed under ambient conditions in a chamber for irradiation, with no external light interfering with the system.

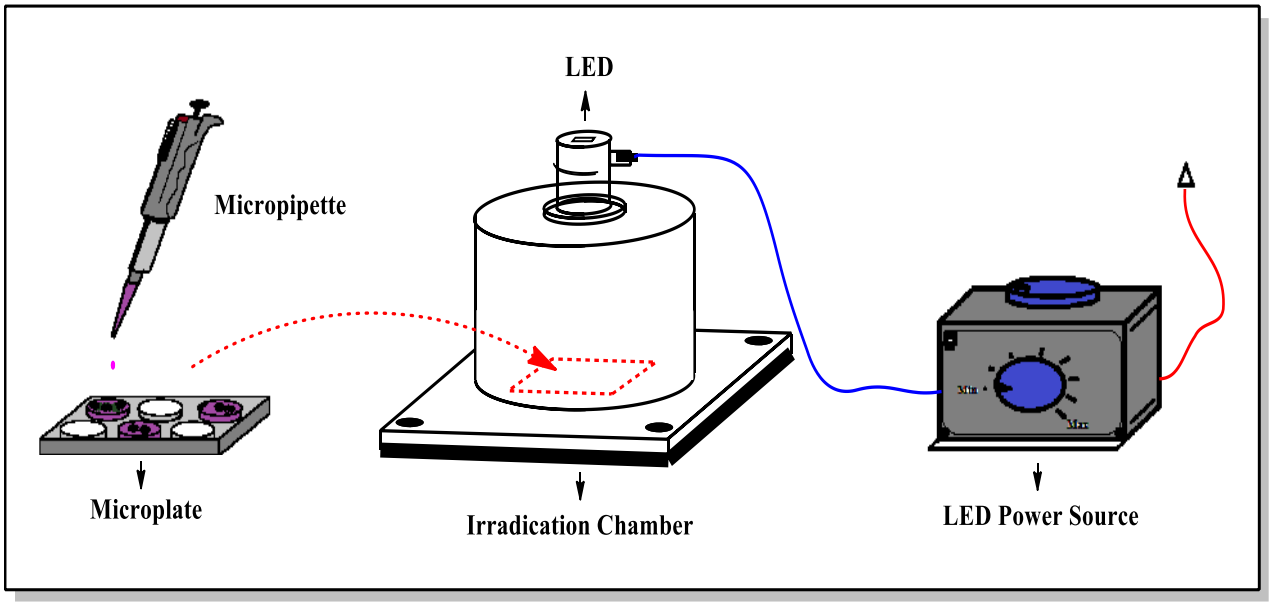

Fig. 2.1 Schematic diagram for PS-bacteria mixture irradiation setup using LED (λ = 415 nm) for light studies in PACT.

2.6.4 Octanol-water partitioning coefficient (log $P_{o/w}$) methods

Lipophilicity of the amphiphilic complexes **1Q-MeI**, **1Q-HexI**, **3Q-MeI**, and **3Q-HexI** were studied through the partition coefficients (log $P_{o/w}$) using the shake-flask procedure reported before [**105**], further delineated by **Fig. 2.2**. Please note; the partitions were done using sealed beakers and separating funnel and the studies for **5Q-MeI** were not represented. The studies were as follows; stork solution of porphyrin complexes, either **1Q-MeI**, **1Q-HexI**, **3Q-MeI**, or **3Q-HexI** was prepared with an absorbance of ~1.5 dissolved in 10 mL of 1-octanol. The mixture was ultra-sonicated to completely dissolve the complexes. UV-Vis absorption spectroscopy was used to measure the Soret band absorbance of the complexes in the as-prepared 1-octanol and the absorbance was named A. This was followed by addition of 3 mL of the as-prepared porphyrin-octanol mixture into 3 mL of water and followed by vigorous stirring at room temperature for 5 h. After 5 h has lapsed, the mixture was allowed to settle and partition overnight. The 1-octanol layer was extracted and the Soret band UV-Vis absorbance was obtained and named A_o.

To calculate the absorbance of the complex dissolved in water (A_w) upon partition, and algebraic expression $A_w = A - A_o$ was used. The log $P_{o/w}$ values were then calculated based on the log (A_o/A_w) using **E.q (2.1)**.

$$logP_{(O/W)} = log\frac{[A_O]}{[A_w]} \qquad (\mathbf{2.1})$$

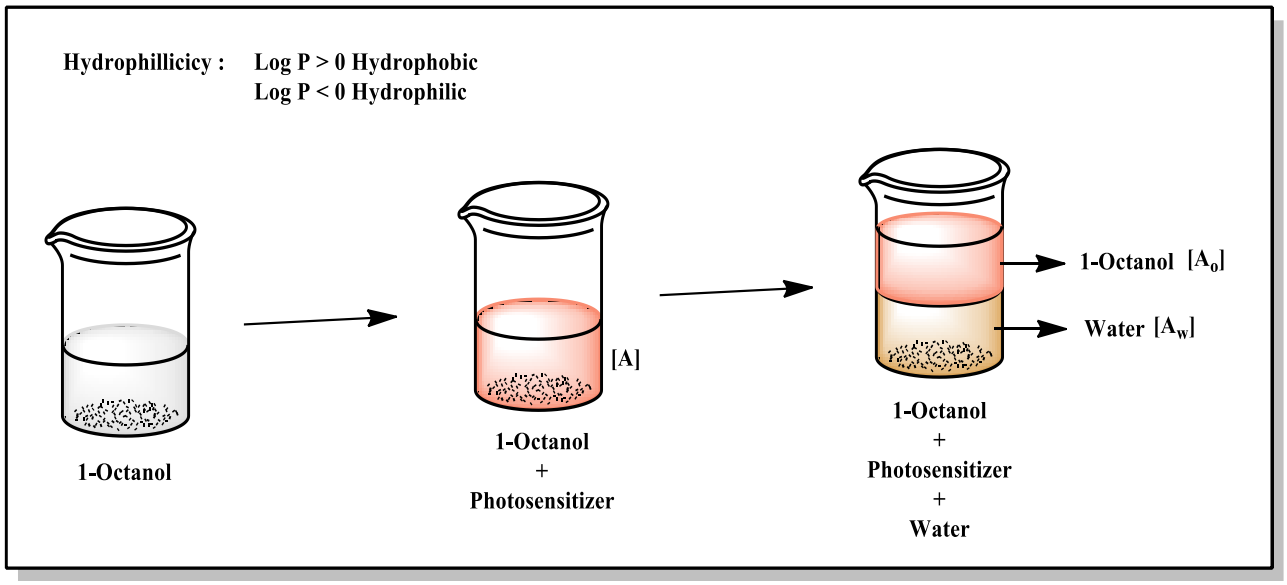

Fig. 2.2 Schematic illustration of octanol-water partitioning coefficient (log $P_{o/w}$) analysis using shake-flask procedure.

2.6.5 Statistical analysis

For statistical analysis, the Kruskal-Wallis test and consequently Mann-Whiteney test were used to compare cell viability over irradiation time in a specific concentration. This test is used to determine if there exists a statistically significant difference between two or more groups of an independent variable on a continuous variable. Regression coefficients are compared, where if there are non-overlapping intervals between the regression coefficients, they are considered to be significantly different. Analysis of variance (ANOVA) using excel data analysis of the variables regression plots was also used for validation of the results. $p< 0.05$ value was considered statistically significant.

Chapter 3

Failed attempted syntheses

This chapter outlines the synthetic procedures in an attempt to the synthesis of novel cationic porphyrins as potential photosensitizers for photodynamic antimicrobial chemotherapy.

3.1 Synthesis of 5-p-Carboxyphenyl-10,15,20-(tris-4-phenoxypyridyl)-porphyrin (complex 6), Scheme 3.1.

3.1.1 Route A: Synthesis of 6 from 4-phenoxypyridine aldehyde (PPyA)

The synthesis of complex **6** was attempt through a prior preparation of a modified aldehyde (**PPyA**). **PPyA** was prepared following a reported literature procedure with a few modifications [**117,118**]. Typically, 4-hydroxypyridine (0.6 g, 5.6 mmol) and K_2CO_3 (2.4 g, 3 eq) were placed in a 100 mL two neck round bottom flask along with dry DMF (15 mL). The contents were degassed and placed under a continuous flow of nitrogen gas, followed by heating gently to a constant temperature of 80°C for 1 h. Afterward, the reaction was allowed to cool before the introduction of 4-nitrobenzaldehyde (1.04 g, 5.6 mmol). Then the reaction mixture was allowed to reflux (120°C) for 24 h. The reaction was placed into a 200 mL beaker containing ice-cooled water and further neutralized with 10% HCl. The precipitates were filtered and dried in a fume-hood, followed by purification using a column chromatograph and DCM used as eluent, resulting in brown-yellow solid 0.76 g, **PPyA**.

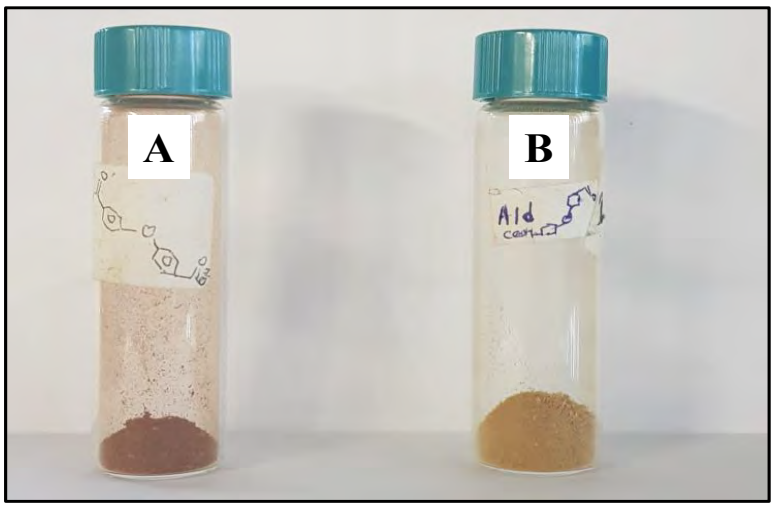

Fig. 3.1 An image of (**PPyA**), (A) under reflux conditions, 120°C (B) at room temperature; as a precursor for the synthesis of complex **6**.

As prepared coupled aldehyde **PPyA** (250 mg, 1.31 mmol) and 4-formylbenzoic acid (62.0 mg, 0.42 mmol) were placed into 75 mL of propionic acid in a 200 mL two neck round bottom flask. The contents were allowed to reflux at 120°C, followed by an edition of prior distilled pyrrole (0.18 mL, 1.73 mmol), and the reaction was allowed to proceed for a further 3 h with a reflux temperature of 120°C. The reaction was monitored using UV-Vis and TLC plate to monitor the formation of complex **6,** based on the appearance of porphyrin absorption bands. However, there was no porphyrin formation in the reaction. This was confirmed using mass spectrometry. The unsuccessful synthetic procedure could be attributed to acid sensitivity if the oxygen-bearing aldehyde, which may have prevented the formation of complex **6**.

3.1.2 Route B: synthesis of 6 from 5-p-Carboxyphenyl-10,15,20-(tris-4-bromophenyl)-porphyrin ($(Br)_3COOH$), Scheme 3.1

Complex **$(Br)_3COOH$** was synthesized using a reported synthetic procedure [**102**]. Typically, 4-bromobenzaldehyde (0.96 g, 5.3 mmol) and 4-formylbenzoic acid (0.265 g, 1.76 mmol) were placed in 200 mL round bottom flask and dissolved in 100 mL of propionic acid. The contents were allowed to reflux with a continuous stirring, followed by a drop-wise edition of pyrrole (0.68 mL, 7.06 mmol). The reaction was left to reflux for 3 h and precipitated using NaOH pellets dissolved in ice-cooled water. The product was separated and purified using silica gel column chromatography and DCM as a mobile phase. The resulting product (**$(Br)_3COOH$**) was then dried under reduced pressure in a rotary evaporator.

Porphyrin complex **$(Br)_3COOH$** was used in an attempt to synthesize complex **6**. A reported procedure was used with a few modifications [**48**]. Typically, as-prepared complex

$(Br)_3COOH$ (0.2 g, 0.24 mmol) and 4-hydroxypyridine (0.78 g, 0.72 mmol) was placed in a 100 mL two neck round bottom flask dissolved in 15 ml of dry DMF and anhydrous K_2CO_3 (1.37 g, 8.03 mmol), the reaction was allowed to heat up gently to 120°C. A constant reflux temperature was kept for 24 h. Thin layer chromatography (TLC) and UV-Vis were used to monitor the progress of the reaction. There were no any significant changes on the UV-Vis spectra, moreover, post TLC analysis showed the starting materials. The reaction was run further overnight and no changes were observed. Mass spectrometry was used and only complex **$(Br)_3COOH$** was observed.

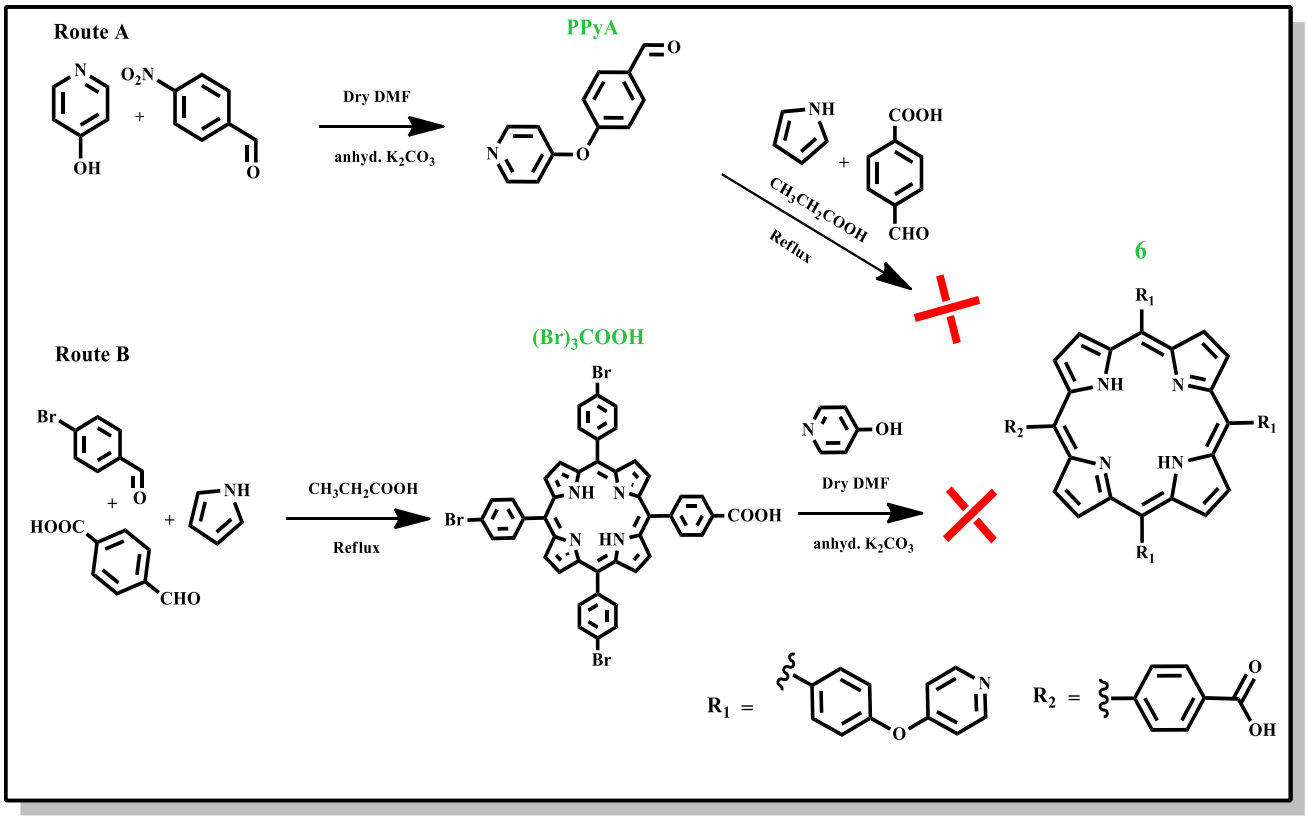

Scheme 3.1 Schematic illustration of attempted synthesis of 5-p-Carboxyphenyl-10,15,20-(tris-4-phenoxypyridyl)-porphyrin (complex **6**).

3.2 Rationale behind the synthesis.

Synthesis of asymmetrically substituted complex **6** was attempted, aiming to achieve an end product that would be metalated with indium (III) chloride and further quaternized with methyl iodide to form two more porphyrin complexes. 5-p-carboxyphenyl-10,15,20-(tris-4-phenoxypyridyl)-porphyrin (**6**) has almost similar meso-substituents to **1** except that **6** has a phenoxy bridges. Photophysical properties and PACT activities of complex **6** were to be studied in comparison to complex **1**, **1Q-MeI**, and **1Q-HexI** based on the effect brought by the phenoxy bridges on the porphyrin complexes. The reaction procedures used in this synthesis are known and have been reported, however, an unknown reason caused the reaction not to occur.

Results and Discussions

This section holds two chapters

Chapter 4: Synthesis, characterization, photophysicochemical parameters, stability studies.

Chapter 5: Antimicrobial studies.

Publications

The results and discussions outlined in the foregoing chapters (4 and 5) are based on the following publications. (* These publications are not referenced in this work).

- **L. Collen Makola**, Muthumuni Managa, Tebello Nyokong*, Enhancement of Photodynamic antimicrobial chemotherapy through the use of Indium Cationic Porphyrin Conjugated to Ag/$CuFe_2O_4$ nanoparticles. Photodiagnosis and Photodynamic Therapy. 30 (**2020**) 101736.
- **L. Collen Makola**, Tebello Nyokong*, Edith K. Amuhaya*, Impact of axial ligation on photophysical and photodynamic antimicrobial properties of Indium (III) methylsulfanylphenyl porphyrin complexes linked to silver-capped copper ferrite magnetic nanoparticles. Polyhedron. 193 (**2021**) 114882.
- **L. Collen Makola**, Sithi Mgidlana, Tebello Nyokong*, Amphiphilic axially modified cationic indium-porphyrins linked to hydrophilic magnetic nanoparticles for photodynamic antimicrobial chemotherapy against gram-negative strain, *Escherichia coli*. Dyes and Pigments. (**2021**) 109262 (In Press)

Chapter 4

Synthesis, characterization, photophysicochemical properties, stability studies.

This chapter outlines detailed synthesis, characterizations, and photophysical parameters of all the synthesized complexes and conjugates and the hydrodynamic and surface stability studies of the conjugates.

4.1 Synthesis and characterizations of porphyrins

4.1.1 Synthesis of complexes a, b, c, 1, 2, and 4, Scheme 4.1

Scheme 4.1 shows a pathway towards the synthesis of free-base porphyrin complexes (**a**, **b**, and **c**) and metalated complexes (**1**, **2**, and **4**). The famous Adler and Longo's porphyrin synthetic procedure was used for the synthesis of the free-base complexes (see **Scheme 2.1**) [**26**]. Complex **1**, **2**, and **4** resulted from indium(III) chloride metal ion insertion into the cavity of the porphyrin complexes **a**, **b**, and **c**, respectively, using a reported synthetic procedure (**Scheme 4.1**) [**103**]. Please note; characterizations for **b** not fully discussed in this work as it is commercially available and is well explored [**10,119–121**].

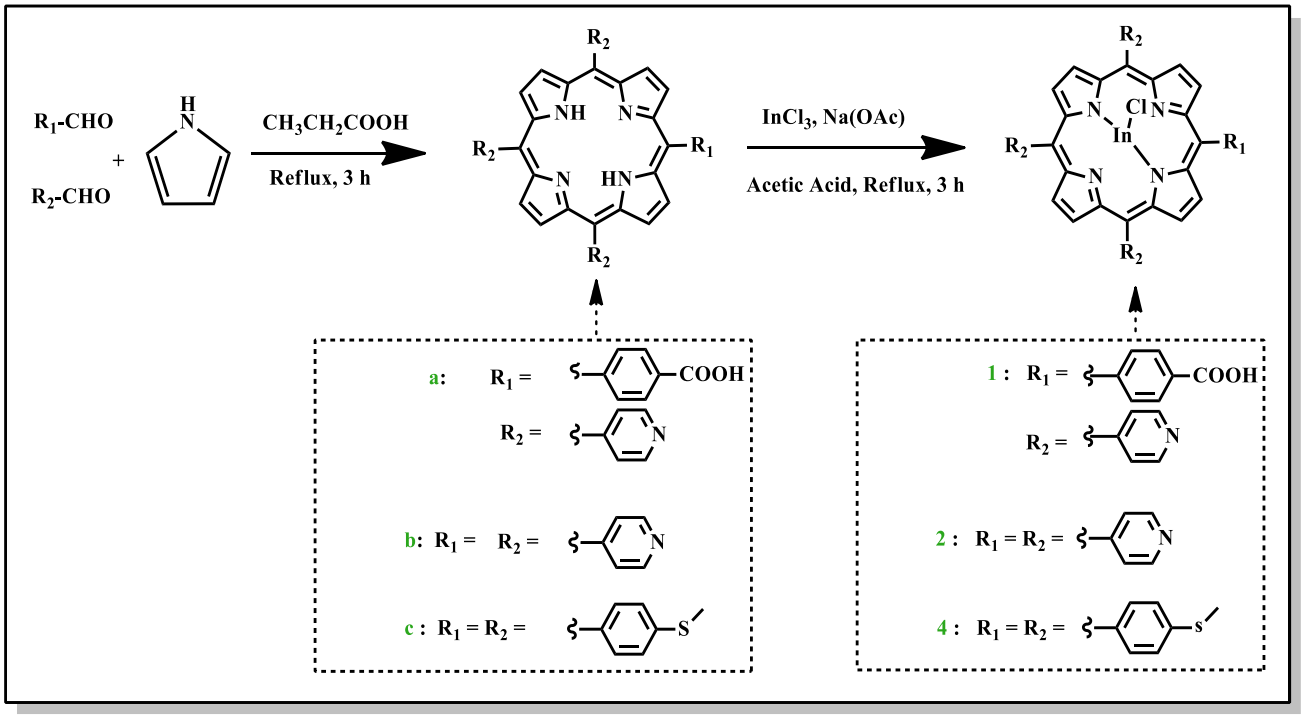

Scheme 4.1. Synthetic pathway for free-base porphyrin complexes **a**, **b**, and **c**, followed by metalation to form metalloporphyrin complexes **1**, **2**, and **4**.

4.1.2 Synthesis of axially modified porphyrin complexes 3 and 5. Scheme 4.2

Scheme 4.2 shows an axial modification of chloro indium metalloporphyrin complexes **2** and **4**. Complexes **3** and **5** were synthesized through light and air-sensitive reported synthetic procedures, where the chloro axial ligands on the indium metalloporphyrins **2** and **4** were replaced by the 4-aminophenol and 2-hydroxypyridine to form complexes **3** and **5**, respectively. Indium (III) porphyrins axially substituted with phenols as axial ligands have been reported[**104,105,122**]. Indium (III) metal ion is known to be oxophilic and thus shows a preference for phenolates, carboxylates, and other oxygen-bearing anionic ligands [**123**].

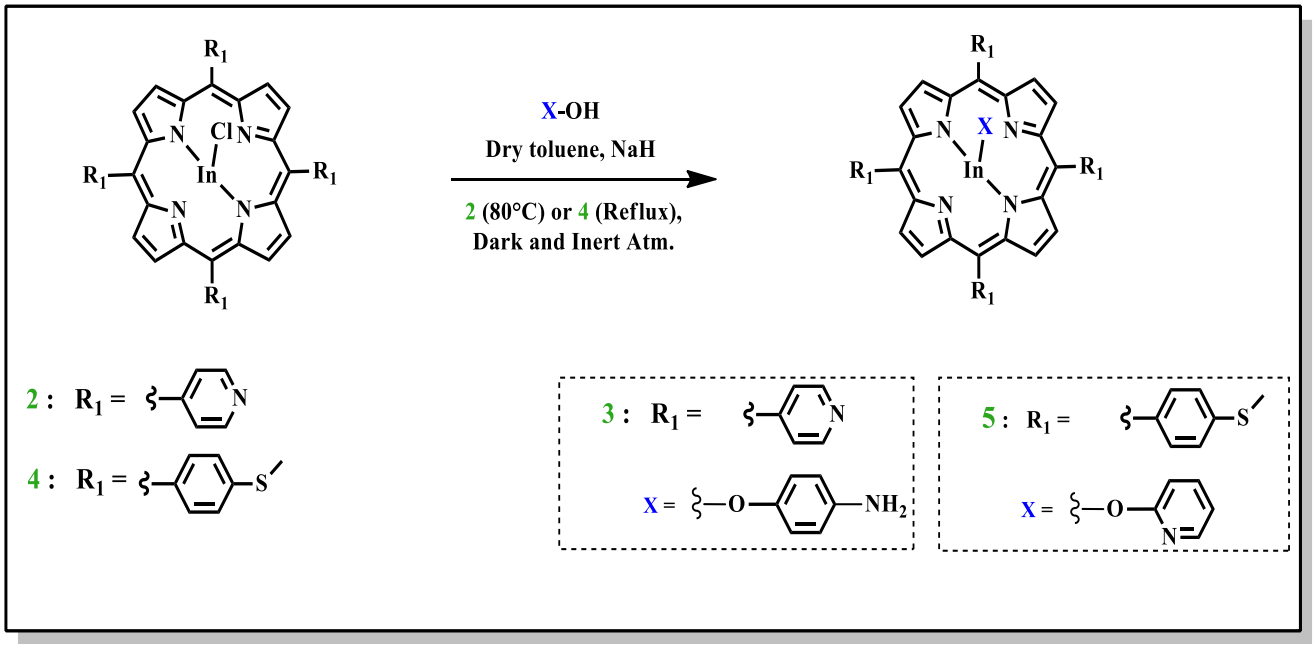

Scheme 4.2. Axial modification of indium(II) chloride metalloporphyrins to form porphyrin complexes **3** and **5**.

4.1.3 Synthesis of cationic porphyrin complexes 1Q-MeI, 1Q-HexI, 3Q-MeI, 3Q-HexI, and 5Q-MeI.

All the cationic porphyrins were synthesized from the as-prepared metalloporphyrins following a previously reported synthetic procedure [105]. Complexes **1Q-MeI** and **1Q-HexI** were synthesized by refluxing complex **1** in the presence methyl iodide or hexyl iodide, respectively, as alkyl halides quaternizing agents. Complexes **3Q-MeI** and **3Q-HexI** were synthesized from **3**, and complex **5Q-MeI** from **5** as shown in **Scheme 4.3**. Please note that it is imperative to use a weaker quaternizing agent over a possible short reaction time to quaternize pyridyl substituents in the presence of -NH_2 bearing ligand, this is to eliminate the chances of quaternizing the -NH_2 of the axial ligand. The quaternization of pyridyl in the presence of -NH_2 has been reported before [108].

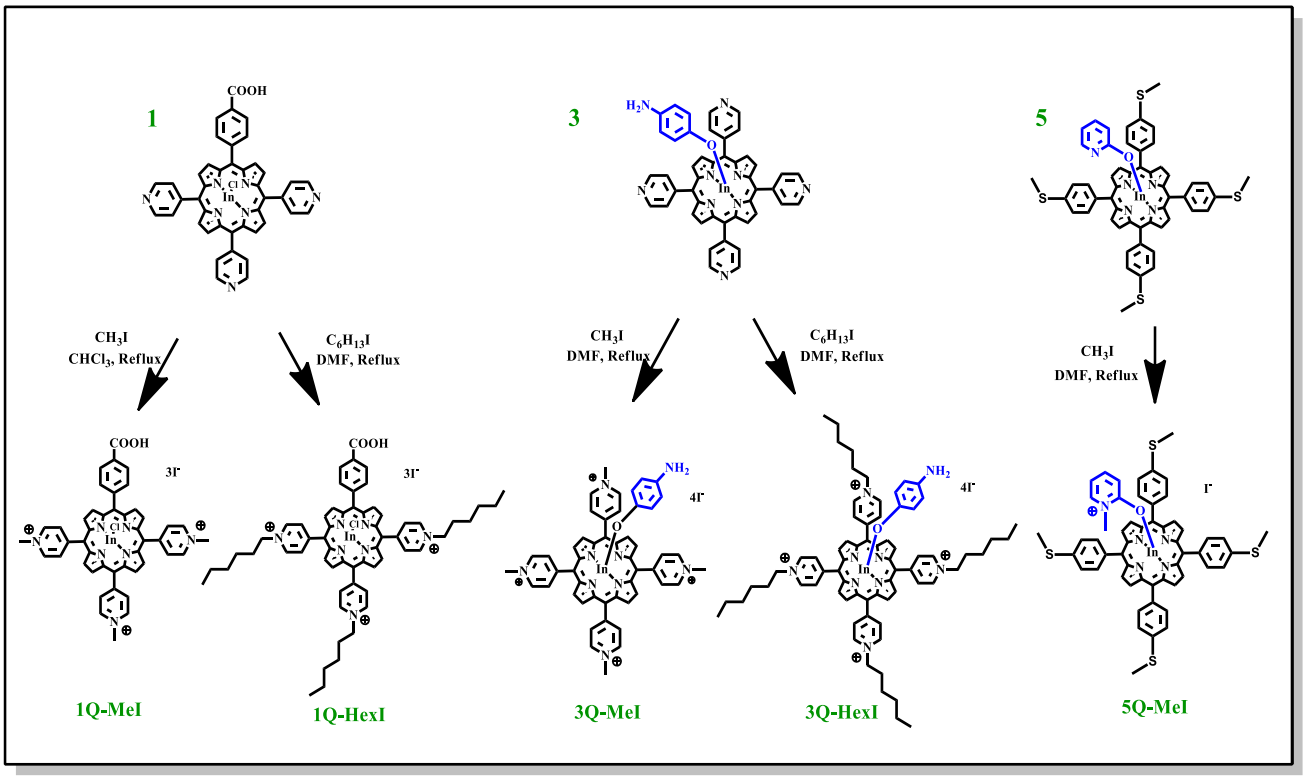

Scheme 4.3 Quaternazation of metalloporphyrins (**1**, **3**, and **5**) to form cationic porphyrins **1Q-MeI**, **1Q-HexI**, **3Q-MeI**, **3Q-HexI**, and **5Q-MeI**.

4.1.4 Characterization of the porphyrin complexes

All the porphyrin complexes were characterized using UV-Visible spectroscopy, elemental analysis, Fourier-transform infrared spectroscopy (FT-IR), MALTI-TOF mass spectra, and ^{1}H NMR spectroscopy. From MALTI-TOF mass spectra, the molecular ion peak was observed at m/z = 662.3 for complex **a**, at m/z = 799.5 for complex **c**, at m/z = 774.5 for complex **1**, at m/z = 731.9 for **2**, at m/z = 838.0 for **3**, at m/z = 946.3 for **4**, and at m/z = 1005.9 for **5** (see **Fig. A1** to **A7**, Appendix). For **4** m/z = 911.78 and 946.27, the two peaks were due to the presence and absence of Cl atoms. The quaternised complexes **1Q-MeI**, **1Q-HexI**, **3Q-MeI**, **3Q-HexI**, and **5Q-MeI** did not ionize, hence mass spectra data not discussed. ^{1}H NMR spectrum for complex **1** was integrated to 24H excluding COOH singlet proton, **1Q-MeI** to 33H excluding the COOH singlet proton, **1Q-HexI** to 63H excluding the COOH singlet proton, **3** to 30H, **3Q-MeI** to 42H, **3Q-HexI** to 82H, **5** to 40H, and **5Q-MeI** to 43H (see **Fig. A8** to **A15**). The elemental analysis results agree with observations that porphyrins are often isolated as hydrates [**124**].

Table 4.1. Optical parameters (UV-Vis and fluorescence spectra) for all the complexes in DMF, and TGA loading studies (mg of porphyrin/ mg of conjugate) for the conjugates.

Complexes	$\lambda_{Abs.}$ (nm) Soret	$\lambda_{Abs.}$ (nm) Q-bands (Q1,Q2,Q3,Q4)	TGA-Loading mg/mg
a	417	514, 548, 587, 644	-
1	426	561, 600	-
1Q-MeI	429	565, 608	-
1Q-HexI	433	564, 605	
b	415	512, 447, 587, 642	-
2	424	563, 601	-
3	424	564, 600	-
3Q-MeI	434	564, 604	-
3Q-HexI	431	564, 608	-
c	424	517, 557, 595, 561,	-
4	433	566, 609	-
5	433	556, 609	-
5Q-MeI	429	563, 605	-
1-MCH-Ag/$CuFe_2O_4$	427	559, 602	0.22
1Q-MeI-MCH-	433	561, 604	0.21

$Ag/CuFe_2O_4$			
1Q-HexI-MCH-$Ag/CuFe_2O_4$	436	568, 604	0.37
3Q-MeI-MCH-$Ag/CuFe_2O_4$	433	567,602	0.35
3Q-HexI-MCH-$Ag/CuFe_2O_4$	435	568, 602	0.50
5-OLM-$Ag/CuFe_2O_4$	433	574, 611	0.57
5Q-MeI-OLM-$Ag/CuFe_2O_4$	429	563, 604	0.40
5-MCH-$Ag/CuFe_2O_4$	432	569,605	0.43
5Q-MeI-MCH-$Ag/CuFe_2O_4$	428	567,603	0.39

- No values recorded

4.1.4.1 Optical Ultraviolet-visible and fluorescence spectroscopy

All the Ultraviolet-visible absorption and fluorescence emission spectra were obtained under ambient conditions using DMF as a solvent unless stated otherwise (**Fig. 4.1** and **Table 4.1**). In the UV-Visible spectra of complex **a**, the Soret band was observed at 417 nm, **Table 4.1** and **Fig. 4.1** (A), with less intense four Q bands, typical for a free-base porphyrin. Similar spectra were observed for **b** with the Soret band observed at 415 nm, and **c** observed at 424 nm. The observed red-shift is as a result of the different meso pyridyl (**a**)

and methylthiophenyl (**b**) substituents, since sulfur containing substituents are known to red-shift the Soret band electronic absorption spectra [**72**]. The four Q-bands in **a**, **b**, and **c** merged into two Q bands upon the formation of the metalated complexes **1** , **2**, and **4**, and the Soret band red-shifting for this complexes to 426 nm, 424 nm, and 433 nm, respectively. Introduction of heavy metal such as indium could result in a degree of perturbation and electron delocalisation within the porphyrin macrocycle [**72,125**], resulting in red-shifts in absorption spectra. Red-shifting of the Soret bands was observed upon quaternization of complex **1** to form **1Q-MeI** (429 nm) and **1Q-HexI** (433 nm). Similar trends were observed upon the formation of **3Q-MeI** (434 nm) and **3Q-HexI** (431 nm) from **3** (424 nm). However, blue shifting was observed upon quaternization of complex **5** (433 nm) to form **5Q-MeI** (429 nm). There was no spectral shifting upon axial modification of complex **2** (424 nm) to form **3** (424 nm) or **4** (433 nm) to form **5** (433 nm) in DMF (see **Fig. 4.1** (B) and **Table 4.1**). UV-Vis absorption spectra of the complexes were obtained using 2% DMSO in water to study the effect of axial modification (**Fig. 4.1**). An improved electronic absorption spectra was observed for **5** as compared to **4** which showed a broad Soret band, signifying aggregation [**105**]. **Fig. 4.1** (D) shows fluorescence emission spectra for **b** as an example, with two fluorescence emission bands observed at 650 nm and 712 nm, typical for free-base porphyrins [**126,127**]. Fluorescence was very weak for complexes **2** due to the presence of the heavy central metal which facilitates intersystem crossing to the triplet state, hence the quenching fluorescence. A similar trend was observed for all the metalated complexes.

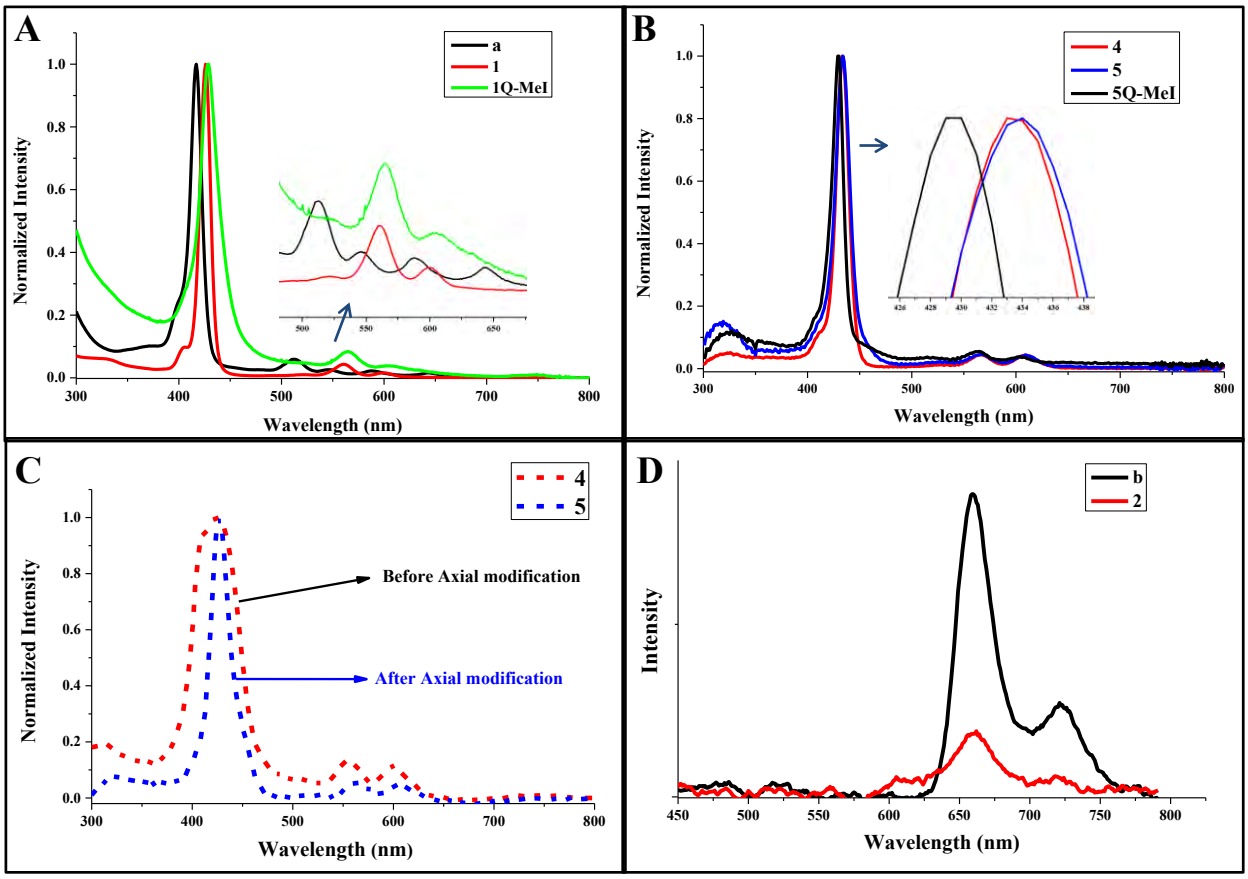

Fig. 4.1. Electronic Absorption spectrum of porphyrin complexes (A) **a**, **1**, and **1Q-MeI** (B) **4**, **5**, and **5Q-MeI** in DMF and (C) **4** and **5** using 2% DMSO in water, (D) Fluorescence emission spectrum of **b** and **2**. (λ_{exc} = ~430 and recorded from 450 to 800 nm in DMF).

4.1.4.2 Fourier-transform infrared spectroscopy

FT-IR spectroscopy (**Fig. 4.2**) was used to trace and analyse the changes in functional groups upon the synthesis of each complex. FT-IR was used to prove axial ligation and further to show consistency in functional groups before and after quaterization of the complexes. Complexes **1**, **4**, and **5** in **Fig. 4.2** are used as examples. The obtained results were consistent with the expected functional groups. FT-IR spectra for the free-base porphyrin complex **c** show the presence of pyrrolic N-H stretch at 3311 cm^{-1}.

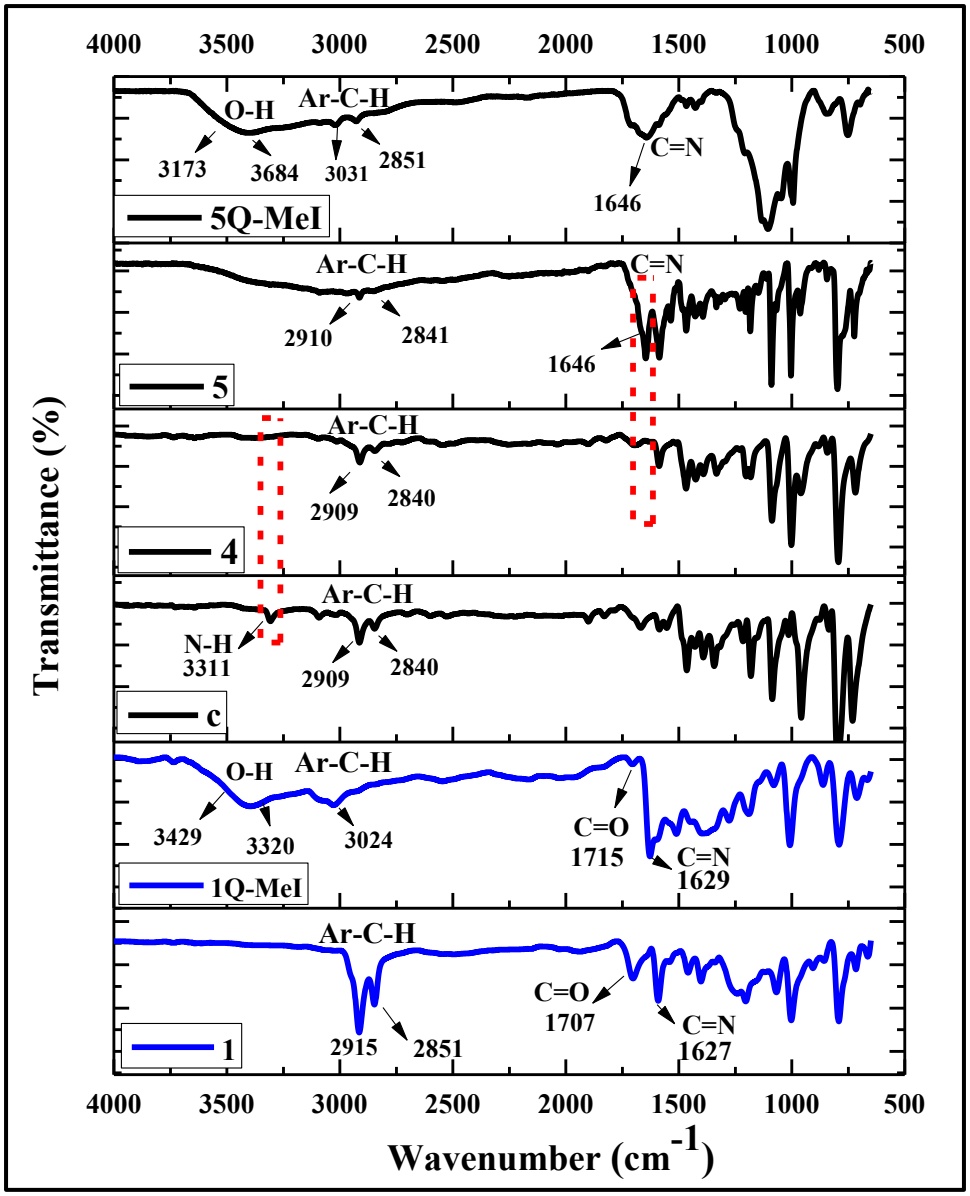

Fig. 4.2 FT-IR spectra analysis for the porphyrin complexes, **1**, **1Q-MeI**, **c**, **4**, **5**, and **5Q-MeI**.

The N-H stretch disappears upon indium metal ion insertion to form complex **4** from **c**; similar phenomena were observed for metalation of all the free-base porphyrins. Asymmetrical complex **1** shows the presence of C=N at 1627 cm^{-1} and C=O at 1707 cm^{-1} as a result of pyridyl and carboxyphenyl substituents, respectively. The FT-IR spectra of **5** show the appearance of a sharp and intense stretch at 1646 cm^{-1} attributed to C=N stretching resulting from axial ligation with 2-hydroxypyridine. Upon the quaternization of complex **5** to form **5Q-MeI**, broadening of C=N stretch at 1646 cm^{-1} was observed, this can be

attributed to the interaction of the quaternizing agent with the C=N to form a cationic side. Similar peak broadening was observed upon the formation of complexes **1Q-MeI** and **1Q-HexI** from **1** and **3Q-MeI** and **3Q-HexI** from **3**. A broad O-H peak observed for complex **5Q-MeI** ranging between 3173 and 3684 cm^{-1} can be attributed to moisture trapped [**128**], and the O-H (3320-3429 cm^{-1}) of the carboxylic acid for complex **1Q-MeI**.

4.2 Synthesis of magnetic nanoparticles and conjugates

Synthesis of the nanoparticles and conjugates were achieved by employing various reported literature procedures outlined below (also in **Chapter 2**).

4.2.1 Synthesis of OLM-Ag/$CuFe_2O_4$ and MCH-Ag/$CuFe_2O_4$ MNPs, Scheme 2.2

The synthesis of OLM-Ag/$CuFe_2O_4$ and MCH-Ag/$CuFe_2O_4$ followed a step by step modification of $CuFe_2O_4$ MNPs (see **Scheme 2.2**). $CuFe_2O_4$ MNPs were synthesized using the conversional co-precipitation method [**111,129**]. The reaction was performed under an inert atmosphere to avoid oxidation of the iron and copper. $CuFe_2O_4$ MNPs were further capped with silver (Ag) in the presence of oleyamine (OLM/OLA) as stabilizing agent to enhance solubility in organic solvents [**130**]. The MNPs are represented as OLM-Ag/$CuFe_2O_4$ MNPs, please note; OLA left out for simplicity. The as-prepared OLM-Ag/$CuFe_2O_4$ MNPs were further functionalized with 6-mercapto-1-hexanol (MCH) through ligand exchange between the OLM/OLA and MCH, which resulted in the formation of MCH-Ag/$CuFe_2O_4$ MNPs.

4.2.2 Covalent conjugation of complex 1, 1Q-MeI, and 1Q-HexI to MCH-Ag/$CuFe_2O_4$ MNPs, Scheme 2.3

Asymmetrical complexes **1**, **1Q-MeI**, and **1Q-MeI** were covalently linked to MCH functionalized MNPs through an ester bond, and the conjugates are represented as **1**-MCH-

Ag/$CuFe_2O_4$, **1Q-MeI**-MCH-Ag/$CuFe_2O_4$, and **1Q-MeI**-MCH-Ag/$CuFe_2O_4$. **1**-MCH-Ag/$CuFe_2O_4$ and **1Q-MeI**-MCH-Ag/$CuFe_2O_4$ were used as examples to demonstrate the conjugation as shown in **Scheme 2.3**. This was made possible due to the presence of a carboxylic acid functional group on the porphyrins and alcohol functional group on the NPs.

A reported synthetic procedure was employed to achieve this conjugation [**102,131**]. Typically, the carboxylic acid was activated using DCC as a coupling agent to form an active carbodiimide ester group followed by the addition of the MCH-Ag/$CuFe_2O_4$ MNPs. It is important to note that Ag-N self-assembly interactions are also possible between complex **1** and the MCH-Ag/$CuFe_2O_4$ MNPs.

4.2.3 Self-assembly of complexes 3Q-MeI and 3Q-HexI onto MCH-Ag/$CuFe_2O_4$, and 5 and 5Q-MeI to both OLM-Ag/$CuFe_2O_4$ and MCH-Ag/$CuFe_2O_4$ NPs, Scheme 4.4

Complexes **3Q-MeI** and **3Q-HexI** were linked to MCH-Ag/$CuFe_2O_4$ MNPs self-assembly (Ag-N) forming **3Q-MeI**-MCH-Ag/$CuFe_2O_4$ and **3Q-HexI**-MCH-Ag/$CuFe_2O_4$, respectively. Please note; OLM-Ag/$CuFe_2O_4$ NPs could have also been used, however, only MCH-Ag/$CuFe_2O_4$ NPs were still available. Complexes **5** and **5Q-MeI** were linked to OLM-Ag/$CuFe_2O_4$ NPs through self-assembly forming **5**-OLM-Ag/$CuFe_2O_4$ (Ag-S and Ag-N bonds) and **5Q-MeI**-OLM-Ag/$CuFe_2O_4$ (Ag-S bond), respectively. Complexes **5** and **5Q-MeI** were also self-assembled onto MCH-Ag/$CuFe_2O_4$ forming **5**-MCH-Ag/$CuFe_2O_4$ (Ag-S and Ag-N bonds) and **5Q-MeI**-MCH-Ag/$CuFe_2O_4$ (Ag-S bond), respectively. The linkages were done following the reported procedures [**113**].

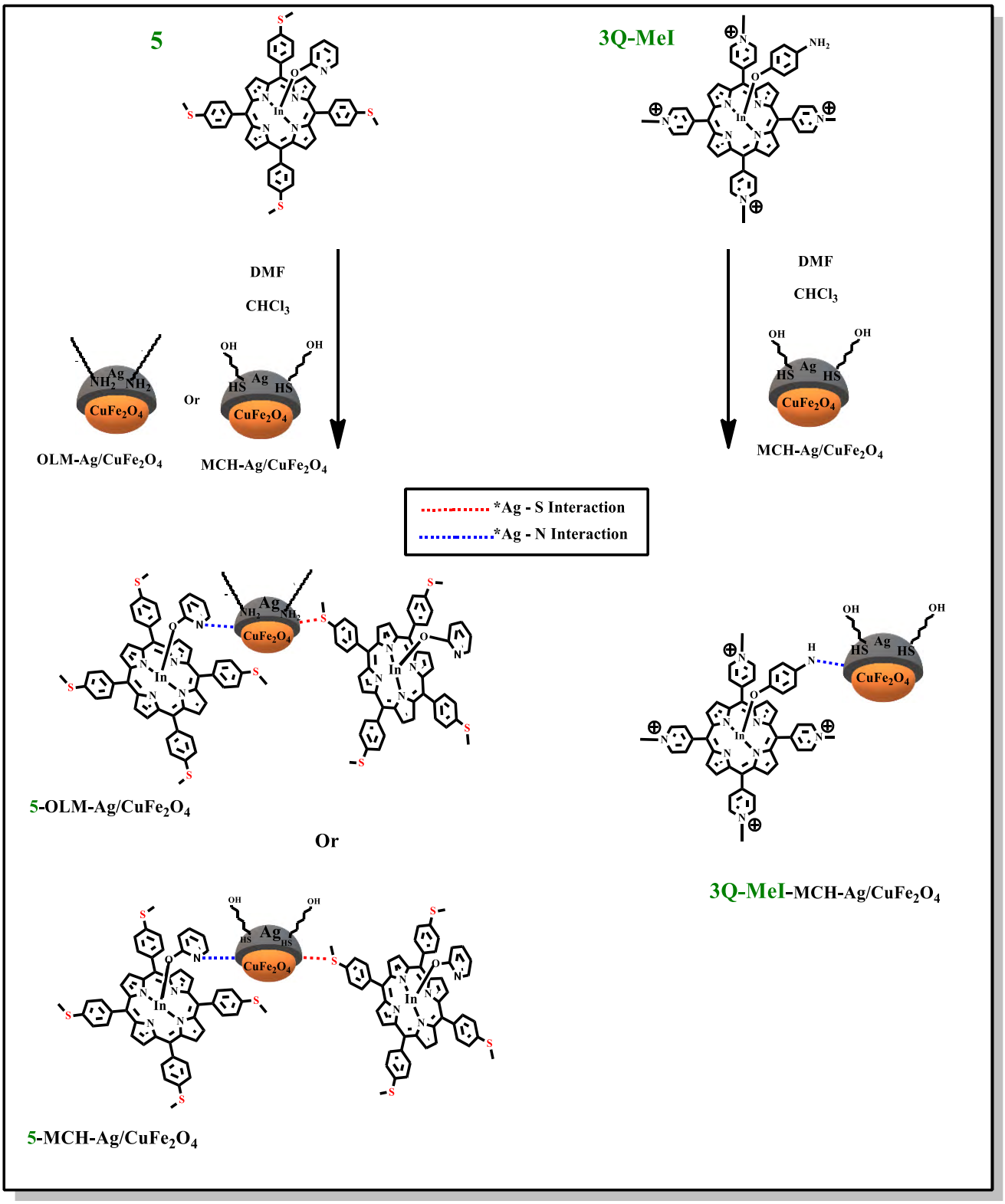

Scheme 4.4 Schematic illustrations of complex **5** and **3Q-MeI** conjugated to OLM-Ag/$CuFe_2O_4$ and OLM-Ag/$CuFe_2O_4$ MNPs through self-assembly (Ag-N and Ag-S).

Complexes **5** and **5Q-MeI** were used as examples to delineate the linkages (**Scheme 4.4**). Ag-N linkage is possible as a result of the pyridine and amino axial ligands. The unquaternized complex **5** has two possible coordination sides; that is through the sulfur meso-substituents (Ag-S) and the nitrogen (Ag-N) on the axial ligands.

4.3 Characterizations of the nanoparticles and the conjugates

The characterization of synthesized MNPs and conjugates were achieved through the use of various characterization techniques. Ultraviolet-visible spectroscopy (UV-Vis), energy dispersive spectroscopy (EDS), transmission electron microscopy (TEM), dynamic light scattering (DLS), Fourier transform infrared (FT-IR), and X-ray diffraction (XRD) were used. FT-IR was employed to prove the conjugation of the complexes to the NPs. The conjugation through self-assembly was further proven using X-ray photoelectron spectroscopy (XPS). The ratio of porphyrins linked to the NPs were quantitatively analysed using thermal gravimetric analysis (TGA) [**132**]. Typically, thermal decomposition profiles of the porphyrin, NPs, and the conjugate were compared. TGA curves and corresponding derivative thermogravimetry (DTG) analysis of complex **3Q-MeI**, MCH-Ag/$CuFe_2O_4$ NPs, and **3Q-MeI**-MCH-Ag/$CuFe_2O_4$ conjugate are shown as examples in **Fig. A16** (appendix). The obtained loading values are listed in **Table 4.1**, where **5**-OLM-Ag/$CuFe_2O_4$ gave the highest loading value, which means that there are more porphyrin molecules attached to the NPs. The relatively high loading value for complex **5** could be due to more than one coordination side.

4.3.1 Ultraviolet-visible spectroscopy

All the UV-Vis absorption spectra were obtained under ambient conditions using DMF as a solvent (**Fig. 4.3**). UV-Vis spectra of the pristine MNPs and conjugates with complexes **3Q-**

MeI, **3Q-HexI**, **5**, and **5Q-MeI** are shown as examples in **Fig. 4.3**. **Fig. 4.3** (A) shows the absorption band for $CuFe_2O_4$ with a peak at 325 nm, typical of iron oxide nanoparticles [**133**]. Capping of $CuFe_2O_4$ MNPs with Ag to form OLM-Ag/$CuFe_2O_4$ resulted in the presence of surface plasmon resonance (SPR) [**134**] observed at 410 nm for the latter. SPR was observed at 349 nm upon further functionalizing with 6-mercapto-1-hexanol to form MCH-Ag/$CuFe_2O_4$. There were no significant changes in Soret band absorption spectra of the complexes upon conjugation to the NPs. However, there was an observed increase in absorption below 400 nm and this was ascribed to the SPR absorption band of the NPs.

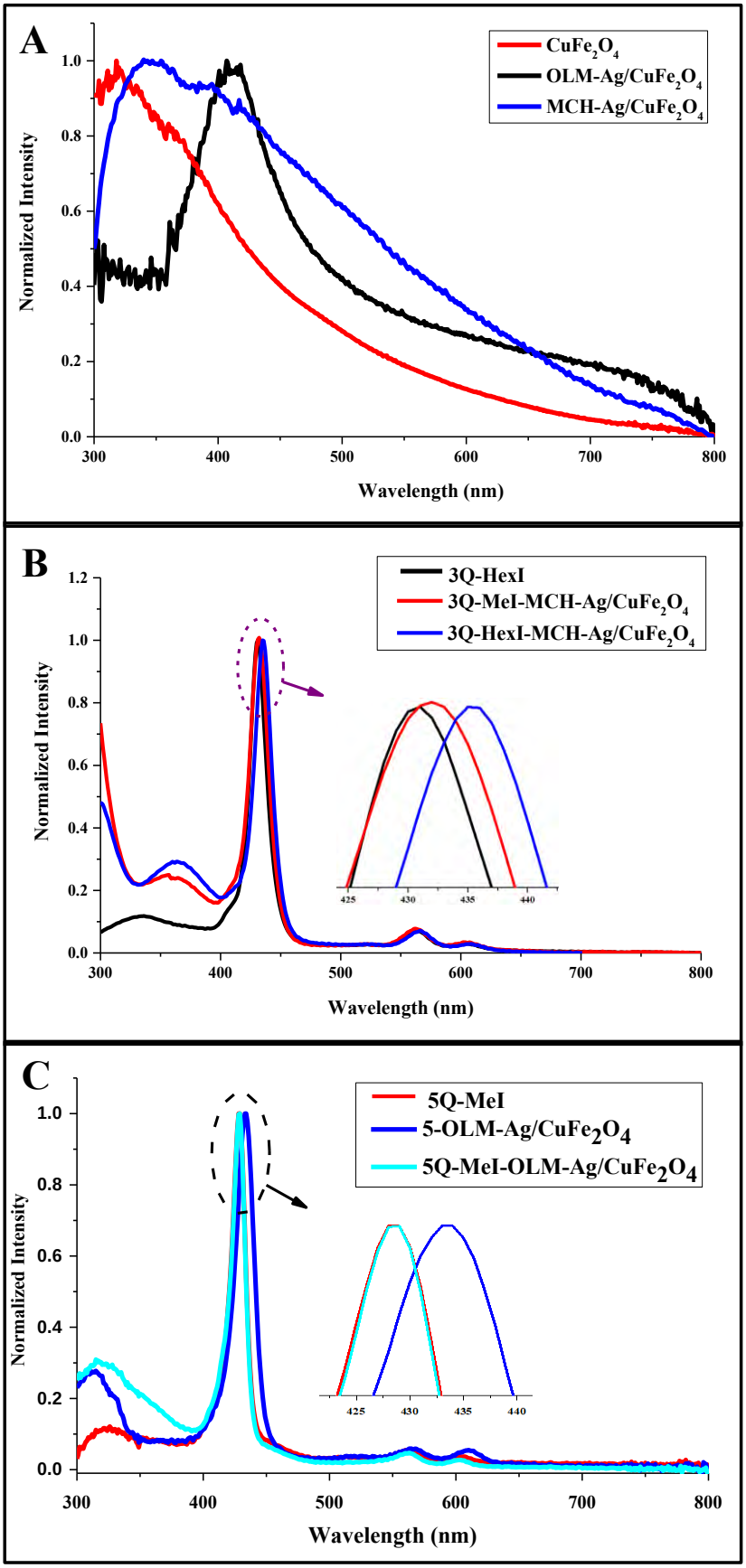

Fig. 4.3 UV-Vis electronic absorption spectrum of (A) nanoparticles, (B and C) porphyrin-MNPs conjugates in DMF.

4.3.2 Energy dispersive microscopy (EDS)

Energy dispersive microscopy (EDS) was used for the qualitative analysis of the elemental compositions of all the synthesized materials. The EDS micrographs (**Fig. 4.4**) of the porphyrins, nanoparticles, and conjugates show the presence of all the expected individual elements within the compounds. The NPs show the presence of all the expected metals; that is silver, copper, and iron. EDS for OLM-Ag/$CuFe_2O_4$ shows the presence of nitrogen which was as a result of oleyamine.

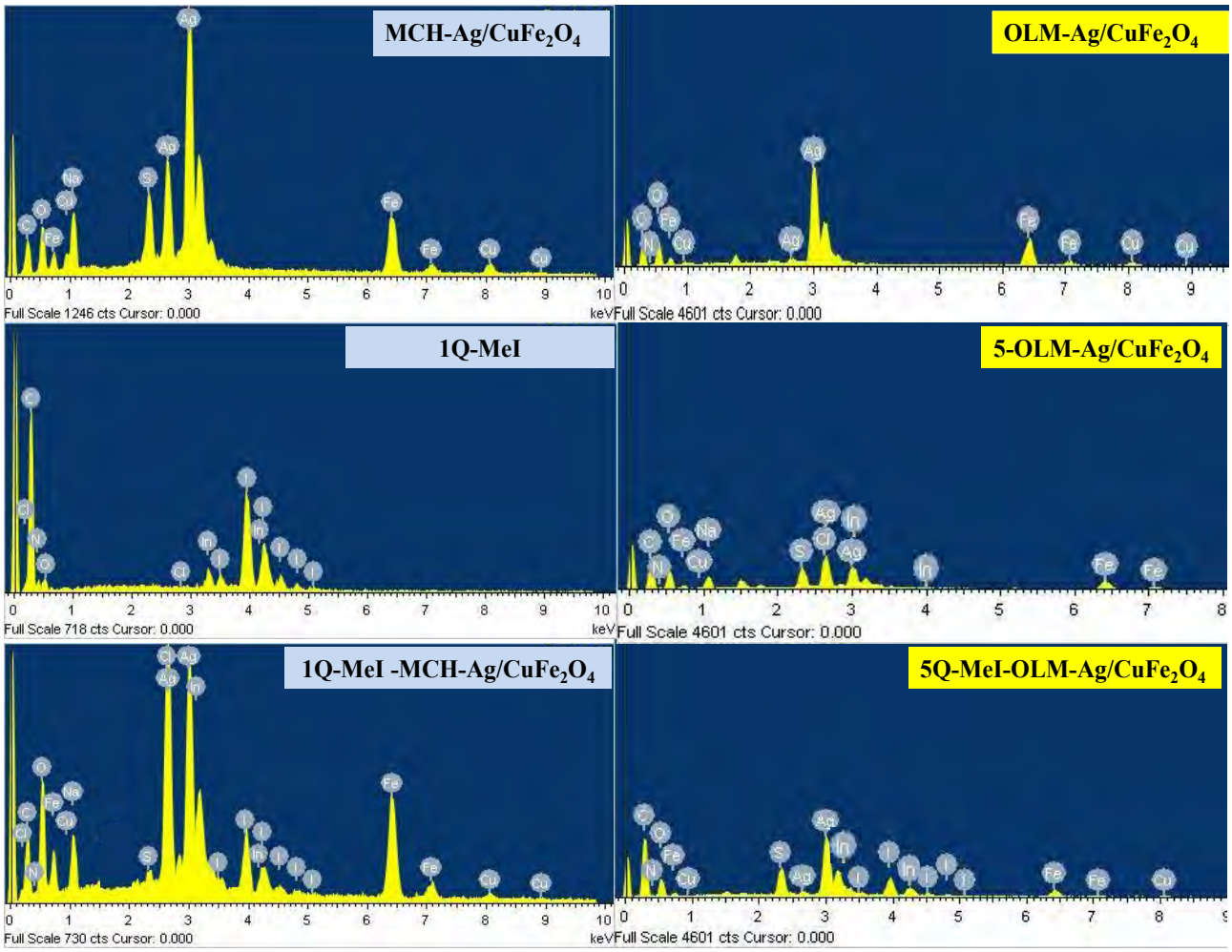

Fig. 4.4 Energy dispersive microscopy (EDS) analysis of pristine nanoparticles and corresponding conjugates.

Sulfur was observed for the MCH-Ag/$CuFe_2O_4$ upon the functionalization of OLM-Ag/$CuFe_2O_4$ with 6-mercapto-1-hexanol. The quaternized (**1Q-MeI** and **5Q-MeI**) conjugates show the presence of iodine, resulting from methyl iodide and hexyl iodide. Indium was observed in all the conjugates since the porphyrin complexes were metalated using indium (III) chloride. All the conjugates show the presence of both the MNPs and the porphyrins.

4.2.3 Transmission electron microscopy (TEM)

Fig. 4.5 shows TEM micrographs used for morphological analysis of Ag/$CuFe_2O_4$ NPs and conjugates. The size distribution values are outlined in **Table 4.2**. TEM micrograph of bare $CuFe_2O_4$ showed aggregation (not shown in **Fig. 4.5**), which is commonly observed for bare magnetic NPs [**135**]. Upon capping with silver to form MCH-Ag/$CuFe_2O_4$ and OLM-Ag/$CuFe_2O_4$ NPs, monodispersed spherical (core-shell like) particles with an average size distribution (**Fig. 4.5**) of 12.0 nm and 12.5 nm, respectively, were observed (**Table. 4.2**). The functionalization of the OLM-Ag/$CuFe_2O_4$ with mercapto-1-hexanol did not show any significant morphological changes. However, upon conjugation of MCH-Ag/$CuFe_2O_4$ (12.0 nm) NPs via covalent linkage to complexes **1** and **1Q-MeI**, aggregation was observed in both conjugates. The average particle size of 14.0 nm and 15.0 nm were obtained for **1**-MCH-Ag/$CuFe_2O_4$ and **1Q-MeI**-MCH-Ag/$CuFe_2O_4$, respectively. A similar trend was observed for the self-assembly linkage of complex **5** and **5Q-MeI** to both MCH-Ag/$CuFe_2O_4$ and OLM-Ag/$CuFe_2O_4$ NPs, where the size of bare NPs increased upon conjugation (see **Table 4.2**). For **1Q-HexI**-MCH-Ag/$CuFe_2O_4$, **3Q-HexI**-MCH-Ag/$CuFe_2O_4$, and **5Q-MeI**-MCH-Ag/$CuFe_2O_4$ TEM micrograph size analysis could not be done due to aggregation.

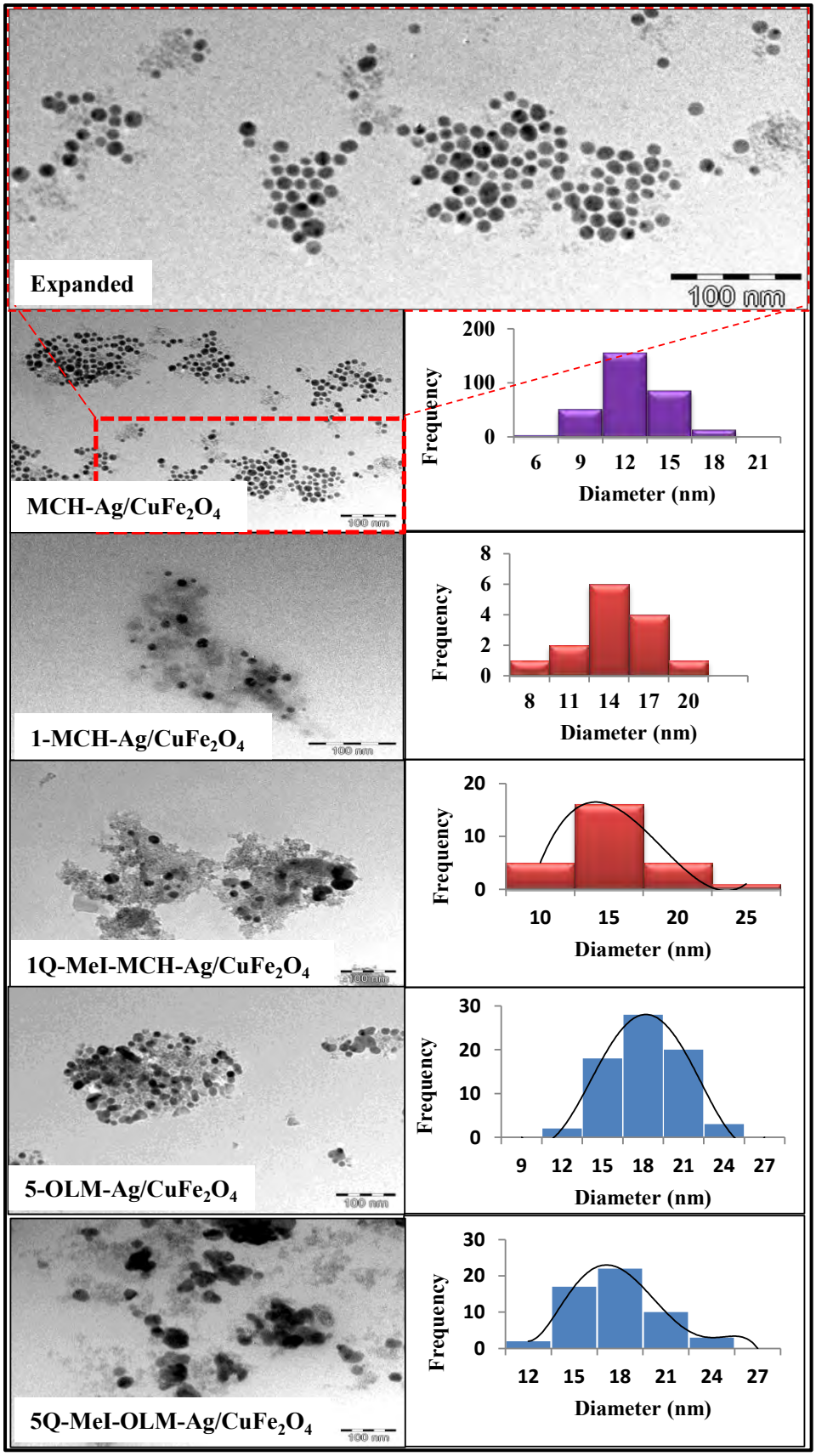

Fig. 4.5 Transmission electron microscopy (TEM) micrographs of the nanoparticles and conjugates together with and the corresponding histogram size distribution curve.

Table 4.2 Nanoparticle and conjugates sizes and Zeta potentials (ζ) analysis

Complexes	TEM size (nm)	AFM size (nm)	D_h (d. nm)	XRD size, D (nm)	Zeta Potential ζ (mV)	PDI
a	-	-	-	-	+14.2	-
1	-	-	-	-	+16.1	-
1Q-MeI	-	-	-	-	+25.3	-
1Q-HexI	-	-	-	-	+32.2	-
b	-	-	-	-	-16.1	-
2	-	-	-	-	+5.63	-
3	-	-	-	-	+4.03	-
3Q-MeI	-	-	-	-	+24.6	-
3Q-HexI	-	-	-	-	+22.4	-
c	-	-	-	-	-16.1	-
4	-	-	-	-	-12.7	-
5	-	-	-	-	-11.8	-
5Q-MeI	-	-	-	-	+17.0	-
OLM-Ag/$CuFe_2O_4$	12.5	13.0	15.0	12.24	-26.8	0.112
MCH-Ag/$CuFe_2O_4$	12.0	14.1	13.5	11.85	-27.3	0.091
1-MCH-Ag/$CuFe_2O_4$	14.0	-	21.5	12.73	-17.5	0.261
1Q-MeI-MCH-Ag/$CuFe_2O_4$	15.0	21.4	24.4	12.08	+12.3	0.284
1Q-HexI-MCH-Ag/$CuFe_2O_4$	-	19.5	26.3	16.9	+17.7	0.453
3Q-MeI-MCH-Ag/$CuFe_2O_4$	16.9	18.7	21.8	18.1	+15.1	0.198

3Q-HexI- MCH-Ag/$CuFe_2O_4$	-	20.3	25.7	15.7	+18.1	0.265
5-OLM-Ag/$CuFe_2O_4$	18.0	28.4	24.0	16.51	-18.6	0.203
5Q-MeI-OLM-Ag/$CuFe_2O_4$	17.0	24.8	22.0	15.87	-28.3	0.129
5-MCH-Ag/$CuFe_2O_4$	18.0	23.7	21.5	14.95	-26.1	0.145
5Q-MeI-MCH-Ag/$CuFe_2O_4$	-	27.4	21.0	16.23	-27.0	0.227

No values (-)

4.3.4 AFM analysis

Atomic force microscopy (AFM) was employed to ascertain the sizes, shapes, and topological surface roughness (microscopic peaks and valleys) of the NPs and nanoconjugates (**Fig. 4.6**). AFM analysis was conducted using a Tapping mode and the nanoconjugates were dissolved in 50:50 % v/v (DMSO: water) before being place on a mica surface and allowed to dry overnight in an oven. MCH-Ag/$CuFe_2O_4$ NPs and the nanoconjugates **5**-MCH-Ag/$CuFe_2O_4$ and **5Q-MeI**-MCH-Ag/$CuFe_2O_4$ were used as examples in **Fig. 4.6**. **Fig. 4.6(A)** shows AFM analysis of NPs alone, where the two-dimensional (2D) image clearly showing defined spherical and monodispersed particles with an average particle size distribution of 14.1 nm. There were no observed significant size, shape, or topological surface variation between MCH-Ag/$CuFe_2O_4$ (14.1 nm) and OLM-Ag/$CuFe_2O_4$ (13.0 nm). The line profiling (**Fig. 4.6(A)**) shows the average height of 14.5 nm for MCH-Ag/$CuFe_2O_4$ NPs which is close to the average particle size of 14.1 nm for the NPs, and this was anticipated since the NPs are spherical NPs. The particle sizes were processed using AFM data analysis and also ImageJ. 3D image (**Fig 4.6(A)**) shows the average roughness and

inhomogeneity of the cluster formation of the NPs. Upon the formation of the nanoconjugates, slight aggregation was observed for all the conjugates, and both the average particle sizes and height of the nanoconjugates increased. The particle sizes are shown in **Table 4.2**.

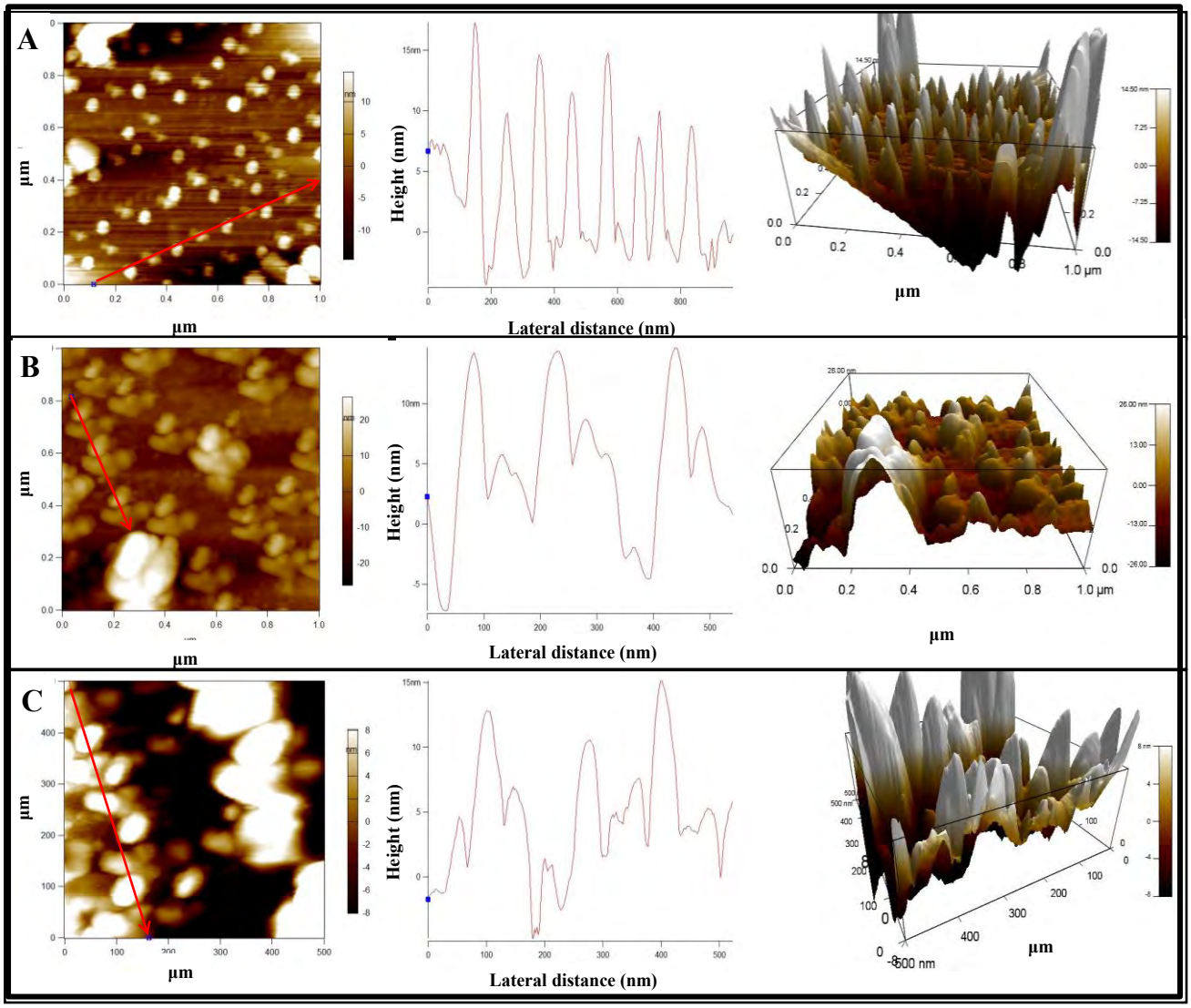

Fig 4.6 AFM analysis of (A) MCH-Ag/$CuFe_2O_4$ NPs (B) **5**-MCH-Ag/$CuFe_2O_4$, and (C) **5Q-MeI**-MCH-Ag/$CuFe_2O_4$. Left = 2D surface topology; middle = line profiling; right = 3D image.

4.3.5 Dynamic light scattering (DLS) and zeta (ζ) potentials measurements

Dynamic light scattering (DLS) was used for hydrodynamic particle size determination using 2% DMSO dissolved in PBS. Complexes **1**, and **5** in **Fig. 4.7** are shown as examples. The hydrodynamic diameter (D_h) (**Fig. 4.7**) of MCH-Ag/$CuFe_2O_4$ and OLM-Ag/$CuFe_2O_4$ NPs were found to be 13.5 nm and 15.0 nm, respectively. The D_h values for the conjugates are shown in **Table 4.2** and **Fig. 4.7**. The DLS particle size estimations were slightly higher as compared to the ones from TEM and XRD, this can be attributed to the interference of the dispersant during the analysis [136]. Polydispersity index (PDI) values were used to measure the broadness of particle size distribution; this was achieved using DLS. PDI values range between 0.0 (for a perfectly monomodal sample dispersion with respect to particle size) and 1.0 (for a highly polydispersed sample with broad size distribution) [137].

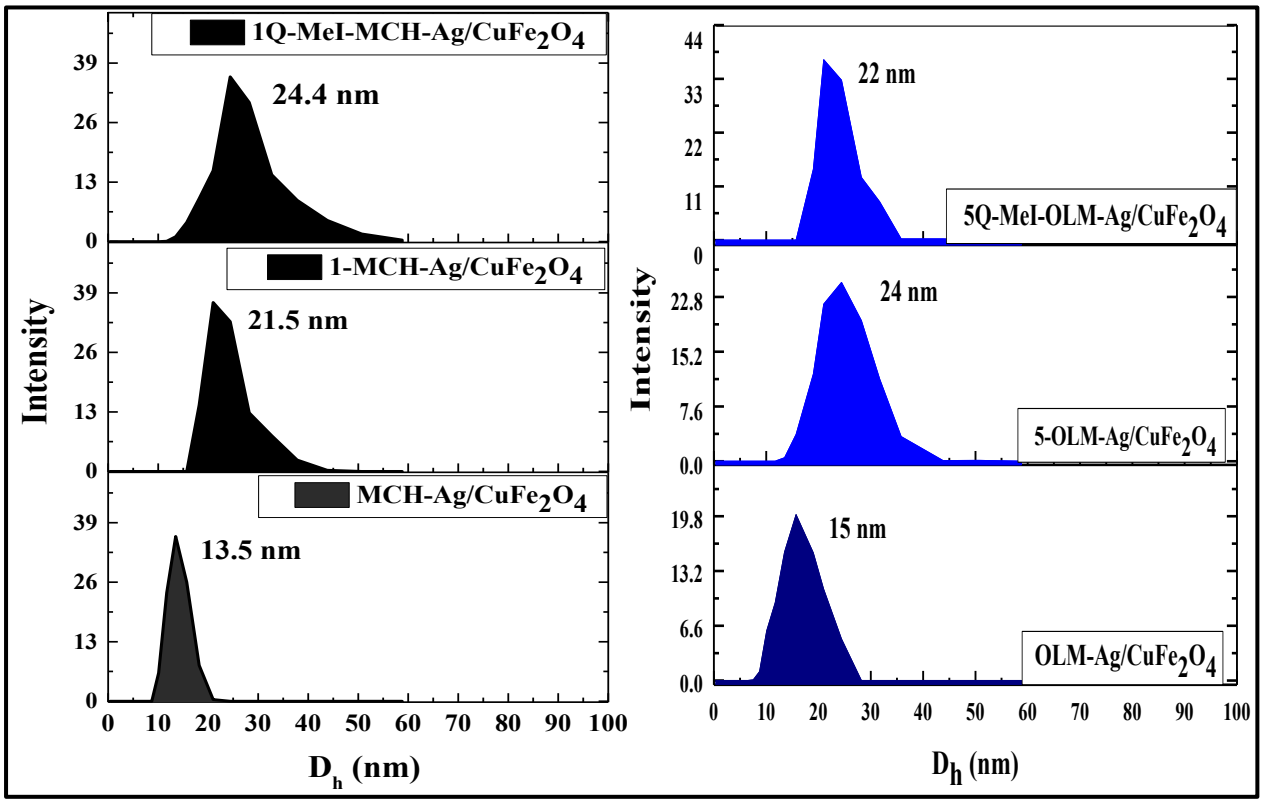

Fig 4.7 Dynamic light scattering (DSL) distribution curve for the nanoparticles and their corresponding nanoconjugates, using 2% DMSO in PBS.

PDI values obtained were 0.112, 0.091, 0.261, 0.284, 0.453, 0.198, 0.265, 0.203, 0.129, 0.145, and 0.227 for OLM-Ag/$CuFe_2O_4$, MCH-Ag/$CuFe_2O_4$, **1**-MCH-Ag/$CuFe_2O_4$, **1Q-MeI**-MCH-Ag/$CuFe_2O_4$, **1Q-HexI**-MCH-Ag/$CuFe_2O_4$, **3Q-MeI**-MCH-Ag/$CuFe_2O_4$, **3Q-HexI**-MCH-Ag/$CuFe_2O_4$, **5**-OLM-Ag/$CuFe_2O_4$, **5Q-MeI**-OLM-Ag/$CuFe_2O_4$, **5**-MCH-Ag/$CuFe_2O_4$, **5Q-MeI**-MCH-Ag/$CuFe_2O_4$, respectively. The observed small PDI values signify monomodal dispersions of the nanoconjugates. Recent studies have shown that various properties of NPs and nanoconjugates such as size, shape, polydispersity index (PDI), and zeta potential play an imperative role in physicochemical and biological properties [**138,139**].

The Zeta potential (ζ) of the NPs and conjugates was measured using DLS shown in **Table 4.2**. **Fig. 4.8** shows ζ of the NPs and nanoconjugates dispersed using 2% DMSO in water on the day of synthesis as an example. It has been reported that ζ outside the range -25 mV to +25 mV typically indicates high stability, since high ζ overcomes the electrostatic attractions between the adjacent nanoparticles [**140**]. A ζ of -26.8 mV for OLM-Ag/$CuFe_2O_4$ and -27.3 for MCH-Ag/$CuFe_2O_4$ signifies a moderate stability, and same applies to **5Q-MeI**-OLM-Ag/$CuFe_2O_4$, **5**-MCH-Ag/$CuFe_2O_4$ and **5Q-MeI**-MCH-Ag/$CuFe_2O_4$ with ζ = -28.3 mV, -26.1 mV, and -27.0 respectively. However, **5**-OLM-Ag/$CuFe_2O_4$ and **1**-MCH-Ag/$CuFe_2O_4$, **1Q-MeI**-MCH-Ag/$CuFe_2O_4$, **1Q-HexI**-MCH-Ag/$CuFe_2O_4$, **3Q-MeI**-MCH-Ag/$CuFe_2O_4$, and **2Q-hexI**-MCH-Ag/$CuFe_2O_4$ (ζ -18.6, -17.5, +12.3, +17.7, +15.1, and +18.1 mV respectively) showed relatively less stability. All the quaternized conjugates show relatively low ζ. Nanoconjugates with low ζ are susceptible to electrostatic attraction and consequently allowing interactions among the NPs, forming fractal aggregates [**141**].

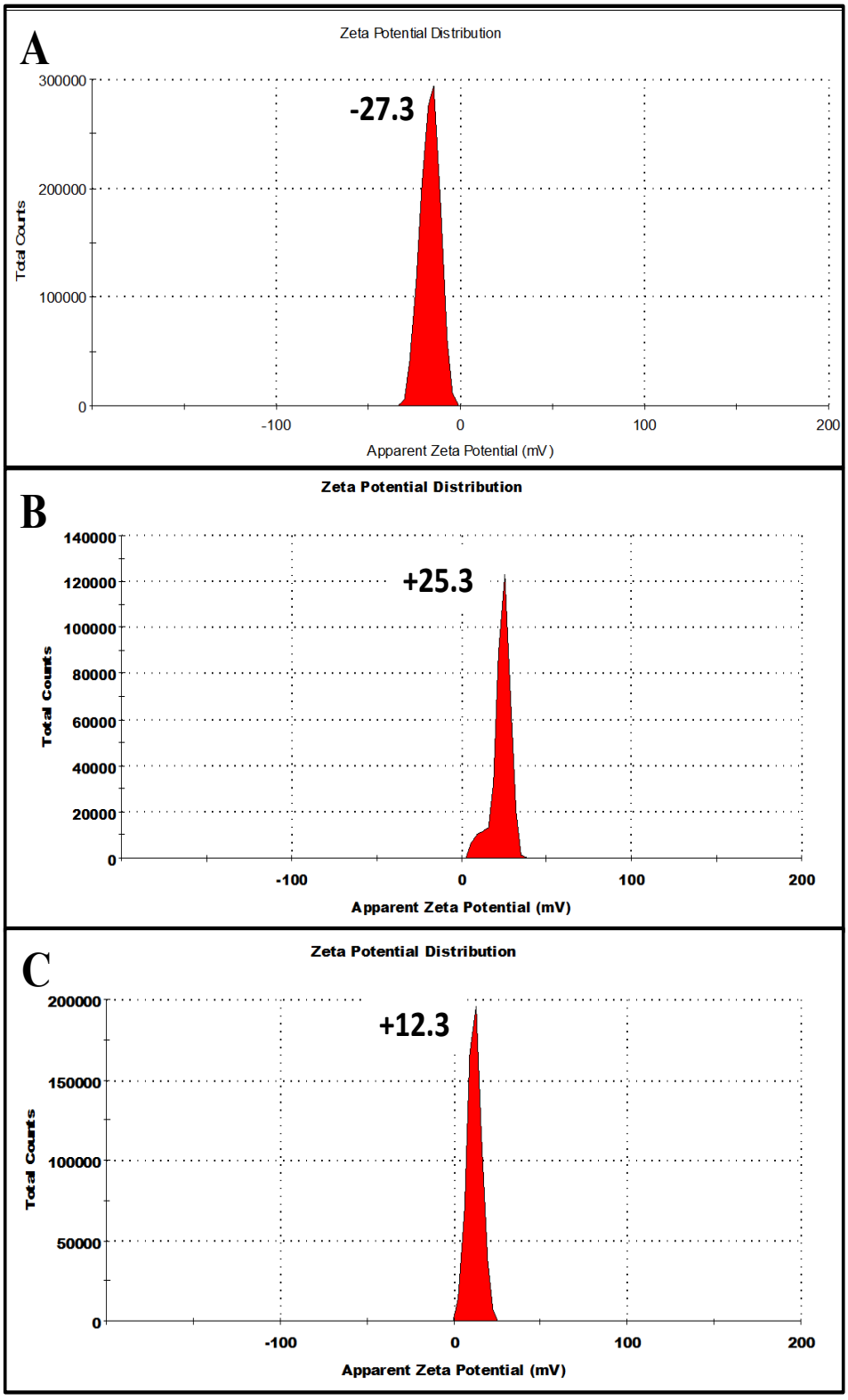

Fig 4.8 Zeta potential (ζ) graphs for (A) MCH-Ag/$CuFe_2O_4$ NPs, (B) complex **1Q-MeI**, and (C) **1Q-MeI**-MCH-Ag/$CuFe_2O_4$ conjugate.

The colloidal stability studies of the NPs (OLM-Ag/$CuFe_2O_4$ and MCH-Ag/$CuFe_2O_4$) and **1Q-MeI**-MCH-Ag/$CuFe_2O_4$, **1Q-HexI**-MCH-Ag/$CuFe_2O_4$, **3Q-MeI**-MCH-Ag/$CuFe_2O_4$, **3Q-HexI**-MCH-Ag/$CuFe_2O_4$, **5**-OLM-Ag/$CuFe_2O_4$, and **5Q-MeI**-OLM-Ag/$CuFe_2O_4$ were analysed using DLS as shown in **Fig. 4.9**. The study was based on monitoring the change in D_h of the NPs and the conjugates overtime for 5 days suspended in water containing 2% DMSO. 2% DMSO was used since **1**-MCH-Ag/$CuFe_2O_4$, **5**-OLM-Ag/$CuFe_2O_4$, and **5**-MCH-Ag/$CuFe_2O_4$ conjugates were not soluble in water. The studies were done over 5 days since biological studies were performed within that period. D_h of the NPs and the conjugates remained practically unchanged over 5 days as shown in **Fig. 4.9**. The variations observed are negligible and might possibly be due to different fractions collected from the solution during analysis and instrumental error. The D_h variation are within 5 nm on average for all the studies.

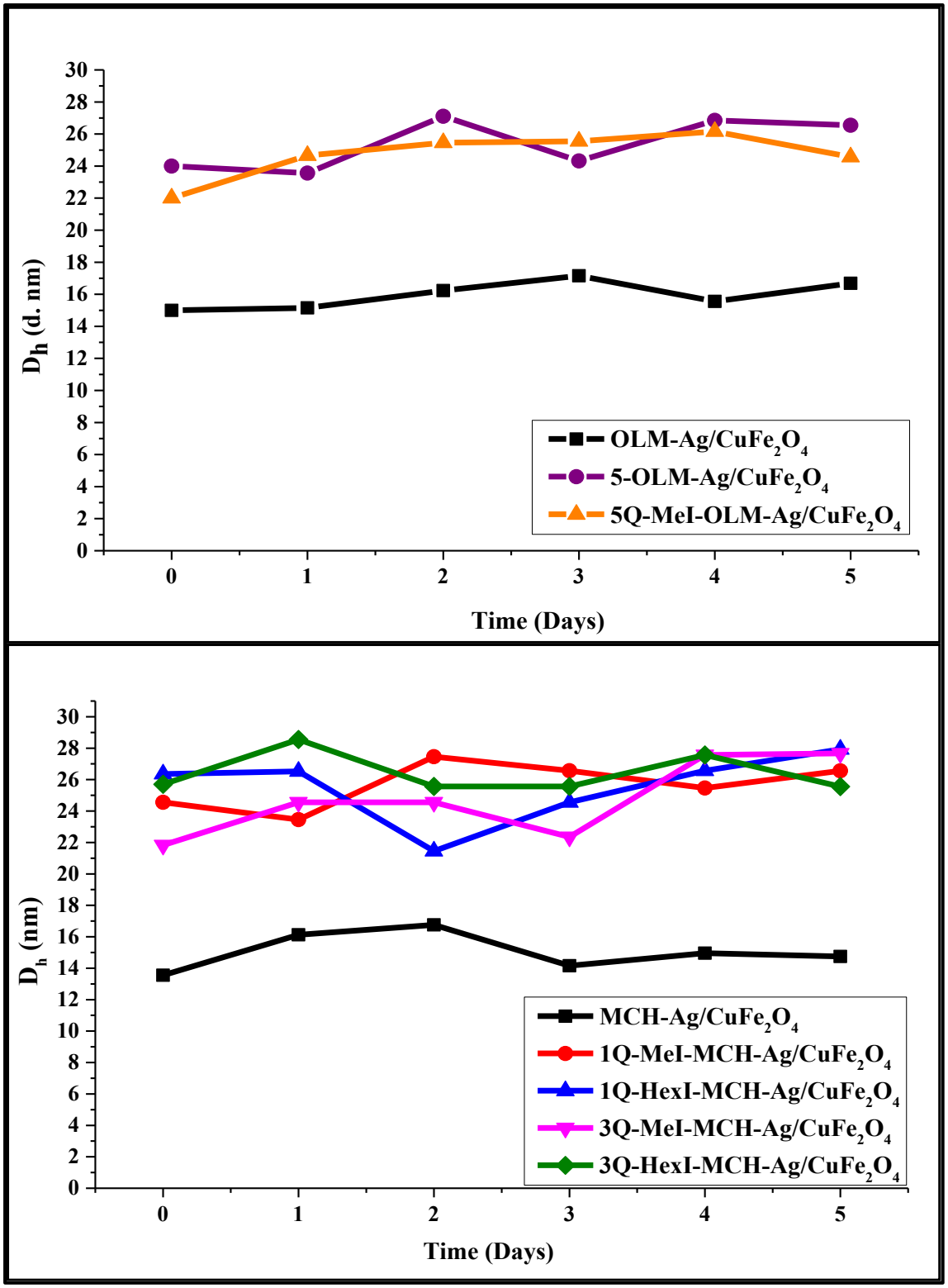

Fig 4.9 Hydrodynamic stability studies of the NPs (OLM-Ag/$CuFe_2O_4$ and MCH-Ag/$CuFe_2O_4$) and conjugates in aqueous dispersion; 2% DMSO in water.

4.3.6 X-ray diffraction (XRD)

X-ray diffraction (XRD) characterization technique was used for phase identification of synthesized NPs and the conjugates, with some of the complexes shown in **Fig. 4.10** as examples. XRD patterns for OLM-Ag/$CuFe_2O_4$ and MCH-Ag/$CuFe_2O_4$ were in agreement with the ones reported in the literature [142–144], demonstrating a successful synthesis of the NPs. The face centred cubic metallic crystalline phases of OLM-Ag/$CuFe_2O_4$ and MCH-Ag/$CuFe_2O_4$ core-shell NPs showed the characteristic peaks for Ag combined with Cu NPs at 111, 200, 220, 311 with 2θ = 39.0, 44.0, 64.5 and 78.5°, respectively. The less intense broad peak near 15° could be ascribed to $CuFe_2O_4$ as a result of the amorphous nature of the Fe_3O_4 NPs reported before [145]. The capping agents showed no impact on the XRD pattern of the NPs. XRD pattern of complex **1** alone as an example was also analysed to delineate the amorphous nature of porphyrins extrapolated by a pink-dotted line in **Fig. 4.10**. XRD spectra for all the conjugates show both the phases for the NPs and porphyrin complexes which validate the presence of the two in each conjugate. The average crystalline size (D) was determined using Debye-Scherrer formula **Eq. (4.1)**.

$$D = \frac{k\lambda}{\beta cos\theta} \qquad \textbf{(4.1)}$$

Where k is Scherrer constant (0.9), λ is the wavelength of the X-ray source (0.15405 nm), β is the FWHM (full-width at half maximum, radians), and θ is the peak position corresponding to FWHM (radians) [146]. The FWHM was estimated using origin 8 professional on a Gaussian plot using the 4 characteristic peaks. The D values obtained were 12.24 nm, 11.85 nm, 12.73 nm, 12.08 nm, 16.9 nm, 18.1 nm, 15.7 nm, 16.51 nm, 15.87 nm, 14.95 nm, and 16.23 nm for OLM-Ag/$CuFe_2O_4$, MCH-Ag/$CuFe_2O_4$, **1**-MCH-Ag/$CuFe_2O_4$, **1Q-MeI**-MCH-

Ag/$CuFe_2O_4$, **1Q-HexI**-MCH-Ag/$CuFe_2O_4$, **3Q-MeI**-MCH-Ag/$CuFe_2O_4$, **3Q-HexI**-MCH-Ag/$CuFe_2O_4$, **5**-OLM-Ag/$CuFe_2O_4$, **5Q-MeI**-OLM-Ag/$CuFe_2O_4$, **5**-MCH-Ag/$CuFe_2O_4$, **5Q-MeI**-MCH-Ag/$CuFe_2O_4$, respectively. These values are closer to the values determined using TEM.

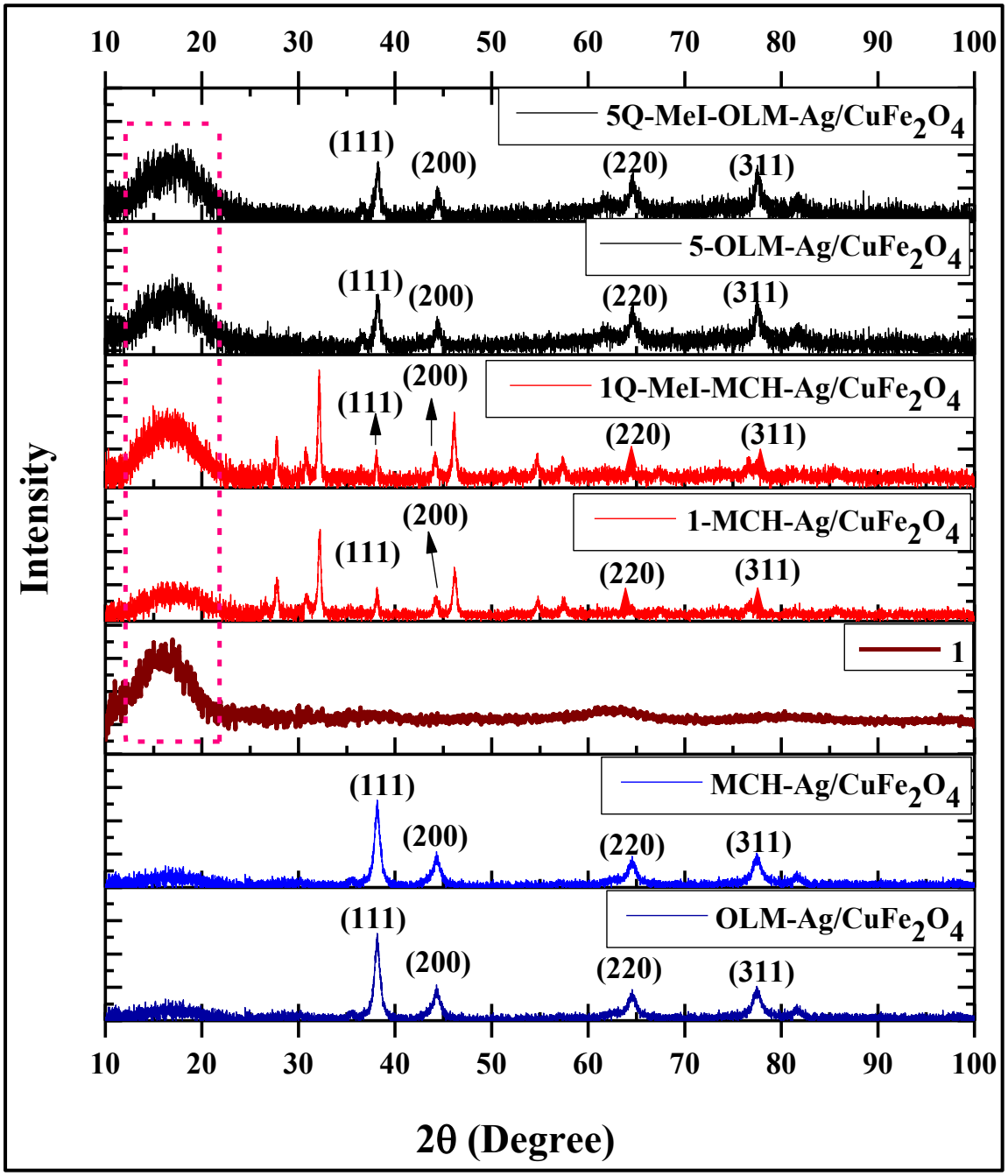

Fig. 4.10 X-ray diffraction (XRD) diffractograms of the NPs (MCH-Ag/$CuFe_2O_4$ and MCH-Ag/$CuFe_2O_4$), porphyrin, and the conjugates.

4.3.7 Fourier transform infrared (FT-IR)

Fig. 4.11 Shows Fourier transform infrared (FT-IR) spectra for some of the synthesised material as examples. The FT-IR spectra of OLM-Ag/$CuFe_2O_4$ NPs show the presence of C-H stretches at 2841-2909 cm^{-1} which can be attributed to C-H of oleyamine capping agent. Upon functionalization of OLM-Ag/$CuFe_2O_4$ NPs with 6-mercapto-1-hexanol, a broad O-H (3178-3533 cm^{-1}) vibration band and sharp C-H (2835-2923 cm^{-1}) vibration band are observed validating successful capping of the NPs. Upon conjugation of complex **1** and **1Q-MeI** to MCH-Ag/$CuFe_2O_4$ NPs, FT-IR spectral changes were observed. C-O vibrational bands were observed at 1012 and 1010 cm^{-1} for **1**-MCH-Ag/$CuFe_2O_4$ and **1Q-MeI**-MCH-Ag/$CuFe_2O_4$, respectively. The carbonyl (C=O) vibrational band for **1** (1707 cm^{-1}) and **1Q-MeI** (1715 cm^{-1}) (**Fig. 4.2**) also shifted to 1592 cm^{-1} and 1624 cm^{-1}, respectively, upon conjugation (**Fig. 4.11**). The pyridyl C=N stretch was observed at 1436 cm^{-1} and 1530 cm^{-1} for **1**-MCH-Ag/$CuFe_2O_4$ and **1Q-MeI**-MCH-Ag/$CuFe_2O_4$, respectively. FT-IR spectra of **5**-OLM-Ag/$CuFe_2O_4$ and **5Q-MeI**-OLM-Ag/$CuFe_2O_4$ shows the presence of both the porphyrins and the NPs. C=N stretch is observed for **5**-OLM-Ag/$CuFe_2O_4$ at 1650 cm^{-1} and for **5Q-MeI**-OLM-Ag/$CuFe_2O_4$ at 1603 cm^{-1}. The FT-IR spectra of the conjugates confirm the presence of both the porphyrins and NPs. However, it is not possible to validate self-assembly conjugation using FT-IR alone. Hence X-ray photoelectron spectroscopy (XPS) below was employed to validate self-assembly (Ag-S and Ag-N) conjugations.

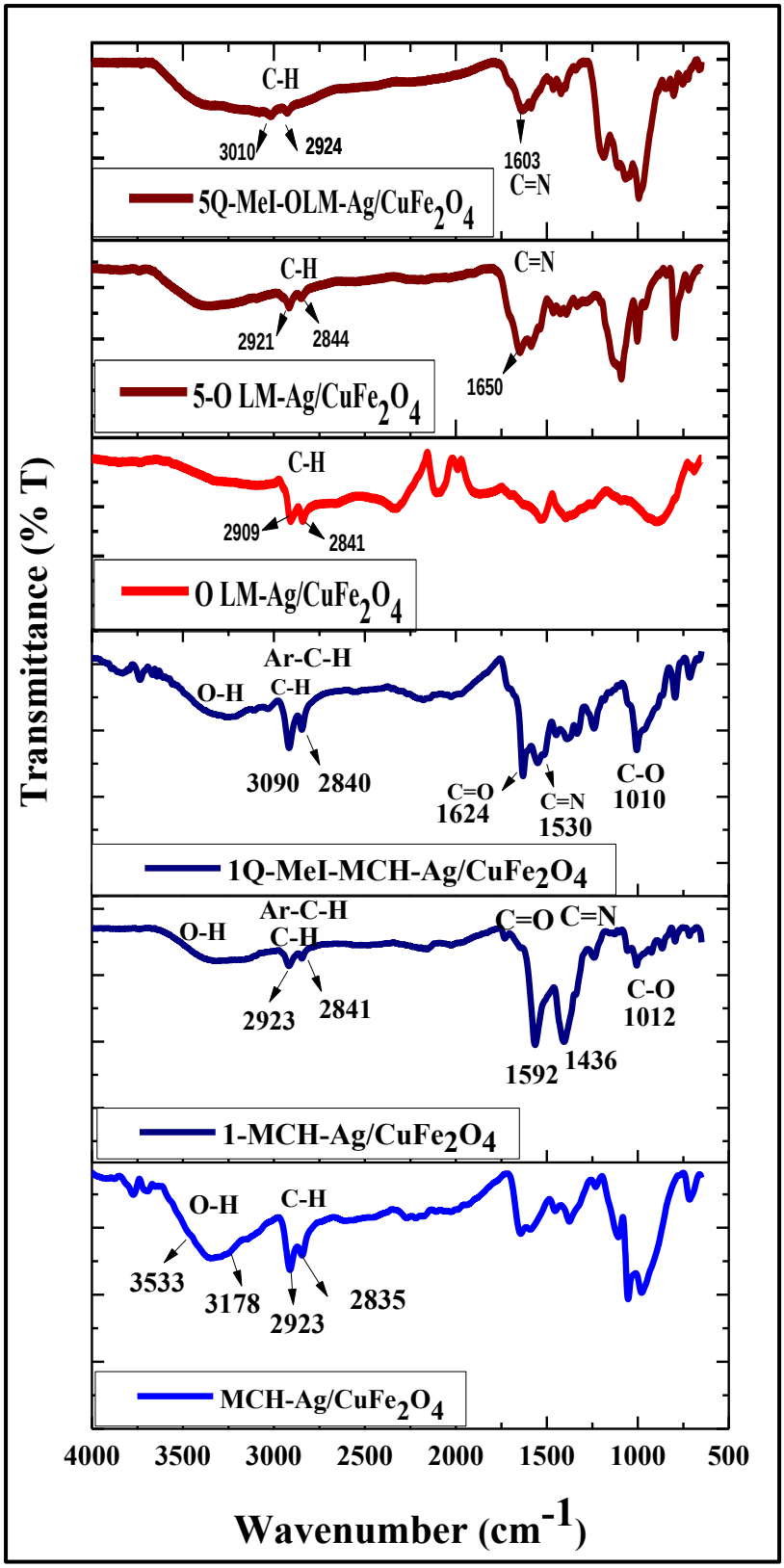

Fig. 4.11 Fourier transforms infrared (FT-IR) spectra of the NPs (MCH-Ag/$CuFe_2O_4$ and OLM-Ag/$CuFe_2O_4$) and corresponding conjugates.

4.3.8 X-ray photoelectron spectroscopy (XPS)

X-ray photoelectron spectroscopy (XPS) also known as electron spectroscopy for chemical analysis (ESCA) was employed in this study to validate the covalent conjugation and self-assembly bonding of the NPs and the porphyrins. XPS analysis is a surface analytical technique used for quantitative composition and surface chemical interactions between elements. Complexes **3Q-MeI**, **3Q-HexI**, **5**, **5Q-MeI** were conjugated to the NPs through self-assembly (N-Ag and S-Ag), whilst complexes **1**, **1Q-MeI**, and **1Q-HexI** were covalently linked to the NPs via an ester bond.

4.3.8.1 XPS covalent conjugation analysis

Shown in **Fig. 4.12** is a high resolution O1s XPS spectra for complex **1Q-MeI**, MCH-Ag/$CuFe_2O_4$, and **1Q-MeI**-MCH-Ag/$CuFe_2O_4$, used as examples to study the ester conjugation. In **Fig. 4.12(B)**, upon the deconvolution of the O1s high resolution curve for MCH-Ag/$CuFe_2O_4$ NPs, three sub curves were observed which were ascribed to C-O/O-H (529.1 eV), C-O-H (530.7 eV), and the Cu-O (534.3 eV) satellite peak. The binding energies C-O, O-H, and C-O-H are due to MCH capping agent on the surface of the NPs. The Cu-O satellite peak observed for the NPs can be ascribed to the electronic shake-up, which has been observed and discussed before [**147,148**]. Complex **1Q-MeI** O1s curve (**Fig. 4.12(C)**) has been deconvoluted into two distinct peaks which were ascribed to carboxylic acid C=O/C-O/O-H (529 eV) and O-C=O (530.9 eV). Upon the formation of **1Q-MeI**-MCH-Ag/$CuFe_2O_4$ conjugate, O1s high resolution XPS curve was deconvoluted into five distinct sub peaks (**(Fig. 4.12(A)**). The sub peaks are ascribed to C=O (527.6 eV), C-O (528.9 eV), O-C=O (530.1 eV), O-C-O (531.8 eV), and the Cu-O (533.7 eV) satellite peak. The appearance of O-C-O sub peak for **1Q-MeI**-MCH-Ag/$CuFe_2O_4$ suggests an ester bond formation.

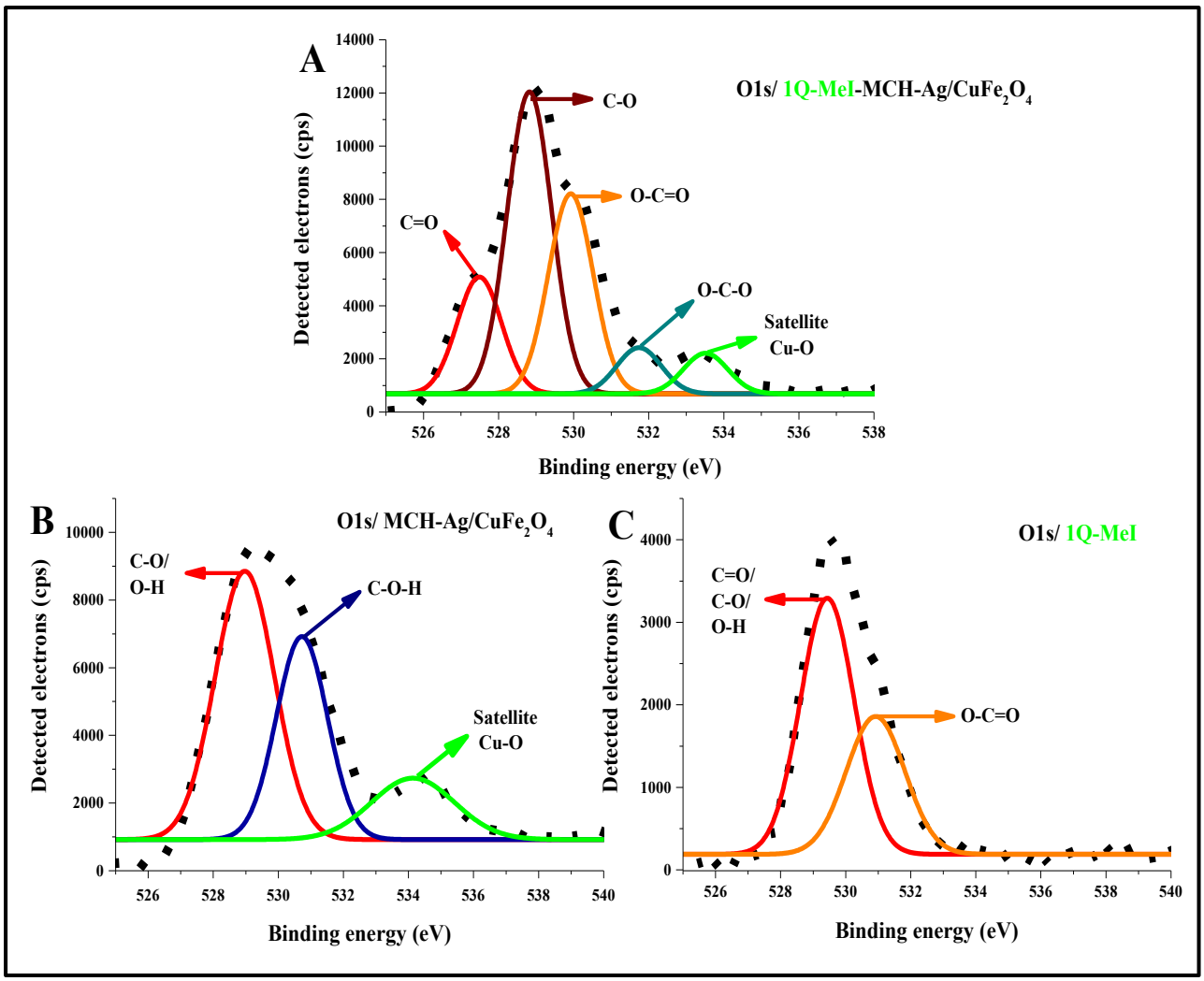

Fig. 4.12 O1s high resolution XPS spectra analysis for (A) **1Q-MeI**-MCH-Ag/$CuFe_2O_4$, (B) MCH-Ag/$CuFe_2O_4$, and (C) complex **1Q-MeI**.

4.3.8.2 XPS self-assembly conjugation analysis

Self-assembly conjugation of the porphyrin complexes to the MNPs was confirmed using XPS. Please note that complex **5** and conjugate **5**-MCH-Ag/$CuFe_2O_4$ in **Fig. 4.13** were used as examples since **5** has both sulfur and nitrogen atoms available for bonding with Ag atoms of the MNPs. **Fig. 4.13(A)** shows XPS survey spectra for MCH-Ag/$CuFe_2O_4$ MNPs, complex **5**, and **5**-MCH-Ag/$CuFe_2O_4$. MCH-Ag/$CuFe_2O_4$ survey spectra show the presence of C (282.3 eV), Ag (365.5 and 372.7 eV), and O (529.1 eV). The observed C and O binding energies are

as a result of 6-mercapot-1-hexanol (MCH) used as a capping agent for the NPs. The survey spectra for complex **5** shows the presence of S (161.7), C (282 eV), N (398.4), In (443.2 eV), and O (530.5 eV). The presence of O was ascribed to the axial ligand. Moreover, **5**-MCH-Ag/$CuFe_2O_4$ conjugate shows the presence of elements from both entities as expected. High resolution, XPS N1s (**Fig. 4.13(B)**) peak for complex **5** alone was deconvoluted to two sub peaks; that is N-In (397.3 eV) and N-C (398.5 eV). Upon deconvolution of N1s spectra of the conjugate (**Fig. 4.13(C)**), three sub peaks were observed at 396. 8 eV, 398.5 eV, and 400.2 eV and were ascribed to N-In, N-C, and N-Ag, respectively. The new sub peak suggests the successful binding of the NPs to the axial ligand's pyridyl lone pares. **Fig. 4.13(D)** shows S2p XPS high resolution spectra of complex **5**, which were deconvoluted to two sub peaks at 161.7 eV (S-C) and 163.1 eV (S) and upon conjugation to form **5**-MCH-Ag/$CuFe_2O_4$ (**Fig. 4.13(E)**), the S2p spectra was deconvoluted to three sub peaks at 161.7 eV (S-C) and 163.1 eV (S), and 167.5 (S-Ag). An additional peak observed at 167.5 eV was ascribed to S-Ag, which confirms the self-assembly of complex **5** and the MNPs through sulfur atoms. Thus, both S and N atoms are involved in the self-assembly of complex **5** onto the exposed Ag surface of the MNPs.

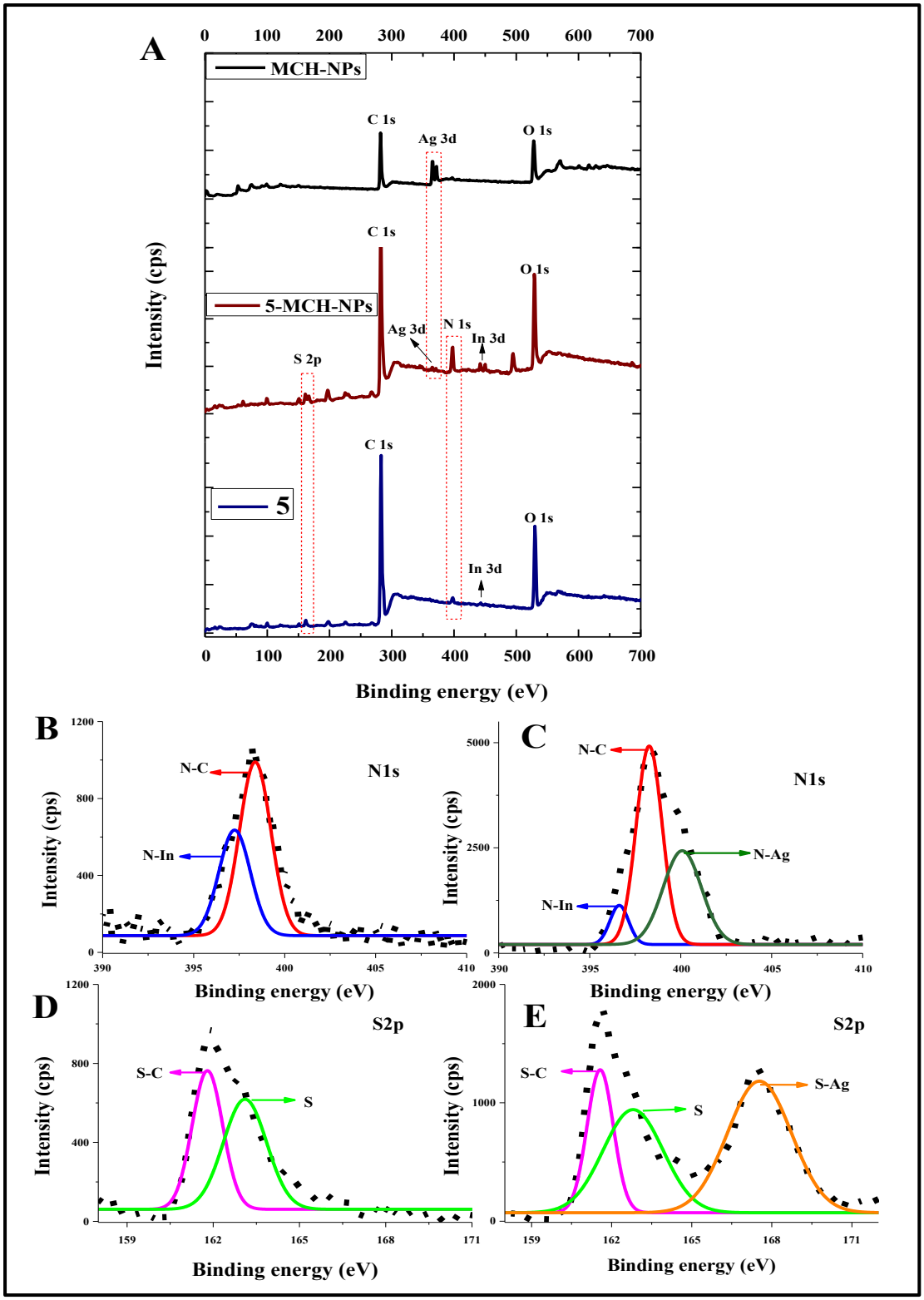

Fig. 4.13 XPS spectra analysis (A) survey spectra for MCH-Ag/$CuFe_2O_4$, complex **5**, and **5**-MCH-Ag/$CuFe_2O_4$. High resolution N1s (B, C) and S2p (D,E) spectra for complex **5** and **5**-MCH-Ag/$CuFe_2O_4$, respectively. Please note; MCH-NPs = MCH-Ag/$CuFe_2O_4$.

4.4 Photophysical parameters

All the photophysical parameters (**Table 4.3**) were studied in DMF unless otherwise stated. Singlet oxygen generation was further studied using 2% DMSO in water to analyse the response of the complexes in aqueous media.

Table 4.3 Photophysical parameters for all the complexes in DMF, unless stated.

Complexes/conjugates	λ_{Abs}, Soret (nm)	ϕ_F (± 0.001)	τ_F (ns)	ϕ_Δ
a		0.050	11.36	0.34
	415[a]	-	-	0.20[a]
1		<0.01	6.76	0.57
	420[a]	-	-	0.27[a]
1Q-MeI		<0.01	5.35	0.59
	426[a]	-	-	0.32[a]
1Q-HexI		<0.01	4.86	0.53
	424[a]	-	-	0.27[a]
1-MCH-Ag/$CuFe_2O_4$		<0.01	1.28	0.61
	421[a]	-	-	0.34[a]
1Q-MeI-MCH-Ag/$CuFe_2O_4$		<0.01	1.20	0.62
	427[a]	-	-	0.35[a]
1Q-HexI-MCH-Ag/$CuFe_2O_4$		<0.01	2.92	0.57
	425[a]	-	-	0.30[a]

b	409[a]	0.094 -	6.42 -	0.36 0.17[a]
2	418[a]	0.015 -	5.09 -	0.54 (0.25)
3	416[a]	0.018 -	5.74 -	0.52 (0.26)
3Q-MeI	422[a]	0.017 -	3.91 -	0.56 0.32[a]
3Q-HexI	422[a]	0.013 -	4.43 -	0.56 0.30[a]
3Q-MeI-MCH-Ag/$CuFe_2O_4$	0.26[a]	0.010 -	3.56 -	0.56 0.34[a]
3Q-HexI-MCH-Ag/$CuFe_2O_4$	0.25[a]	<0.01 -	3.91 -	0.60 0.28[a]
c	419[a]	0.080 -	6.21 -	0.31 0.19[a]
4	426[a]	<0.01 -	5.36 -	0.53 0.24[a]
5	427[a]	0.016 -	4.88 -	0.56 0.22[a]

5Q-MeI		0.015	4.21	0.56
	425[a]	-	-	0.25[a]
5-OLM-Ag/$CuFe_2O_4$		0.017	4.21	0.57
	427[a]	-	-	0.24[a]
5Q-MeI-OLM-Ag/$CuFe_2O_4$		0.011	3.98	0.59
	425[a]	-	-	0.22[a]
5-MCH-Ag/$CuFe_2O_4$		0.013	4.12	0.56
	426[a]	-	-	0.24[a]
5Q-MeI-MCH-Ag/$CuFe_2O_4$		<0.01	3.73	0.59
	425[a]	-	-	0.26[a]

a = values for 2% DMSO in PBS

4.4.1 Fluorescence quantum yields (ϕ_F) and lifetimes (τ_F)

ϕ_F values were studied in DMF for all the complexes and their corresponding conjugates using the comparative method reported in literature [**50**] using ZnTPP (ϕ_F = 0.030 [**49**]) as standard. **Eq. 1.2** was used to calculate the ϕ_F values. The ϕ_F values in **Table 4.3** are high for free-base complexes **a**, **b**, and **c** compared to their corresponding metalated derivative complexes **1**, **2**, and **4**, respectively. This behaviour demonstrate the quenching of the fluorescence upon insertion of indium metal ion and the chloride axial ligand [**149**]. The values were also observed to be low for the conjugates, and this could be attributed to Ag/$CuFe_2O_4$ NPs. This process can be explained in terms of the heavy atom effect of indium and the nanoparticles which favours intersystem crossing other than fluorescence [**150**].

There was a slight increase in ϕ_F upon exchange of axial ligands complexes **3** and **5** relative to chloro indium complexes **2** and **4**, and this was attributed to the removal of heavy atom axial Cl ligand which encourages ISC to the triplet excited state (shown in **Fig. 1.6**). Phenylmethylthio meso-substituents (**4**) shows a high fluorescence quenching compared to the pyridyl meso-substituents (**2**) (see **Table 4.3**), and this is due to heavy atom effect of sulfur. The ϕ_F values were observed to be low for MCH-Ag/$CuFe_2O_4$ NPs conjugated to **5** compared to the **5** conjugated to OLM-Ag/$CuFe_2O_4$ NPs, and this could be attributed to heavy atom effect of sulfur from MCH capping agent. There was no clear trend observed upon quaternization, since there were no changes in ϕ_F values for complex **5** compared to **5Q-MeI**, **1** compared to **1Q-MeI**, and **3** compared to **3Q-MeI**, however, there was a decrease from **3** to **3Q-Hex** (**Table 4.3**).

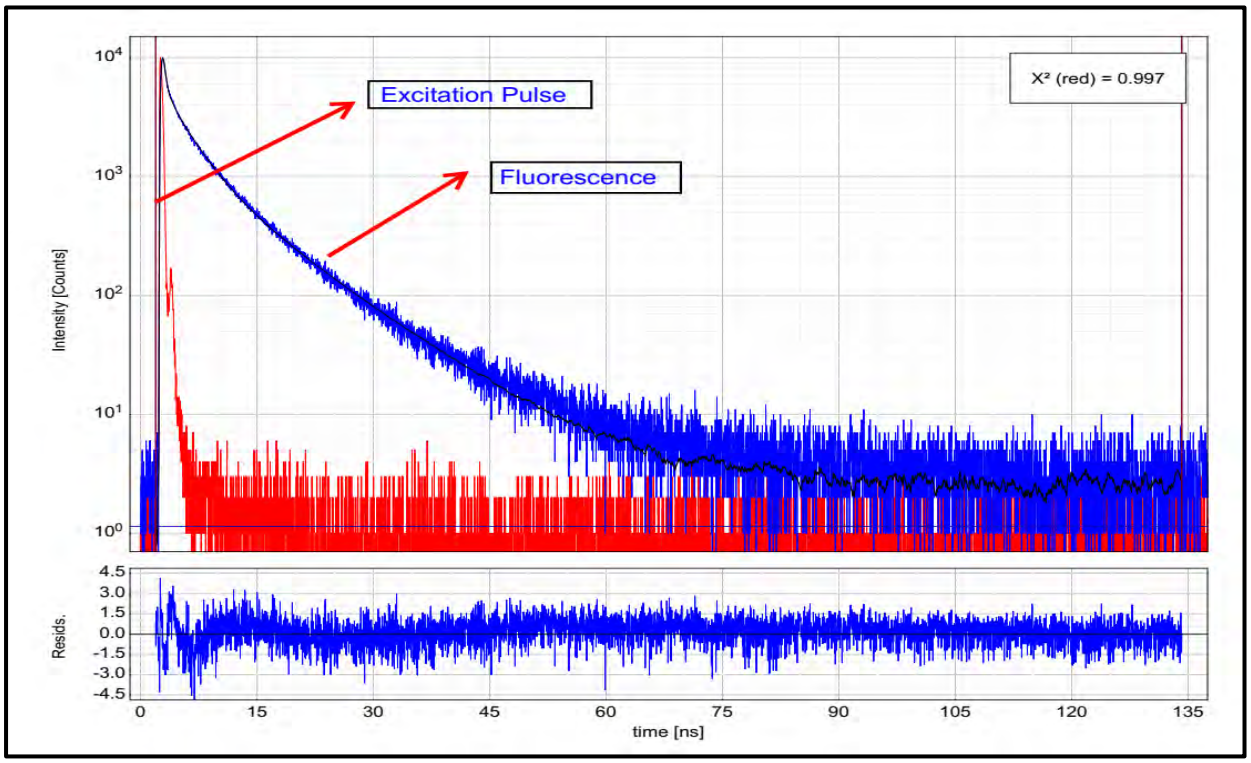

Fig. 4.14 Fluorescence lifetime decay curve fitting for complex **2** in DMF, using LUDOX HS-40 colloidal silica as a scatter sample.

Moreover, there was no clear trend on the effect of the number of positive charges on ϕ_F. The use of different quaternizing agents showed no significant impact on ϕ_F for **1**, **1Q-MeI**, **1Q-HexI**, and **3Q-MeI** but decreases for **3Q-HexI**. The τ_F followed the same trend as ϕ_F (see **Table 4.3**), since τ_F is proportional to ϕ_F. The fluorescence lifetime decay curve for complex **4** is shown in **Fig. 4.14** as an example of how the fitting was done to obtain the τ_F values (see **Table 4.3**).

4.4.2 Singlet oxygen quantum yields (ϕ_Δ)

$^1O_2$ generation is one of the major factors which signifying the effectiveness of the photosensitizer since is responsible for bacteria cell obliterations through lethal oxidative stress [151]. ϕ_Δ was studied under ambient conditions in DMF using DMA as a singlet oxygen quencher and ZnTPP (ϕ_Δ^{std} = 0.53) [52] as a standard, and the calculations were done using **Eq. (1.3)**. The degradation of the DMA was observed, whilst the Soret and Q bands of the porphyrin complexes remained unchanged confirming the photostability of the porphyrin complexes, delineated by **Fig. 4.15** using complex **4** as an example. As expected, the free-base complexes **a** (ϕ_Δ = 0.34), **b** (ϕ_Δ = 0.36) and **c** (ϕ_Δ = 0.31) showed a lower ϕ_Δ as compared to the metalated complexes (**Table 4.3**). The low ϕ_Δ values corresponds to the high ϕ_F values observed for the free-base complexes. The effect of axial modification on ϕ_Δ was as expected for complex **2** compared to **3**, which showed a decrease in ϕ_Δ upon the replacement of Cl (facilitating heavy atom effect) with aminophenol, however, it was not the case for complex **4** compared to **5**, which showed an increment (**Table 4.3**). The capping agents showed no significant impact on the ϕ_Δ, this can be observed on conjugate **5**-OLM-Ag/$CuFe_2O_4$ (ϕ_Δ = 0.57) compared to **5**-MCH-Ag/$CuFe_2O_4$ (ϕ_Δ = 0.56) and **5Q-MeI**-OLM-Ag/$CuFe_2O_4$ (ϕ_Δ = 0.59) compared to **5Q-MeI**-MCH-Ag/$CuFe_2O_4$ (ϕ_Δ = 0.59) (**Table 4.3**). There

was no clear trend observed for the effect of quaternization on ϕ_Δ; slight increase in ϕ_Δ was observed from **1** to **1Q-MeI** and from **3** to **3Q-MeI** and from **3** to **3Q-HexI**, however, ϕ_Δ remain unchanged from **5** to **5Q-MeI** but decreased from **1** to **1Q-hexI** (**Table 4.3**). The use of different quaternizing agents (MeI and HexI) showed an undefined trend on ϕ_Δ, since **3Q-MeI** and **3Q-HexI** have the same ϕ_Δ value, and **1Q-MeI** and **1Q-HexI** showed a decrease for the latter (**Table 4.3**). The unclear trends in the ϕ_Δ of the materials before and after quaternizations could be due to the insignificant effect brought by the quaternizing agents, and the observed disparities might be as a result of the singlet oxygen being studies on different days depending on the readiness of the complexes, which might lead to experimental errors based on the different temperatures on the day of the study.

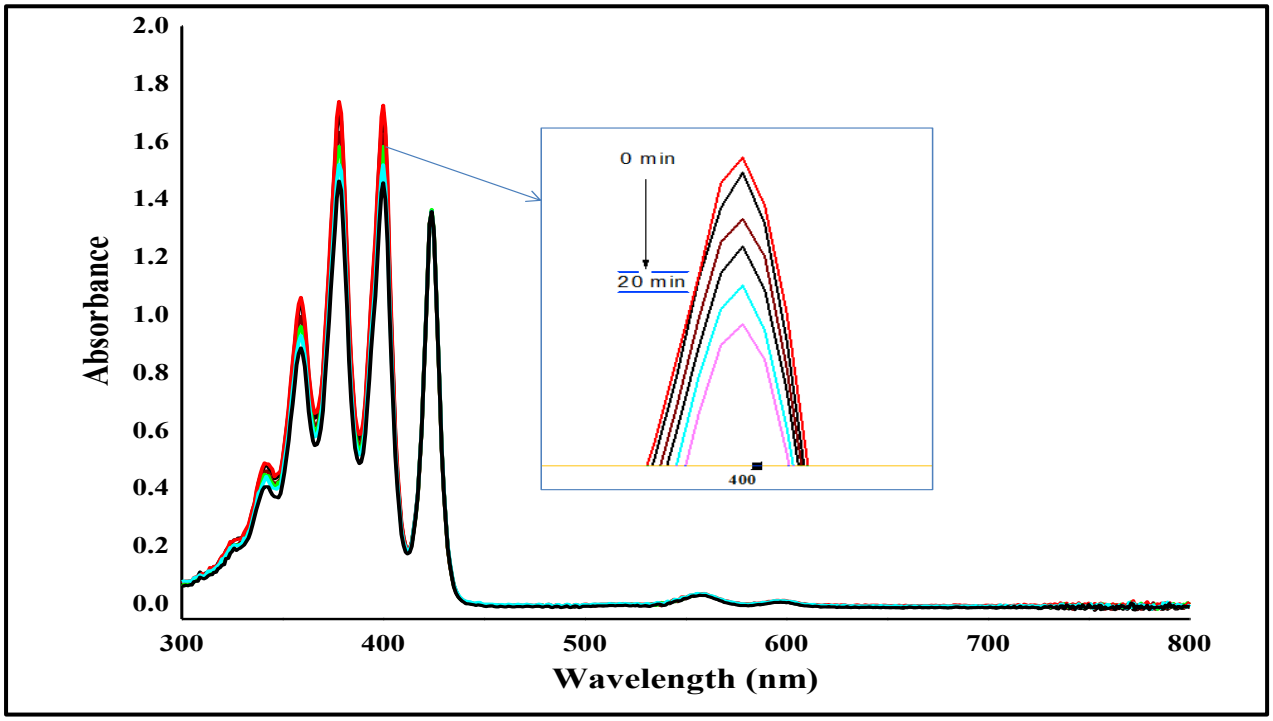

Fig. 4.15 Shows degradation of 9,10-dimethylanthracene (DMA) in the presence of complex **4** (solvent: DMF).

The conjugation of the porphyrin complexes to the NPs showed an increase in the ϕ_Δ, and these phenomena could be attributed to the heavy atom effect brought by the NPs. The effect of symmetry for complex **1** (ϕ_Δ = 0.57) compared to **2** (ϕ_Δ = 0.54) showed an increase, suggesting improved ϕ_Δ for asymmetrically substituted porphyrins. By comparing the effect of phenylmethylthio meso-substituents (**4**) and pyridyl meso-substituents (**2**), there was no significant different in the ϕ_Δ between the two complexes, contrary to ϕ_F due to sulfur heavy atom effect. For PACT application purpose, ϕ_Δ for all the complexes was determined in aqueous media using 2% DMSO in PBS since complex **a, b**, **c**, **1**, **2**, **3**, **4**, and **5** were not water soluble. Rose Bengal (RB) ($\phi_{\Delta RB}$ = 0.75 in water) was used as a standard and ADMA as singlet oxygen quencher for ϕ_Δ determination in aqueous media [**151**]. ϕ_Δ for all the complexes in an aqueous medium is relatively low, almost half ϕ_Δ in DMF (see **Table. 4.3**), this phenomena can be attributed to the quenching effect brought by water on the singlet oxygen generation [**50**].

4.5 Summary of the chapter

Asymmetrically substituted (**1**, **1Q-MeI**, and **1Q-HexI**) and symmetrically substituted (**2**, **3**, **3Q-MeI**, and **3Q-HexI**) porphyrin complexes as potential PSs for PACT were successfully synthesized and characterized using appropriate analytical techniques. Silver-capped copper ferrite MNPs ($Ag/CuFe_2O_4$) were also synthesized, functionalized, and conjugated to the porphyrins. Photophysicochemical properties of all the synthesized materials were studied. In this chapter, axial modification of the porphyrins and capping of the NPs have been achieved, moreover, axial modifications of the porphyrins and capping of the NPs showed some effect on the overall photophysical properties of the complexes. Improved ϕ_Δ values were observed for the indium metalated complexes and their corresponding conjugates

with the NPs. ϕ_Δ values in water were relatively lower compared to the values in DMF, however, they followed similar trends. ϕ_Δ values in water were good enough for PACT application. Hydrodynamic diameters and zeta potentials were analysed to study the stabilities of the conjugates and the nanoparticles, moreover, the materials were found to be relatively stable.

Chapter 5

Photodynamic antimicrobial chemotherapy (PACT) studies

This chapter outlines detailed photodynamic antimicrobial chemotherapy in vitro photoinactivation studies of *Staphylococcus aureus and Escherichia coli* using the as-prepared porphyrin complexes, nanoparticles and their corresponding conjugates.

5.1 Amphiphilicity and Lipophilicity studies

Amphiphiles are complexes possessing both hydrophilic and lipophilic traits. It has been reported that an increase in the amphiphilicity character of photosensitizers (PSs) is closely associated with its affinity for bacteria, which consequently improves cellular uptake and overall PACT activity [67,105,152]. The hydrophilicity of the PSs is imperative for distribution and the intercellular localizations. Lipophilicity structural analogues were studies between the porphyrins of longer alkyl chain quaternizing agent (zinc(II) meso-tetrakis(N-n-hexylpyridinium-3-yl) porphyrin) and shorter alkyl chain quaternizing agent (5-(4-trifluoromethylphenyl)-10,15,20-tris(4- trimethylammoniumphenyl) porphyrin), where a PS with shorter alkyl chain quaternizing agent was observed to be more hydrophilic [153]. The octanol-water partitioning coefficient (log $P_{o/w}$) was employed to estimate the ability of the complexes to penetrate biomembranes or bind to liposomes. The Log $P_{o/w}$ values for the complexes were determined using a procedure reported before [105], and the calculations were done using **E.q (2.1)** and **Fig. 2.2**. Complexes **1Q-HexI** (log $P_{o/w}$ = 0.77) and **3Q-HexI** (log $P_{o/w}$ = 0.66) with longer alkyl (hexyl) chains on their pyridyl meso-substituents were observed to have a positive log $P_{o/w}$ values, which suggests a higher concentration in the lipid phase (i.e hydrophobic character) (**Table 5.1**). Complexes **1Q-MeI** (log $P_{o/w}$ = -1.65) and **3Q-MeI** (log $P_{o/w}$ = -0.95) with shorter alkyl (methyl) chain gave negative log $P_{o/w}$ values, suggesting higher affinity for aqueous phase (i.e hydrophilicity character) (**Table 5.1**). Complexes with a more negative log $P_{o/w}$ are preferred due to their higher hydrophilicity, the proviso is based on the fact that more hydrophilic complexes diffuse easily through the plasma membranes and consequently maximizing cellular uptake [154,155]. This suggests the role played by the alkyl halides chain length as quaternizing agents on the lipophilicity of the complexes. Please note; lipophilicity studies were only conducted for cationic complexes

(**1Q-MeI**, **1Q-HexI**, **3Q-MeI**, and **3Q-HexI**) used against *E. coli*. All the four cationic porphyrins have closely related meso-substituents but different log $P_{o/w}$ and subsequently PACT activity. Other factors not accounted by log $P_{o/w}$, such as axial ligand and the number of cationic charges could be responsible for the PACT efficiency [**105,156,157**].

Table 5.1 Partition coefficients (log $P_{o/w}$) using octanol and water.

Complexes	log $P_{o/w}$
1Q-MeI	-1.65
1Q-HexI	0.77
3Q-MeI	-0.95
3Q-HexI	0.66

5.2 Antimicrobial studies

All the antimicrobial studies were conducted using 2% DMSO in PBS, since some of the unquaternized complexes were not completely water soluble. For assurance, validation, and reliability of the results, PACT studies were performed in triplicates. Gram (+) and Gram (-) bacterial strains *Staphylococcus aureus* and *Escherichia coli*, respectively, were employed to study the antibacterial activity of the synthesized complexes. The reported procedure involving the standard (viable, plate count) and turbidimetric analysis were employed to perform PACT studies, with slight modifications [**116,158**]. **Eq. (5.1)** and **Eq. (5.2)** were employed to quantify the % viable colony and log reductions, respectively.

Cell studies definitions:

$$\text{Viable colony (\%)} = \frac{(A-B)}{A} \times 100 \qquad \textbf{5.1}$$

$$\text{Log reduction} = \log(A) - \log(B) \quad \textbf{5.2}$$

where A is the number of colony count before treatment and B is the number after treatment. A lower viable colony percentage after treatment signifies the effectiveness of the PSs and consequently the high the log reduction. The minimum log reduction value recommended by FDA (Food and Drug Administration) regulations for a potential PS to be applicable for PACT is 3 log CFU [159].

5.2.1 Porphyrins concentration studies

Concentration optimizations were done for the porphyrin complexes alone under light exposure and dark conditions. Complexes **1**, **1Q-MeI**, **4**, **5**, and **5Q-MeI** PACT studies were performed using *S. aureus*, whereas complexes **1Q-MeI**, **1Q-HexI**, **3Q-MeI**, **3Q-HexI**, **2**, and **3** PACT activities were studied against *E. coli*. Thus, complex **1Q-MeI** PACT activities were studied against both *S. aureus* and *E. coli* to compare their susceptibility. Concentration optimizations of the PSs were done in order to obtain the minimum concentration that completely obliterates the bacteria upon light exposure. It can clearly be observed that PACT activity increases with an increase in the concentration of the complexes. **Fig. 5.1** shows the PACT activity of complexes **1** and **1Q-MeI** against *S. aureus* over 60 min, both the complexes show ~80% ($p < 0.05$) and ~65% ($p < 0.05$) viable colonies for dark studies at 12.5 µM concentrations, hence signifying dark toxicity. The higher dark toxicity for complex **1Q-MeI** can be attributed to its high solubility which allows it to interact effectively with the cell membrane [8,109,110,152]. Upon light exposure for 60 min, the lowest concentration of 2.5 µM for **1Q-MeI** was observed to have completely obliterated the bacteria resulting log reduction of 9.27 against *S. aureus* (**Table 5.2**). However, at concentration 2.5 µM for

complex **1** gave a log reduction of 0.46 upon irradiation. **Fig. 5.1 (B)** shows the PACT activity (dark and light) of complexes **5** and **5Q-MeI**, where the quaternized complex **5Q-MeI** was observed to have the highest dark toxicity compared to **5**, **1**, and **1Q-MeI**, and this could be ascribed to the combined effect of positive charge and thiols meso-substituents for **5Q-MeI** [72]. Upon irradiation for 30 min (**Fig. 5.1 (B)**), the concentration of 1.5 µM for complexes **5Q-MeI** was observed to have completely eradicated the bacteria; however, there was still viable colony for complex **5**. The quaternized complexes were observed to have impressive PACT activity against *S. aureus* at relatively low concentrations; however, they have a relatively higher dark toxicity.

Fig. 5.2 shows PACT activities of complexes **2**, **3**, **1Q-MeI**, **1Q-HexI**, **3Q-MeI**, and **3Q-HexI** against *E. coli*. The complexes show minimal dark toxicity, with >80% ($p < 0.05$) viable colony for complex **1Q-MeI** against *E. coli* (**Fig. 5.2 (A)**), which was ~65% viable colony against *S. aureus*. The lower dark cytotoxicity of the complexes against *E. coli* as compared to *S. aureus* could be as a result of their difference in the structural cell wall [13]. Upon light exposure (**Fig. 5.2 (B)**), complexes **1Q-MeI** and **3Q-MeI** were observed to have eradicated *E. coli* completely (0% viable colonies), at the lowest concentration of 2.5 µM and corresponding log reductions of 9.58 (**Table 5.3**). However, complexes **1Q-HexI** and **3Q-HexI** have viable colonies at concentration 2.5 µM. The unquaternized complexes **2** and **3** show relatively low PACT activity against *E. coli* at low concentrations. Comparing **1Q-MeI** against *S. aureus* and *E. coli*; a log reduction value of 9.58 was observed for *E. coli* and 9.27 observed for *S. aureus* (**Table 5.2** and **Table 5.3**), however, *E. coli* was expected to be less susceptible, but this is not the case. Thus showing the complex is more effective towards photoinactivation of the difficult *E. coli*.

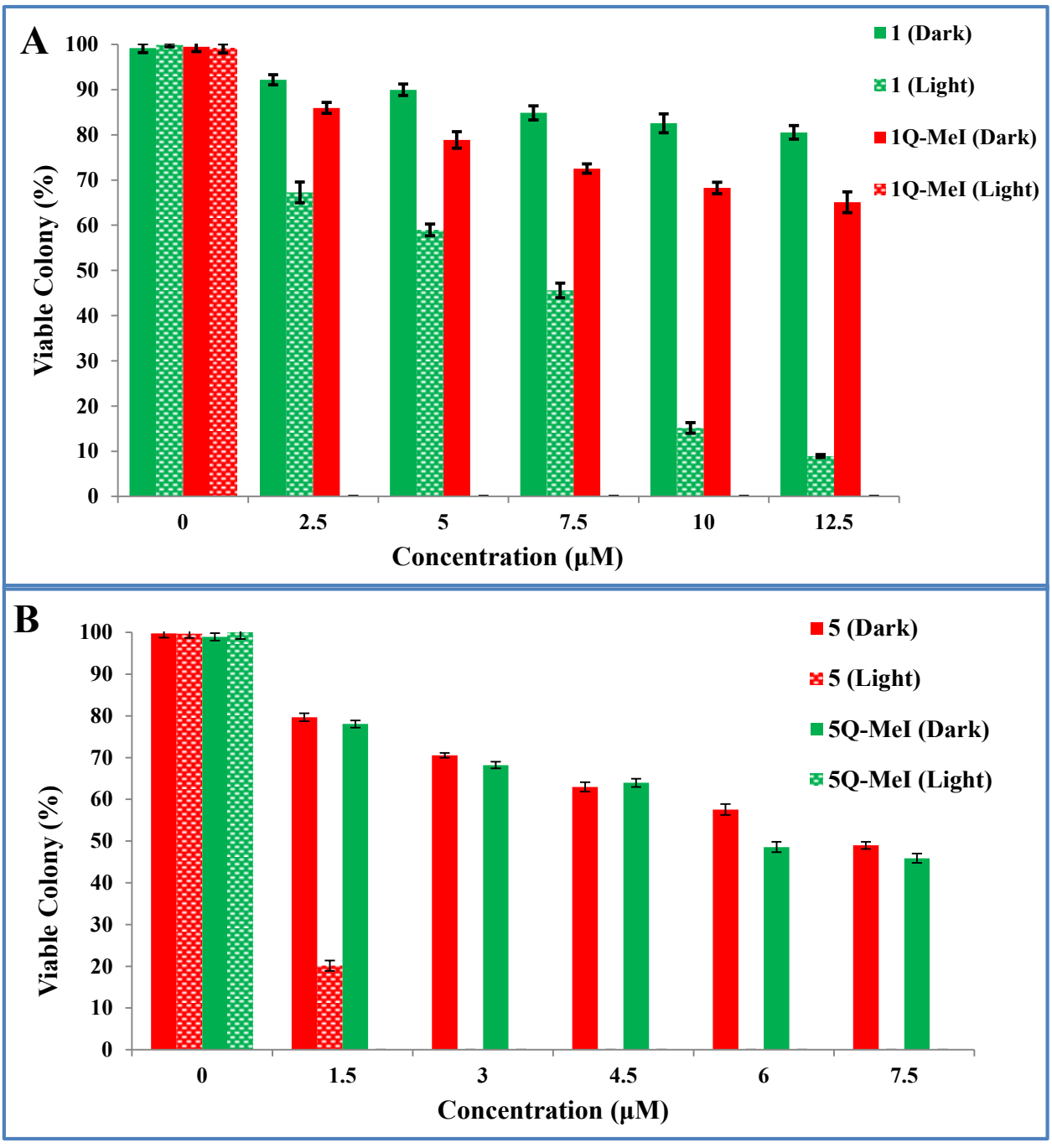

Fig. 5.1 PACT PSs concentration optimization for (A) **1** and **1Q-MeI**, 60 min exposure (B) **5** and **5Q-MeI**, 30 min exposure. Studies were done against ***S. aureus*** and irradiation using 415 nm LED.

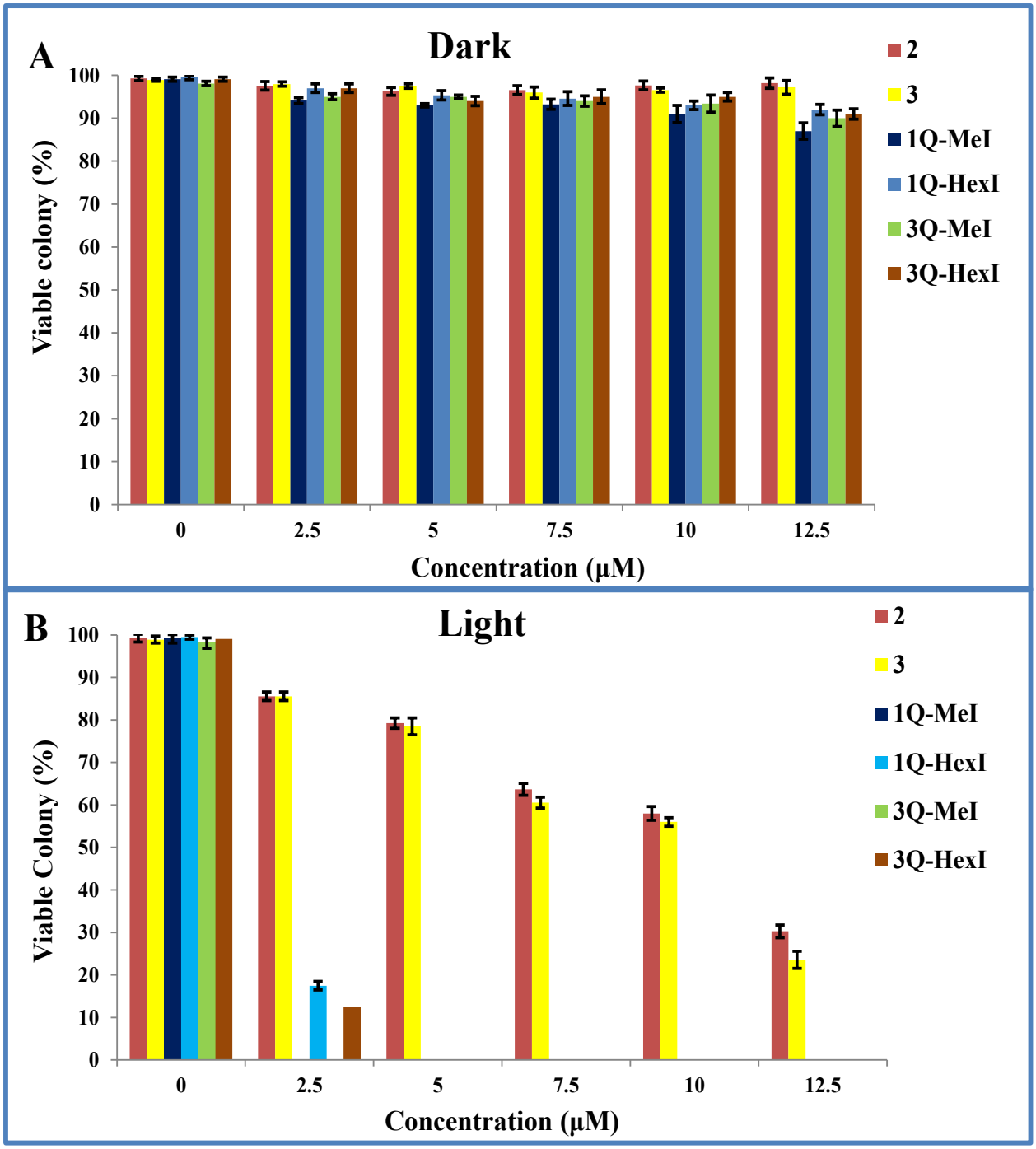

Fig. 5.2 PACT PSs concentration optimization for complexes **2**, **3**, **1Q-MeI**, **1Q-HexI**, **3Q-MeI**, **3Q-HexI** (A) dark toxicity studies and (B) photoinactivation for 30 min exposure; studies were done against ***E. coli*** and irradiation using 415 nm LED.

5.2.2 Nanoparticles toxicity studies

PACT activities of the bare NPs (OLM-Ag/$CuFe_2O_4$ and MCH-Ag/$CuFe_2O_4$) were assessed on *S. aureus* (**Fig. 5.3**). This study was conducted to analyse the cytotoxicity of the NPs and also to analyse the impact brought by the capping agents used in this study. Metallic NPs including silver NPs are known to have cytotoxicity towards microbial [**77,140,142,160**]. The concentrations of 0.25 g/mL were used for the NPs and the studies were conducted using 2% DMSO dissolved in PBS. The concentration of 0.25 g/mL for the nanoparticles was used as it was the smallest concentration that showed a clear surface plasmon resonance (SRP) on the UV-Vis spectroscopy (**Fig. 4.3 (A)**). Cytotoxicity of the NPs was studied under the dark and irradiation conditions with a 415 nm LED (at the SRP) over 25 min and 60 min for OLM-Ag/$CuFe_2O_4$ and MCH-Ag/$CuFe_2O_4$ NPs, respectively. The 60 min eradiation time was conducted for MCH-NPs to see if there were any effects when the light exposure is elongate, however, there was no any sudden change in the PACT activity of the NPs. As shown in **Fig. 5.3**, there was no significant difference between the viable colonies of the NPs when exposed to light or under dark conditions at a specific time. After 25 min of light exposure (**Fig 5.3 (A)**), >90% ($p > 0.05$) viable colony counts were observed for OLM-Ag/$CuFe_2O_4$ NPs and at 30 min of light exposure (**Fig 5.3 (B)**), ≥90% ($p < 0.05$) viable colony counts were observed for MCH-Ag/$CuFe_2O_4$ NPs. This signifies that the thiol capping agents on the NPs had a slight influence on the PACT activity against *S. aureus* relative to oleyamine capping agent. The observed cytotoxicity is as a result of the release of silver or copper metal ions which interact effectively with the cell membrane and leading to protein coagulation and consequently cell death [**161**].

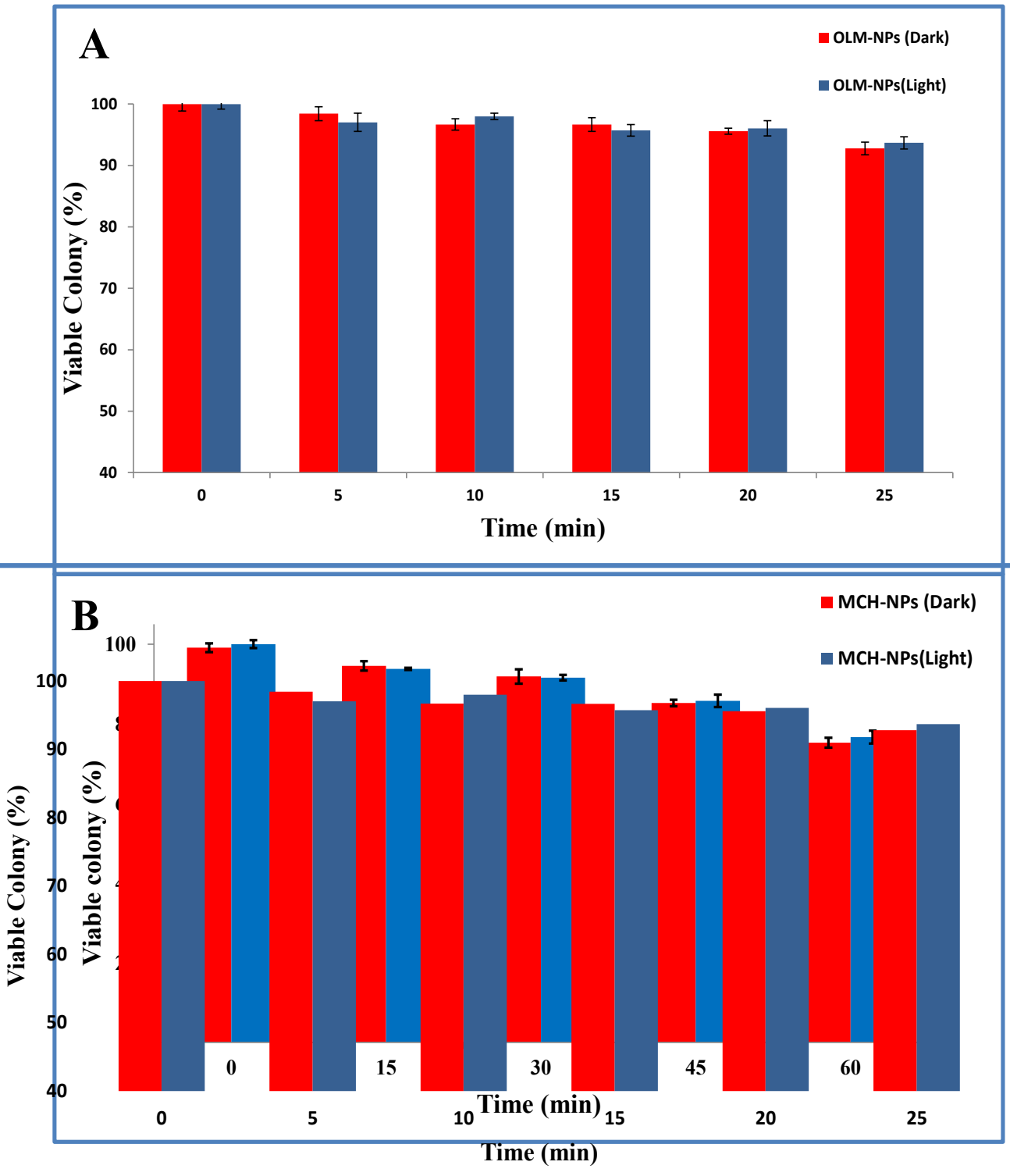

Fig. 5.3 Antibacterial activity of (A) OLM-Ag/$CuFe_2O_4$ (dark and light) for 25 min and (B) MCH-Ag/$CuFe_2O_4$ (dark and light) for 60 min against ***S. aureus***. Concentration 0.25 g/mL using 2% DMSO in PBS; NPs = Ag/$CuFe_2O_4$.

5.2.3 Porphyrins and nanoconjugates

Phototoxicity time studies of the complexes and conjugates were studied in specific time intervals, these studies were conducted to analyse the PACT activity over time.

5.2.3.1 Staphylococcus aureus

Complexes **1**, **1Q-MeI**, **4**, **5**, and **5Q-MeI** were employed as examples for *S. aureus*. **Fig. 5.4** shows PACT activity of asymmetrically substituted complexes **1**, **1Q-MeI**, and their conjugates with MCH-Ag/$CuFe_2O_4$ NPs against *S. aureus*. The concentration of 2.5 μM was used since for the porphyrins alone there were still viable cells at this concentration (**Fig. 5.1(A)**). Conjugates **1**-MCH-Ag/$CuFe_2O_4$ and **1Q-MeI**-MCH-Ag/$CuFe_2O_4$ showed dark toxicity, and this could be attributed to the presence of the NPs, however, >75% ($p< 0.05$) cell viability was observed which is still high (**Fig 5.4 (A)**). Upon irradiation (λ = 415 nm), complex **1Q-MeI** and its conjugate **1Q-MeI**-MCH-Ag/$CuFe_2O_4$ completely obliterated the bacteria at time 30 min (Log = 9.27, $p< 0.05$), which signifies high PACT activity against *S. aureus* (**Fig. 5.4 (B)** and **Table 5.2**). Phototoxicity of all the complexes was observed to increase with an increase in the irradiation time. Complex **1** and its conjugate **1**-MCH-Ag/$CuFe_2O_4$ showed lower log reduction values (**Table. 5.2**) of 0.46 and 3.71, respectively, at time 30 min. The quaternized complex **1Q-MeI** and its conjugate **1Q-MeI**-MCH-Ag/$CuFe_2O_4$ showed a high PACT activity against *S. aureus* compared to their unquternized derivatives **1** and **1**-MCH-Ag/$CuFe_2O_4$, and this was attributed to their solubility. The higher Log reduction values for the conjugate **1**-MCH-Ag/$CuFe_2O_4$ (Log = 3.71) compared to complex **1** (Log = 0.46) alone at time 30 min of irradiation could be ascribed to the cytotoxicity of the NPs in the nanoconjugate (**Table 5.2**). PACT activity of symmetrically substituted methylthio porphyrin complexes **4**, **5**, **5Q-MeI**, and their corresponding conjugates with OLM-Ag/$CuFe_2O_4$ and

MCH-Ag/$CuFe_2O_4$ NPs was studies against *S. aureus* at a PS concentration of 1.5 µM (used as it showed activity for all) in a 5 min interval up to 25 min exposure (**Fig. 5.5**). The conjugates (**5Q-MeI**-MCH-Ag/$CuFe_2O_4$ and **5Q-MeI**-OLM-Ag/$CuFe_2O_4$) were observed to have higher dark toxicity against *S. aureus*, which increases with an increase in exposure time (**Fig. 5.5(A)**). The quaternized conjugate **5Q-MeI**-MCH-Ag/$CuFe_2O_4$ completely obliterated the bacteria in 15 min of exposure (**Fig. 5.5(B)**). However **4**, **5**, **5Q-MeI**, **5**-OLM-Ag/$CuFe_2O_4$, **5Q-MeI**-OLM-Ag/$CuFe_2O_4$, and **5**-MCH-Ag/$CuFe_2O_4$ showed viable colonies at 15 min (**Fig. 5.5(B)**). The log reduction values for the methylthio porphyrins and their conjugates were recorded at 25 min (**Table 5.2**). The unquaternized complexes **4** (log = 0.26, $p< 0.05$) and **5** (Log = 0.79, $p< 0.05$) showed the lowest log reduction values against *S. aureus* (**Table 5.2**). The highest log reduction values of 8.31 ($p< 0.05$) were observed for **5Q-MeI**, **5Q-MeI**-MCH-Ag/$CuFe_2O_4$, **5Q-MeI**-OLM-Ag/$CuFe_2O_4$ against *S. aureus* after 25 min of irradiation (**Table 5.2**).

The effect of the NPs upon conjugation brought slight improvement in PACT activity; as can be seen for complexes **5** (log = 0.79) compared to conjugates **5**-OLM-Ag/$CuFe_2O_4$ (log = 2.76) and **5**-MCH-Ag/$CuFe_2O_4$ (log = 2.76) (**Table 5.2**). PACT activity for MCH conjugates compared to OLM conjugates were observed to be the same by comparing **5**-MCH-Ag/$CuFe_2O_4$ (log = 2.76, $p< 0.05$) to **5**-OLM-Ag/$CuFe_2O_4$ (log = 2.76, $p< 0.05$) and by comparing **5Q-MeI**-OLM-Ag/$CuFe_2O_4$ (log = 8.31, $p< 0.05$) to **5Q-MeI**-MCH-Ag/$CuFe_2O_4$ (log = 8.31, $p< 0.05$) at time 25 min (**Table 5.2**). No clear trend on the effect of the number of positive charges of **1Q-MeI** (three) compared to **5Q-MeI** (one) since the complexes have different meso-substituents. Axial modifications (**4** to **5**) showed an improved PACT, activity and this could be less aggregation.

5.2.3.2 Escherichia coli

PACT photoinactivation of *E. coli* was studied using complexes **2**, **3**, **1Q-MeI**, **5Q-HexI**, **3Q-MeI**, and **3Q-HexI** and their corresponding conjugates with MCH-Ag/$CuFe_2O_4$ NPs. **Fig. 5.6B** shows the photoinactivation of *E. coli* over time, where it can be observed that complexes **1Q-MeI** and **3Q-MeI** have obliterated all the colonies at 30 min of irradiation, however, complexes **1Q-HexI** and **3Q-HexI** still have viable colonies remaining (**Fig. 5.6 (A)**). The higher PACT activity of complex **3Q-MeI** and **1Q-MeI** could be ascribed to their higher hydrophilicity character. The complexes quaternized with the alkyl halides of longer chain lengths **3Q-HexI** (log = 7.34) and **1Q-HexI** (log = 7.19) showed a relatively lower PACT activity against *E. coli*, compared to alkyl halides of short chain lengths **3Q-MeI** (log = 9.58) and **1Q-MeI** (log = 9.58) (**Table 5.3**). This phenomena could be ascribed to the limited solubility of complexes **3Q-HexI** and **1Q-HexI** which reduces their ability to penetrate the bacteria cell membrane and becoming retained. Based on the log reduction values of the complexes, the number of positive charges on PACT activity against *E. coli* can be observed to be relatively the same by comparing complex **1Q-MeI** (three charges, Log = 9.58, $p< 0.05$) to **3Q-MeI** (four charges, Log = 9.58, $p< 0.05$) at time 30 min of light exposure (**Table 5.3**). However, complexes **1Q-HexI** (three charges, log = 7.19, $p< 0.05$) to **3Q-HexI** (four charges, log = 7.34, $p< 0.05$), suggesting a direct proportion between PACT activity and the number of positive charges through different substituents (**Table 5.3**). PACT activity of the axial modified complex **3** (log = 1.61, $p< 0.05$) was observed to be improved compared to complex **2** (log = 0.87, $p< 0.05$) and this could be attributed to less aggregation for **3** (**Table 5.3**). PACT activity of the conjugates was observed to have increased compared to the porphyrin complexes

alone. Moreover, all the conjugates were observed to have 0% viable colonies at time 30 min except complex **3Q-HexI**-MCH-Ag/$CuFe_2O_4$ with only 5% viable colony (**Fig. 5.6 (B)**). This higher PACT efficacy of the conjugates compared to the complexes alone can be attributed to the presence of silver and copper which are well known to eradicate the bacteria cells by realising Ag^+ and electrically charged copper ions in addition to the increased ϕ_Δ in water (**Table 5.2** and **5.3**) [78,161]. **Fig. 5.7** shows agar plated Petri dishes for colony control study (3.80×10^9 CFU/mL), dark study (3.93×10^7 CFU/mL), and phototoxicity (0.00 CFU/mL) against *E. coli* in the presence of complex **1Q-MeI** using a concentration of 2.5 µM at time 30 min, captured on colony counter after incubation for 18 h.

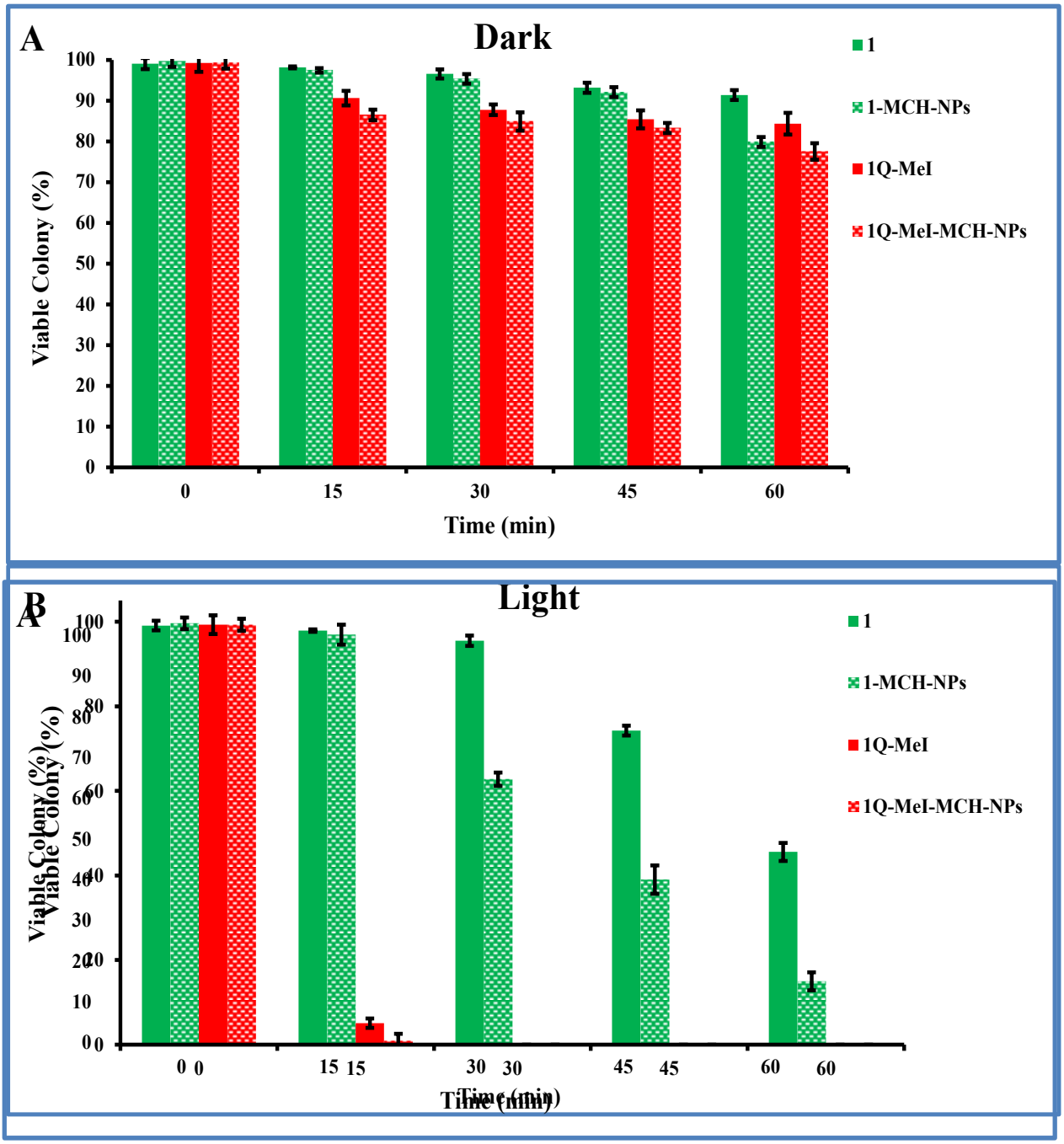

Fig. 5.4 PACT activity time study for 60 min of complexes **1**, **1Q-MeI**, **1**-MCH-Ag/$CuFe_2O_4$, **1Q-MeI**-MCH-Ag/$CuFe_2O_4$ (A) dark studies (B) light studies; concentration of 2.5 µM against ***S. aureus***; Note: NPs = Ag/$CuFe_2O_4$.

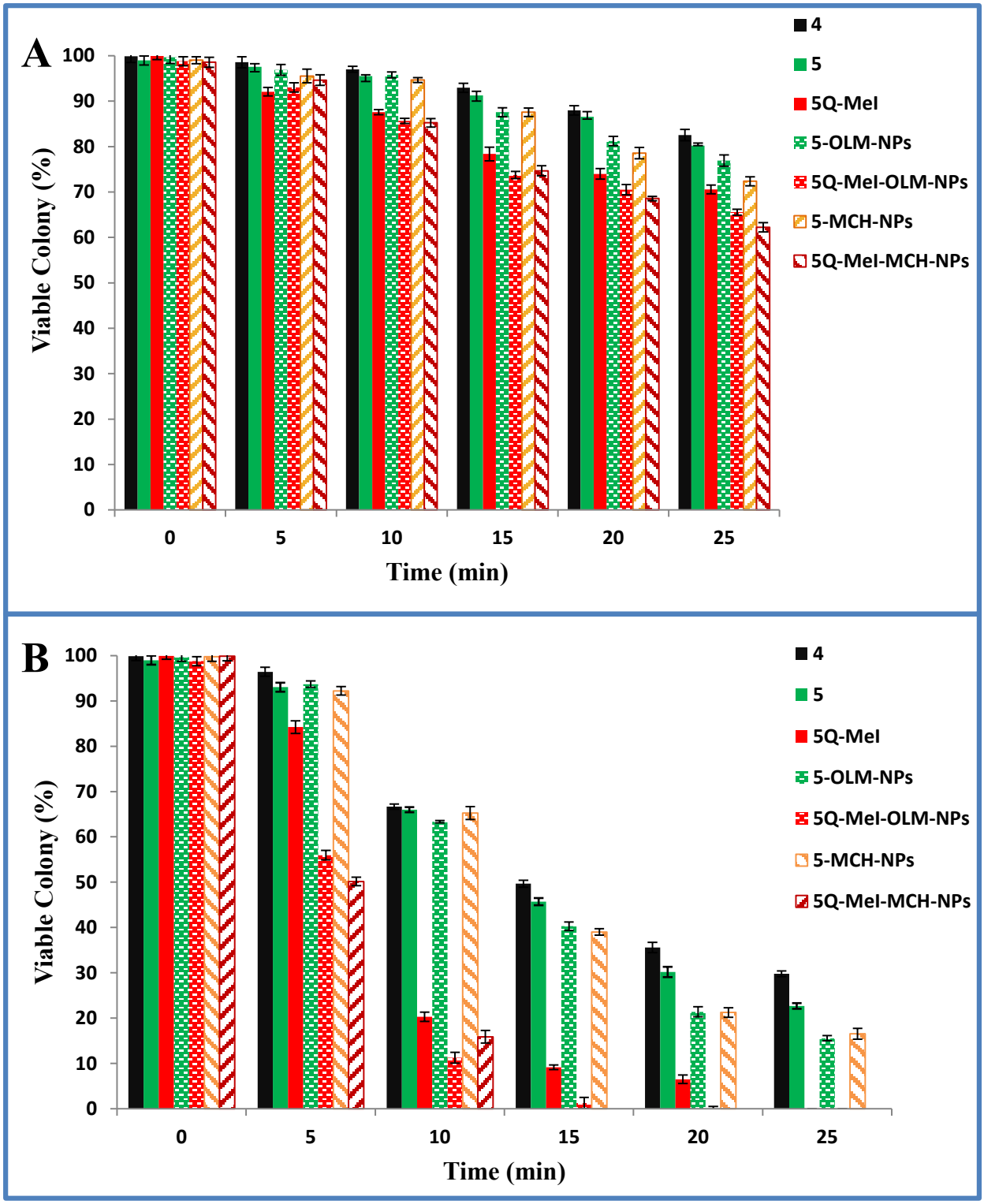

Fig. 5.5 PACT activity time study for 25 min of complexes **4**, **5**, **5Q-MeI**, **5**-OLM-NPs, **5Q-MeI**-OLM-NPs, **5**-MCH-NPs, **5Q-MeI**-MCH-NPs, (A) dark studies (B) light studies; concentration of 2.5 µM against ***S. aureus***; Note: NPs = $Ag/CuFe_2O_4$.

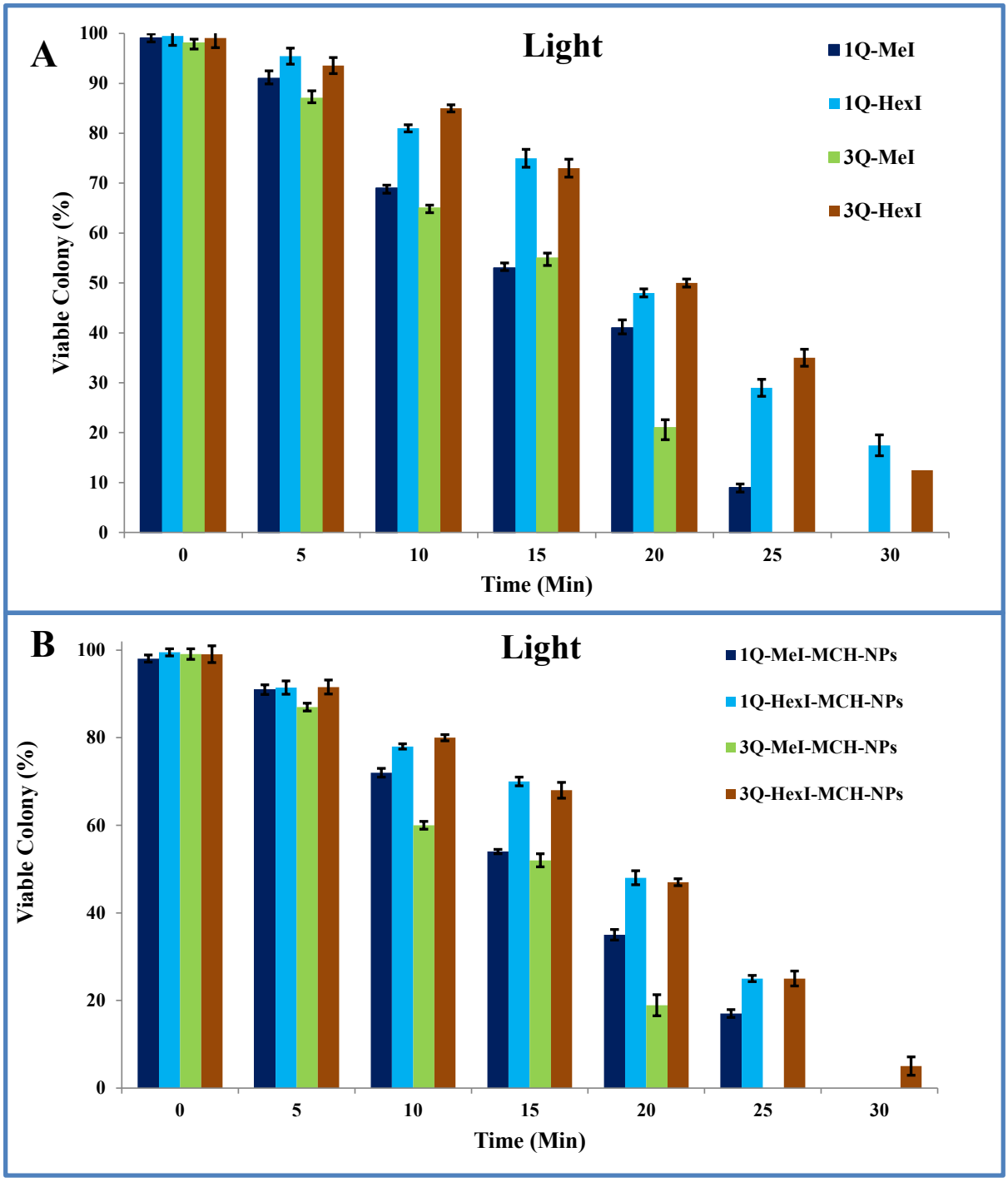

Fig. 5.6 PACT photoactivity time study of complexes (A) **1Q-MeI**, **1Q-HexI**, **3Q-MeI**, **3Q-HexI** and (B) **1Q-MeI**-MCH-NPs, **1Q-HexI**-MCH-NPs, **3Q-MeI**-MCH-NPs, **3Q-HexI**-MCH-NPs; 30 min irradiation time and concentration of 2.5 µM against ***E. coli***; Note: NPs = Ag/$CuFe_2O_4$.

Table 5.2 (A) Log reduction values upon photoinactivation of *S. aureas* and ϕ_Δ values in 2% DMSO/PBS.

Complexes/Conjugates	Time (min)	Concentration (μM)	Log reduction	ϕ_Δ in water
1	30	2.5	0.46	0.27
1Q-MeI	30	2.5	9.27	0.32
1-MCH-Ag/$CuFe_2O_4$	30	2.5	3.71	0.34
1Q-MeI-MCH-Ag/$CuFe_2O_4$	30	2.5	9.27	0.35
4	25	1.5	0.26	0.24
5	25	1.5	0.79	0.22
5Q-MeI	25	1.5	8.31	0.25
5-OLM-Ag/$CuFe_2O_4$	25	1.5	2.76	0.24
5Q-MeI-OLM-Ag/$CuFe_2O_4$	25	1.5	8.31	22
5-MCH-Ag/$CuFe_2O_4$	25	1.5	2.76	0.24
5Q-MeI-MCH-Ag/$CuFe_2O_4$	25	1.5	8.31	0.26

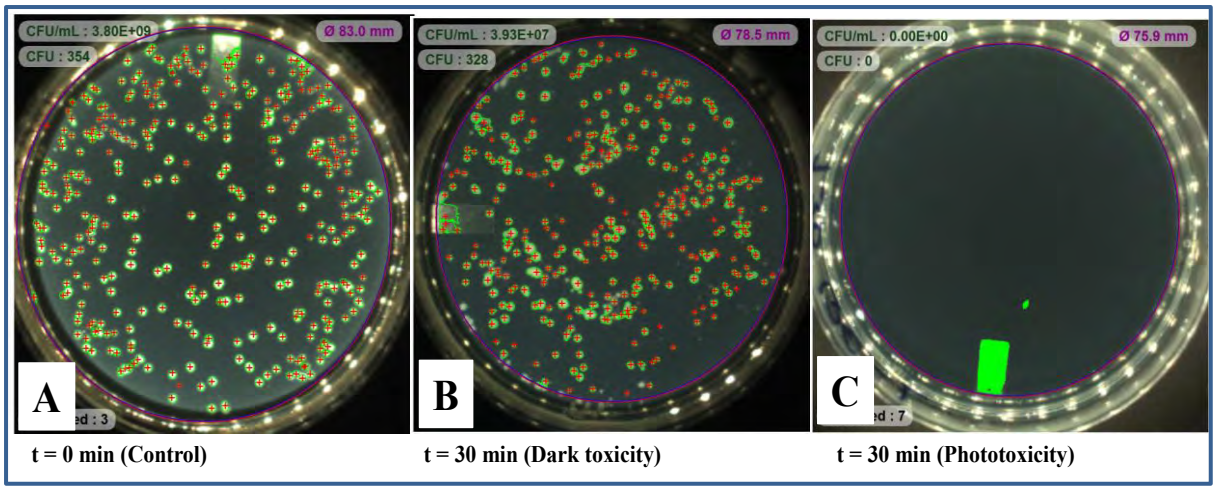

Fig. 5.7 Agar plates of showing mitigation of *E. coli* (A) control t = 0 min (no PS), (B) complex **1Q-MeI** (2.5 μM, Dark studies) at t = 30 min, and (C) complex **1Q-MeI** (2.5 μM, Light studies) at t = 30 min.

Table 5.3 Log reduction values upon photoinactivation of *E. coli* using 2.5 µM concentration of the PS and 30 min irradiation in 1% DMSO/PBS and ϕ_Δ values in 2% DMSO/PBS.

Complexes/Conjugates	Log reduction	ϕ_Δ in water
2	0.87	0.25
3	1.61	0.26
1Q-MeI	9.58	0.32
1Q-HexI	7.19	0.27
3Q-MeI	9.58	0.32
3Q-HexI	7.34	0.30
1Q-MeI-MCH-Ag/$CuFe_2O_4$	9.58	0.35
1Q-HexI-MCH-Ag/$CuFe_2O_4$	9.58	0.30
3Q-MeI-MCH-Ag/$CuFe_2O_4$	9.58	0.34
3Q-HexI-MCH-Ag/$CuFe_2O_4$	7.67	0.28

5.3 Summary of the chapter

In vitro Photodynamic antimicrobial chemotherapy activity of the porphyrin complexes **1**, **1Q-MeI**, **1Q-HexI, 2**, **3**, **3Q-MeI**, **3Q-HexI**, **4**, **5**, **5Q-MeI**, and conjugates **1**-MCH-Ag/$CuFe_2O_4$, **1Q-MeI**-MCH-Ag/$CuFe_2O_4$, **1Q-HexI**-MCH-Ag/$CuFe_2O_4$, **3Q-MeI**-MCH-Ag/$CuFe_2O_4$, **3Q-HexI**-MCH-Ag/$CuFe_2O_4$, **5**-OLM-Ag/$CuFe_2O_4$, **5Q-MeI**-OLM-Ag/$CuFe_2O_4$, **5**-MCH-Ag/$CuFe_2O_4$, and **5Q-MeI**-MCH-Ag/$CuFe_2O_4$ were assessed on either *S. aureus* or *E. coli*. Both dark and light toxicity were assessed at different concentrations over a specific time. MCH-Ag/$CuFe_2O_4$

and OLM-Ag/$CuFe_2O_4$ alone showed some PACT activity against S. aureus, and this was expected since the metals NPs are known to be cytotoxic against microbial. PACT activity of MCH-Ag/$CuFe_2O_4$ NPs and OLM-Ag/$CuFe_2O_4$ NPs were both >90% viable colonies after 30 min of irradiation, signifying the insignificant effect brought by the capping agents on the NPs alone. The cationic porphyrins **1Q-MeI** and its conjugate **1Q-MeI**-MCH-Ag/$CuFe_2O_4$ showed similar log reduction of 9.27 ($p< 0.05$) against *S. aureus* after 30 min of irradiation at concentration 2.5 µM, however, the log reduction for complex **1** and its conjugate **1**-MCH-Ag/$CuFe_2O_4$ were 0.46 and 3.71 against *S. aureus* after 30 min of irradiation at concentration 2.5 µM, respectively . Log reduction values of 8.31 ($p< 0.05$) were observed for **5Q-MeI**, **5Q-MeI**-OLM-Ag/$CuFe_2O_4$, and **5Q-MeI**-OLM-Ag/$CuFe_2O_4$ against *S. aureus* after 25 min of irradiation at concentration 1.5 µM. The highest log reduction of 9.58 ($p< 0.05$) was observed for complexes **1Q-MeI**, **3Q-MeI**, and their conjugates against *E. coli* after 30 min of irradiation. **1Q-MeI** showed a higher PACT efficacy on both *S. aureus* (log reduction = 9.27, $p< 0.05$, 30 min) and to *E. coli* (log reduction = 9.58, $p< 0.05$, 30 min) at a concentration of 2.5 µM. The higher log reduction against *E. coli* shows a better PACT activity, which was not expected since *E. coli* is known to be less sensitive to PSs.

All the cationic porphyrins and their conjugates used in this study showed a high PACT activity against both gram-positive (*S. aureus*) and gram-negative (*E. coli*) strain, rendering them as potential PS for PACT applications.

Chapter 6

Conclusions and recommendations

This chapter outlines summarised results and conclusive remarks based on the studies conducted, and moreover, recommendations for further studies.

6.1 Conclusions

This thesis reports for the first time asymmetrically and symmetrically substituted cationic porphyrins linked to bimetallic ferrite core-shell nanoparticles either through axial ligand or meso-substituents for in vitro PACT photoinactivation of gram-positive and gram-negative bacterial strains. Validation of the successful syntheses of the porphyrins, nanoparticles, and conjugates was assessed using appropriate analytical instruments. The porphyrins were either covalently linked (ester bonding) to the NPs or self-assembled on the NP's exposed silver (Ag) surface via Ag-S or Ag-N bond formation. FT-IR and XPS were employed to prove the conjugations and bond formations.

All the porphyrin complexes were metalated with indium metal to improve the photophysicochemical properties. Pyridyl meso-substituents and axial ligands were employed to improve the water solubility of the complexes and the thiol meso-substituents were used since they are known to have higher toxicity against a broad spectrum of microbials. All the metalated porphyrins were observed to have relatively improved singlet oxygen quantum yields compared to the free-base porphyrins, and this was expected since the heavy indium metal atom is known to facilitate the intersystem crossing of the singlet excited PSs to the triplet excited states which positively impact the singlet oxygen generation. Upon the formation of the conjugates, overall improved singlet oxygen quantum yields were observed, and this was attributed to the presence of the NPs which brings heavy atom effect. Axial modifications had unclear trends on the singlet oxygen quantum yields. However, higher fluorescence quantum yields were observed after axial modification, and this could be ascribed to the replacement of heavy chloride axial ligand by either amino or pyridine linked through phenoxy to the metal. The highest singlet oxygen

generation in DMF was observed for **1Q-MeI**-MCH-Ag/$CuFe_2O_4$ (ϕ_Δ = 0.62) conjugate followed by **1**-MCH-Ag/$CuFe_2O_4$ (ϕ_Δ = 0.61), **3Q-HexI**-MCH-Ag/$CuFe_2O_4$ (ϕ_Δ = 0.60), **1Q-MeI** (ϕ_Δ = 0.59), **5Q-MeI**-OLM-Ag/$CuFe_2O_4$ (ϕ_Δ = 0.59), and **5Q-MeI**-MCH-Ag/$CuFe_2O_4$ (ϕ_Δ = 0.59). The singlet oxygen generation for all the complexes and the conjugates were relatively low in water (containing 2% DMSO), where the highest ϕ_Δ was observed for **1Q-MeI**-MCH-Ag/$CuFe_2O_4$ (ϕ_Δ = 0.35 in water). It can be observed that the quaternized conjugates possess improved singlet oxygen in both organic solvents and aqueous media.

The amphiphilic porphyrin complexes quaternized with alkyl halide of shorter chain length (methyl iodide) were observed to be more hydrophilic compared to complexes quaternized with alkyl halides of longer chain length (hexyl iodide). Log $P_{o/w}$ of -1.65 was observed for **1Q-MeI** which is more negative relative to **3Q-MeI** (Log $P_{o/w}$ = -0.95), and the negative log $P_{o/w}$ value signifies hydrophilicity character which consequently suggests a better cellular uptake. Upon in vitro PACT studies, impressive PACT activities were observed for most of the quaternized complexes and their conjugates. All the studied quaternized complexes showed log reduction values >7 against both *S. aureus* and *E. coli* upon light exposure for the duration of the studies. Upon photoinactivation of *E. coli*, complexes **1Q-MeI**, **3Q-MeI**, **1Q-MeI**-MCH-Ag/$CuFe_2O_4$, **3Q-MeI**-MCH-Ag/$CuFe_2O_4$, and **1Q-HexI**-MCH-Ag/$CuFe_2O_4$ were observed to have completely obliterated the bacteria after irradiation for 30 min with 415 nm LED. Complexes **1Q-HexI** and **3Q-HexI** showed >10% viable colony after irradiation for 30 min. These phenomena could be ascribed to the higher water solubility and ϕ_Δ for complexes **1Q-MeI** and **3Q-MeI** compared to **1Q-HexI** and **3Q-HexI**. It was observed that the complexes with shorter alkyl chains gave a better PACT activity against either *S. aureus* or *E. coli*, based on the comparison of **1Q-MeI**, **3Q-MeI**, **1Q-HexI,** and **3Q-HexI**. PACT activity was

improved upon conjugation; where log reduction of 3.71 ($p< 0.05$) was observed for conjugate **1**-MCH-Ag/$CuFe_2O_4$ after 30 min of light exposure compared to 0.46 ($p< 0.05$) for complex **1** and log reduction of 9.58 ($p< 0.05$) was observed for conjugate **1Q-HexI**-MCH-Ag/$CuFe_2O_4$ compared to 7.19 ($p< 0.05$) for complex **1Q-HexI**. Moreover, the NPs capped with 6-mercapto-1-hexanol (MCH) showed a relatively similar PACT activity compared to oleyamine capped NPs, suggesting the capping agent played had a minimal to no impact on PACT activity of the NPs. The difference in PACT activity of complex **1Q-MeI** against *S. aureus* and *E. coli* could be ascribed to the difference in cell walls of the bacteria. *E. coli* is known to be less sensitive to neutral and anionic PSs than *S. aureus*. For the first time high log reduction values were observed against *E. coli* compared to *S. aureus*.

6.2 Recommendations

Towards the development of potential photosensitizers for PACT, it is imperative not only to study photophysicochemical properties of the complexes, however, to also take into consideration the stability and solubility of the complexes. In this work it was observed that singlet oxygen generation alone was not a distinct factor on the PACT efficacy of the complexes, since some of the complexes have practically the same ϕ_Δ but different PACT activity. Solubility of the complexes plays a major role on antimicrobial efficacy of the photosensitizer. An ideal photosensitizer would have a more balance between hydrophilicity and hydrophobicity character. Synthesis of a photosensitizer with more positive charges and shorter alkyl halide chain lengths quaternizing agent gives a better hydrophilicity character and consequently a higher cellular uptake. As delineated in this thesis, symmetrically substituted porphyrin complexes with unquaternizable meso-substituents can be made positively charged by the use of quaternizable axial ligands such as hydroxypyridine or

aminophenol. Nanoparticles with more exposed metal surfaces can be employed to allow more release metal ions (e.g. Cu^{2+} or Ag^{3+}) which are known to eradicate microbial. It is also imperative to conjugate the photosensitizers to nanomaterials in order to facilitate synergy PACT activity between the PSs and the nanomaterials, and moreover recovery after use.

References

[1] M.M. Gois, C. Kurachi, E.J.B. Santana, E.G.O. Mima, D.M.P. Spolidório, J.E.P. Pelino, V.S. Bagnato, Susceptibility of Staphylococcus aureus to porphyrin-mediated photodynamic antimicrobial chemotherapy: An in vitro study, Lasers Med. Sci. 25 (2010) 391. https://doi.org/10.1007/s10103-009-0705-0.

[2] A. Lipovsky, Y. Nitzan, H. Friedmann, R. Lubart, Sensitivity of Staphylococcus aureus strains to broadband visible light, Photochem. Photobiol. 85 (2009) 255. https://doi.org/10.1111/j.1751-1097.2008.00429.x.

[3] Y. Nitzan, M. Gutterman, Z. Malik, B. Ehrenberg, Inactivation of Gram-Negative Bacteria By Photosensitized Porphyrins, Photochem. Photobiol. 55 (1992) 89. https://doi.org/10.1111/j.1751-1097.1992.tb04213.x.

[4] A.J. MacRobert, S.G. Bown, D. Phillips, What are the ideal photoproperties for a sensitizer?, Ciba Found. Symp. 14 (1989) 4. https://doi.org/10.1002/9780470513842.ch2.

[5] A.P. Castano, T.N. Demidova, M.R. Hamblin, Mechanisms in photodynamic therapy: Part one-Photosensitizers, photochemistry and cellular localization, Photodiagnosis Photodyn. Ther. 1 (2004) 279. https://doi.org/10.1016/S1572-1000(05)00007-4.

[6] I.J. Macdonald, T.J. Dougherty, Basic principles of photodynamic therapy, J. Porphyr. Phthalocyanines. 5 (2001) 105. http://dx.dio.org/10.1002/jpp.328.

[7] Z. Luksiene, Photodynamic therapy: mechanism of action and ways to improve the efficiency of treatment, Medicina (B. Aires). 39 (2003) 1137.

[8] E. Alves, M.A.F. Faustino, J.P.C. Tomé, M.G.P.M.S. Neves, A.C. Tomé, J.A.S. Cavaleiro, Â. Cunha, N.C.M. Gomes, A. Almeida, Nucleic acid changes during photodynamic inactivation of bacteria by cationic porphyrins, Bioorganic Med. Chem. 21 (2013) 4311. https://doi.org/10.1016/j.bmc.2013.04.065.

[9] H.A. Khan, A. Ahmad, R. Mehboob, Nosocomial infections and their control strategies, Asian Pac. J. Trop. Biomed. 5 (2015) 505.

[10] S. Banfi, E. Caruso, L. Buccafurni, V. Battini, S. Zazzaron, P. Barbieri, V. Orlandi, Antibacterial activity of tetraaryl-porphyrin photosensitizers: An in vitro study on Gram negative and Gram positive bacteria, J. Photochem. Photobiol. B Biol. 85 (2006) 28. https://doi.org/10.1016/j.jphotobiol.2006.04.003.

[11] M.R. Hamblin, Antimicrobial photodynamic inactivation: a bright new technique to kill resistant microbes, Curr. Opin. Microbiol. 33 (2016) 67. https://doi.org/10.1016/j.mib.2016.06.008.

[12] G. Bertolini, F. Rossi, G. Valduga, G. Jori, J. van Lier, Photosensitizing activity of water- and lipid-soluble phthalocyanines on Escherichia coli, FEMS Microbiol. Lett. 71 (1990) 149. https://doi.org/10.1016/0378-1097(90)90048-U.

[13] B.M. Amos-Tautua, S.P. Songca, O.S. Oluwafemi, Application of porphyrins in antibacterial photodynamic therapy, Molecules. 24 (2019) 2456. https://doi.org/10.3390/molecules24132456.

[14] F. Gábor, K. Szocs, P. Maillard, G. Csík, Photobiological activity of exogenous and endogenous porphyrin derivatives in Escherichia coli and Enterococcus hirae cells, Radiat. Environ. Biophys. 40 (2001) 145. https://doi.org/10.1007/s004110100092.

[15] W. Küster, Beitrage zur kenntnis des Bilirubins und Hamins, Hoppe Seyler's Z. Physiol. Chem. 82 (1912) 463.

[16] H. Fischer, K. Zeile, Synthese des Hämatoporphyrins, Protoporphyrins, und Hämins Liebig's, Ann. Chem. 468 (1929) 98.

[17] J.C. Kendrew, The structure of globular proteins, Comp. Biochem. Physiol. 4 (1962) 249. https://doi.org/10.1016/0010-406X(62)90009-9.

[18] L.R. Malgrom, The Colours of Life: An Introduction to the Chemistry of Porphyrins and Related Compounds; Oxford University Press: New York, NY, USA, 1997.

[19] M. Imran, M. Ramzan, A.K. Qureshi, M. Azhar Khan, M. Tariq, Emerging applications of porphyrins and metalloporphyrins in biomedicine and diagnostic magnetic resonance imaging, Biosensors. 8 (2018) 95. https://doi.org/10.3390/bios8040095.

[20] G.B. Kharkwal, K. Sharma, Y. Huang, T. Dai, Photodynamic Therapy for Infections : Clinical Applications, Lasers Surg. Med. 43 (2011) 755. https://doi.org/10.1002/lsm.21080.

[21] F.F. Sperandio, Y. Huang, M.G. Hospital, M. Hamblin, M.G. Hospital, Antimicrobial Photodynamic Therapy To Kill Gram-Negative Bacteria, Recent Patents Anti-Infective Drug Discov. 8 (2013) 108. https://doi.org/10.2174/1574891X113089990012.

[22] P. Zucca, C.M.B. Neves, M.M.Q. Simões, G.P.M.S. Neves, G. Cocco, E. Sanjust, Metalloporphyrins as Reusable Catalysts in Oxidative Bleaching of Industrial Dyes, Molecules. 21 (2016) 264. https://doi.org/10.3390/molecules21070964.

[23] M.L. Embleton, S.P. Nair, W. Heywood, D.C. Menon, B.D. Cookson, M. Wilson,

Development of a Novel Targeting System for Lethal Photosensitization of Antibiotic-Resistant Strains of Staphylococcus aureus, Antimicrob. Agents Chemother. 49 (2005) 3690. https://doi.org/10.1128/AAC.49.9.3690.

[24] S.M.A. Pinto, C.S. Vinagreiro, Synthesis of meso-substituted porphyrins using sustainable chemical processes, J. Porphyr. Phthalocyanines. 20 (2016) 45. https://doi.org/10.1142/S1088424616300020.

[25] P. Rothemund, A.R. Menotti, Porphyrin Studies. IV.1 The Synthesis of α,β,γ,δ-Tetraphenylporphine, J. Am. Chem. Soc. 63 (1941) 267.

[26] A.D. Adler, F.R. Longo, J.D. Finarelli, J. Goldmacher, J. Assour, L.A. Korsakoff, A simplified synthesis for meso-tetraphenylporphin, J. Org. Chem. 32 (1967) 476. http://dx.doi.org/10.1021/jo01288a053.

[27] M.G.H. Vicente, K.M. Smith, Porphyrins and Derivatives : Synthetic Strategies and Reactivity Profiles, Curr. Org. Chem. 4 (2000) 139.

[28] J.S. Lindsey, Synthesis of meso-substituted porphyrins. In The Porphyrin Handbook; M. Kadish, K. M. Smith, R. Guilard, Eds; Academic Press: San Diego, CA, USA, 2000.

[29] P. Faugeras, J. Vergnaud, R. Lucas, B. Boe, K. Teste, R. Zerrouki, Iodine-catalyzed one-pot synthesis of unsymmetrical meso-substituted porphyrins, Tetrahedron. 66 (2010) 1994. https://doi.org/10.1016/j.tet.2010.01.055.

[30] M.M. Babu, M. Amaravathi, L. Giribabu, G. Chandramouli, Synthesis of meso-substituted porphyrins in room temparature ionic liquid, J. Chem Res. Synop. 11 (2008) 666.

[31] C.O. Kappe, A. Stadler, D. Dalinger, In Microwaves in Organic and Medicinal Chemistry, 2nd ed., R. Mannhold, H. Kubinyi, G.Folkers, Wiley-VCH; Weinheim, Germany, 2012.

[32] R. Naik, P. Joshi, S.P. Kaiwar, R.K. Deshpande, Facile synthesis of meso-substituted dipyrromethanes and porphyrins using cation exchange resins, Tetrahedron. 59 (2003) 2207. https://doi.org/10.1016/S0040-4020(03)00245-X.

[33] S. Nia, X. Gong, C. Michael, M. Jurow, Solvent-free synthesis of meso-tetraarylporphyrins in air : product diversity and yield optimization, J. Porphyr. Phthalocyanines. 14 (2010) 621. https://doi.org/10.1142/S1088424610002422.

[34] X. Feng, M.O. Senge, Anefficient synthesis of highly functionalized asymmetric porphyrins with organolithium reagents, J. Chem. Soc., Perkin Trans. 1 (2001) 1030. https://doi.org/10.1039/b100012h.

[35] E. Milanesio, S.M. Chiacchiera, J.J. Silber, E.N. Durantini, Synthesis of Asymmetrical Porphyrins Substituted in the meso-position from Dipyrrolomethanes, Molecules. 5 (2000) 531.

[36] M. Gouterman, Spectra of Porphyrins, J. Mol. Spectrosc. 6 (1961) 138.

[37] R. Giovannetti, The Use of Spectrophotometry UV-Vis for the Study of Porphyrins, In Macro to nano spectroscopy, J. Uddin, IntechOpen, Camerino Italy, 2012. https://doi.org/10.5772/38797.

[38] R. Yang, K. Li, K. Wang, F. Zhao, N. Li, F. Liu, Porphyrin Assembly on beta-Cyclodextrin for Selective Sensing and Detection of a Zinc Ion Based on the Dual Emission

Fluorescence Ratio, Anal. Chem. 30 (2003) 612. https://doi.org/10.1021/ac020467n.

[39] K.M. Smith, Development of porphyrin synthesis, New J. Chem. 40 (2016) 5644.

[40] U. Noomnarm, R.M. Clegg, Fluorescence lifetimes: fundamentals and interpretations, Photosynth. Res. 101 (2009) 181. https://doi.org/10.1007/s11120-009-9457-8.

[41] Q. Zhou, W. Lei, J. Chen, C. Li, Y. Hou, X.S. Wang, B.W. Zhang, A New Heteroleptic Ruthenium (II) Polypyridyl Complex with Long-Wavelength Absorption and High Singlet-Oxygen Quantum Yield, Chem. Eur. J. 16 (2010) 3157. https://doi.org/10.1002/chem.200902563.

[42] F. Ricchelli, Photophysical properties of porphyrins in biological membranes, J. Photochem. Photobiol. B Biol. 29 (1995) 109.

[43] K. Lang, P. Kubát, P. Lhoták, J. Mosinger, D.M. Wagnerová, Photophysical Properties and Photoinduced Electron Transfer Within Host–Guest Complexes of 5,10,15,20-Tetrakis(4-N-methylpyridyl)porphyrin with Water-soluble Calixarenes and Cyclodextrins, J. Photochem. Photobiol. 74 (2001) 558.

[44] Y. Li, Solvent effects on photophysical properties of copper and zinc porphyrins, Chinese Sci. Bull. 53 (2008) 3615. https://doi.org/10.1007/s11434-008-0498-8.

[45] J. Kubat, P. Mosinger, Photophysical properties of metal complex of meso-tetrakis(4-sulphonatophenyl) porphyrin, J. Photochem. Photobiol. A Chem. 96 (1996) 93.

[46] P. Henke, J. Mosinger, Effect of Temperature on Photophysical Properties of Polymeric Nano fiber Materials with Porphyrin Photosensitizers, J. Phys. Chem. B. 118 (2014) 6167.

[47] A. Matarazzo, R.H.E. Hudson, Fluorescent adenosine analogs: a comprehensive survey, Tetrahedron. 71 (2015) 1627. http://dx.doi.org/10.1016/j.tet.2014.12.066.

[48] M. Guergueb, J. Brahmi, S. Nasri, S. Nasri, F. Loiseau, K. Aouadi, V. Guerineau, S. Najmudin, H. Nasri, Zinc(ii) triazole: Meso-arylsubstituted porphyrins for UV-visible chloride and bromide detection. Adsorption and catalytic degradation of malachite green dye, RSC Adv. 10 (2020) 22712. https://doi.org/10.1039/d0ra03070h.

[49] A. Lyubimtsev, A. Semeikin, N. Zheglova, V. Sheinin, O. Kulikova, S. Syrbu, Synthesis and photophysical properties of low symmetrical porphyrin-amino acid conjugates and their Zn complexes, Macroheterocycles. 11 (2018) 103. https://doi.org/10.6060/mhc171151l.

[50] A. Ogunsipe, J. Chen, T. Nyokong, Photophysical and photochemical studies of zinc(II) phthalocyanine derivatives-effects of substituents and solvents, New. J. Chem. 28 (2004) 822.

[51] R.T. Kuznetsova, I. V Aksenova, D.E. Bashkirtsev, A.S. Shulev, E. V Antina, M.B. Berezin, N.A. Bumagina, Determination of the Quantum Yield of Singlet Oxygen Sensitized by Halogenated Boron Difluoride Dipyrromethenes, High Energy Chem. 51 (2017) 190. https://doi.org/10.1134/S0018143917030079.

[52] H. Ling, J. Bhaumik, J.R. Diers, P. Mroz, M.R. Hamblin, D.F. Bocian, J.S. Lindsey, D. Holten, Photophysical characterization of imidazolium-substituted Pd(II), In(III), and Zn(II) porphyrins as photosensitizers for photodynamic therapy, J. Photochem. Photobiol. A Chem. 200 (2008) 346. https://doi.org/10.1016/j.jphotochem.2008.08.006.

[53] L. Lucantoni, M. Magaraggia, G. Lupidi, R.K. Ouedraogo, F. Esposito, C. Fabris, G. Jori, A. Habluetzel, Novel , Meso-Substituted Cationic Porphyrin Molecule for Photo-Mediated Larval Control of the Dengue Vector Aedes aegypti, PloS Negl.Trop. Dis. 5 (2011) 1434. https://doi.org/10.1371/journal.pntd.0001434.

[54] A. Orenstein, D. Klein, J. Kopolovic, E. Winkler, Z. Malik, N. Keller, Y. Nitzan, The use of porphyrins for eradication of Staphylococcus aureus in burn wound infections, FEMS Immunol. Med. Microbiol. 19 (1998) 307.

[55] J.A. González-delgado, P. Kennedy, M. Ferreira, J.P.C. Tome, B. Sarmento, Use of photosensitizers in semisolid formulations for microbial photodynamic inactivation, J. Med. Chem. 59 (2016) 4428. https://doi.org/10.1021/acs.jmedchem.5b01129.

[56] A. Kawada, Y. Aragane, H. Kameyama, Y. Sangen, T. Tezuka, Acne phototherapy with a high-intensity, enhanced, narrow-band, blue light source: an open study and in vitro investigation, J. Dermatol. Sci. 30 (2002) 129.

[57] J. Mbakidi, F. Bregier, T. Ouk, R. Granet, S. Alves, E. Riviere, S. Chevreux, G. Lemercier, V. Sol, Magnetic Dextran Nanoparticles That Bear Hydrophilic Porphyrin Derivatives : Bimodal Agents for Potential Application in Photodynamic Therapy, Chempluschem. 80 (2015) 1416. https://doi.org/10.1002/cplu.201500087.

[58] M. Nowostawska; S.A Corr; S.J. Byrne; J. Conroy; Y Volkov; Y.K Gun'ko, Porphyrin-magnetite nanoconjugates for biological imaging, J. Nanobiotechnology. 9 (2011) 13. https://doi.org/10.1186/1477-3155-9-13.

[59] J. Hollingsworth, Synthesis, characterization, and self-assembly of porphyrins conjugated to superparamagnetic colloidal particles for enhanced photodynamic

therapy. Louisiana State University and Agricultural and Mechanical College Doctoral Dissertations, 2012. https://digitalcommons.lsu.edu/gradschool_dissertations/3647%0AThis.

[60] M. Thandu, V. Rapozzi, L. Xodo, F. Albericio, " Clicking " Porphyrins to Magnetic Nanoparticles for Photodynamic Therapy, Chempluschem. 79 (2014) 90. https://doi.org/10.1002/cplu.201300276.

[61] M.M. Rodrigues, M.A.F. Faustino, M.G.P.M.S. Neves, E. Alves, A.S. Cavaleiro, Z. Lin, A. Almeida, Dyes and Pigments A new insight on nanomagnet-porphyrin hybrids for photodynamic inactivation of microorganisms, Dye. Pigment. 110 (2014) 80. https://doi.org/10.1016/j.dyepig.2014.05.016.

[62] C.M.B. Carvalho, E. Alves, L. Costa, P.C. Tome, M.A.F. Faustino, A.S. Cavaleiro, A. Almeida, Z. Lin, Functional Cationic Nanomagnet-Porphyrin Hybrids for the Photoinactivation of Microorganisms, ACS Nano. 4 (2010) 7133.

[63] D. Mondal, S. Bera, Porphyrins and phthalocyanines : promising molecules for light-triggered antibacterial nanoparticles, Adv. Nat. Sci. Nanosci. Nanotechnol. 5 (2014) 033002. https://doi.org/10.1088/2043-6262/5/3/033002.

[64] H. Gu, K. Xu, Z. Yang, K. Chang, B. Xu, Synthesis and cellular uptake of porphyrin decorated iron oxide nanoparticles — a potential candidate for bimodal anticancer therapy, Chem. Commun. 34 (2005) 4270. https://doi.org/10.1039/b507779f.

[65] R. Rahimi, A. Tadjarodi, M. Imani, M. Rabbani, Synthesis of tetrakis (carboxyphenyl) porphyrin coated paramagnetic iron oxide nanoparticles via amino acid for photodegradation of methylene blue, Turk. J. Chem. 37 (2013) 879.

https://doi.org/10.3906/kim-1204-19.

[66] O.J. Fakayode, S.P. Songca, O.S. Oluwafemi, Singlet oxygen generation potential of thiolated methoxy-polyethyleneglycol encapsulated superparamagnetic iron oxide nanoparticles-gold core-shell meso-5, 10, 15, 20-tetrakis (4-hydroxyphenyl) porphyrin, Mater. Lett. 199 (2017) 37. https://doi.org/10.1016/j.matlet.2017.04.045.

[67] B.M. Amos-Tautua, O.J. Fakayoe, S. Vuuren, S.P. Songca, O.S. Oluwafemi, Non-distorted visible light-absorbing thiol-PEGylated gold-coated superparamagnetic iron oxide nanoparticles–porphyrin conjugates and their inhibitory effects against nosocomial patho, MRS Commun. 9 (2019) 1335. https://doi.org/10.1557/mrc.2019.141.

[68] A.O. Eshilokun, Synthesis, Characterization and Kinetic Studies of Porphyrins With Thiolated Side Chains for Functionalization of Paramagnetic Iron Oxide-Gold, Core-Shell Nanoparticles, University of Limpopo, Medunsa campus, Doctoral dessertation, 2011.

[69] L.D. Dias, R.M.B. Carrilho, C.A. Henriques, G. Piccirillo, A recyclable hybrid manganese (III) porphyrin magnetic catalyst for selective olefin epoxidation using molecular oxygen, J. Porphyr. Phthalocyanines. 22 (2018) 331. https://doi.org/10.1142/S108842461850027X.

[70] Y. Zhang, W. Yan, Z. Sun, X. Lic, J. Gao, Fabrication of magnetically recyclable catalytic activity for p-nitrophenol reduction, RSC Adv. 4 (2014) 38040. https://doi.org/10.1039/C4RA05514D.

[71] J. Habdas, B. Boduszek, J. Wiley, Synthesis of 5-(4-carboxyphenyl)-10,15,20-tris- (4

pyridyl)-porphyrin and its peptidyl phosphonate derivatives, J. Pept. Sci. 15 (2009) 305. https://doi.org/10.1002/psc.1117.

[72] R.C. Soy, B. Babu, D.O. Oluwole, N. Nwaji, J. Oyim, E.K. Amuhaya, E. Prinsloo, J. Mack, T. Nyokong, Photophysicochemical properties and photodynamic therapy activity of chloroindium(III) tetraarylporphyrins and their gold nanoparticle conjugates, J. Porphyr. Phthalocyanines. 23 (2019) 1. https://doi.org/10.1142/S1088424618501146.

[73] M. Tadic, S. Kralj, M. Jagodic, D. Hanzel, D. Makovec, Magnetic properties of novel superparamagnetic iron oxide nanoclusters and their peculiarity under annealing treatment, Appl. Surf. Sci. 322 (2014) 255. https://doi.org/10.1016/j.apsusc.2014.09.181.

[74] A. Akbarzadeh, M. Samiei, S. Davaran, Magnetic nanoparticles: preparation, physical properties, and applications in biomedicine, Nanoscale Res. Lett. 7 (2012) 144.

[75] H.M. Williams, Review article The application of magnetic nanoparticles in the treatment and monitoring of cancer and infectious diseases, Biosci. Horizons Int. J. Student Res. 10 (2017) hzx009. http://dio.org/10.1093/biohorizons/hzx009.

[76] J. Wallyn, N. Anton, T.F. Vandamme, Synthesis, Principles, and Properties of Magnetite Nanoparticles for In Vivo Imaging Applications-A Review, Pharmaceutics. 11 (2019) 601.

[77] A. Magadla, D.O. Oluwole, M. Managa, T. Nyokong, Physicochemical and antimicrobial photodynamic chemotherapy (against E . coli) by indium phthalocyanines in the presence of silver-iron bimetallic nanoparticles, Polyhedron. 162 (2019) 30. https://doi.org/10.1016/j.poly.2019.01.032.

[78] S. Mathews, M. Hans, F. Mücklich, M. Solioz, Contact killing of bacteria on copper is suppressed if bacterial-metal contact is prevented and is induced on iron by copper ions, Appl. Environ. Microbiol. 79 (2013) 2605. https://doi.org/10.1128/AEM.03608-12.

[79] J. Kudr, Y. Haddad, L. Richtera, Z. Heger, M. Cernak, Magnetic Nanoparticles: From Design and Synthesis to Real World Applications, Nanomaterials. 7 (2017) 243. https://doi.org/10.3390/nano7090243.

[80] C.H. Chen, T.K. Lu, Development and Challenges of Antimicrobial Peptides for Therapeutic Applications, Antibiotics. 9 (2020) 24.

[81] A. Eatemadi, H. Daraee, H. Karimkhanloo, M. Kouhi, N. Zarghami, Carbon nanotubes : properties , synthesis , purification , and medical applications, Nanoscale Res. Lett. 9 (2014) 13.

[82] R. Peymanfar, F. Azadi, Y. Yassi, Preparation and Characterization of CuFe2O4 Nanoparticles by the Sol-Gel Method and Investigation of Its Microwave Absorption Properties at Ku-Band Frequency Using Silicone Rubber, Proceedings. 2 (2018) 1155. https://doi.org/10.3390/ecms2018-05218.

[83] M.M. Rashad, E.M. Elsayed, M.M. Moharam, R.M. Abou-shahba, A.E. Saba, Structure and magnetic properties of Nix $Zn_{1-x}Fe_2O_4$ nanoparticles prepared through co-precipitation method, J. Alloys Compd. 486 (2009) 759. https://doi.org/10.1016/j.jallcom.2009.07.051.

[84] S.P. Schwaminger, C. Syhr, S. Berensmeier, Controlled Synthesis of Magnetic Iron Oxide: Magnetite or Maghemite?, Crystals. 10 (2020) 214.

[85] N.A. Yazid, Y.C. Joon, Co-precipitation synthesis of magnetic nanoparticles for efficient removal of heavy metal from synthetic wastewater Co-precipitation Synthesis of Magnetic Nanoparticles for Efficient Removal of Heavy Metal from Synthetic Wastewater, AIP Conf. Proc. 2124 (2019) 020019. https://doi.org/10.1063/1.5117079.

[86] E. Agouriane, B. Rabi, A. Essoumhi, A. Razouk, M. Sahlaoui, B.F.O. Costa, M. Sajieddine, Structural and magnetic properties of $CuFe_2O_4$ ferrite nanoparticles synthesized by co-precipitation, J. Mater. Environ. Sci. 7 (2016) 4116.

[87] K.A. San, Y. Shon, Synthesis of Alkanethiolate-Capped Metal Nanoparticles Using Alkyl Thiosulfate Ligand Precursors: A Method to Generate Promising Reagents for Selective Catalysis, Nanomaterials. 8 (2018) 346. https://doi.org/10.3390/nano8050346.

[88] E. Shah, P. Upadhyay, M. Singh, M.S. Mansuri, R. Begum, N. Sheth, H.P. Soni, EDTA Capped Iron Oxide Nanoparticles Magnetic Micelles: Drug Delivery Vehicle for Treatment of Chronic Myeloid Leukemia and T1-T2 Dual Contrast Agent for Magnetic Resonance Imaging, New J. Chem. 40 (2016) 9507. https://doi.org/10.1039/C6NJ00655H.

[89] C.M. Phan, H.M. Nguyen, Role of Capping Agent in Wet Synthesis of Nanoparticles, J. Phys. Chem. A. 121 (2017) 3213. https://doi.org/10.1021/acs.jpca.7b02186.

[90] J.M. Chem, S. Sharma, N.S. Gajbhiye, R.K. Vatsa, N. Pandey, R.S. Ningthoujam, Induction heating studies of Fe_3O_4 magnetic nanoparticles capped with oleic acid and polyethylene glycol for hyperthermia, J. Mater. Chem. 21 (2011) 13388.

https://doi.org/10.1039/c1jm10092k.

[91] Y. Bao, T. Wen, A. Cristina, S.S. Amit, K.M. Krishnan, A.C.S. Samia, Magnetic nanoparticles: material engineering and emerging applications in lithography and biomedicine, J. Mater. Sci. 51 (2016) 513. https://doi.org/10.1007/s10853-015-9324-2.

[92] J. Philip, V. Mahendran, L.J. Felicia, A Simple, In-Expensive and Ultrasensitive Magnetic Nanofluid Based Sensor for Detection of Cations, Ethanol and Ammonia, J. Nanofluid. 2 (2013) 112. https://doi.org/10.1166/jon.2013.1050.

[93] A. Lu, W. Schmidt, N. Matoussevitch, H. Bönnemann, B. Spliethoff, B. Tesche, E. Bill, W. Kiefer, F. Schüth, Nanoengineering of a Magnetically Separable Hydrogenation Catalyst, Angew. Chem. Int. Ed. 43 (2004) 4303. https://doi.org/10.1002/anie.200454222.

[94] B. Gleich, Tomographic imaging using the nonlinear response of magnetic particles, Nature. 435 (2005) 1214. https://doi.org/10.1038/nature03808.

[95] V. Chaudhary, R. V Ramanujan, Magnetocaloric Properties of Fe-Ni-Cr Nanoparticles for Active Cooling, Sci. Rep. 6 (2016) 35156. https://doi.org/10.1038/srep35156.

[96] L. Josephson, In Magnetic Nanoparticles for MR Imaging, BioMEMS and Biomedical Nanotechnology. Springer, Boston, (2007). https://doi.org/10.1007/978-0-387-25842-3_8.

[97] T. Hyeon, Chemical synthesis of magnetic nanoparticles, Chem. Commun. 8 (2003) 927.

[98] I. Rabias, D. Tsitrouli, E. Karakosta, T. Kehagias, G. Diamantopoulos, M. Fardis, D. Stamopoulos, N. Diamantis, G. Panayotou, D.A. Verganelakis, G.I. Drossopoulou, E.C. Tsilibari, G. Papavassiliou, Rapid magnetic heating treatment by highly charged maghemite nanoparticles on Wistar rats exocranial glioma tumors at microliter volume, Biomicrofluidics. 4 (2010) 024111. https://doi.org/10.1063/1.3449089.

[99] A. Schätz, O. Reiser, W.J. Stark, Nanoparticles as Semi-Heterogeneous Catalyst Supports, Chem. Eur. J. 16 (2010) 8950. https://doi.org/10.1002/chem.200903462.

[100] R. Jurgons, C. Seliger, A. Hilpert, L. Trahms, S. Odenbach, C. Alexiou, Drug loaded magnetic nanoparticles for cancer therapy, J. Phys. Condens. Matter. 18 (2006) S2893. https://doi.org/10.1088/0953-8984/18/38/S24.

[101] S.M. Shabangu, B. Babu, R.C. Soy, J. Oyim, E. Amuhaya, T. Nyokong, Susceptibility of Staphylococcus aureus to porphyrin-silver nanoparticle mediated photodynamic antimicrobial chemotherapy, J. Lumin. 222 (2020) 117158.

[102] M. Managa, E.K. Amuhaya, T. Nyokong, Photodynamic antimicrobial chemotherapy activity of (5,10,15,20-tetrakis(4-(4-carboxyphenycarbonoimidoyl)phenyl)porphyrinato) chloro gallium(III), Spectrochim. Acta - Part A Mol. Biomol. Spectrosc. 151 (2015) 867. https://doi.org/10.1016/j.saa.2015.06.088.

[103] P. Dechan, G.D. Bajju, Synthesis and spectroscopic properties of axial phenoxide and para amino phenoxide incorporated indium (III) porphyrins, J. Mol. Struct. 1195 (2019) 140. https://doi.org/10.1016/j.molstruc.2019.05.120.

[104] G.D. Bajju, A. Ahmed, D. Gupta, A. Kapahi, G. Devi, Synthesis and Spectroscopic

Characterization of Some New Axially Ligated Indium(III) Macrocyclic Complexes and Their Biological Activities, Bioinorg. Chem. Appl. 2014 (2014) 865407. https://doi.org/10.1155/2014/865407.

[105] B. Babu, R.C. Soy, J. Mack, T. Nyokong, Non-aggregated lipophilic water-soluble tin porphyrins as photosensitizers for photodynamic therapy and photodynamic antimicrobial chemotherapy, New J. Chem. 44 (2020) 11006. https://doi.org/10.1039/d0nj01564d.

[106] P. Sen, A. Sindelo, D.M. Mafukidze, T. Nyokong, Synthesis and photophysicochemical properties of novel axially di-substituted silicon (IV) phthalocyanines and their photodynamic antimicrobial chemotherapy (PACT) activity against Staphylococcus aureus, Synth. Met. 258 (2019) 116203. https://doi.org/10.1016/j.synthmet.2019.116203.

[107] N. Amiri, F. Ben, S. Chevreux, E. Wenger, G. Lemercier, H. Nasri, F. Ben Taheur, S. Chevreux, E. Wenger, G. Lemercier, H. Nasri, Synthesis, crystal structure and spectroscopic characterizations of porphyrin-based Mg(II) complexes – Potential application as antibacterial agent, Tetrahedron. 73 (2017) 7011. https://doi.org/10.1016/j.tet.2017.10.029.

[108] O.L. Osifeko, I. Uddin, P.N. Mashazi, T. Nyokong, Physicochemical and antimicrobial photodynamic chemotherapy of unsymmetrical indium phthalocyanines alone or in the presence of magnetic nanoparticles, New J. Chem. 40 (2016) 2710. https://doi.org/10.1039/c5nj01922b.

[109] N.M.M. Moura, C.I.V. Ramos, I. Linhares, S.M. Santos, M.A.F. Faustino, A. Almeida,

J.A.S. Cavaleiro, F.M.L. Amado, C. Lodeiro, M.G.P.M.S. Neves, Synthesis, characterization and biological evaluation of cationic porphyrin-terpyridine derivatives, RSC Adv. 6 (2016) 110674. https://doi.org/10.1039/c6ra25373c.

[110] T.A.F. Cardote, J.F.B. Barata, C. Amador, E. Alves, M.G.P.M.S. Neves, J.A.S. Cavaleiro, Â. Cunha, A. Almeida, M.A.F. Faustino, Evaluation of meso-substituted cationic corroles as potential antibacterial agents, An. Acad. Bras. Cienc. 90 (2018) 1175. https://doi.org/10.1590/0001-3765201820170824.

[111] M. Gholinejad, B. Karimi, F. Mansouri, Synthesis and characterization of magnetic copper ferrite nanoparticles and their catalytic performance in one-pot odorless carbon-sulfur bond formation reactions, J. Mol. Catal. A Chem. 386 (2014) 20. https://doi.org/10.1016/j.molcata.2014.02.006.

[112] O.M. Bankole, T. Nyokong, Comparative studies on photophysical and optical limiting characterizations of low symmetry phthalocyanine linked to Fe_3O_4-Ag core-shell or hybrid nanoparticles, New J. Chem. 40 (2016) 10016. https://doi.org/10.1039/c6nj01511e.

[113] I. Venditti, L. Fontana, I. Fratoddi, C. Battocchio, C. Cametti, S. Sennato, F. Mura, F. Sciubba, M. Delfini, M.V. Russo, Direct interaction of hydrophilic gold nanoparticles with dexamethasone drug: Loading and release study, J. Colloid Interface Sci. 418 (2014) 52. https://doi.org/10.1016/j.jcis.2013.11.063.

[114] N. Nwaji, B. Jones, J. Mack, D.O. Oluwole, T. Nyokong, Nonlinear optical dynamics of benzothiazole derivatized phthalocyanines in solution, thin films and when conjugated to nanoparticles, J. Photochem. Photobiol. A Chem. 346 (2017) 46.

https://doi.org/10.1016/j.jphotochem.2017.05.042.

[115] S. Bhat, U. Maitra, Facially amphiphilic thiol capped gold and silver nanoparticles, J. Chem. Sci. 120 (2008) 507. https://doi.org/10.1007/s12039-008-0079-z.

[116] P. Dalgaard, T. Ross, L. Kamperman, K. Neumeyer, T.A. McMeekin, Estimation of bacterial growth rates from turbidimetric and viable count data, Int. J. Food Microbiol. 23 (1994) 391. https://doi.org/10.1016/0168-1605(94)90165-1.

[117] A. Hafeez, Z. Akhter, J.F. Gallagher, N.A. Khan, A. Gul, F.U. Shah, Synthesis, Crystal Structures, and Spectroscopic Characterization of Bis-aldehyde Monomers and Their Electrically Conductive Pristine Polyazomethines, Polymers (Basel). 11 (2019) 1498. https://doi.org/10.3390/polym11091498.

[118] N. Akdemir, Synthesis, characterization and investigation of the spectroscopic properties of novel peripherally 2,3,5-trimethylphenoxy substituted Cu and Co phthalocyanines, the computational and experimental studies of the 4-(2,3,5-trimethylphenoxy)phthalonitrile, J. Turkish Chem. Soc. Sect. A Chem. 3 (2016) 683. https://doi.org/10.18596/jotcsa.287303.

[119] V.A. Oliveira, B.A. Iglesias, B.L. Auras, A. Neves, H. Terenzi, Photoactive: Meso - tetra(4-pyridyl)porphyrin-tetrakis-[chloro(2,2'bipyridine)platinum(II) derivatives recognize and cleave DNA upon irradiation, Dalt. Trans. 46 (2017) 1660. https://doi.org/10.1039/c6dt04634g.

[120] S. Kitaoka, K. Nobuoka, K. Ihara, Y. Ishikawa, A simple method for efficient synthesis of tetrapyridyl-porphyrin using Adler method in acidic ionic liquids, RSC Adv. 4 (2014) 26777. https://doi.org/10.1039/c4ra02522a.

[121] C.M.R. Almeida, B.F.O. Nascimento, M. Pineiro, A.J.M. Valente, Thermodynamic study of the interaction between 5,10,15,20-tetrakis-(N-methyl-4-pyridyl)porphyrin tetraiodine and sodium dodecyl sulfate, Colloids Surfaces A Physicochem. Eng. Asp. 480 (2015) 279. https://doi.org/10.1016/j.colsurfa.2014.12.030.

[122] P. Dechan, G.D. Bajju, P. Sood, U.A. Dar, Crystallographic elucidations of indium(III) porphyrin conformations, morphology and aggregation behaviour: Comparative optical study of free base porphyrins and their indium(III) derivatives at varying pH, J. Mol. Struct. 1183 (2019) 87. https://doi.org/10.1016/j.molstruc.2019.01.064.

[123] K.P. Kepp, A quantitative scale of oxophilicity and thiophilicity, Inorg. Chem. 55 (2016) 9461. https://doi.org/10.1021/acs.inorgchem.6b01702.

[124] M.G. Ribeiro, G.C. Azzellini, Synthesis of New Cationic Metalloporphyrins and Heterodimer Formation with Anionic Metallophthalocyanines, J. Braz. Chem. Soc. 14 (2003) 914. https://doi.org/10.1590/S0103-50532003000600008.

[125] A. Giraudeau, H.J. Callot, M. Gross, Effects of Electron-Withdrawing Substituents on the Electrochemical Oxidation of Porphyrins, Inorg. Chem. 18 (1979) 201. https://doi.org/10.1021/ic50191a042.

[126] M. Uttamlal, A. Sheila Holmes-Smith, The excitation wavelength dependent fluorescence of porphyrins, Chem. Phys. Lett. 454 (2008) 223. https://doi.org/10.1016/j.cplett.2008.02.012.

[127] D. Topkaya, S.Y. Ng, Y. Bretonnière, D. Lafont, L.Y. Chung, H.B. Lee, F. Dumoulin, Iodination improves the phototoxicity of an amphiphilic porphyrin, Photodiagnosis Photodyn. Ther. 16 (2016) 12. https://doi.org/10.1016/j.pdpdt.2016.07.008.

[128] R.M. Amir, F.M. Anjum, M.I. Khan, M.R. Khan, I. Pasha, M. Nadeem, Application of Fourier transform infrared (FTIR) spectroscopy for the identification of wheat varieties, J. Food Sci. Technol. 50 (2013) 1018. https://doi.org/10.1007/s13197-011-0424-y.

[129] M. Kanagaraj, P. Sathishkumar, G.K. Selvan, I.P. Kokila, S. Arumugam, Structural and magnetic properties of $CuFe_2O_4$ as-prepared and thermally treated spinel nanoferrites, Indian J. Pure Appl. Phys. 52 (2014) 124.

[130] M. Chen, Y.G. Feng, X. Wang, T.C. Li, J.Y. Zhang, D.J. Qian, Silver nanoparticles capped by oleylamine: Formation, growth, and self-organization, Langmuir. 23 (2007) 5296. https://doi.org/10.1021/la700553d.

[131] M. Managa, T. Nyokong, Photodynamic antimicrobial chemotherapy activity of gallium tetra-(4-carboxyphenyl) porphyrin when conjugated to differently shaped platinum nanoparticles, J. Mol. Struct. 1099 (2015) 432. https://doi.org/10.1016/j.molstruc.2015.06.077.

[132] K. Gulati, M.S. Aw, D. Losic, Nanoengineered drug-releasing Ti wires as an alternative for local delivery of chemotherapeutics in the brain, Int. J. Nanomedicine. 7 (2012) 2069. https://doi.org/10.2147/IJN.S29917.

[133] T. Mai, J.Z. Hilt, Functionalization of iron oxide nanoparticles with small molecules and the impact on reactive oxygen species generation for potential cancer therapy, Colloids Surfaces A Physicochem. Eng. Asp. 576 (2019) 9. https://doi.org/10.1016/j.colsurfa.2019.05.003.

[134] G. Xu, Y. Chen, M. Tazawa, P. Jin, Surface plasmon resonance of silver nanoparticles

on vanadium dioxide, J. Phys. Chem. B. 110 (2006) 2051. https://doi.org/10.1021/jp055744j.

[135] H. Jia, F. Huang, Z. Gao, C. Zhong, H. Zhou, M. Jiang, P. Wei, Immobilization of ω-transaminase by magnetic PVA-Fe_3O_4 nanoparticles, Biotechnol. Reports. 10 (2016) 49. https://doi.org/10.1016/j.btre.2016.03.004.

[136] T.G.F. Souza, V.S.T. Ciminelli, N.D.S. Mohallem, A comparison of TEM and DLS methods to characterize size distribution of ceramic nanoparticles, J. Phys. Conf. Ser. 733 (2016) 012039. https://doi.org/10.1088/1742-6596/733/1/012039.

[137] M. Danaei, M. Dehghankhold, S. Ataei, F. Hasanzadeh Davarani, R. Javanmard, A. Dokhani, S. Khorasani, M.R. Mozafari, Impact of particle size and polydispersity index on the clinical applications of lipidic nanocarrier systems, Pharmaceutics. 10 (2018) 57. https://doi.org/10.3390/pharmaceutics10020057.

[138] G.L. Flower, S.V. Latha, K.V. Rao, Novel characterization of nanosilver fluid through ultrasonic studies supported by UV-Vis spectroscopy, DLS and TEM studies, J. Mol. Liq. 221 (2016) 333. https://doi.org/10.1016/j.molliq.2016.06.017.

[139] A. Tzani, S. Koutsoukos, D. Koukouzelis, A. Detsi, Synthesis and characterization of silver nanoparticles using biodegradable protic ionic liquids, J. Mol. Liq. 243 (2017) 212. https://doi.org/10.1016/j.molliq.2017.08.039.

[140] S. Sanyasi, R.K. Majhi, S. Kumar, M. Mishra, A. Ghosh, M. Suar, P.V. Satyam, H. Mohapatra, C. Goswami, L. Goswami, Polysaccharide-capped silver Nanoparticles inhibit biofilm formation and eliminate multi-drug-resistant bacteria by disrupting bacterial cytoskeleton with reduced cytotoxicity towards mammalian cells, Sci. Rep. 6

(2016) 24929. https://doi.org/10.1038/srep24929.

[141] M.F. Meléndrez, G. Cárdenas, J. Arbiol, Synthesis and characterization of gallium colloidal nanoparticles, J. Colloid Interface Sci. 346 (2010) 279. https://doi.org/10.1016/j.jcis.2009.11.069.

[142] K. Jyoti, M. Baunthiyal, A. Singh, Characterization of silver nanoparticles synthesized using Urtica dioica Linn. leaves and their synergistic effects with antibiotics , J. Radiat. Res. Appl. Sci. 9 (2016) 217. https://doi.org/10.1016/j.jrras.2015.10.002.

[143] H. Zhang, S. Gao, N. Shang, C. Wang, Z. Wang, Copper ferrite-graphene hybrid: A highly efficient magnetic catalyst for chemoselective reduction of nitroarenes, RSC Adv. 4 (2014) 31328. https://doi.org/10.1039/c4ra05059b.

[144] M.H. Habibi, B. Karimi, Effect of the annealing temperature on crystalline phase of copper oxide nanoparticle by copper acetate precursor and sol-gel method, J. Therm. Anal. Calorim. 115 (2014) 419. https://doi.org/10.1007/s10973-013-3255-4.

[145] A.M. Predescu, E. Matei, A.C. Berbecaru, C. Pantilimon, C. Drăgan, R. Vidu, C. Predescu, V. Kuncser, Synthesis and characterization of dextran-coated iron oxide nanoparticles, R. Soc. Open Sci. 5 (2018) 171525. https://doi.org/10.1098/rsos.171525.

[146] S.P. Dubey, M. Lahtinen, M. Sillanpää, Tansy fruit mediated greener synthesis of silver and gold nanoparticles, Process Biochem. 45 (2010) 1065. https://doi.org/10.1016/j.procbio.2010.03.024.

[147] Y. Ávila-Torres, L. Huerta, N. Barba-Behrens, XPS-characterization of heterometallic

coordination compounds with optically active ligands, J. Chem. 2013 (2013) 370637. https://doi.org/10.1155/2013/370637.

[148] Y. Wang, L. Yinyun, Z. Wenwen, X. Zhaoxiong, Q. Kuang, L. Zheng, Synthesis of Porous Cu2O/CuO Cages using Cu-based Metal-Organic-Framework as Templates and their Gas-sensing Properties, J. Mater. Chem. B. 3 (2015) 12796. https://doi.org/10.1039/x0xx00000x.

[149] K. Hayashi, M. Nakamura, H. Miki, S. Ozaki, M. Abe, T. Matsumoto, T. Kori, K. Ishimura, Photostable iodinated silica/porphyrin hybrid nanoparticles with heavy-atom effect for wide-field photodynamic/photothermal therapy using single light source, Adv. Funct. Mater. 24 (2014) 503. https://doi.org/10.1002/adfm.201301771.

[150] E. Dube, D.O. Oluwole, N. Njemuwa, E. Prinsloo, T. Nyokong, Photophysicochemical and photodynamic therapy properties of metallophthalocyanines linked to gold speckled silica nanoparticles, Photodiagnosis Photodyn. Ther. 25 (2019) 325. https://doi.org/10.1016/j.pdpdt.2019.01.019.

[151] M.C. DeRosa, R.J. Crutchley, Photosensitized singlet oxygen and its applications, Coord. Chem. Rev. 233 (2002) 351. https://doi.org/10.1016/S0010-8545(02)00034-6.

[152] E. Alves, L. Costa, C.M.B. Carvalho, J.P. Tomé, M.A. Faustino, M.G. Neves, A.C. Tomé, J.A. Cavaleiro, A. Cunh, A. Almeida, Charge effect on the photoinactivation of gram-negative and gram-positive bacteria by cationic meso-substituted porphyrins, BMC Microbiol. 9 (2009) 70. https://doi.org/10.1186/1471-2180-9-70.

[153] N. Malatesti, Porphyrin-based cationic amphiphilic photosensitisers as potential anticancer , antimicrobial and immunosuppressive agents, Biophys. Rev. 9 (2017) 149.

https://doi.org/10.1007/s12551-017-0257-7.

[154] B.W. Henderson, D.A. Bellnier, W.R. Greco, A. Sharma, R.K. Pandey, L.A. Vaughan, K.R. Weishaupt, T.J. Dougherty, An in vivo quantitative structure-activity relationship for a congeneric series of pyropheophorbide derivatives as photosensitizers for photodynamic therapy, Cancer Res. 57 (1997) 4000.

[155] N. Malatesti, A. Harej, S. Kraljević Pavelić, M. Lončarić, H. Zorc, K. Wittine, U. Andjelkovic, D. Josic, Synthesis, characterisation and in vitro investigation of photodynamic activity of 5-(4-octadecanamidophenyl)-10,15,20-tris(N-methylpyridinium-3-yl)porphyrin trichloride on HeLa cells using low light fluence rate, Photodiagnosis Photodyn. Ther. 15 (2016) 115. https://doi.org/10.1016/j.pdpdt.2016.07.003.

[156] D.A. Caminos, M.B. Spesia, P. Pons, E.N. Durantini, Mechanisms of Escherichia coli photodynamic inactivation by an amphiphilic tricationic porphyrin and 5,10,15,20-tetra(4-N,N,N-trimethylammoniumphenyl) porphyrin, Photochem. Photobiol. Sci. 7 (2008) 1071. https://doi.org/10.1039/b804965c.

[157] F.M. Engelmann, I. Mayer, D.S. Gabrielli, H.E. Toma, A.J. Kowaltowski, K. Araki, M.S. Baptista, Interaction of cationic meso-porphyrins with liposomes, mitochondria and erythrocytes, J. Bioenerg. Biomembr. 39 (2007) 175. https://doi.org/10.1007/s10863-007-9075-0.

[158] D.M. Mafukidze, A. Sindelo, T. Nyokong, Spectroscopic characterization and photodynamic antimicrobial chemotherapy of phthalocyanine-silver triangular nanoprism conjugates when supported on asymmetric polymer membranes,

Spectrochim. Acta - Part A Mol. Biomol. Spectrosc. 219 (2019) 333. https://doi.org/10.1016/j.saa.2019.04.054.

[159] L. Sobotta, P. Skupin-Mrugalska, J. Piskorz, J. Mielcarek, Porphyrinoid photosensitizers mediated photodynamic inactivation against bacteria, Eur. J. Med. Chem. 175 (2019) 72. https://doi.org/10.1016/j.ejmech.2019.04.057.

[160] S.M. Shabangu, B. Babu, R.C. Soy, M. Managa, K.E. Sekhosana, T. Nyokong, Photodynamic antimicrobial chemotherapy of asymmetric porphyrin-silver conjugates towards photoinactivation of Staphylococcus aureus porphyrin-silver conjugates towards photoinactivation of Staphylococcus aureus, J. Coord. Chem. 73 (2020) 593. https://doi.org/10.1080/00958972.2020.1739273.

[161] K.J. Woo, C.K. Hye, W.K. Ki, S. Shin, H.K. So, H.P. Yong, Antibacterial activity and mechanism of action of the silver ion in Staphylococcus aureus and Escherichia coli, Appl. Environ. Microbiol. 74 (2008) 2171. https://doi.org/10.1128/AEM.02001-07.

Appendix

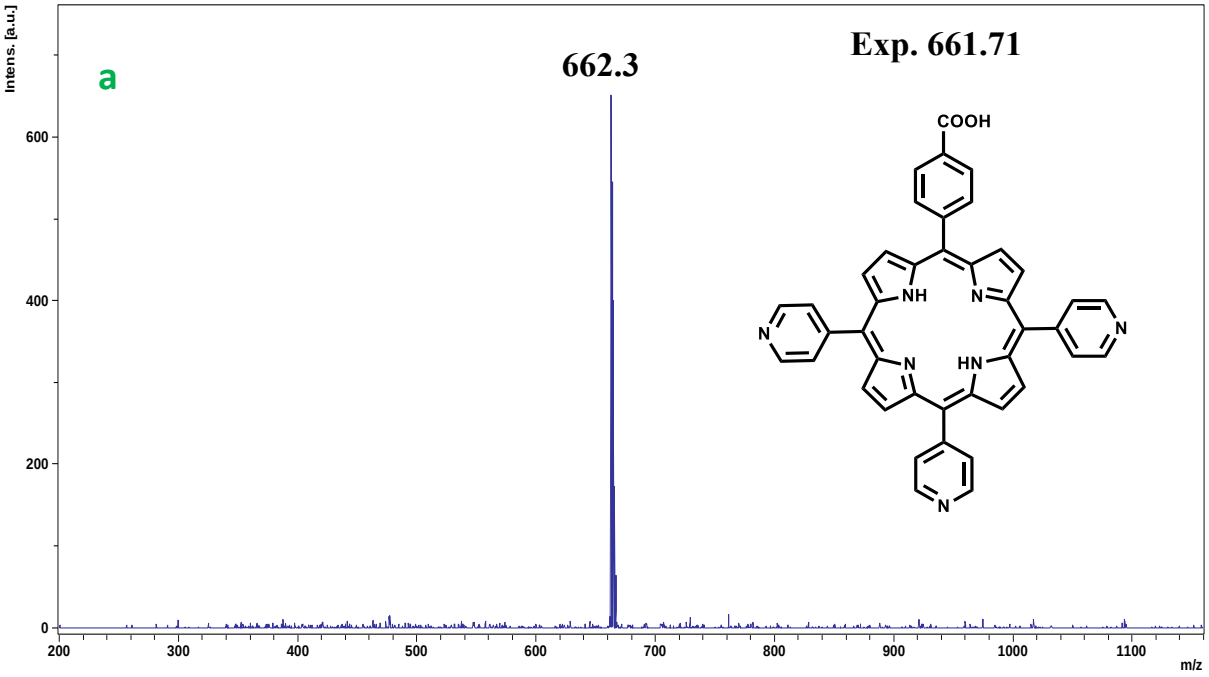

Fig. A1 MALTI-TOF mass spectra for complex **a**.

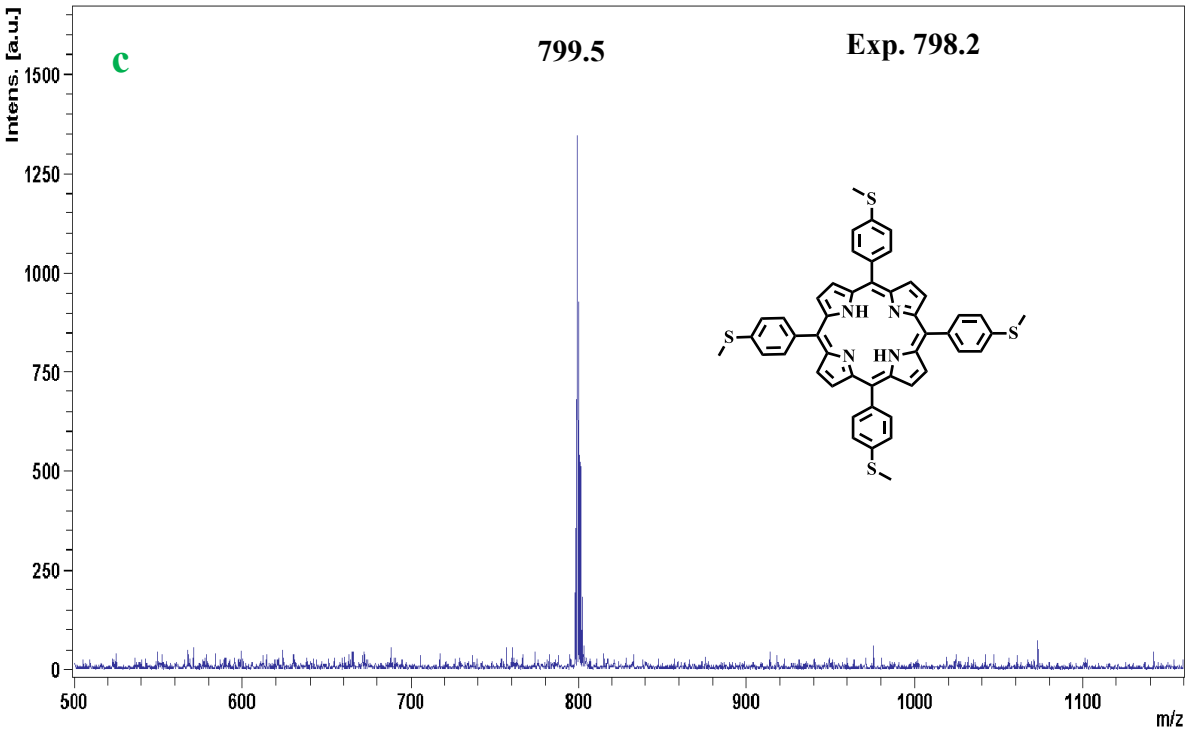

Fig. A2 MALTI-TOF mass spectra for complex **c**.

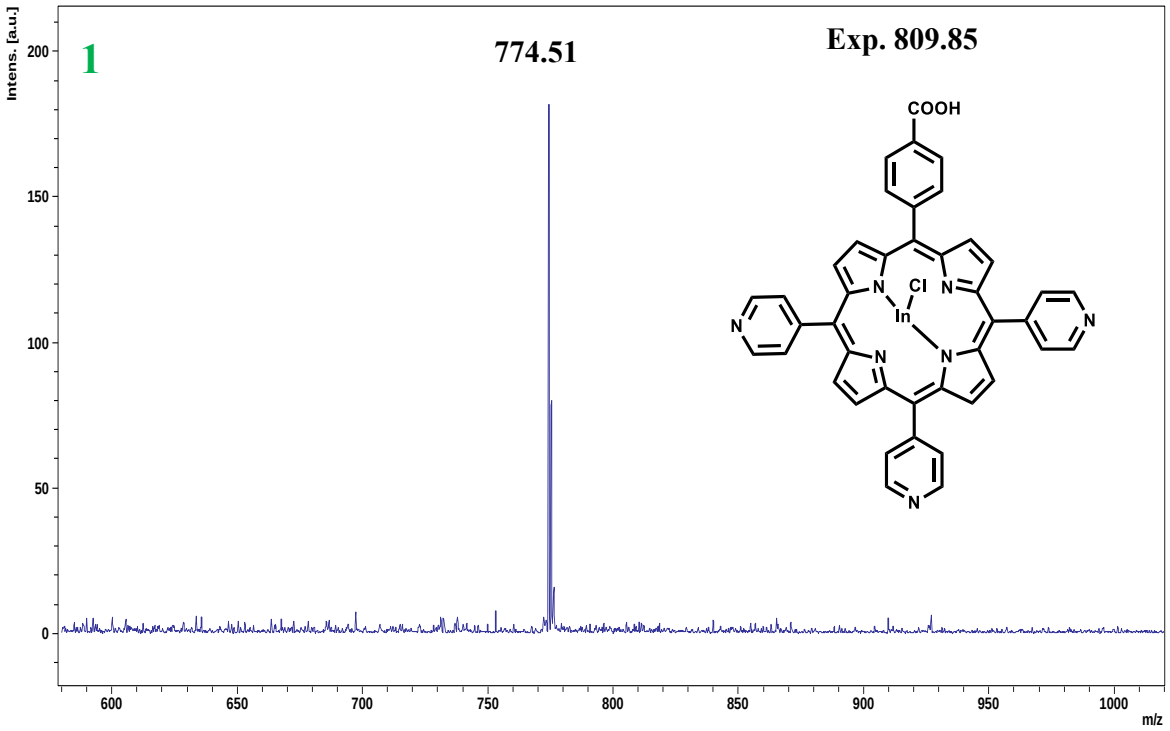

Fig. A3 MALTI-TOF mass spectra for complex **1**.

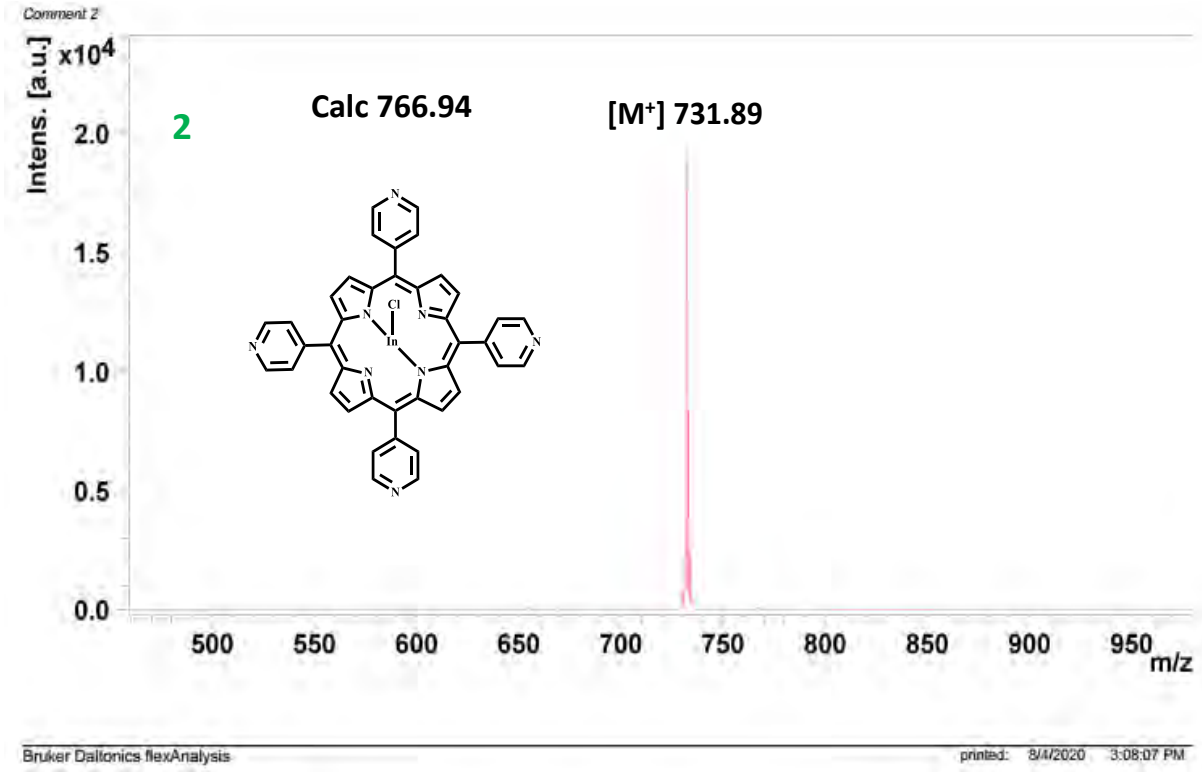

Fig. A4 MALDI-TOF MS data for complex **2**.

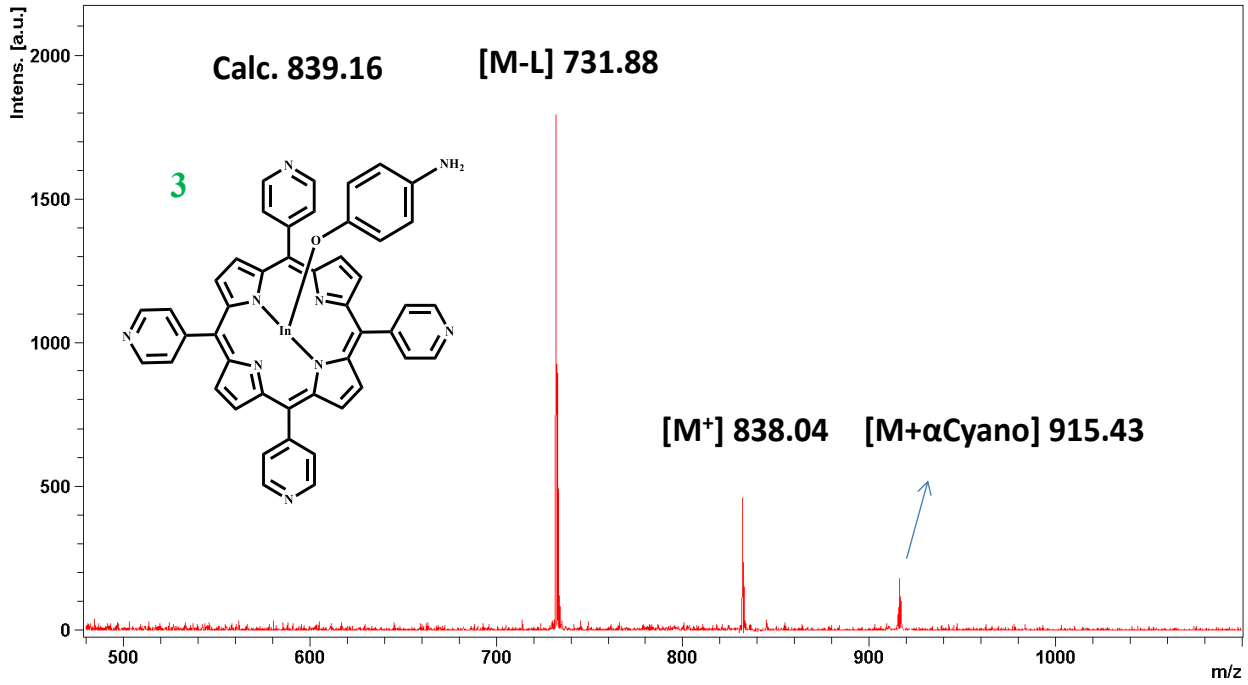

Fig. A5 MALDI-TOF MS data for complex **3**.

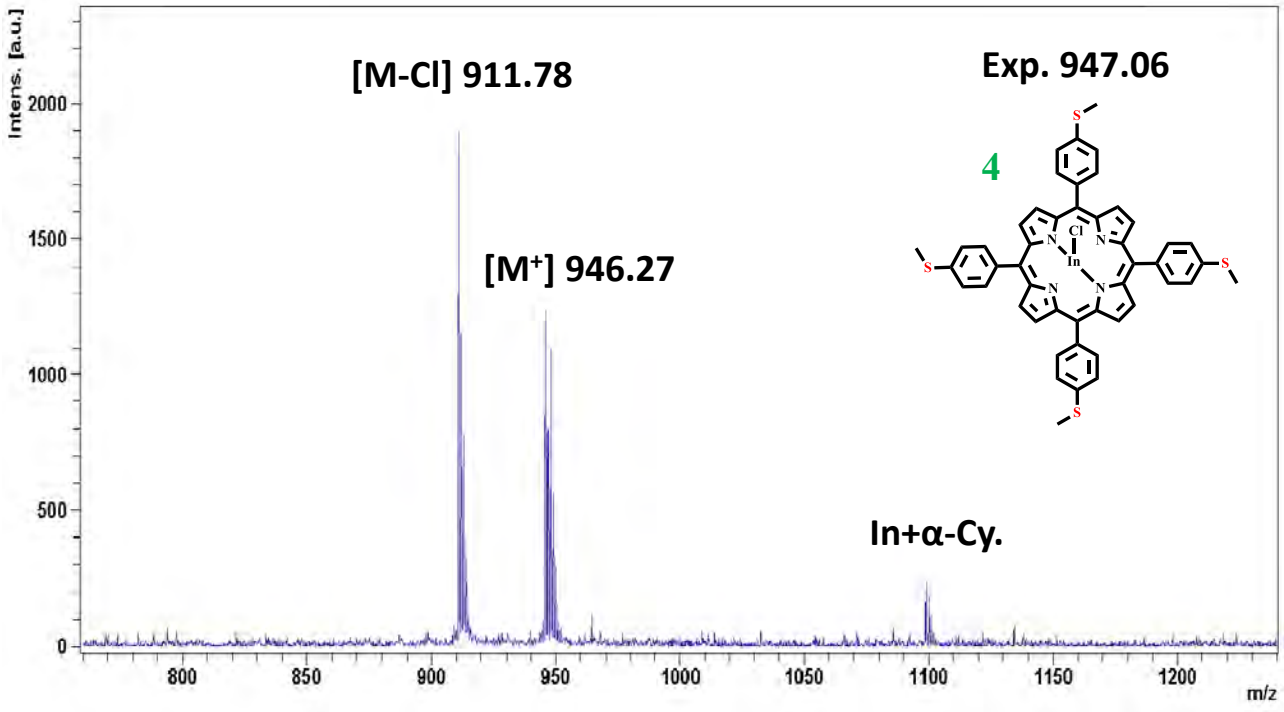

Fig. A6 MALDI-TOF MS data for complex **4**.

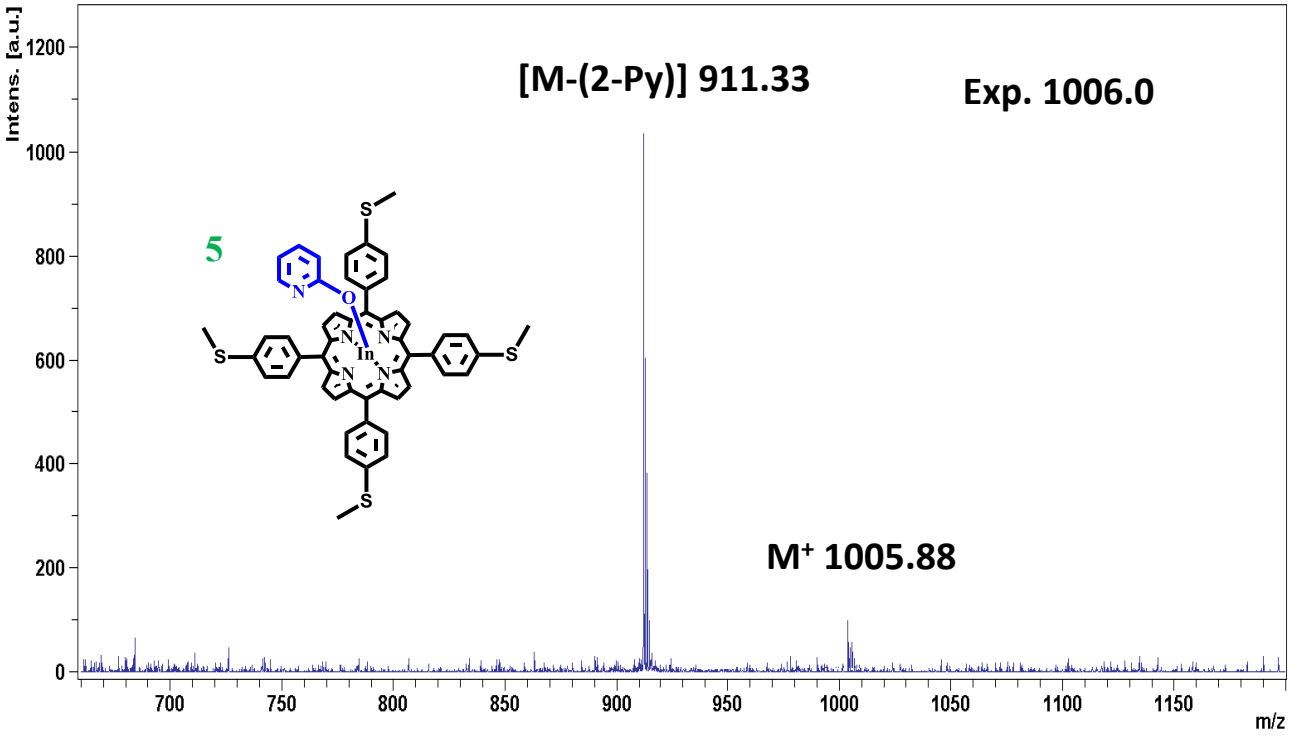

Fig. A7 MALDI-TOF MS data for complex **5**.

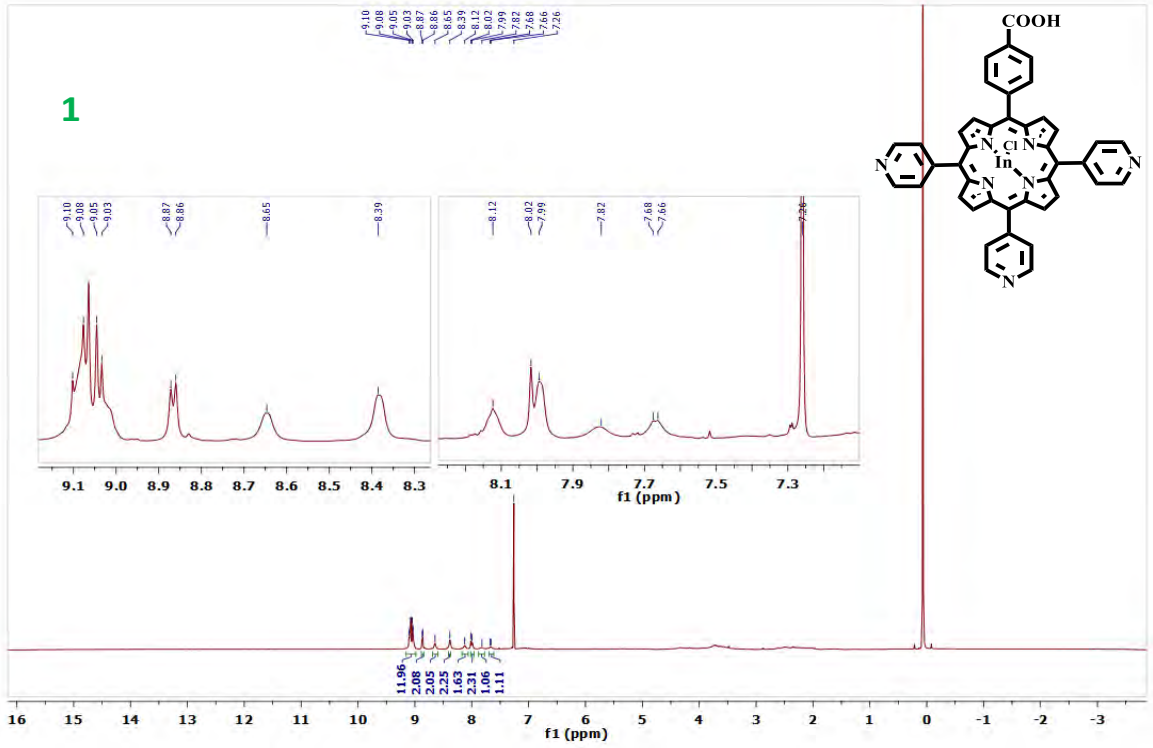

Fig. A8 H^1-NMR spectra for complex **1** in $CdCl_3$

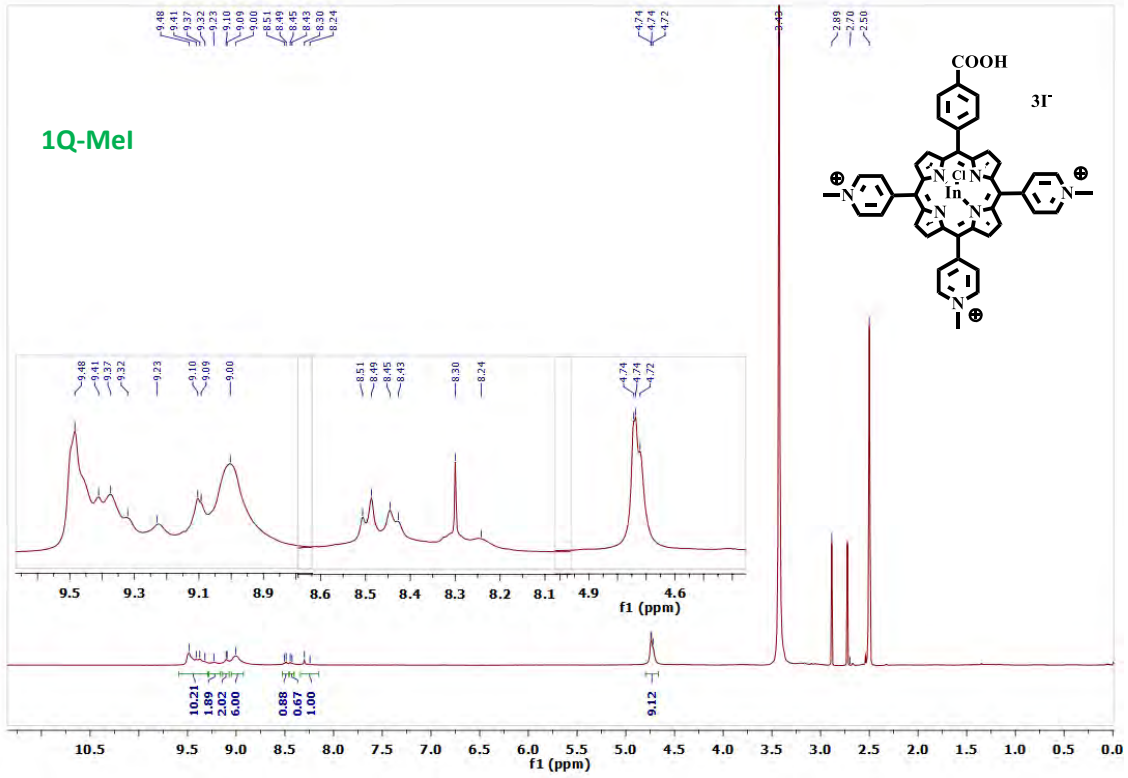

Fig. A9 H^1-NMR spectra for complex **1Q-MeI** in DMSO-d_6

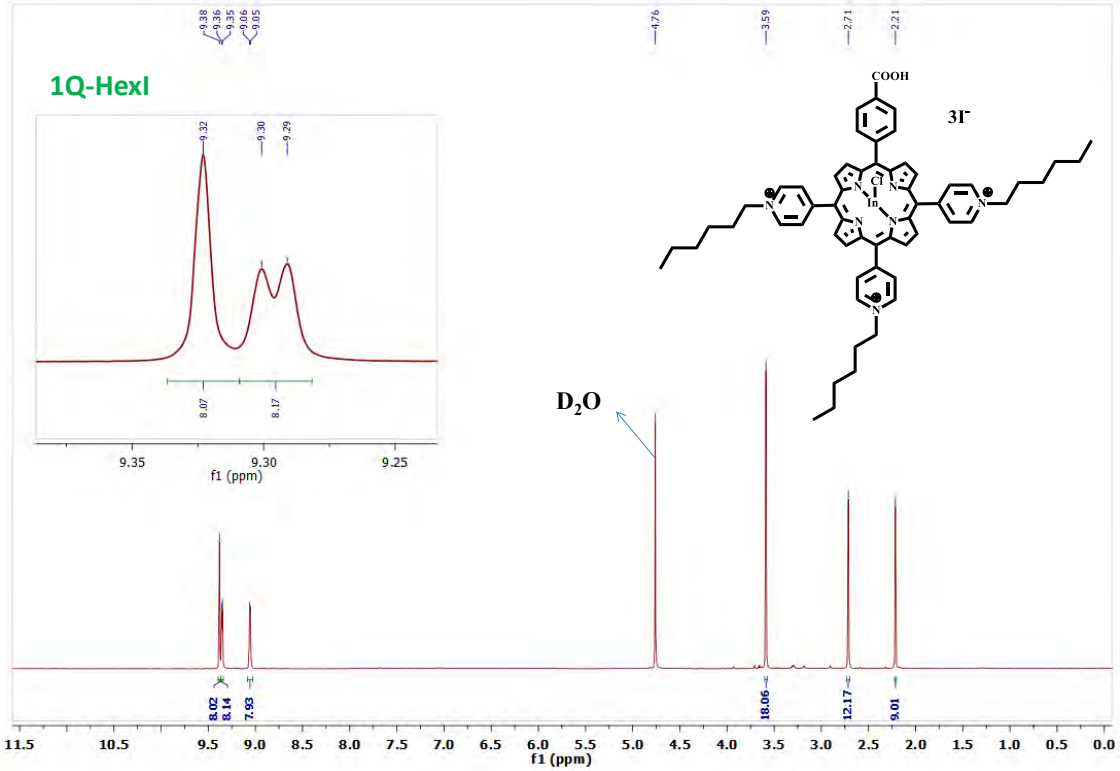

Fig. A10 H^1-NMR spectra for complex **1Q-HexI** in D_2O

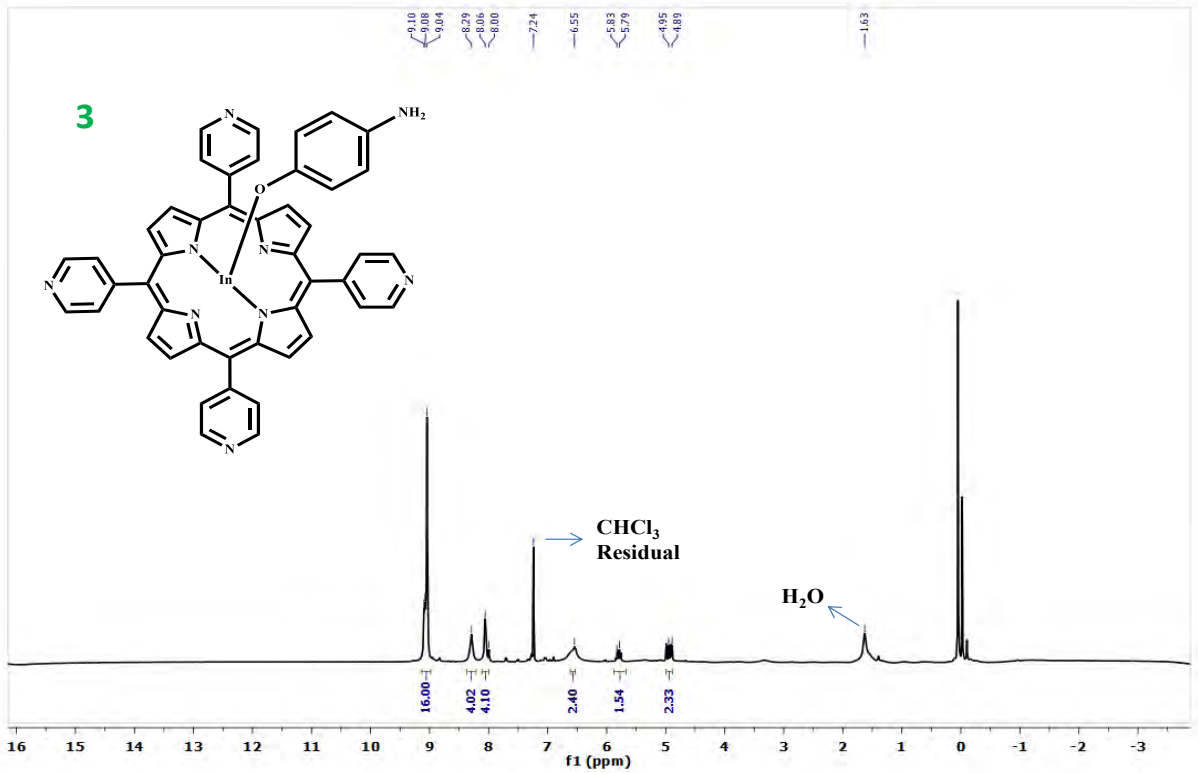

Fig. A11 H^1-NMR spectra for complex **3** in $CdCl_3$

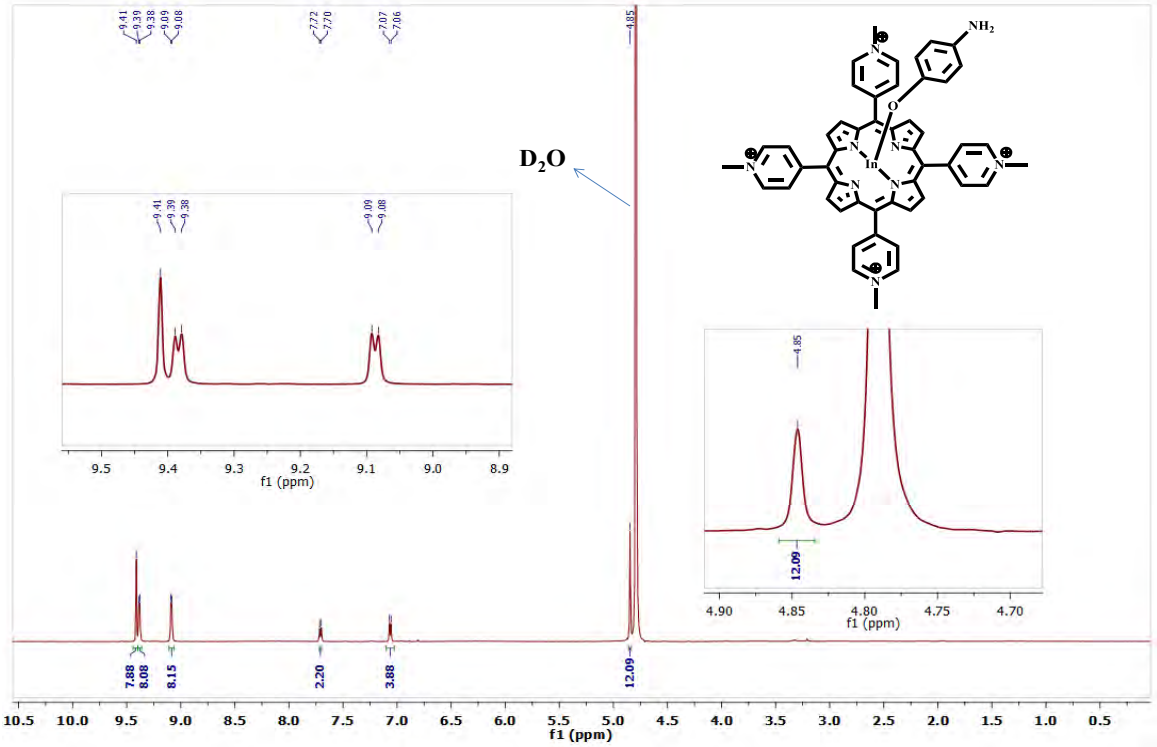

Fig. A12 H^1-NMR spectra for complex **3Q-MeI** in D_2O

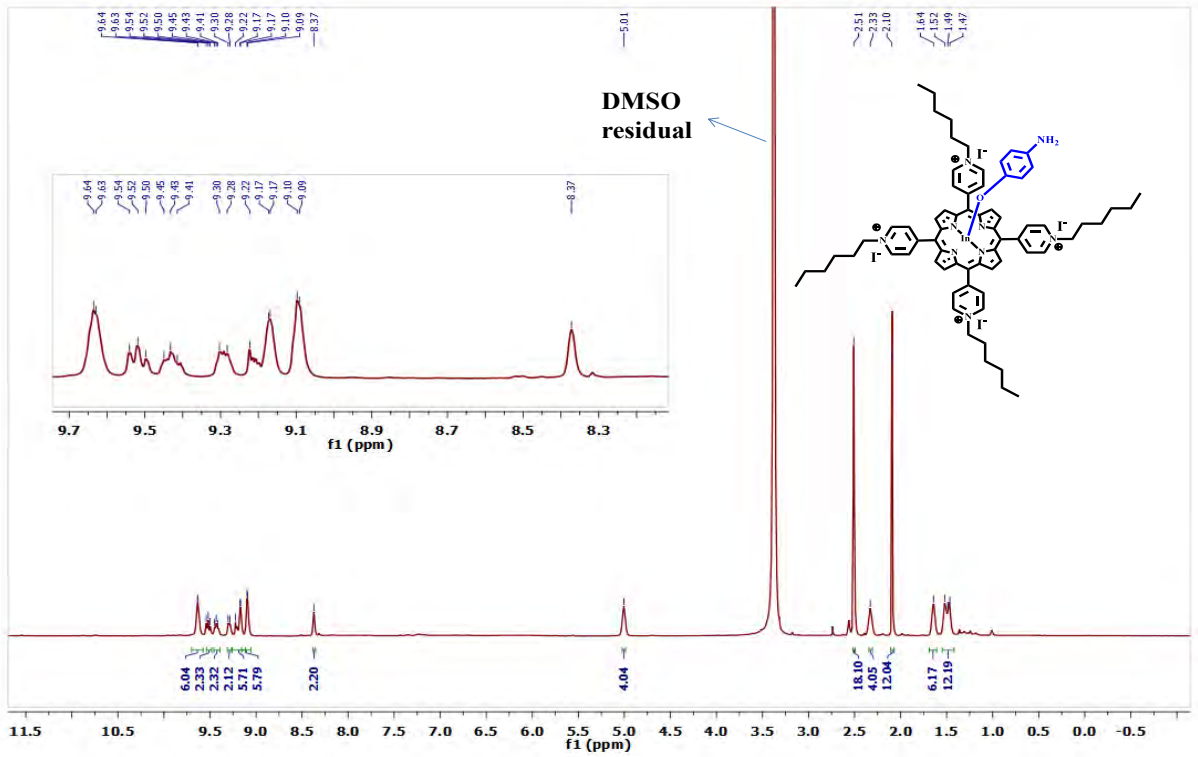

Fig. A13 H^1-NMR spectra for complex **3Q-HexI** in DMSO

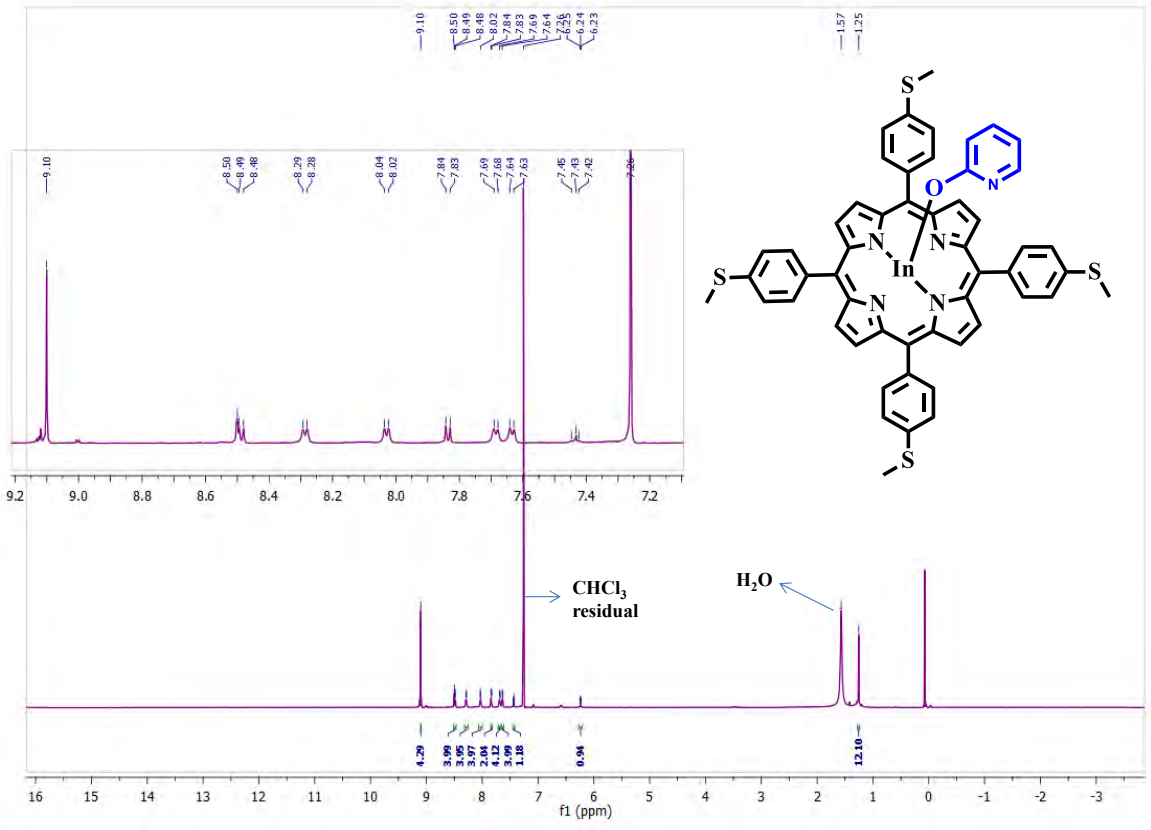

Fig. A14 H^1-NMR spectra for complex **5** in $CdCl_3$

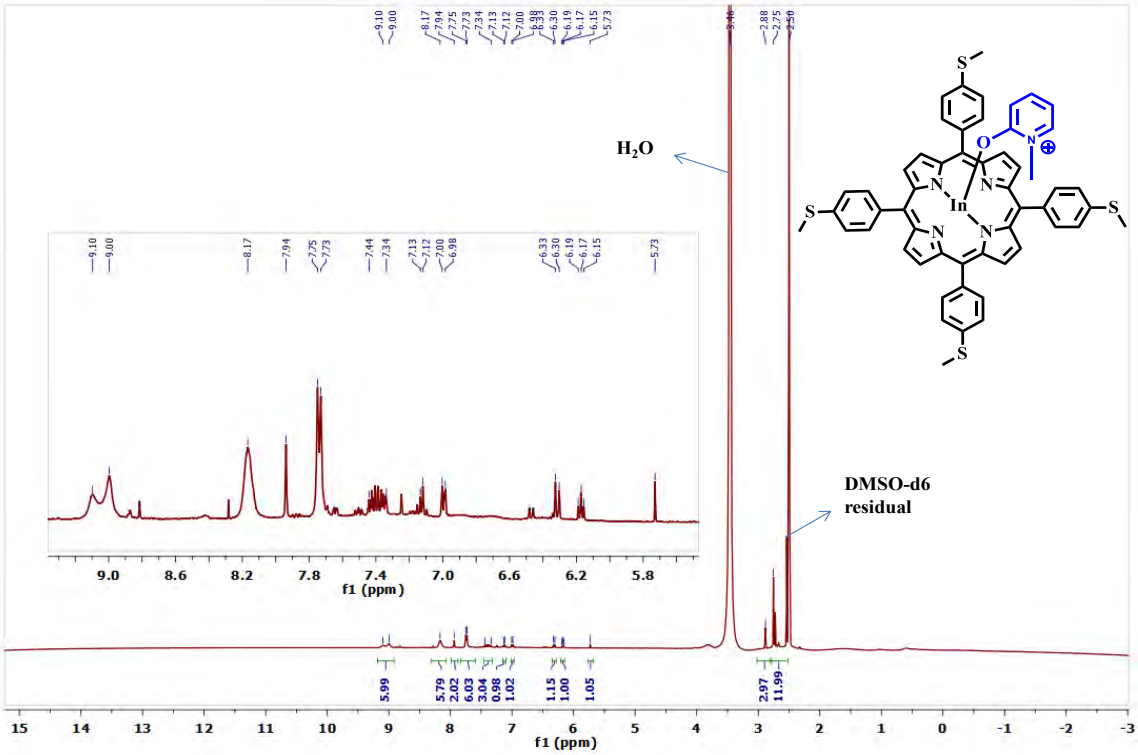

Fig. A15 H^1-NMR spectra for complex **5Q-MeI** in DMSO

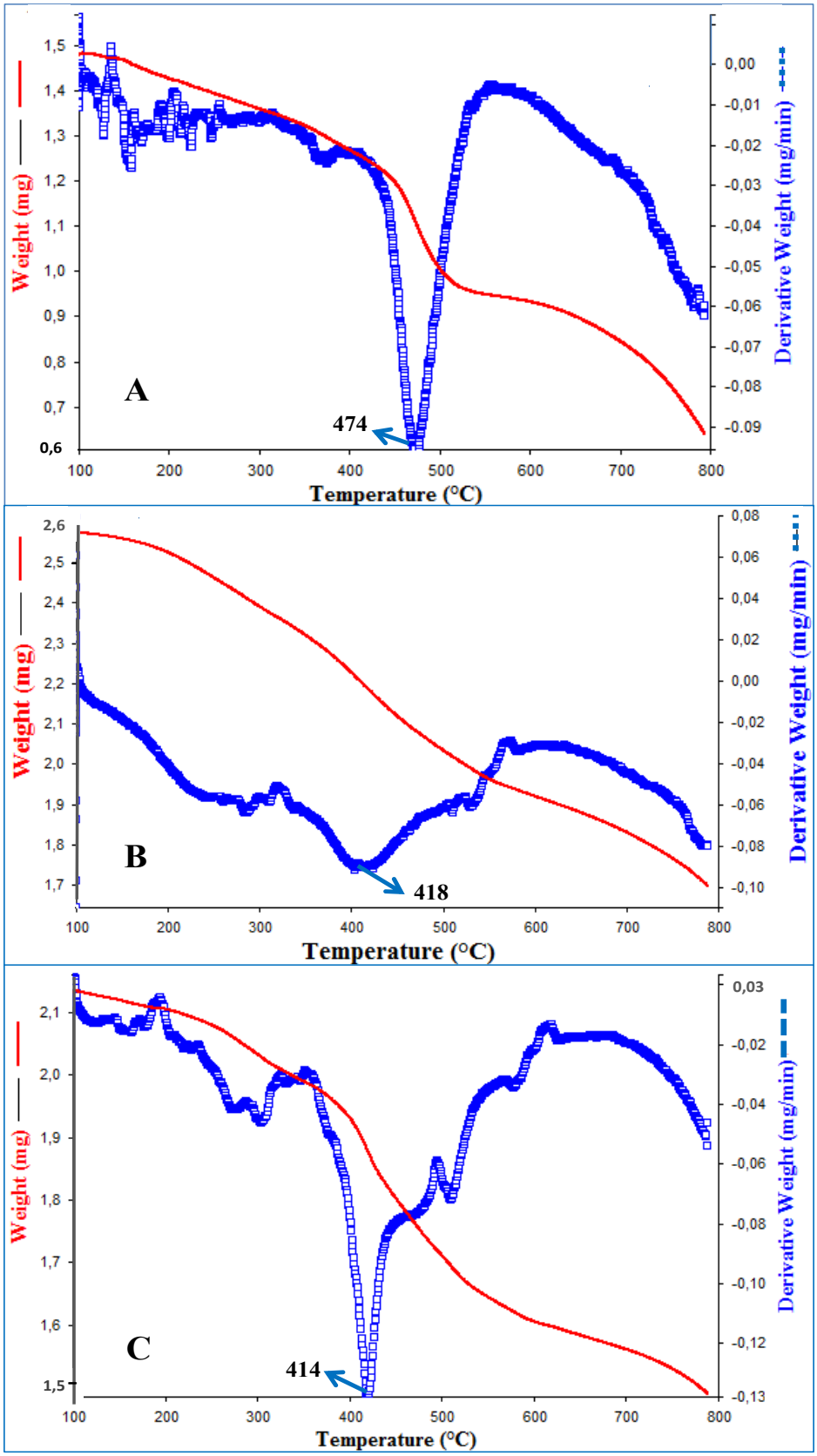

Fig. A16 TGA curves and corresponding DTG analysis of (A) complex **3Q-MeI**, (B) MCH-Ag/$CuFe_2O_4$ nanoparticles, and (C) **3Q-MeI**-MCH-Ag/$CuFe_2O_4$ conjugate.